UNIVERSITY OF OKLAHOMA

GRADUATE COLLEGE

IN SITU AND SATELLITE-BASED ESTIMATES OF AEROSOL-CLOUD INTERACTIONS BETWEEN BIOMASS BURNING AEROSOLS AND MARINE STRATOCUMULUS CLOUDS OVER THE SOUTHEAST ATLANTIC OCEAN

A DISSERTATION

SUBMITTED TO THE GRADUATE FACULTY

in partial fulfillment of the requirements for the

Degree of

DOCTOR OF PHILOSOPHY

By

Siddhant Gupta
Norman, Oklahoma
2021

IN SITU AND SATELLITE-BASED ESTIMATES OF AEROSOL-CLOUD INTERACTIONS BETWEEN BIOMASS BURNING AEROSOLS AND MARINE STRATOCUMULUS CLOUDS OVER THE SOUTHEAST ATLANTIC OCEAN

A DISSERTATION APPROVED FOR THE
SCHOOL OF METEOROLOGY

BY THE COMMITTEE CONSISTING OF

Dr. Greg McFarquhar, Chair

Dr. Jens Redemann

Dr. Evgeni Fedorovich

Dr. Cameron Homeyer

Dr. Jay McDaniel

ABSTRACT

Ubiquitous low-level, marine stratocumulus clouds provide the largest contribution of all cloud types to the shortwave cloud radiative forcing. A cooling effect from small changes in low-level cloud properties due to aerosol-cloud interactions (ACIs) could partially offset the global warming due to increasing greenhouse gas concentrations in the atmosphere. A large marine stratocumulus cloud deck exists over the southeast Atlantic Ocean where the clouds are overlaid by biomass burning aerosols with instances of contact and separation between the aerosol and cloud layers. Biases in satellite retrievals of aerosol and cloud properties and the vertical distance between the aerosol and cloud layers have led to uncertainties in the regional estimates of ACIs and the effective radiative forcing due to ACIs (ERF_{aci}). ERF_{aci} remains the largest source of uncertainty in climate model estimates of Earth's energy budget in future climate scenarios.

In this study, in situ data are used to quantify aerosol-induced changes in stratocumulus cloud properties and to evaluate satellite-based estimates of the aerosol-induced changes. Size distributions of aerosols and cloud droplets were sampled during the three phases of the NASA ObseRvations of Aerosols above CLouds and their intEractionS (ORACLES) field campaign using in situ probes onboard the NASA P-3B aircraft. Size distributions from vertical profiles of aerosol and cloud layers over the southeast Atlantic were used to estimate aerosol concentration (N_a) along with cloud microphysical properties like droplet concentration (N_c), effective radius (R_e), and liquid water content (LWC), optical properties like cloud optical thickness (τ), and macrophysical properties like liquid water path (LWP), cloud geometric thickness (H) and precipitation rate (R_p).

Across the ORACLES campaigns in September 2016, August 2017, and October 2018, 173 "contact" profiles had $N_a > 500$ cm^{-3} within 100 m above cloud tops and 156 "separated" profiles had $N_a < 500$ cm^{-3} up to 100 m above cloud tops. The average N_c, LWC, and τ for contact profiles were 87 cm^{-3}, 0.02 g m^{-3}, and 1.8 higher and R_e was 1.5 μm lower compared to separated profiles. These differences were associated with higher below-cloud N_a and weaker droplet evaporation near cloud top in the presence of high N_a immediately above cloud tops. Larger differences were observed between N_c and R_e for contact and separated profiles in high N_a boundary layers (108 cm^{-3} and 1.8 μm) compared to low N_a boundary layers (31 cm^{-3} and 0.5 μm). A smaller decrease in humidity across cloud top during contact profiles led to a smaller decrease in median N_c and LWC near cloud top (25% and 12%) compared to separated profiles (33% and 18%).

Higher N_c and lower R_e for contact profiles resulted in precipitation suppression with 50% lower R_p compared to separated profiles along with 20% lower precipitation susceptibility to aerosols (S_o). S_o depends on both N_c and R_p, and differences between S_o for contact and separated profiles varied with H due to the co-variability between changes in N_c and R_p due to droplet growth with height and increasing N_a. Based on reanalysis data, contact and separated profiles had statistically similar meteorological conditions like surface temperature (T_o), lower tropospheric stability (LTS), and estimated inversion strength (EIS), on average.

For 67 contact and 82 separated profiles, in situ data were co-located with a retrieval from the Moderate Resolution Imaging Spectroradiometer (MODIS) onboard the Terra or Aqua satellite with a time gap of less than 1 hour. On average, the MODIS R_e, τ, and N_c (11.4 μm, 11.7, and 150.3 cm^{-3}) were 1.7 μm, 2.4, and less than 1 cm^{-3} higher than the in situ R_e, τ, and N_c with Pearson's correlation coefficient (R) = 0.78, 0.72, and 0.90, respectively. The 67 contact profiles had 103 cm^{-3} and 2.8 higher in situ N_c and τ with 2.2 μm lower in situ R_e compared to the 82 separated profiles. MODIS estimates of the differences in R_e, τ, and N_c between contact and separated profiles were within 0.5 μm, 0.7, and 5 cm^{-3} of the in situ estimates when profiles with MODIS R_e > 15 μm and MODIS τ > 25 were removed. Agreement between MODIS and in situ estimates of R_e, τ, and N_c and the aerosol-induced changes in R_e, τ, and N_c was observed due to low biases in MODIS retrievals which were consistent for contact and separated profiles.

The aerosol-induced changes in cloud properties quantified in this study could impact the stratocumulus-to-cumulus or closed-to-open cell transitions in the region. Future work should examine in-cloud aerosol samples from the counterflow virtual impactor inlet to examine the extent of entrainment mixing of aerosols into the cloud layer. Modeling studies should examine the impact of precipitation suppression on cloud lifetime and boundary layer dynamics. Model parameterizations of R_p should be adjusted to account for changes in the relationship between N_c, R_p, and H under different aerosol conditions. Future work should also be aimed at improving satellite-based estimates of the vertical displacement between the aerosol and cloud layers. Combined with MODIS retrievals, this would allow studies of ACIs in marine stratocumulus over longer timescales and larger domains than possible using in situ data alone.

ACKNOWLEDGEMENTS

This work would not be possible without the guidance of my research advisor, Dr. Greg McFarquhar. I want to thank him for giving me the opportunity to attend graduate school, spending countless hours on advising, working through logistics of field campaigns/graduate requirements, and tirelessly reviewing my work. The ORACLES cloud physics research group, consisting of Joe O'Brien, Michael Poellot, David Delene, and Rose Miller, was critical for the development of this work. I am deeply grateful to each of them for their support and guidance during field operations, processing a lot of the cloud probe data, helping analyze the data, and serving as co-authors on the manuscripts written based on this research.

I thank every member of the NASA ORACLES science team led by Jens Redemann, Paquita Zuidema, and Rob Wood. The entire team helped collect the data presented here and guided the data analysis through discussions in the field and during science team meetings and conferences. Data acquisition during ORACLES would not be possible without the support of the Earth Science Project Office at the NASA Ames Research Center and the NASA P-3 flight and maintenance crew at the NASA Wallops flight facility.

I acknowledge the co-authors who helped write the manuscripts based on this research. This includes Amie Dobracki, James Podolske, Jens Redemann, Samuel LeBlanc, Michal Segal-Rozenhaimer, Kristina Pistone, Jennifer Griswold, Ian Chang, Lan Gao, and Feng Xu. All of them reviewed the manuscripts and helped improve the quality of this research. I also thank Jonathan Taylor and 4 anonymous referees for reviewing the manuscripts, and Peter Knippertz and James Haywood for editing the manuscripts.

I am grateful to NASA headquarters for awarding me the NASA Earth and Space Science Fellowship (grant nos. NNX15AF93G and NNX16A018H) for financial support. This research was also supported by NASA under grant no. 80NSSC18K0222. ORACLES was funded by NASA Earth Venture Suborbital-2 grant no. NNH13ZDA001N-EVS2. Some of the computing for this research was performed at the OU Supercomputing Center for Education & Research (OSCER) at the University of Oklahoma (OU).

I thank the staff at the Department of Atmospheric Sciences at the University of Illinois and the School of Meteorology and CIMMS/CIWRO at the University of Oklahoma. They helped me navigate graduate school with ease. I am thankful for having wonderful friends and colleagues at these departments who made the graduate school experience fun, exciting, and enriching. The faculty at these departments have taught me everything I know about meteorology. I thank Drs. Jens Redemann, Evgeni Fedorovich, Cameron Homeyer, Hernan Moreno, and Jay McDaniel for serving on my Ph.D. committee and guiding my progress as a graduate student.

I thank my partner and friends for keeping me motivated throughout the graduate journey. None of this is possible without my mother, father, brother, and family. They have sacrificed before and during my graduate journey, provided support and motivation, and remained enthusiastic about my interests and pursuits throughout my life.

Thank you all.

COPYRIGHT NOTICE

Chapter 2 is adapted from a paper published in *Atmospheric Chemistry and Physics* (Gupta et al., 2021a) with minor formatting changes. The paper is available to public with open access at https://doi.org/10.5194/acp-21-4615-2021. Chapter 3 is adapted from a preprint under peer review in *Atmospheric Chemistry and Physics* (Gupta et al., 2021b). The preprint was edited to include changes based on author responses to reviewer comments. The original preprint is available to public with open access at https://doi.org/10.5194/acp-2021-677. Appendix A is adapted from a supplement to the preprint used for Chapter 3 with minor formatting changes. The supplement is available to public with open access at https://doi.org/10.5194/acp-2021-677.

These documents are distributed under the Creative Commons Attribution 4.0 License (https://creativecommons.org/licenses/by/4.0/) by Copernicus Publications. Under this license, the documents can be shared and adapted if appropriate credit is given, the license is linked, and changes are indicated. For more information on journal policy regarding license and copyright: https://www.atmospheric-chemistry-and-physics.net/policies/licence_and_copyright.html.

Chapter 4 is adapted from a paper planned for submission to *Atmospheric Chemistry and Physics*. This draft is under co-author review and will be submitted to the journal in the near future. Appendix B includes processing codes and tools which are available for public use with proper credit. Some of these codes were developed and modified by previous group members before modifications were made for the current study. Users are advised to contact the author to ensure proper application.

TABLE OF CONTENTS

LIST OF TABLES

LIST OF FIGURES

1 INTRODUCTION

1.1. Marine Stratocumulus Clouds (MSC)

Clouds cover about two-thirds of the Earth's surface (Stubenrauch et al., 2013) and exert a net cloud radiative forcing (CRF) of - 17.1 Wm^{-2} on Earth's energy budget (Loeb et al., 2009). The net CRF includes reflection of shortwave solar radiation to space, which cools the Earth, and the absorption (emission) of longwave radiation, which warms (cools) the Earth. Small changes in low-level cloud properties can modulate global climate. For example, the radiative forcing due to well-mixed greenhouse gases (+ 2.83 W m^{-2}) (Myhre et al., 2013) could be offset by the radiative forcing from a 15 to 20% decrease in droplet sizes for low-level clouds (Slingo, 1990).

MSC are the most common type of low-level clouds with an annual mean coverage of over 20% of the ocean surface (Eastman et al., 2011). These low-level, boundary layer clouds exist over subtropical oceans in regions with large-scale subsidence (Klein and Hartmann, 1993). Cloud cover in these regions depends on sea surface temperature (SST) (Eastman et al., 2011). CRF is thus sensitive to changes in SST but there is a large spread in model estimates of the CRF sensitivity (Bony and Dufresne, 2005). MSC have higher albedo than the ocean surface and a strong shortwave CRF. From 35 ˚S to 35 ˚N, the MSC CRF is between -150 and -200 Wm^{-2} with a 10 - 20% contribution to the CRF (Oreopoulos and Rossow, 2011).

1.2. Aerosol-Cloud Interactions (ACIs)

Among other factors, CRF for MSC depends on the horizontal and vertical distribution of cloud droplets and their size distribution. Cloud droplet size distributions depend on the number, size, composition, and vertical distribution of aerosols. An increase in aerosols acting as cloud condensation nuclei can increase cloud droplet concentration (N_c) and decrease effective radius (R_e). This increases the cloud optical thickness (τ) and shortwave CRF if liquid water content (LWC) remains constant (Twomey, 1974, 1977). The presence of smaller droplets can also inhibit droplet growth and lead to lower precipitation rate (R_p), higher LWC and liquid water path (LWP), and longer cloud lifetime (Albrecht, 1989). Neglecting cloud adjustments in LWP can lead to underestimates of the aerosol effect on cloud albedo because τ has a stronger dependence on LWP than N_c (Platnick and Twomey, 1994; Brenguier et al., 2000).

Precipitation susceptibility to aerosols (S_o) relates the change in R_p due to aerosol-induced changes in N_c as a function of LWP or H (Feingold and Seibert, 2009). S_o depends on processes like collision-coalescence which are parameterized in models (Morrison and Gettelman, 2008; Geoffroy et al., 2010). Estimating the changes in S_o and the aerosol effects on N_c and R_p can help constrain biases associated with climate model parameterizations of N_c and R_p (Geoffroy et al., 2008). The effective radiative forcing due to ACIs (ERF_{aci}) provides the largest source of uncertainty in climate model estimates of Earth's energy budget (Boucher et al., 2013). ERF_{aci} includes the radiative forcing due to aerosol effect on cloud albedo (RF_{aci}) and subsequent cloud adjustments in LWC or LWP (Gryspeerdt et al., 2020).

1.3. Factors that influence ACIs

ACIs depend on thermodynamic parameters like humidity, buoyancy, and inversion strength. For example, enhanced dry-air entrainment can lead to droplet evaporation and decrease the LWC in clouds affected by increasing aerosol concentration (N_a). This can weaken the increase in τ associated with ACIs (Coakley and Walsh, 2002; Rosenfeld et al., 2014). Evaporative cooling from mixing between cloudy air and free-tropospheric air leads to cloud-top instability which is the dominant source of turbulence in MSC (Mellado, 2017). Smaller droplets evaporate more easily leading to cloud-top evaporative cooling and the evaporation-entrainment feedback (Ackerman et al., 2004; Xue and Feingold, 2006; Hill et al., 2008).

LWP can have a positive or negative response to increasing N_c due to aerosols (Toll et al., 2019). The LWP response varies with lower tropospheric stability (LTS), boundary layer depth (H_{BL}), or relative humidity, droplet size distribution, R_p, and by N_c and LWP themselves (Chen et al., 2014; Gryspeerdt et al., 2019; Toll et al., 2019; Possner et al., 2020). The changes in LWP due to increasing N_a must be quantified to estimate the ERF_{aci} (Douglas and L'Ecuyer, 2019; 2020). The difference between process scales for ACIs and the resolution of climate models or satellite retrievals is a major source of uncertainties in RF_{aci} estimates (McComiskey and Feingold, 2012). This can be addressed by combining satellite retrievals with in situ data for specific regimes.

1.4. The Southeast Atlantic Ocean (SEAO)

An important regime for ACIs exists over the SEAO where a large deck of MSC is overlaid by biomass burning aerosols (BBAs) (Haywood et al., 2004). Between July and October, extensive BBA plumes are lofted into the free troposphere over southern Africa (van der Werf et al., 2010; Gui et al., 2021). The BBA plumes are transported by the African easterly jet (Adebiyi and Zuidema, 2016) and overlay MSC with cloud fractions above 60% over the SEAO (Devasthale and Thomas, 2011). Rajapakshe et al. (2017) found the BBA layer was located within 360 m above the MSC for about 60 % of the lidar nighttime scenes over the SEAO. The BBAs are associated with elevated water vapor content (Pistone at al., 2021) and their location can influence cloud-top dynamics (Ackerman et al., 2004) and lead to ACIs (Costantino and Breon, 2010).

Satellite retrievals indicate the SEAO provides the largest contribution to the global RF_{aci} (Douglas and L'Ecuyer, 2020). However, the vertical overlap between BBAs and MSC can impact satellite retrievals of cloud and aerosol properties (Coddington et al., 2010; Meyer et al., 2015). Climate models struggle to estimate the aerosol radiative forcing and the altitude of the BBA layer which has led to biases in climate model estimates of cloud feedbacks and ACIs over the SEAO (Das et al., 2020; Mallet et al., 2021). Recent field campaigns have thus focused on the SEAO due to the unique meteorological conditions present in the region (Zuidema et al., 2016; Redemann et al., 2021).

1.5. ACIs over the southeast Atlantic

In situ observations were made over the SEAO during the NASA ObseRvations of Aerosols above CLouds and their intEractionS (ORACLES) field campaign in September 2016, August 2017, and October 2018 (Redemann et al., 2021). Based on observations from ORACLES, BBAs over the SEAO had 500 nm single scattering albedo between 0.83 and 0.89 which indicates a significant absorbing component (Pistone et al., 2019). However, the sign of the radiative forcing due to shortwave absorption by BBAs depends on the albedo of the underlying MSC (Cochrane et al., 2019). Aerosols above a reflective cloud layer absorb more radiation than aerosols below or within cloud, which can also affect cloud formation (Haywood and Shine, 1997). Warming aloft due to shortwave absorption by BBAs can strengthen the temperature inversion, decrease dry air entrainment, increase LWP, and decrease the shortwave CRF (Wilcox, 2010).

The warming effect of shortwave absorption by BBAs is amplified by droplet evaporation due to the semidirect effect (Hansen et al., 1997; Ackerman et al., 2000). Large-eddy simulations indicate the location of the aerosol layer can impact both the magnitude and sign of the semi-direct forcing (Johnson et al., 2004; McFarquhar and Wang, 2006). Satellite retrievals have been used to quantify ACIs and RF_{aci} over the SEAO (Painemal et al., 2014; Douglas and L'Ecuyer, 2020). However, such studies can have uncertainties depending on the biases in satellite retrievals (Painemal and Zuidema, 2011) and uncertainties in the vertical placement of the aerosol layer (Rajapakshe et al., 2017).

Sinks of N_c, LWC, and LWP like precipitation and entrainment lead to uncertainties in satellite retrievals of N_c which poses a challenge for satellite estimation of RF_{aci} (Quaas et al., 2020). Retrievals from the Moderate Resolution Imaging Spectroradiometer (MODIS) can have biases relative to in situ N_c, R_e, and τ depending on the occurrence of drizzle (Zinner et al., 2010), width and shape of droplet size distributions (Chang and Li, 2002; Brenguier et al., 2011), vertical profile of R_e (McFarquhar and Heymsfield, 1998; Platnick, 2000), or cloud adiabaticity (Min et al., 2012; Braun et al., 2018). Based on a review of N_c from satellite retrievals, Grosvenor et al. (2018) concluded airborne datasets were under-utilized for satellite retrieval evaluation.

Observational studies of ACIs are thus needed to quantify N_c and LWP in different aerosol regimes and complement satellite observations (McComiskey and Feingold, 2012). During ORACLES, N_a, N_c, R_e, and τ were sampled using in situ aerosol and cloud probes at locations where the base of the BBA layer was in contact or separated from the stratocumulus cloud tops. This study quantifies the aerosol-induced changes in cloud and precipitation properties and evaluates MODIS retrievals of N_c, R_e, and τ over the SEAO. The dissertation is organized as follows:

Chapter 2 quantifies aerosol effects on N_c, R_e, and τ using a case study from September 6, 2016. A statistical analysis of six research flights from the 2016 ORACLES campaign quantified the differences between N_c, R_e, and LWC for clouds with variable above- and below-cloud N_a. Chapter

3 examines cloud adjustments associated with the aerosol effects on N_c, R_e, and τ. A statistical analysis of data from 24 research flights from all three ORACLES campaigns was used to quantify aerosol-induced changes in R_p and S_o as a function of H for different aerosol regimes. Chapter 4 quantifies biases in satellite retrievals of N_c, R_e, τ and the aerosol perturbations in N_c, R_e, and τ relative to in situ estimates. The results are used to determine the conditions under which MODIS retrievals can be used to study ACIs over the SEAO. Appendix A describes data comparisons conducted to estimate uncertainties associated with the in situ cloud probes used during ORACLES. Appendix B describes the codes and data processing algorithms developed to process data collected by the 2-Dimensional Stereo Probe (2D-S) and the High Volume Precipitation Sampler (HVPS-3).

2 Impact of the variability in vertical separation between biomass burning aerosols and marine stratocumulus on cloud microphysical properties over the Southeast Atlantic

2.1. Introduction

Clouds cover about two-thirds of the Earth's surface (Stubenrauch et al., 2013) and exert a global net cloud radiative effect (CRE) of about – 17.1 W m^{-2} on Earth's energy budget (Loeb et al., 2009). In comparison, the estimated radiative forcing from 1750 to 2011 due to well-mixed greenhouse gases is +2.83 W m^{-2} (Myhre et al., 2013). The net CRE includes reflection of shortwave solar radiation to space, which cools the Earth, and the absorption (emission) of longwave radiation, which warms (cools) the Earth. Marine stratocumulus is a common cloud type that is observed over oceans off western continental coasts where sea-surface temperatures are low and the boundary layer is capped by a strong inversion (Klein and Hartmann, 1993). From 35° S to 35° N, stratocumulus clouds have a shortwave-plus-longwave top-of-the-atmosphere CRE between −150 and −200 W m^{-2} with a 10 to 20 % contribution to the net CRE (Oreopoulos and Rossow, 2011). General circulation models have large uncertainties and inter-model spread in estimates of the net CRE (Boucher et al., 2013). This is partly due to strong underestimation of the subtropical marine stratocumulus cloud cover and the associated CRE (Wang and Su, 2013).

The radiative impact of stratocumulus depends on many factors, including the horizontal and vertical distribution of cloud droplets, their size distribution, and their number concentration. Stratocumulus properties depend on the number, size, composition, and vertical distribution of aerosols, and meteorological parameters such as boundary layer height, air mass history, and cloud-top instability, all of which can modulate the aerosol loading and influence aerosol–cloud interactions. Increases in aerosols acting as cloud condensation nuclei can increase cloud droplet concentration (N_c) and decrease effective radius (R_e), which increases the cloud optical thickness and shortwave reflectance under conditions of constant liquid water content (LWC) (Twomey, 1974, 1977). Cloud adjustments in response to this aerosol indirect effect can modulate LWC. For example, precipitation suppression in clouds with smaller droplets increases LWC and cloud lifetime, which increases the CRE (Albrecht, 1989). The indirect effect and rapid adjustments in clouds contribute to the effective radiative forcing due to aerosol–cloud interactions (Boucher et al., 2013). Estimates of the effective radiative forcing (−1.2 to 0.0 W m^{-2}) have uncertainties that contribute to the total aerosol radiative forcing, which is "the dominant contributor to overall net Industrial Era forcing uncertainty" (Myhre et al., 2013).

The impact of the indirect effect can depend on above-cloud thermodynamic parameters such as humidity, buoyancy, and inversion strength. Depending on the free-tropospheric humidity, dry-air entrainment can decrease the LWC in clouds with higher N_c due to the indirect effect (Ackerman et al., 2004; Coakley and Walsh, 2002). Enhanced dry-air entrainment can weaken the increase in cloud optical thickness associated with smaller droplets (Small et al., 2009; Rosenfeld et al., 2014). A weak inversion can lead to increased cloud-top entrainment and initiate a stratocumulus-to-cumulus transition by deepening and decoupling the boundary layer, and cutting off the surface moisture source (Wood, 2012). Evaporative cooling from mixing cloudy air with the warm and dry free-tropospheric air entraining into clouds leads to cloud-top instability, which is the dominant source of turbulence in stratocumulus (Mellado, 2017).

One of the largest stratocumulus cloud decks on Earth exists off the coast of Namibia over the Southeast Atlantic Ocean with a cloud fraction of over 60 % between July and October (Devasthale and Thomas, 2011; Zuidema et al., 2016). Biomass burning aerosols (BBAs) that originate from fires in southern Africa (van der Werf et al., 2010) are transported over the stratocumulus by the southern branch of the African easterly jet and overlay the clouds (Adebiyi and Zuidema, 2016). The aerosol layer over time descends and mixes with clouds, affecting cloud microphysical properties and their satellite retrievals (Haywood et al., 2004; Costantino and Breon, 2010). Rajapakshe et al. (2017) found the aerosol layer was located within 360 m above the cloud layer for about 60 % of the Cloud-Aerosol Transport System (CATS) lidar nighttime scenes over the Southeast Atlantic. Observations from the NASA ObseRvations of Aerosols above CLouds and their intEractionS (ORACLES) field campaign found the vertical gap between the aerosol layer and cloud tops changed with longitude, having a maximum separation near 7° E, and had a wide range of values (0 to 2000 m) with near-zero gap for 48 % of the scenes (LeBlanc et al., 2020). The Southeast Atlantic thus serves as a natural laboratory to examine the effects of varying vertical profiles of above-cloud aerosols on cloud microphysics due to instances of both separation and contact between the BBA layer and the stratocumulus.

BBAs over the Southeast Atlantic have 500 nm single-scattering albedo ranging between 0.83 and 0.89 (Pistone et al., 2019), which indicates a significant absorbing component to the BBA layer. The warming associated with shortwave absorption by BBAs over the Southeast Atlantic can be amplified by the evaporation of cloud droplets, the semi-direct effect (Hansen et al., 1997; Ackerman et al., 2000). Aerosols above a reflective cloud layer absorb more solar radiation than aerosols below or within cloud, which affects cloud formation (Haywood and

Shine, 1997) and the region's aerosol direct radiative effect (Keil and Haywood, 2003; Cochrane et al., 2019). Shortwave absorption by above-cloud aerosols can increase the buoyancy above cloud tops, inhibit cloud-top entrainment, and increase liquid water path (Wilcox, 2010). Large-eddy simulations indicate that the location of the aerosol layer impacts both the magnitude and sign of the semi-direct forcing (Johnson et al., 2004; McFarquhar and Wang, 2006). For example, aerosols above the boundary layer lead to a stronger inversion and decrease entrainment. Additionally, aerosols within the boundary layer cause cloud evaporation and boundary layer decoupling.

The treatment of aerosol effects results in inter-model differences in climate simulations, along with biases in satellite retrievals of clouds and aerosols (Haywood et al., 2004; Brioude et al., 2009; Chand et al., 2009; Coddington et al., 2010; Painemal and Zuidema, 2011). Many large-scale models do not adequately consider cloud microphysical responses to the vertical separation of aerosols when evaluating aerosol–cloud interactions (Hill et al., 2008). The ORACLES field campaign provides a unique dataset of in situ observations of cloud and aerosol properties over the Southeast Atlantic (Redemann et al., 2021). The impact of above-cloud BBAs on stratocumulus properties is quantified by comparing in situ cloud measurements from instances with layer separation to instances of contact between the aerosol layer and the clouds.

The remainder of the chapter is organized as follows. The instrumentation used in the analysis is described in Sect. 2.2 along with the procedures for processing the data. A case study of the 6 September 2016 research flight is presented in Sect. 2.3. The meteorological and aerosol conditions present are examined, and profiles of N_c, R_e, and LWC are compared for four sawtooth maneuvers flown at locations where clouds were in contact with and separated from above-cloud

BBAs. In Sect. 2.4, measurements from six research flights are analyzed to investigate buoyancy associated with cloud-top evaporative cooling, and profiles of N_c, R_e, and LWC are compared for boundary layers with similar and varying aerosol loading. Finally, the conclusions and their impact on the understanding of aerosol–cloud interactions are discussed in Sect. 2.5 and 2.6.

2.2. Instrumentation

This study presents in situ measurements of cloud and aerosol properties acquired during the first intensive observation period (IOP) of ORACLES based at Walvis Bay, Namibia (23° S, 14.6° E). The NASA P-3B aircraft conducted research flights west of Africa over the Southeast Atlantic Ocean between 1° W to 15° E and 5° S to 25° S from 27 August to 27 September 2016. The aircraft typically flew 50 m to 7 km above the ocean surface and was equipped with in situ probes for sampling aerosols, clouds, and meteorological conditions (Table 1), among other instrumentation. The Passive Cavity Aerosol Spectrometer Probe (PCASP) measured aerosol from approximately 0.1 to 3.0 µm using three voltage amplifiers: high-, middle-, and low-gain stages (Cai et al., 2013). Laboratory sampling of ammonium sulfate particles conducted after the IOP with the PCASP and a scanning mobility particle size spectrometer (SMPS) adjusted the PCASP concentration within each amplification stage to match the measured SMPS concentration. Thereby, a low bias within the middle- and high-gain stages was corrected to calculate the total aerosol concentration (N_a).

A high-resolution time-of-flight aerosol mass spectrometer (HR-ToF-AMS, or AMS) is used to derive the aerosol mass (M_a) and chemistry, including organic aerosols (OAs) (Table 1). A time- and composition-dependent collection efficiency (CE) was applied to AMS data. The molar ratio of ammonium to sulfate ($NH_4 / (2 \times SO_4)$) was calculated to assess the acidity of liquid aerosol, which is collected more efficiently compared to neutralized aerosol. Thus, CE was determined as the maximum between 0.5 and ($1 - NH_4 / (2 \times SO_4)$), with a value of 0.5 serving as the lower limit, consistent with estimates from most previous field campaigns (Middlebrook et al., 2012). A Single Particle Soot Photometer (SP2) measured refractory black carbon (rBC) concentration, and a $CO/CO_2/H_2O$ gas analyzer measured carbon monoxide (CO) concentration. The Spectrometer for Sky-Scanning, Sun-Tracking Atmospheric Research (4STAR) was used to measure column aerosol optical depth (AOD) and retrieve trace gas concentrations above the aircraft (Dunagan et al., 2013; LeBlanc et al., 2020).

The suite of in situ cloud probes included the Cloud and Aerosol Spectrometer (CAS) on the Cloud, Aerosol, and Precipitation Spectrometer (CAPS); Cloud Droplet Probe (CDP); Phase Doppler Interferometer; Two-Dimensional Stereo Probe (2D-S); Cloud Imaging Probe (CIP) on the CAPS; High Volume Precipitation Sampler (HVPS-3); and the CAPS and King hot wires. These instruments sampled the droplet number distribution function (n(D)) for droplets with diameters ranging from 0.5 to 19 200 µm. The CAPS and King hot wires measured the bulk LWC. Baumgardner et al. (2017) discuss the general operating characteristics and measurement uncertainties of the in situ cloud probes, and McFarquhar et al. (2017) summarize data processing algorithms. Therefore, only aspects of instrument performance unique to ORACLES 2016 are summarized herein. The in situ probes used here (CAS, 2D-S, HVPS-3, and PCASP) were calibrated by the manufacturers prior to and shortly after the deployment. During the deployment, performance checks according to the instrument manuals were completed to determine any change in instrument performance. This included monitoring the CAS and 2D-S voltages and temperatures during flights and passing calibration particles through the CAS sample volume to determine any change in the relationship between particle size and peak signal voltage.

CDP data were unusable for the entire 2016 IOP due to an optical misalignment issue. Data from the components of CAPS (CAS, CIP, and CAPS hot wire) were not available before 6 September 2016 because of improper seating of the analog-to-digital interface board, which resulted in no measurements of droplets less than 50 µm in diameter prior to this flight. The optical lenses were cleaned with isopropyl before each flight, which was especially important during ORACLES since the aircraft frequently flew through aerosol layers that deposited soot on optical lenses of the cloud probes. Stuck bits (photodiodes continuously occluded due to soot deposition) on the optical array probes (2D-S and HVPS-3) were masked during each flight to reduce the presence of artifacts in particle images. The 2D-S vertical channel consistently had photodiode voltages below 1.0 V due to soot deposition on the inside of the receive-side mirror. Therefore, only data from the horizontal channel are used.

The aircraft's true air speed (TAS) was about 15 % higher than the TAS measured by a Pitot tube alongside the CIP. Previous work has shown uncertainties with using the Pitot tube TAS to represent airflow near the probes (Lance et al., 2010; Johnson et al., 2012). Therefore, CAPS, 2D-S, and HVPS-3 probes used the aircraft's TAS, in the absence of reliable TAS measured at these probes' locations. CAPS and PCASP data were processed using the Airborne Data Processing and Analysis processing package (Delene, 2011). 2D-S and HVPS-3 data were processed using the University of Illinois/Oklahoma Optical Array Probe Processing Software (McFarquhar et al., 2018). Droplets measured by the 2D-S and HVPS-3 having aspect ratios greater than 4 or area ratios less than 0.5 were rejected as artifacts because this study focuses on warm clouds with liquid drops sampled above 0 °C. Droplets with inter-arrival times less than 6 µs, indicative of intermittently stuck diodes or drizzle breakup, were removed (Field et al., 2006). Out-of-focus hollow particles were reconstructed following Korolev (2007).

The droplet size distributions from the CAS and 2D-S were merged at 50 µm in diameter to create a combined 1 Hz size distribution, which was used to calculate N_c, R_e, and LWC. While the HVPS-3 sampled droplets larger than 1280 µm in diameter, only three such 1 s samples, with $N < 0.005$ L^{-1}, were sampled during the cloud profiles from the IOP. A threshold of $N_c > 10$ cm^{-3} and bulk LWC > 0.05 g m^{-3} for 1 Hz measurements was used to define cloud samples (cf. Lance et al., 2010; Bretherton et al., 2010). The cloud threshold eliminated the inclusion of optically thinner clouds that a lower LWC threshold of 0.01 g m^{-3} would have included (e.g., Heymsfield and McFarquhar, 2001). Water vapor mixing ratio (q) was determined using a chilled-mirror hygrometer as well as the Los Gatos Research CO/CO_2/H_2O gas analyzer. The hygrometer suffered from cold soaking during descents from higher elevation and measured lower q near cloud tops during descents compared to ascents into cloud. Measurements of q from the gas analyzer had to be masked for near- and in-cloud samples during both ascents and descents due to residual water in the inlet. Therefore, only hygrometer data collected during ascents are used for the analyses involving q.

2.3. Observations on 6 September 2016

2.3.1. Flight track and meteorological conditions

ORACLES research flight tracks included in situ cloud sampling during individual ascents or descents through cloud or during a series of ascents and descents through cloud along a constant heading (sawtooth maneuvers). A case study of the fifth P-3 research flight (PRF5) flown on 6 September 2016 was used to examine aerosol and cloud properties sampled under conditions of both contact and separation between the aerosol layer and cloud tops. PRF5 was selected because it had the highest cloud profiling time among the six PRFs with at least eight cloud profiles (Table 2). Four sawtooth maneuvers (S1–S4) were flown during PRF5 (Fig. 1) along with four individual cloud profiles (P1–P4). Each sawtooth maneuver consisted of four to six individual profiles (Table 2), which were numbered sequentially (S1-1, S1-2, etc.). South-southeasterly winds (5–8 m s^{-1}) were observed at the surface and at 925 mb (Fig. 2a and b). This wind field was associated with a surface low-pressure system east of the study region centered around 17° S, 13° E, which resulted in advection of low clouds toward the northwest. Open and closed cells of marine stratocumulus persisted along with pockets of open cells (POCs) (Fig. 1). S1, S2, and S3 were flown along 9° E in closed cells of marine stratocumulus. S4 was flown closer to the coast in a shallow boundary layer with thin closed-cell stratocumulus (Fig. 1) later in the day compared to S1–S3 (Fig. 3). Ambient temperature sampled by the aircraft sensor was 3 to 6 °C higher during S2 and S3 compared to S1 because the 500 mb geopotential height and relative humidity (RH) were higher toward the north (Fig. 2b). Cloud-top height (Z_T) is identified as the highest altitude satisfying the criteria used to define cloud ($N_c > 10$ cm^{-3} and bulk LWC > 0.05 g m^{-3}). S1, S2, and S3 had higher Z_T compared to S4 (Fig. 3) due to the advection of cold, dry continental air from the southeast and low RH (< 70 %) where S4 was flown, which resulted in cloud thinning and a shallower boundary layer (Fig. 2b and c).

The aircraft intermittently entered and exited cumulus clouds below the stratocumulus layer during 33 of the 71 cloud profiles flown during the IOP (Table 2), which resulted in fluctuating values of N_c and R_e, with bulk LWC < 0.05 g m^{-3}. For example, during S1-3, N_c varied between 10 and 240 cm^{-3}, and R_e varied between 3 and 12 µm up to 130 m below where the stratocumulus base was identified with bulk LWC > 0.05 g m^{-3}. Images from a forward-facing camera on the aircraft contrast a boundary layer with multiple cloud layers (Fig. 4a; image taken at 08:53 UTC) during S1-3 and a shallow, well-mixed boundary layer capped by stratocumulus (Fig. 4b; image taken at 13:16 UTC) during S4-1. It is likely the stratocumulus layer was decoupled from the surface where S1-3 was flown because the boundary layer was deepened by the entrainment of free-tropospheric air. Subsequently, the sub-cloud layer was well-mixed with the surface and topped by shallow cumulus similar to observations by Wood (2012). The cloud base height (Z_B) for the 33 profiles was determined as the lowest altitude with N_c > 10 cm^{-3} and bulk LWC > 0.05 g m^{-3} above which a continuous cloud layer was sampled. S4 had lower Z_B (195–249 m) compared to S1 (676–691 m), S2 (534–598 m), and S3 (501–775 m) (Fig. 3).

2.3.2. Above- and below-cloud aerosol composition

For each sawtooth maneuver, the above- and below-cloud air mass source region was identified using 5 d back trajectories computed using the NOAA Hybrid Single-Particle Lagrangian Integrated Trajectory model (Stein et al., 2015) applied to the National Centers for Environmental Prediction Global Data Assimilation System model (Fig. 5). The concentrations listed in Table 3 indicate measurements up to 100 m above and below the clouds averaged across the cloud profiles for each sawtooth maneuver. The variability in above-cloud M_a and N_a for S1–S4 was driven by the above-cloud air mass source region. The above-cloud air mass sampled near S1 and S4 originated from the boundary layer from the southeast, and the above-cloud air mass sampled near S2 and S3 descended from higher altitudes over the African continent (Fig. 5b and c). The above-cloud OA M_a and N_a for S2 and S3 were over 5 times higher than the corresponding values for S1 and S4 (Table 3). The below-cloud air mass sampled during S1–S4 was advected from the boundary layer from the southeast (Fig. 5a and c). During S1 and S4, the above- and below-cloud rBC and CO concentrations were similar (Table 3) since the above-cloud air mass also originated from the southeast (Fig. 5b and c). During S2 and S3, the continental above-cloud air mass had much higher rBC and CO (over 500 cm^{-3} and 190 ppb) compared to the below-cloud air mass from the southeast (below 150 cm^{-3} and 120 ppb). Since OA, rBC, and CO are indicators of combustion, this suggests the continental above-cloud air mass had greater exposure to biomass burning products compared to the air masses from the southeast. S2 and S3 also had higher below-cloud rBC and CO compared to S1 and S4 (Table 3), which suggests the BBAs with high N_a within 100 m above clouds could be mixing into the cloud layer and polluting the boundary layer. This is also likely to be associated with the history of entrainment mixing of polluted free-tropospheric air into the boundary layer prior to these observations (Diamond et al., 2018).

2.3.3. Cloud profile classification

Every sawtooth maneuver was preceded by a 5–10 min constant-altitude flight leg about 100 m above the cloud layer to retrieve the above-cloud AOD using 4STAR. Average above-cloud AOD at 550 nm within 50 km of the sampling locations for S1–S4 ranged between 0.33 and 0.49, indicating a BBA layer was located at some altitude above the clouds sampled during S1–S4. During S1, above-cloud $N_a < 500$ cm^{-3} was sampled up to 200 m above cloud tops (Fig. 3), which indicates the BBA layer was separated from cloud tops. During S4, the level of above-cloud $N_a > 500$ cm^{-3} was identified over 200 m above cloud tops, indicating a similar separation. Therefore, cloud profiles flown during S1 and S4 were classified as *separated* profiles. During S2 and S3, the level of above-cloud $N_a > 500\ cm^{-3}$ was located within 100 m above cloud tops, and the BBA layer was likely in contact with the cloud tops. Therefore, cloud profiles flown during S2 and S3 were classified as *contact* profiles. In a previous study, a significantly higher threshold (PCASP $N_a = 1000\ cm^{-3}$) was used to identify the BBA layer above stratocumulus clouds off the coast of California (Mardi et al., 2018). The sensitivity of the threshold chosen in this study is examined in Appendix 2.1, and using a threshold of $1000\ cm^{-3}$ would have no significant impact on the results presented in this study.

2.3.4. Vertical profiles of N_c, R_e, and LWC

Since Z_B and cloud thickness (H) varied between profiles, N_c, R_e, and LWC were examined as a function of normalized height above cloud base (Z_N), where $Z_N = (Z-ZB)/(ZT-ZB)$ and varied from 0 (cloud base) to 1 (cloud top). Measurements from the four sawtooth maneuvers were compared following McFarquhar et al. (2007) and divided into 10 Z_N bins, where each bin represented 10 % of the cloud layer (Fig. 6). For example, the bin with $0 < Z_N < 0.1$ (represented by the midpoint, $Z_N = 0.05$) included data collected over the bottom 10 % of the cloud layer. For separated profiles, droplet nucleation occurred near cloud base with the median N_c increasing up to $Z_N = 0.25$ (S1: 132 to $179\ cm^{-3}$; S4: 23 to $85\ cm^{-3}$). The impact of droplet nucleation decreased above cloud base ($Z_N = 0.25$ to 0.75), and median N_c increased by up to $30\ cm^{-3}$ for S1 and decreased by up to $15\ cm^{-3}$ for S4 (Fig. 6a). Condensational growth occurred over these levels as the median R_e increased with Z_N (Fig. 6b). The median N_c decreased near cloud top ($Z_N = 0.75$ to 0.95) due to droplet evaporation resulting from cloud-top entrainment mixing between cloudy and non-cloudy air. Contact profiles (S2 and S3) had higher median N_c at cloud base compared to separated profiles, which decreased with height up to $Z_N = 0.25$ (S2: 190 to

169 cm^{-3}, S3: 180 to 131 cm^{-3}). The median N_c for S2 and S3 increased by up to 43 cm^{-3} over Z_N = 0.25 to 0.75 and decreased near cloud top due to droplet evaporation. S4 had the lowest N_c at cloud base because the below-cloud M_a and N_a for S4 were over a factor of 3 lower than the corresponding values for S1–S3 (Table 3).

Consistent with condensational growth and collision–coalescence, median R_e increased with Z_N from cloud base to top, from 6.0 to 6.7 µm, 4.6 to 6.9 µm, 4.9 to 8.3 µm, and 8.7 to 9.9 µm for S1–S4, respectively (Fig. 6b). S1 and S4 had higher median R_e at cloud base due to higher drizzle (droplets with diameters larger than 50 µm) concentrations (41 and 31 L^{-1}) compared to S2 and S3 (14 and 18 L^{-1}). For S4, drizzle concentration decreased from Z_N = 0.05 to 0.25, which led to the decrease in median R_e over these heights. The median LWC increased with height up to at least Z_N = 0.75 and decreased near cloud tops due to droplet evaporation (Fig. 6c). The LWC for each sawtooth maneuver was lower than the adiabatic LWC (aLWC) due to cloud-top entrainment mixing, and the ratio of LWC to aLWC was used to quantify the degree of mixing. Lower LWC / aLWC (averaged over the cloud layer) for S2 and S3 (0.37 and 0.41) compared to S1 and S4 (0.51 and 0.55) indicated that contact profiles had greater mixing between cloudy and non-cloudy air in the cloud layer, on average. The boundary layer was capped by an inversion with warmer, drier air above the clouds. During S1–S4, the temperature increased above cloud top by 10.3, 9.3, 8.9, and 1.5 °C, and the total water mixing ratio decreased by 6.2, 5.4, 2.3, and 0.4 g kg^{-1}, respectively (Fig. 7). The decreases in N_c and LWC near stratocumulus tops have been attributed to cloud-top entrainment of the overlying warm and sub-saturated air (Wood, 2012). Droplet evaporation due to the entrainment mixing resulted in decreases of 14, 28, 12, and 26 % in the median N_c near cloud tops during S1–S4, respectively.

2.3.5. Evidence of the aerosol indirect effect

N_c and R_e were compared between sawtooth maneuvers, and the differences reported hereafter refer to 95 % confidence intervals for the difference in the variable means (based on a two-sample t test, $p < 0.02$). Between the contact profiles, S2 had significantly higher N_c (differences of 37 to 56 cm^{-3}) compared to S3. This was despite having statistically insignificant differences in below-cloud N_a, a greater fractional decrease in median N_c near cloud top compared to S3, and greater entrainment mixing (lower LWC / aLWC). S2 had significantly higher above-cloud N_a compared to S3 and the mixing of above-cloud air with high N_a likely resulted in droplet nucleation above cloud base, where the median N_c for S2 increased from 169 to 220 cm^{-3} over $Z_N = 0.25$ to 0.75. Between the separated profiles, S1 had significantly higher N_c (differences of 108 to 126 cm^{-3}), which could be attributed to significantly higher above-cloud N_a and greater entrainment mixing during S1 compared to S4. However, these differences could also be due to the meteorological differences at their sampling locations (lower boundary layer height, RH, and 500 mb geopotential height for S4 along with a smaller decrease in T and q_T across cloud tops) or the significantly higher below-cloud N_a for S1 compared to S4.

Contact profiles had significantly higher N_c (differences of 45 to 61 cm^{-3}) and lower R_e (differences of 1.4 to 2.0 μm) compared to separated profiles. Contact profiles also had significantly higher above-cloud N_a and greater entrainment mixing in the cloud layer (lower LWC / aLWC). These microphysical changes would also impact cloud reflectance (Twomey, 1991) as seen by the significantly higher cloud optical thickness (τ) of contact profiles compared to separated profiles (differences of 2.5 to 8.2). The increase in τ and the cloud reflectance provides observational evidence of the aerosol indirect effect over the Southeast Atlantic due to contact between above-cloud BBAs and the stratocumulus clouds.

However, contact profiles also had significantly higher below-cloud N_a (differences of 145 to 190 cm^{-3}), which contribute to the higher N_c relative to separated profiles. Therefore, a statistical analysis was conducted with a larger number of profiles in an attempt to attribute these differences in N_c and R_e to the vertical distance between the above-cloud BBA layer and cloud tops. Building on this case study, 71 cloud profiles flown on six flights between 6 and 25 September 2016 were examined, and the impact of above-cloud BBAs on the free-tropospheric humidity and buoyancy across cloud tops was explored. Sixty-one contact and separated profiles were further classified as low-N_a or high-N_a profiles based on the below-cloud N_a. This was done to quantify the differences in N_c and R_e between contact and separated profiles within boundary layers with similar below-cloud N_a.

2.4. Statistical Analysis

2.4.1. Meteorological conditions and above-cloud aerosols

Six flights (including PRF5) are included in the statistical analysis. On 10, 12, and 25 September, the P-3 took off from Walvis Bay, Namibia (23° S, 14.6° E), and flew northwest from 23° S, 13.5° E toward 10° S, 0° E, returning along the same track (Fig. 8). Different tracks were followed on 6, 14, and 20 September, which included meridional legs along 9, 7.5 and 9° E, and 9 and 10.5° E, respectively. Meteorological conditions on 10, 12, and 14 September were similar to the conditions described for the case study. South-southeasterly surface winds were associated with a surface low-pressure system over Africa. The surface wind speeds varied between 5 and 10 m s^{-1} depending on the pressure gradient between the continental low and a surface high toward the southwest. A region of 925 mb RH < 60 % persisted along the coast due to dry-air advection from Africa. A different meteorological setup on 20 September had westerly surface winds and easterly winds at 925 mb. The aerosol plume was sampled immediately above the boundary layer (600 m) as warm surface air was overlaid by drier, polluted air from the continent. The continental surface low was located farther south on 25 September compared to other flight days with the region of low 925 mb RH to the south of the flight track. The study region had RH > 60 % with south-southeasterly surface winds and southerly 925 mb winds. The BBA layer with above-cloud $N_a > 500$ cm^{-3} was sampled during each flight with variability in its vertical location (Table 4). Only separated profiles were flown on 10 and 14 September (Table 2), when the BBA layer and cloud tops were separated by over 600 and 1500 m, respectively (Table 4). On 12 September, profile 1 (P1) had $N_a > 500$ cm^{-3} within 75 above cloud tops and was classified as a contact profile, while P2 and S1 were classified as separated profiles. On 20 September, each profile had above-cloud AOD > 0.4 and was classified as a contact profile. On 25 September, the profiles had above-cloud AOD > 0.27, and each profile (except from a sawtooth near 11° S, 1° E) was classified as a contact profile.

2.4.2. N_c, R_e, and LWC for contact and separated profiles

Since clouds sampled on different flight days had variable Z_B and Z_T (Fig. 9), vertical profiles of N_c, R_e, and LWC from the contact and separated profiles were compared as a function of Z_N. The frequency distributions of N_c, R_e, and LWC as a function of Z_N are examined in Fig. 10 using violin plots (Hintze and Nelson, 1998; Wang et al., 2020), where the width of the shaded area represents the proportion of data there. The average N_c for contact profiles was significantly higher than the average N_c for separated profiles (differences of 60 to 68 cm^{-3}). During separated profiles, the median N_c had little variability up to $Z_N = 0.75$ (114 to 122 cm^{-3}) and decreased thereafter with Z_N to 73 cm^{-3} due to droplet evaporation (Fig. 10a). During contact profiles, the median N_c decreased slightly up to $Z_N = 0.25$ (183 to 174 cm^{-3}), increased to 214 cm^{-3} at $Z_N = 0.75$, and decreased near cloud top to 157 cm^{-3} due to droplet evaporation. Contact profiles had significantly lower R_e than the separated profiles (differences of 1.1 to 1.3 µm), and the median R_e increased with Z_N from 4.9 to 7.0 µm for contact and from 6.6 to 8.6 µm for separated profiles (Fig. 10b). The differences in R_e were likely due to the significantly lower drizzle concentrations for contact profiles (differences of 5 to 20 L^{-1}).

The average LWC for contact and separated profiles were within 0.01 g m^{-3}, and the median LWC increased with Z_N to 0.23 g m^{-3} at $Z_N = 0.85$ for contact and 0.21 g m^{-3} at $Z_N = 0.75$ for separated profiles (Fig. 10c). Contact profiles had lower LWC / aLWC in the cloud layer (0.45) compared to separated profiles (0.57), which suggests there was greater entrainment mixing during contact profiles, on average. However, droplet evaporation near cloud top had a stronger impact on separated profiles as the median LWC decreased to 0.16 g m^{-3} for separated and 0.20 g m^{-3} for contact profiles (Fig. 10c). Separated profiles had a greater decrease in LWC / aLWC near cloud top (0.41 to 0.26) compared to contact profiles (0.38 to 0.30) and greater fractional decreases in median N_c and LWC (40 and 16 %) compared to contact profiles (25 and 9 %). The stronger impact of droplet evaporation during separated profiles contributed to the differences between N_c for contact and separated profiles.

2.4.3. Cloud-top evaporative cooling

Buoyancy and humidity across cloud tops were determined to explore the cloud-top entrainment mechanisms resulting in the differential impact of droplet evaporation for these profiles. Cloud-top instability is the dominant source of turbulence in stratocumulus, with evaporative cooling being a key driver of instability (Mellado, 2017). Recent studies have shown there is strong correlation between above-cloud AOD and water vapor within air masses originating from the African continent (Deaconu et al., 2019; Pistone et al., 2021). Longwave cooling by water vapor within the BBA layer leads to decreased cloud-top cooling, and cloud-top dynamics are influenced by distinct radiative contributions from water vapor and absorbing aerosols. Evaporative cooling in a mixture of dry and cloudy air near cloud top generates negatively buoyant air mixtures, which further enhances mixing and leads to an entrainment feedback called cloud top entrainment instability, or CTEI (Kuo and Schubert, 1988). Under such conditions, negative buoyancy leads to an unstable feedback, unlike the conventional association of negative buoyancy with atmospheric stability. The critical condition for cloud-top stability is given by Kuo and Schubert (1988) as

$$\Delta\theta_e > k\left(\frac{L_v}{C_p}\right)\Delta q_T \quad , \tag{1}$$

where k is the CTEI parameter, θ_e is the equivalent potential temperature, L_v is the latent heat of vaporization, and C_p is the specific heat capacity of air at constant pressure. The Δ operator represents gradients across the cloud top, defined here as the difference between θ_e (or q_T) measured 100 m above cloud top and the vertical average of θ_e (or q_T) over the top 100 m of the cloud profile. Following Eq. (13) from Kuo and Schubert (1988), $k > 0.23$ indicates negative buoyancy across cloud tops. Water vapor mixing ratio measured by the chilled-mirror hygrometer was used to calculate θ_e and q_T. Since lower Δq_T was sampled during descents into cloud due to condensation on the hygrometer, k values for descents were determined to be measurement artifacts and not usable here.

All separated profiles (except PRF5 S1-3 and S4-1, S4-3, and S4-5) laid within the region of cloud-top instability ($k > 0.23$) on a $\Delta\vartheta_e$–Δq_T plane (Fig. 11) and showed negative buoyancy across cloud tops. During PRF5 S1-3, low $\Delta\vartheta_e$ was sampled due to higher above-cloud humidity associated with the presence of $N_a > 100\ cm^{-3}$ within 50 m above cloud tops. During PRF5 S4, a weak cloud-top inversion led to positive $\Delta\vartheta_e$ and $\Delta q_T < -2\ g\ kg^{-1}$ (Fig. 7). For the remaining separated profiles, negative buoyancy across cloud tops led to forced descent of dry free-tropospheric air into the clouds. Since the free-tropospheric air was warmer and drier than the cloudy air, droplet evaporation led to the decreases in median N_c and LWC near cloud top. The positive evaporative cooling feedback and greater Δq_T compared to contact profiles (Fig. 11) explain the stronger impact of droplet evaporation on median N_c and LWC for separated profiles. While evaporative cooling triggered the CTEI feedback, the clouds persisted, consistent with cloud-top radiative cooling or surface evaporation leading to boundary layer moistening (Lock, 2009; Mellado, 2017).

All contact profiles (except PRF13 S1-3) laid within the region of cloud-top stability and showed positive buoyancy across cloud tops. Entrainment mixing for these profiles likely occurred when the clouds penetrated the inversion. This is consistent with significantly higher average H (267 m) for contact profiles compared to separated profiles (213 m). Braun et al. (2018) found a negative correlation between H and adiabaticity (ratio of the measured and the adiabatic liquid water path), which is consistent with contact profiles having lower LWC / aLWC and higher H compared to separated profiles. In the presence of above-cloud BBAs, the above-cloud air was more humid, and the above-cloud N_a was significantly higher compared to separated profiles (differences of 768 to 831 cm^{-3}). Contact profiles had greater entrainment mixing compared to separated profiles, and the median N_c increased with height over $Z_N = 0.25$ to 0.75. It is likely the entrainment of BBAs into clouds resulted in additional droplet nucleation over these Z_N levels. Therefore, weaker droplet evaporation near cloud top and additional droplet nucleation above cloud base in the presence of above-cloud BBAs likely contributed to the differences between N_c for contact and separated profiles.

2.4.4. N_c, R_e, and LWC in boundary layers with similar N_a

Contact profiles had significantly higher below-cloud N_a (differences of 93 to 115 cm^{-3}) and below-cloud CO (differences of 13 to 16 ppb) in addition to higher above-cloud N_a (differences of 768 to 831 cm^{-3}) compared to separated profiles. Enhanced aerosol loading within the boundary layer is consistent with BBAs immediately above cloud tops entraining into the cloud layer and polluting the boundary layer. This is consistent with higher above-cloud CO (240 ppb) sampled for contact profiles with below-cloud CO > 100 ppb compared to above-cloud CO (104 ppb) for profiles with below-cloud CO < 100 ppb. The correlations between above- and below-cloud aerosols could be partly due to the history of entrainment mixing between free-tropospheric and boundary layer air masses (Diamond et al., 2018). To investigate the contribution of below-cloud N_a relative to the impact of above-cloud BBAs on cloud properties, 28 contact and 33 separated profiles were classified into four new regimes defined as follows: contact high N_a (C-H), separated high N_a (S-H), contact low N_a (C-L), and separated low N_a (S-L), where high- and low-N_a boundary layers were separated using a threshold concentration of 350 cm^{-3}. Cloud microphysical properties and above- and below-cloud N_a were compared between 20 C-H and 11 S-H profiles and between 8 C-L and 22 S-L profiles (Table 5) to compare contact and separated profiles with minor differences in below-cloud N_a.

Within low-N_a boundary layers, C-L and S-L profiles had insignificant differences in below-cloud N_a despite significantly higher above-cloud N_a for C-L profiles (differences of 592 to 669 cm^{-3}), higher N_c (differences of 22.8 to 34.9 cm^{-3}), and lower R_e (differences of 0.5 to 1.0 µm) compared to S-L profiles. Within high-N_a boundary layers, C-H profiles had significantly higher below-cloud N_a compared to S-H profiles (differences of 39.1 to 70.5 cm^{-3}), but the differences were much smaller than those in the above-cloud N_a (differences of 738 to 884 cm^{-3}). Further, the C-H profiles had significantly higher N_c (differences of 75.5 to 88.5 cm^{-3}) and lower R_e (differences of 1.1 to 1.3 µm) than the S-H profiles. Previous studies have argued the changes in N_c due to the impact of BBAs are more strongly correlated with below-cloud N_a compared to above-cloud N_a (Diamond et al., 2018; Mardi et al., 2019). However, these results suggest that, although the differences in N_c were lower than the differences in above-cloud N_a, significant changes in N_c and R_e were associated with contact with above-cloud BBAs, and these changes were independent of the below-cloud aerosol loading.

Vertical profiles of N_c, R_e, and LWC are examined (Fig. 12) to further investigate the microphysical changes due to contact with above-cloud BBAs. Within low-N_a boundary layers, there were minor deviations in N_c with Z_N up to $Z_N = 0.75$ (Fig. 12a). Over the top 20 % of the cloud layer, S-L profiles had a decrease in median N_c (32 cm^{-3}), with a smaller change for C-L profiles (8 cm^{-3}) over the same levels. There was also a weaker decrease in water vapor mixing ratio across cloud tops for contact profiles. Thus, cloud-top entrainment of more humid air likely occurred for the C-L profiles. This is consistent with higher median R_e and LWC over $Z_N = 0.75$ to 0.95 for C-L profiles compared to S-L profiles despite having lower R_e and LWC closer to cloud base (Fig. 12b and c). Thus, the microphysical differences between contact and separated profiles within low-N_a boundary layers (where most separated profiles were sampled) are consistent with the processes of cloud-top entrainment and droplet evaporation.

The differences between below-cloud N_a for C-H profiles and that for S-H profiles (39.1 to 70.5 cm^{-3}) were lower than the corresponding differences in N_c (75.5 to 88.4 cm^{-3}). C-H profiles had significantly higher N_c and lower R_e compared to S-H profiles throughout the cloud layer (Fig. 12a and b). There was a significant increase in median N_c for C-H profiles over Z_N = 0.25 to 0.75, which was accompanied by higher median LWC for C-H profiles in the top half of the cloud layer. This is consistent with additional droplet nucleation above cloud base during C-H profiles. Additionally, there was a stronger decrease in N_c near cloud top for S-H profiles (N_c decreased by 66 cm^{-3}) compared to C-H profiles (N_c decreased by 29 cm^{-3}) likely due to cloud-top entrainment. It is difficult to separate the impact of changes in droplet nucleation on differences in N_c between C-H and S-H profiles from the impact of changes in droplet evaporation due to cloud-top entrainment. Therefore, it is speculated the microphysical changes within high-N_a boundary layers were likely driven by the combination of higher below-cloud N_a, potential droplet nucleation above cloud base, and weaker droplet evaporation near cloud tops in the presence of above-cloud BBAs. The sensitivity of these results to using different thresholds to locate BBAs (other than 500 cm^{-3}), to define “separation” between the aerosol and cloud layers (other than 100 m), and to define a “high-N_a boundary layer” (other than 350 cm^{-3}) is discussed in Appendix 2.1 but does not affect the qualitative findings.

2.5. Discussion

The presence of water vapor and absorbing aerosols within the BBA layer can have distinct impacts on cloud-top cooling and cloud-top dynamics (Deaconu et al., 2019; Herbert et al., 2020; Kuo and Schubert, 1988). In the presence of above-cloud BBAs during ORACLES, the above-cloud air was more humid than in its absence, and cloud-top entrainment of free-tropospheric air with a higher water vapor mixing ratio likely contributed to the microphysical differences between contact and separated profiles, consistent with previous observations (Ackerman et al., 2004). Further, C-H profiles had significantly lower drizzle concentration compared to S-H profiles (differences of 4 to 21 L^{-1}), but C-L and S-L profiles had similar drizzle concentrations (61 and 62 L^{-1}). Research is ongoing to examine the changes in cloud and precipitation properties in different aerosol regimes since precipitation suppression could also impact below-cloud N_a through reduced aerosol scavenging by drizzle (Pennypacker et al., 2020).

Within polluted boundary layers, the below-cloud N_a was larger for instances of contact between above-cloud BBAs and cloud tops. It is speculated the increase in below-cloud N_a alone would be insufficient to cause the microphysical differences between contact and separated profiles, and this is particularly true for polluted boundary layers. The N_c also depends on other factors, including updraft strength and aerosol composition and hygroscopicity (Fuchs et al., 2018; Kacarab et al., 2020; Mardi et al., 2019). High-resolution modeling studies with bin-resolved microphysics are needed to examine cloud-top entrainment processes and investigate the relative impact of semidirect and indirect effects of BBAs on marine stratocumulus over the Southeast Atlantic. Additionally, aerosol–cloud–precipitation interactions must be examined under different aerosol and meteorological regimes to investigate the buffering effects of local meteorology and thermodynamic profiles associated with the absorbing aerosols (Deaconu et al., 2019; Diamond et al., 2018; Fuchs et al., 2018; Herbert et al., 2020; Sakaeda et al., 2011; Stevens and Feingold, 2009).

The changes in N_c, R_e, and drizzle concentration presented here could lead to aerosol-induced precipitation suppression and impact stratocumulus-to-cumulus transitions over the Southeast Atlantic (Yamaguchi et al., 2015; Zhou et al., 2017). Subsequently, changes in precipitation rate could affect the balance between aerosol scavenging and entrainment and modulate the reversible open–closed-cell transitions (Abel et al., 2020; Feingold et al., 2015). These processes would affect the cloud radiative forcing and the direct aerosol radiative forcing, which depends on the albedo of the underlying cloud layer (Cochrane et al., 2019). Research is ongoing to quantify precipitation susceptibility as a function of the vertical displacement of above-cloud absorbing aerosols from cloud tops. A larger dataset including additional ORACLES observations from August 2017 and October 2018 will allow evaluation of cloud and precipitation retrievals (Dzambo et al., 2019; Painemal et al., 2020) and investigations of aerosol–cloud–precipitation interactions over a broader range of environmental conditions. Better understanding of these processes will help reduce uncertainties in the estimates of cloud radiative effects due to changes in cloud cover and cloud reflectance (Albrecht, 1989; Twomey, 1974, 1991).

2.6. Conclusions

This study provides observational evidence of the aerosol indirect effect on marine stratocumulus cloud properties due to contact between above-cloud biomass burning aerosols and stratocumulus cloud tops over the Southeast Atlantic Ocean. Biomass burning aerosols overlay marine stratocumulus clouds there with variability in the vertical separation (0 to 2000 m) between the aerosol layer and cloud tops. In situ measurements of cloud and aerosol properties from six research flights during the NASA ORACLES field campaign in September 2016 are presented. These observations suggest the presence of biomass burning aerosols immediately above cloud tops was associated with changes in vertical profiles of N_c, R_e, and LWC due to cloud-top entrainment and increases in the free-tropospheric temperature and humidity. Meteorological conditions and the vertical profiles of N_c, R_e, LWC, and above- and below-cloud N_a are examined for a case study of 6 September 2016. Thinner clouds with lower cloud base and top heights were sampled closer to the coast due to lower relative humidity and boundary layer height compared to clouds sampled along 9° E. For 33 cloud profiles, cloud-top entrainment deepened the boundary layer, decoupled the stratocumulus layer from the surface, and resulted in cumulus formation below the stratocumulus. The vertical profiles of cloud (N_c, R_e, and LWC) and thermodynamic (q_T and T) properties sampled on 6 September 2016 were consistent with observations of stratocumulus-topped boundary layers capped by an inversion with warm, dry free-tropospheric air above the clouds (Wood, 2012).

Above-cloud air masses originating from Africa were composed of biomass burning products (OA, rBC, and CO) with higher N_a compared to above-cloud air masses originating from the boundary layer over the Southeast Atlantic Ocean. Thirty contact profiles were flown, where the level of $N_a > 500\ \mathrm{cm^{-3}}$ was within 100 m above cloud tops, and 41 separated profiles were flown, where $N_a > 500\ \mathrm{cm^{-3}}$ was sampled at least 100 m above cloud tops. For contact profiles, the average N_c in the cloud layer was up to $68\ \mathrm{cm^{-3}}$ higher, the average R_e was up to 1.3 µm lower, and the average LWC was within $0.01\ \mathrm{g\ m^{-3}}$ compared to separated profiles. During the contact profiles, q_T decreased across cloud tops by up to $6\ \mathrm{g\ kg^{-1}}$. With positive buoyancy across cloud tops, mixing between free-tropospheric and cloudy air occurred when clouds penetrated the inversion and median N_c and LWC decreased by 25 and 9 % near cloud tops due to droplet evaporation. The entrainment mixing of free-tropospheric air with $N_a > 500\ cm^{-3}$ likely resulted in droplet nucleation above cloud base, and the median N_c for contact profiles increased within the middle of the cloud layer. During separated profiles, q_T decreased across cloud tops by up to $9\ g\ kg^{-1}$. With negative buoyancy across cloud tops, forced descent of drier free-tropospheric air into the clouds resulted in a positive feedback of evaporative cooling, and median N_c and LWC decreased by 30 and 16 % due to droplet evaporation. The median N_c during separated profiles had little variability with height above cloud base before decreasing near cloud top due to droplet evaporation. Therefore, contact profiles had higher N_c due to a combination of weaker droplet evaporation near cloud tops and additional droplet nucleation above cloud base in the presence of above-cloud biomass burning aerosols.

Biomass burning aerosols located immediately above cloud top mixed into the cloud and polluted the boundary layer. During the case study, sawtooth maneuvers with contact profiles had higher below-cloud rBC and CO concentrations (by up to $60\ cm^{-3}$ and 30 ppb) compared to maneuvers with separated profiles. Among the 71 profiles across six research flights, contact profiles had significantly higher below-cloud CO and N_a compared to separated profiles due to the contact between biomass burning aerosols and cloud tops. Twenty-eight contact and 33 separated profiles were further classified as contact high N_a (C-H), contact low N_a (C-L), separated high N_a (S-H), and separated low N_a (S-L) to represent contact or separated profiles within high-N_a ($> 350\ cm^{-3}$) or low-N_a ($< 350\ cm^{-3}$) boundary layers. C-L profiles had up to $34.9\ cm^{-3}$ higher average N_c and up to 0.9 µm lower average R_e compared to S-L profiles despite statistically insignificant differences between the below-cloud N_a. C-H profiles had up to $70.5\ cm^{-3}$ higher below-cloud N_a, up to $88.4\ cm^{-3}$ higher N_c, and up to 1.6 µm lower R_e compared to S-H profiles. The differences between contact and separated profiles in low-N_a boundary layers were likely driven by weaker droplet evaporation in the presence of above-cloud biomass burning aerosols. Within high-N_a boundary layers, the median N_c increased with height in the middle of the cloud layer, potentially due to droplet nucleation above cloud base. The differences between contact and separated profiles within high-N_a boundary layers were likely driven by a combination of higher below-cloud N_a, droplet nucleation above cloud base, and weaker droplet evaporation in the presence of biomass burning aerosols above cloud tops.

Appendix 2.1

Cloud profiles were classified as contact or separated according to whether above-cloud N_a greater than 500 cm^{-3} was measured at a level within 100 m above cloud tops. The classification of cloud profiles remained unchanged when N_a = 400 cm^{-3} instead of N_a = 500 cm^{-3} was used to locate the aerosol layer. When the level of N_a = 300 cm^{-3} was used, 3 of the 26 separated profiles (PRF5 S1, PRF5 P2, and PRF7 P6) switched to the contact regime. The qualitative results were unchanged as contact profiles had higher N_c (differences of 63 to 71 cm^{-3}) and lower R_e (differences of 1.1 to 1.3 µm) compared to separated profiles. When a level of N_a = 600 cm^{-3} was used, 2 of the 15 contact profiles (PRF5 P1 and P3) switched to the separated regime and contact profiles had higher N_c (differences of 59 to 67 cm^{-3}) and lower R_e (differences of 1.0 to 1.2 µm). No additional changes were observed upon changing the definition of the BBA layer. Thus, the results obtained were robust as relates to this threshold.

A gap of 100 m was used to define separation between the BBAs and the clouds. When this gap was decreased to 50 m, 4 of the 15 contact profiles (PRF5 P4, PRF8 P1, and PRF11 S1 and P6) switched to the separated regime and the contact regime had higher N_c (differences of 50 to

59 cm^{-3}) and lower R_e (differences of 0.67 to 0.92 µm). There was no change in the profile classification when increasing the gap from 100 m to 200 m. On increasing the gap to 300 m, PRF5 S4 switched to the contact regime and contact profiles had higher N_c (differences of 36 to 45 cm^{-3}) and lower R_e (differences of 0.4 to 0.6 µm). The same profile switches were observed when the definition of the gap was varied between 50 and 300 m for a threshold of above-cloud N_a = 400 cm^{-3} to locate the BBA layer. Thus, the findings were robust as relates to the choice of these thresholds.

There were no profiles with maximum below-cloud N_a < 100 cm^{-3}, and only three contact profiles (with 139 1 Hz measurements) had maximum below-cloud N_a < 200 cm^{-3}. A threshold of 300 cm^{-3} used to define a "high-N_a boundary layer", and cloud microphysical properties and above- and below-cloud N_a were compared between 22 C-H and 13 S-H profiles and between 6 C-L and 20 S-L profiles (Table 5). Within low-N_a boundary layers, C-L profiles had slightly lower below-cloud N_a (differences of 1.3 to 26.5 cm^{-3}) and similar N_c (insignificant differences) compared to S-L profiles. All other comparisons between the four regimes were consistent with the discussion in Sect. 4.3, where a threshold of below-cloud N_a = 350 cm^{-3} was used to define a "high-N_a boundary layer". When the threshold was increased to 400 cm^{-3} and 450 cm^{-3}, the qualitative results were unchanged, and C-H (and C-L) profiles had significantly higher N_c and lower R_e compared to S-H (and S-L) profiles. Additionally, there were minor differences between C-H and C-L profiles and between S-H and S-L profiles for these thresholds. Thus, the findings are robust as relates to the choice of this threshold.

TABLES AND FIGURES

Table 1: The main parameter used, sampling frequency, and measurement range for in situ instruments installed on the P-3 research aircraft and used within this study.

Instrument	Parameter used	Sampling Frequency	Measurement Range	Reference
Rosemount 102	Temperature	1 Hz	Nominally -50° to 50°C	Rosemount, Incorporated
Rosemount MADT 2014	Pressure	1 Hz	Nominally 30 - 1300 mb	Rosemount, Incorporated
EdgeTech 137 Chilled-Mirror Hygrometer	Dew Point Temperature	1 Hz	Nominally -40° to 60°C	EdgeTech Instruments
Global Positioning System	Latitude, Longitude, Altitude	1 Hz	-90 to 90° -180 to 180°	
CO/CO2/H2O Analyzer	CO, H_2O (v)	1 Hz	5 to 50,000 ppb, 100 ppm to 100% humidity	Los Gatos Research
CAS	Droplet n(D)	10 Hz	0.5 - 50 µm	Baumgardner et al. (2001)
2D-S	Droplet Images, asynchronous n(D)		Nominally 10 - 1,280 µm	Lawson et al. (2006)
HVPS-3	Droplet Images, asynchronous n(D)		Nominally 150 - 19,200 µm	Lawson et al. (1998)
King Hot-wire	Bulk LWC	25 Hz	0.05 - 3 g m^{-3}	King et al. (1978)
PCASP	Aerosol n(D)	10 Hz	0.1 - 3 µm	Strapp et al. (1992)
SP2	Aerosol Absorption	1 Hz	55 - 524 nm	Stephens et al. (2003)
HR-ToF-AMS	Aerosol Mass	0.2 Hz	50 - 700 nm	Drewnick et al. (2005)

Table 2: List of research flights analyzed with the number of cloud profiles flown and total time spent profiling clouds during each flight. The number of profiles during sawtooth maneuvers are reported within parentheses. The number of profiles and the corresponding sampling time are reported for contact and separated profiles during each flight.

Flight	Sawtooth + Individual Profiles	Cloud Time	Contact Profiles	Separated Profiles
PRF5: September 06	4 (4, 5, 4, 6) + 5	1327 s	13 (857 s)	11 (470 s)
PRF7: September 10	1 (2) + 7	461 s	0 (0 s)	9 (461 s)
PRF8: September 12	1 (6) + 2	504 s	1 (32 s)	7 (472 s)
PRF9: September 14	0 (0) + 8	574 s	0 (0 s)	8 (574 s)
PRF11: September 20	1 (7) + 6	669 s	13 (669 s)	0 (0 s)
PRF13: September 25	2 (2, 3) + 4	511 s	3 (148 s)	6 (363 s)
Total	9 (39) + 32	1h 7m 26s	30 (1706 s)	41 (2340 s)

Table 3: The total (OA + SO_4^{2+} + NH_4 + NO_3^-) and OA M_a, PCASP N_a, and rBC and CO concentrations sampled up to 100 m below cloud base and 100 m above cloud top during four sawtooth maneuvers (S1–S4) flown on 6 September 2016. These values correspond to averages across the individual profiles flown during S1–S4. AOD was sampled during constant altitude flight legs and corresponds to the atmospheric column above the aircraft (N/A : not available).

Parameter	Location	S1	S2	S3	S4
Total M_a ($\mu g\ m^{-3}$)	Above-cloud	3.4	22.9	21.7	0.8
	Below-cloud	4.5	5.9	5.7	1.4
OA M_a ($\mu g\ m^{-3}$)	Above-cloud	2.0	16.9	13.2	0.4
	Below-cloud	1.9	3.5	3.4	1.0
PCASP N_a (cm^{-3})	Above-cloud	241	1515	1334	16
	Below-cloud	354	327	390	72
rBC (cm^{-3})	Above-cloud	66	516	700	10
	Below-cloud	72	111	130	N/A
CO (ppb)	Above-cloud	95	196	230	96
	Below-cloud	93	103	117	88
AOD	Above-cloud	0.33	0.37	0.49	0.39

Table 4: The range of time, latitude, longitude, above-cloud AOD, and cloud-top height (Z_T) for cloud profiles flown during the six flights. The lowest altitude where above-cloud N_a > 500 cm^{-3} occurred during the flight (Z_{500}) is in the far-right column.

Date	Time (UTC)	Latitude (°S)	Longitude (°E)	AOD	Z_T (m)	Z_{500} (m)
Sept 6	08:46 - 12:35	10.2 - 19.7	9.0 - 11.9	0.27 - 0.49	359 - 1002	680
Sept 10	09:09 - 12:36	14.1 - 18.7	4.0 - 8.6	0.21 - 0.29	990 - 1201	1800
Sept 12	11:16 - 12:26	9.7 - 12.9	-0.3 - 3.0	0.25 - 0.29	1146 - 1226	1200
Sept 14	09:36 - 14:16	16.4 - 18.1	7.5 - 9.0	0.31 - 0.32	635 - 824	2350
Sept 20	08:44 - 13:11	15.7 - 17.3	8.9 - 10.5	0.42 - 0.56	432 - 636	600
Sept 25	10:59 - 13:51	10.9 - 14.3	0.8 - 4.3	0.27 - 0.38	729 - 1124	1170

Table 5: Aerosol and cloud properties were averaged across all contact and separated profiles flown in low-N_a and high-N_a boundary layers. These averages were compared between contact and separated profiles. The values listed below represent the 95% confidence intervals (from a two-sample t test) when the differences were statistically significant. Positive values indicate the average for contact profiles was higher, and "insig" denotes the differences were statistically insignificant.

Maximum below-cloud N_a (cm^{-3})	Below-cloud N_a (cm^{-3})	Above-cloud N_a (cm^{-3})	N_c (cm^{-3})	R_e (μm)	LWC (g m^{-3})
Low N_a (< 300 cm^{-3})	-1.3 - -26.5	498.0 - 565.5	insig	-0.1 - -0.6	insig
High N_a (> 300 cm^{-3})	48.3 - 78.2	746.7 - 884.3	80.8 - 92.8	-1.1 - -1.3	0.0 – 0.02
Low N_a (< 350 cm^{-3})	insig	592.7 - 669.4	22.8 - 34.9	-0.3 - -0.9	insig
High N_a (> 350 cm^{-3})	39.1 - 70.5	737.8 - 884.4	75.5 - 88.4	-1.2 - -1.6	0.0 - 0.02

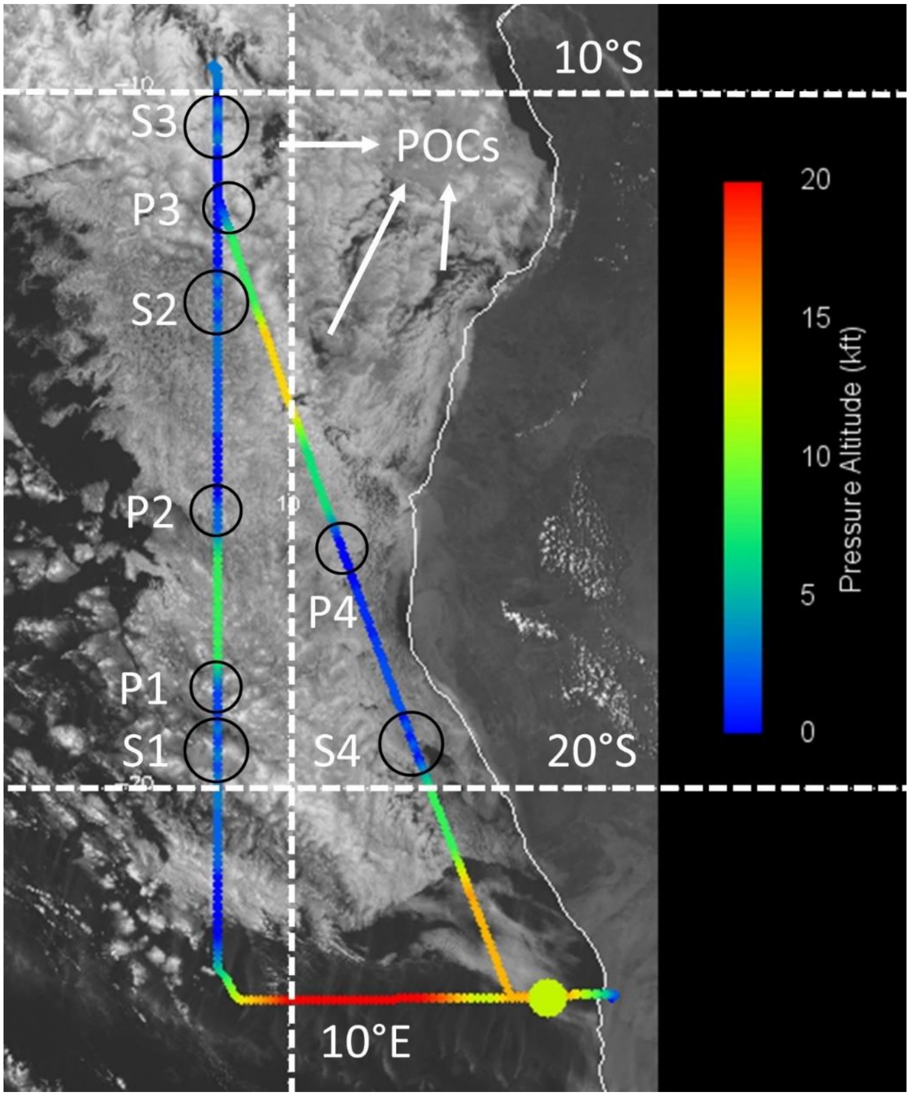

Figure 1: Visible image from the Spinning Enhanced Visible and Infrared Imager at 14:00 UTC on 6 September 2016 (PRF5), overlaid by the PRF5 flight track and colored by flight altitude. Circles indicate sawtooth maneuver (S) and individual cloud profile (P) locations (https://bocachica.arc.nasa.gov/ORACLES/, last access: 22 March 2021).

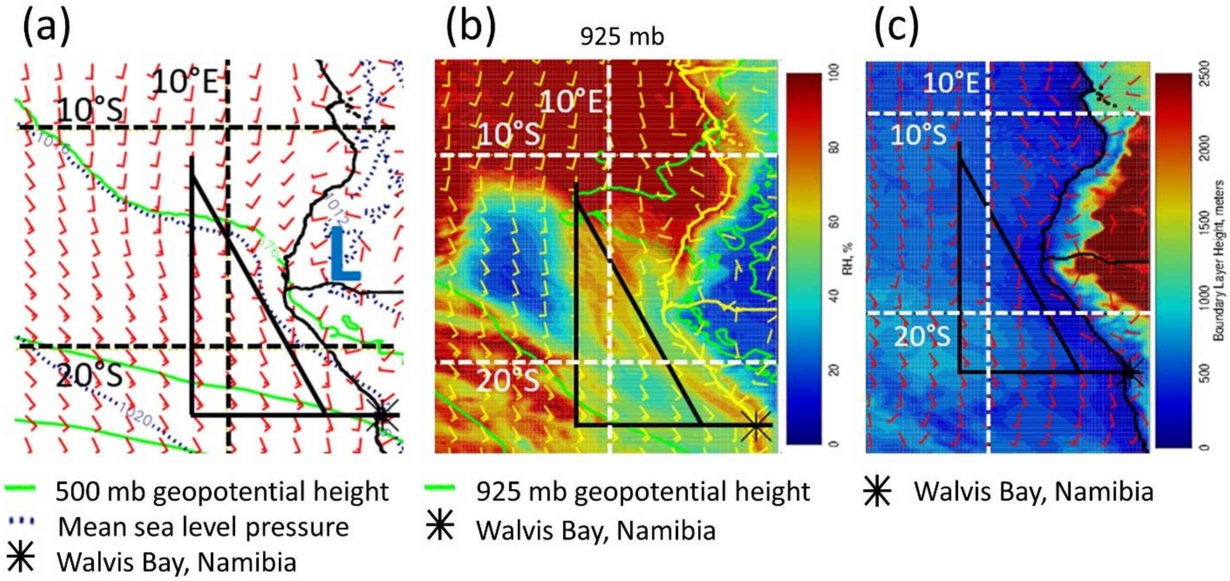

Figure 2: Zero-hour European Centre for Medium-Range Weather Forecasts reanalysis at 12:00 UTC on 6 September 2016 for (a) mean sea level pressure, 500 mb geopotential height, and surface wind; (b) 925 mb relative humidity, geopotential height, and wind; and (c) boundary layer height and 900 mb wind (https://bocachica.arc.nasa.gov/ORACLES/, last access: 22 March 2021).

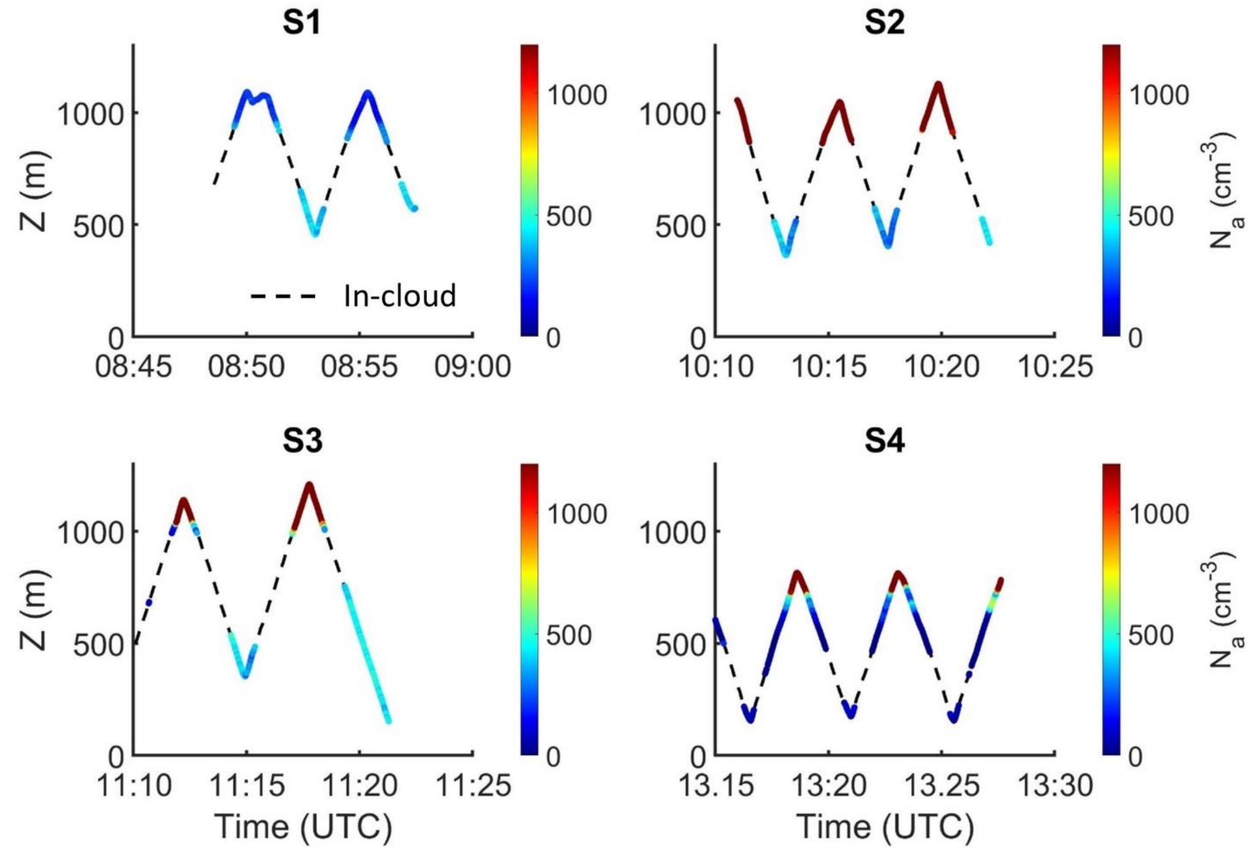

Figure 3: P-3 aircraft altitude as a function of time, colored by PCASP accumulation mode (0.1 < D < 3 µm) N_a for four sawtooth maneuvers flown on 6 September 2016. In-cloud N_a are masked due to potential for droplet shattering on the PCASP probe inlet.

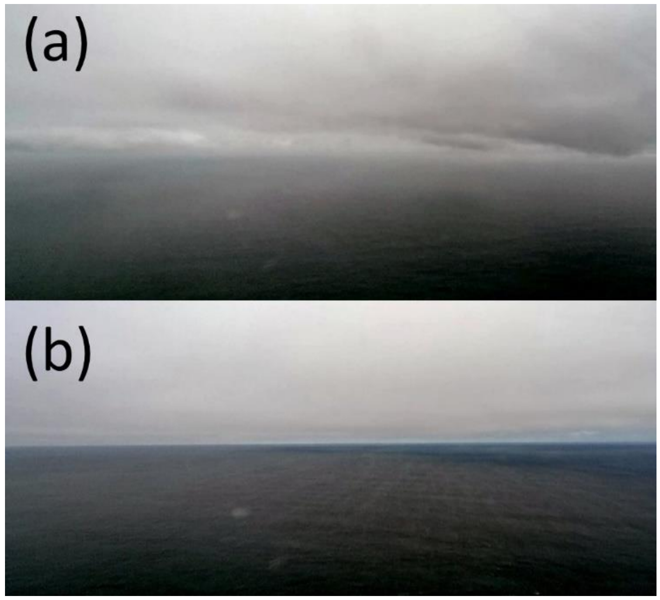

Figure 4: Snapshots of the boundary layer sampled below (a) S1 showing shallow cumulus and stratocumulus layers with varying bases, and (b) S4 showing stratocumulus clouds with a uniform base (NSRC/NASA Airborne Science Program).

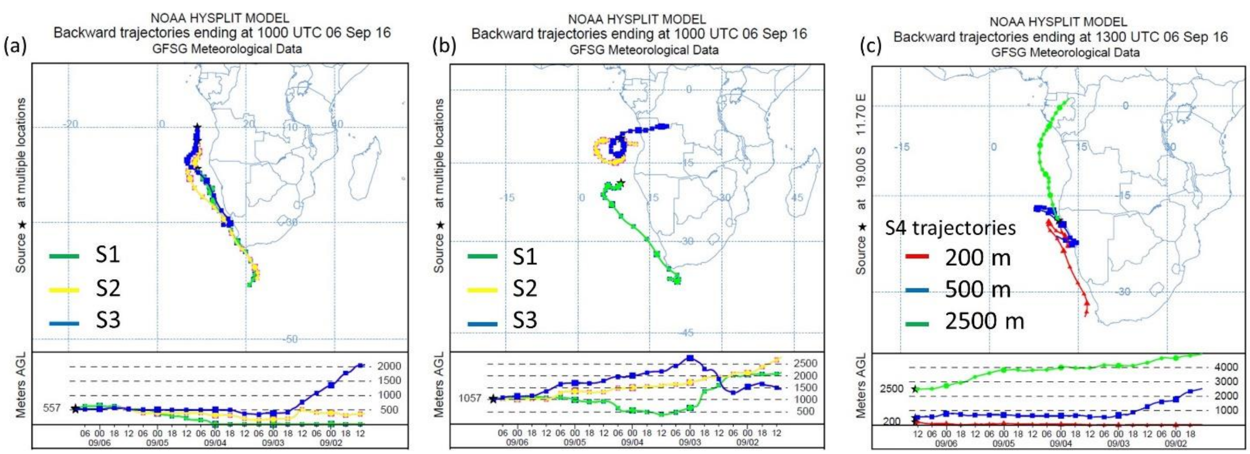

Figure 5: Five-day back trajectories from the Hybrid Single-Particle Lagrangian Integrated Trajectory model for sawtooth maneuvers flown on 6 September 2016 (a) ending at 10:00 UTC for S1–S3 at 500 m a.m.s.l.; (b) ending at 10:00UTC for S1–S3 at 1000m a.m.s.l; and (c) ending at 13:00 UTC for S4 at 200, 500, and 2500 m a.m.s.l.

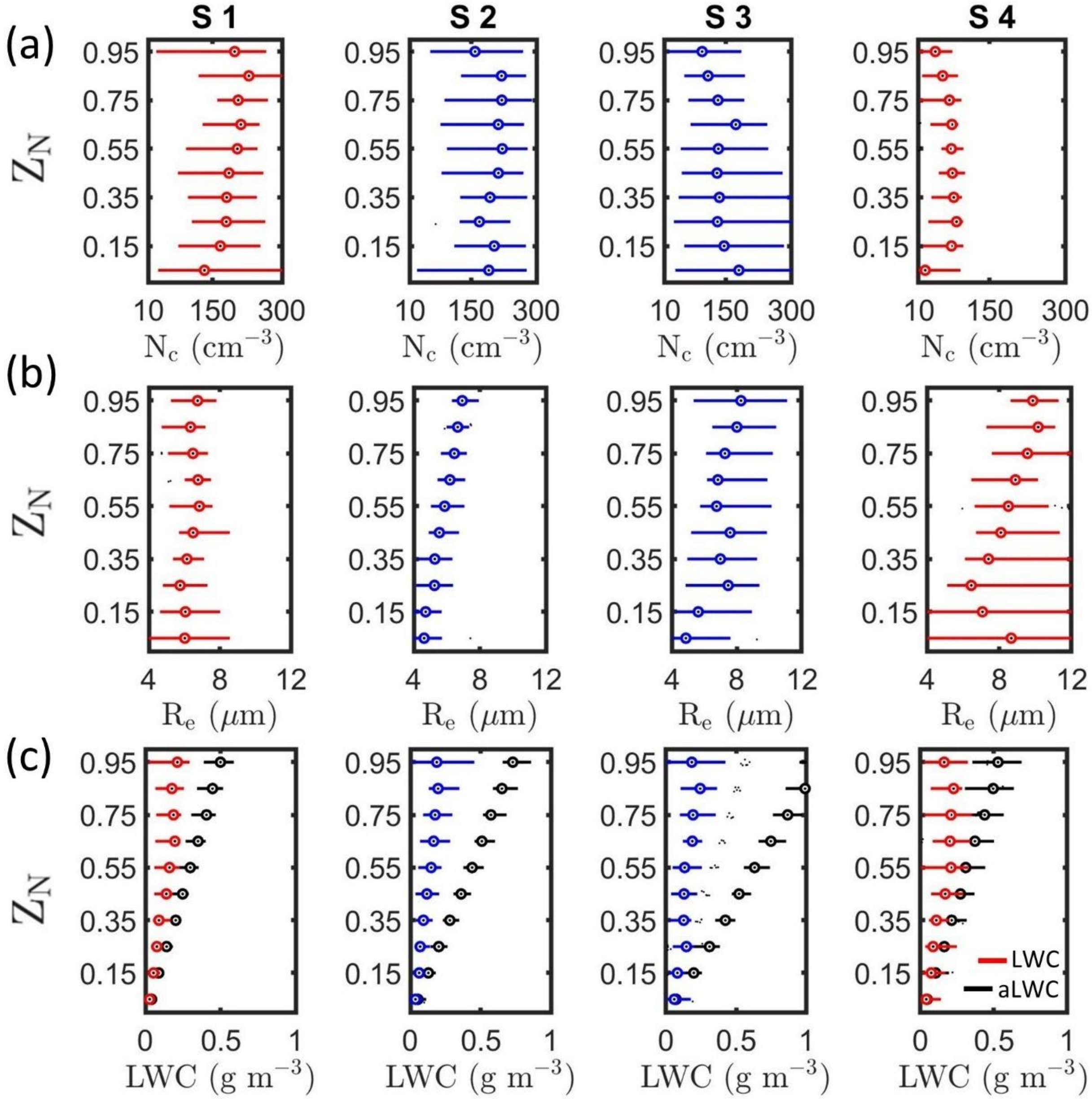

Figure 6: Vertical profiles of (a) N_c, (b) R_e, and (c) LWC and aLWC as a function of Z_N for the four sawtooth maneuvers. Maneuvers with contact (separation) between the biomass burning aerosol layer and cloud tops shown in blue (red).

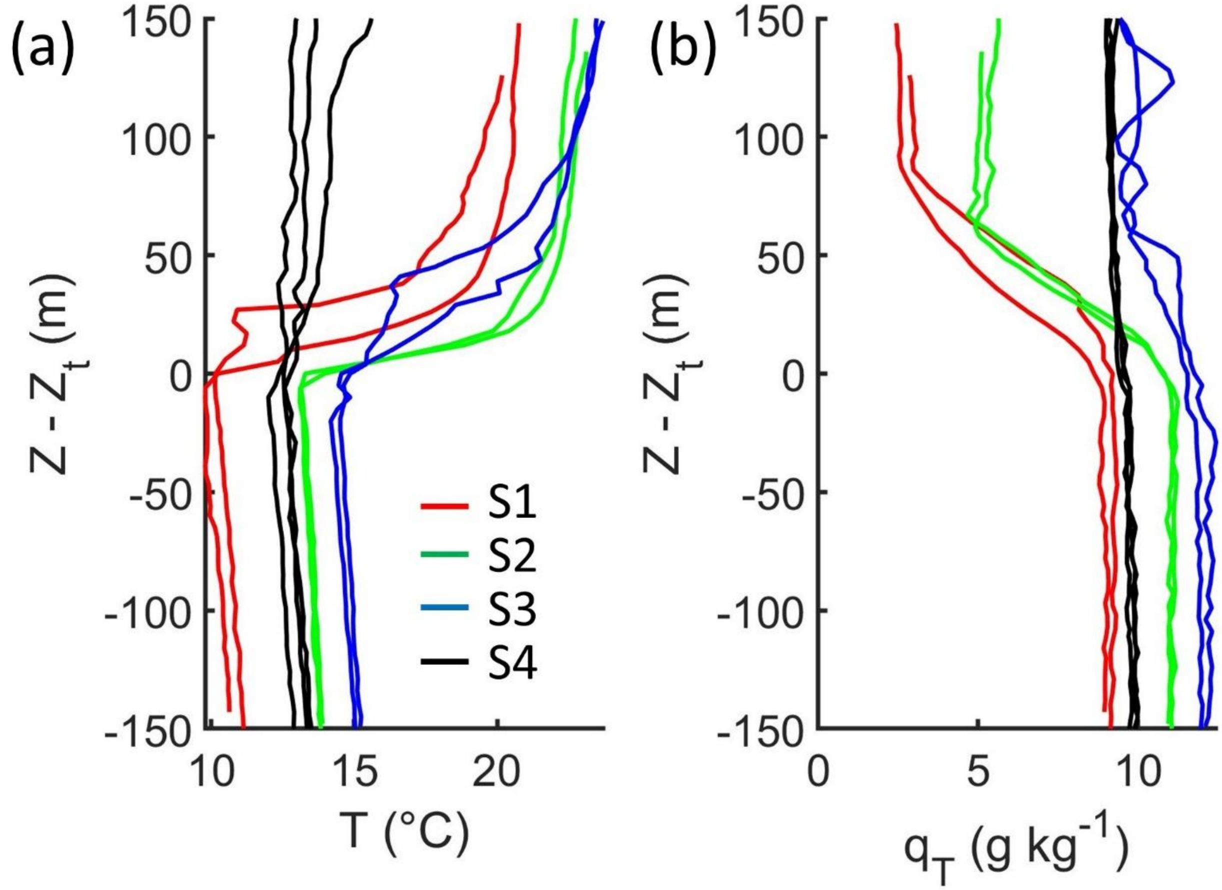

Figure 7: Vertical profiles of (a) *T* and (b) q_T as a function of distance from cloud top. Each line corresponds to an individual ascent through cloud during a sawtooth. The profiles flown during S2 and S3 (S1 and S4) had contact (separation) between the above-cloud biomass burning aerosol layer and cloud tops.

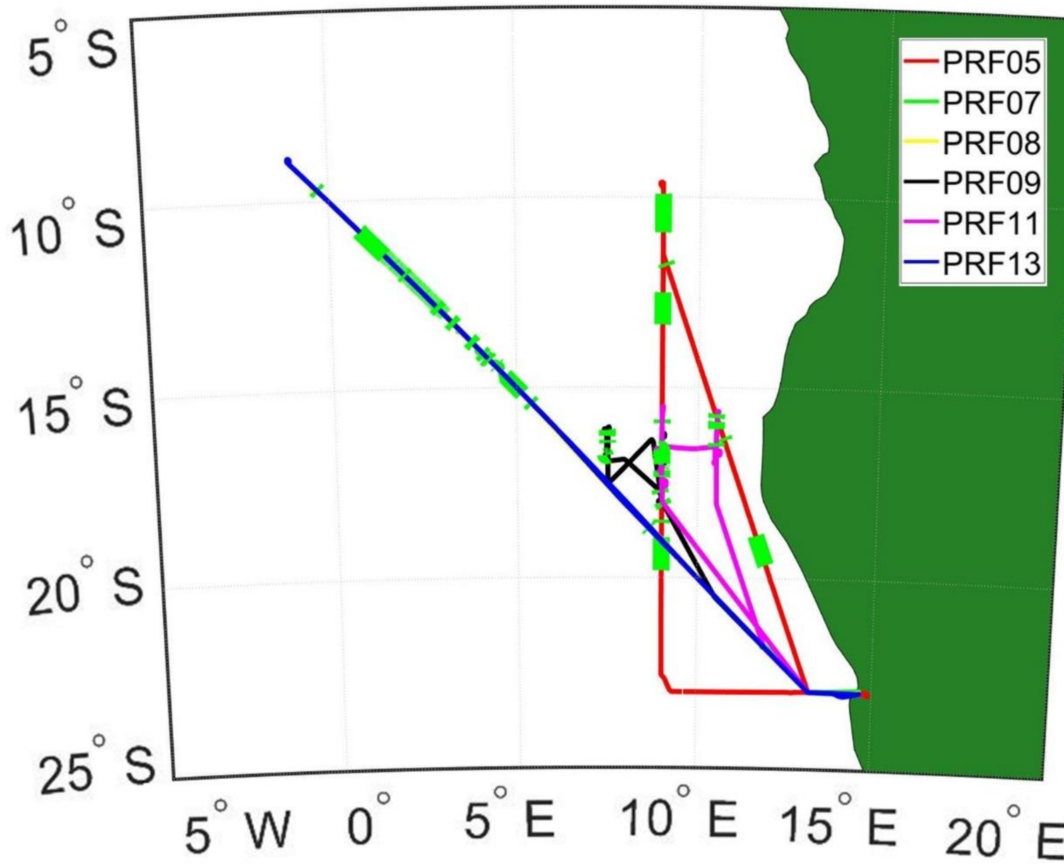

Figure 8: Flight tracks from PRFs 5, 7, 8, 9, 11, and 12 flown on 6, 10, 12, 14, 20, and 25 September 2016 with green segments indicating location of cloud profiles (flight tracks from PRFs 7 and 8 coincide with PRF13 and hence are not visible).

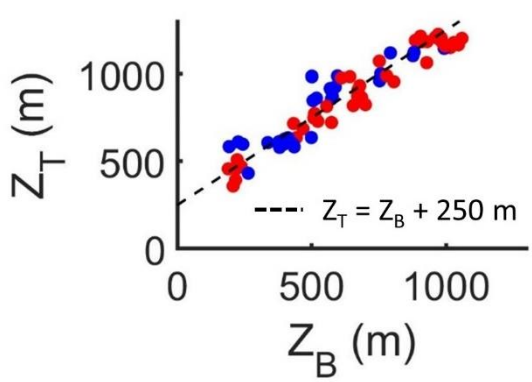

Figure 9: Cloud base and top heights for contact (blue) and separated (red) profiles flown during the six PRFs.

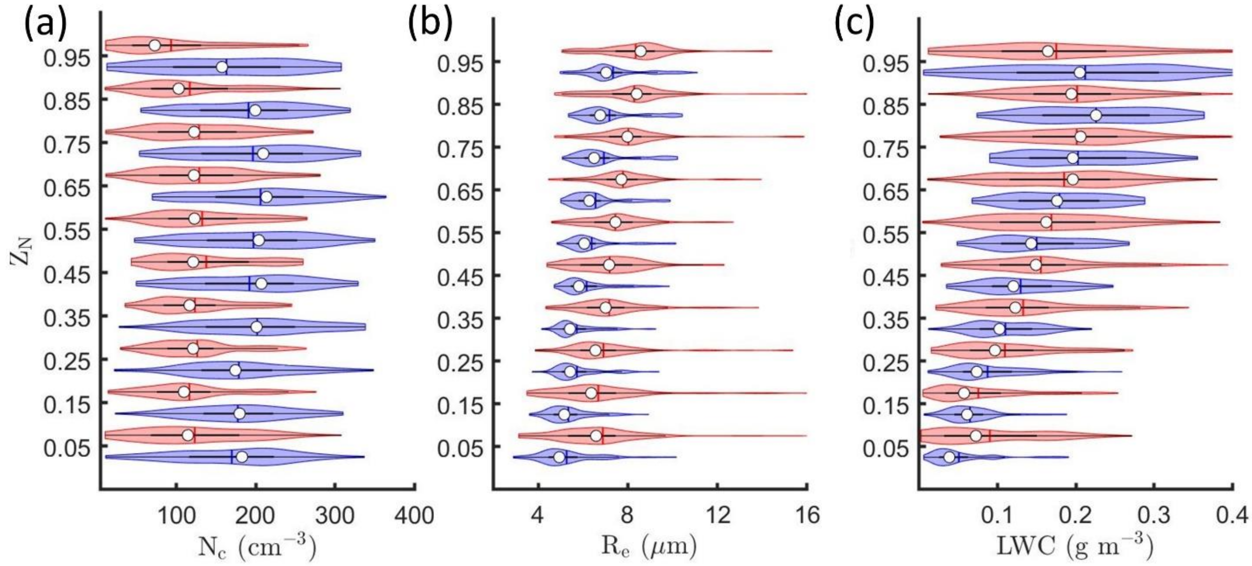

Figure 10: Kernel density estimates (indicated by the width of shaded area) and boxplots showing the 25th (Q1), 50th (white point), and 75th (Q3) percentile for (a) N_c, (b) R_e, and (c) LWC as a function of Z_N for contact (blue) and separated (red) profiles.

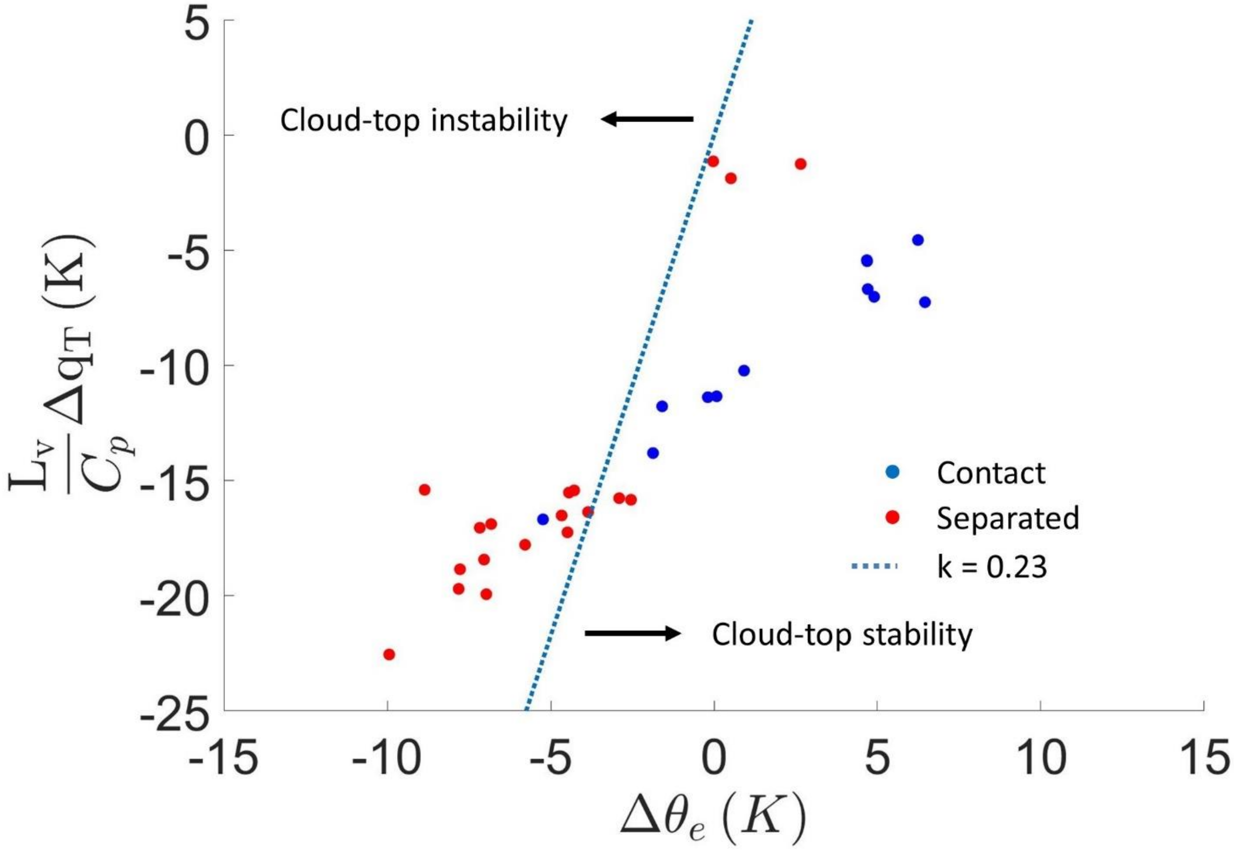

Figure 11: Difference between equivalent potential temperature (θ_e) and total water mixing ratio (q_T) measured within cloud and 100 m above cloud top for contact (blue) and separated (red) profiles (only ascents through cloud shown).

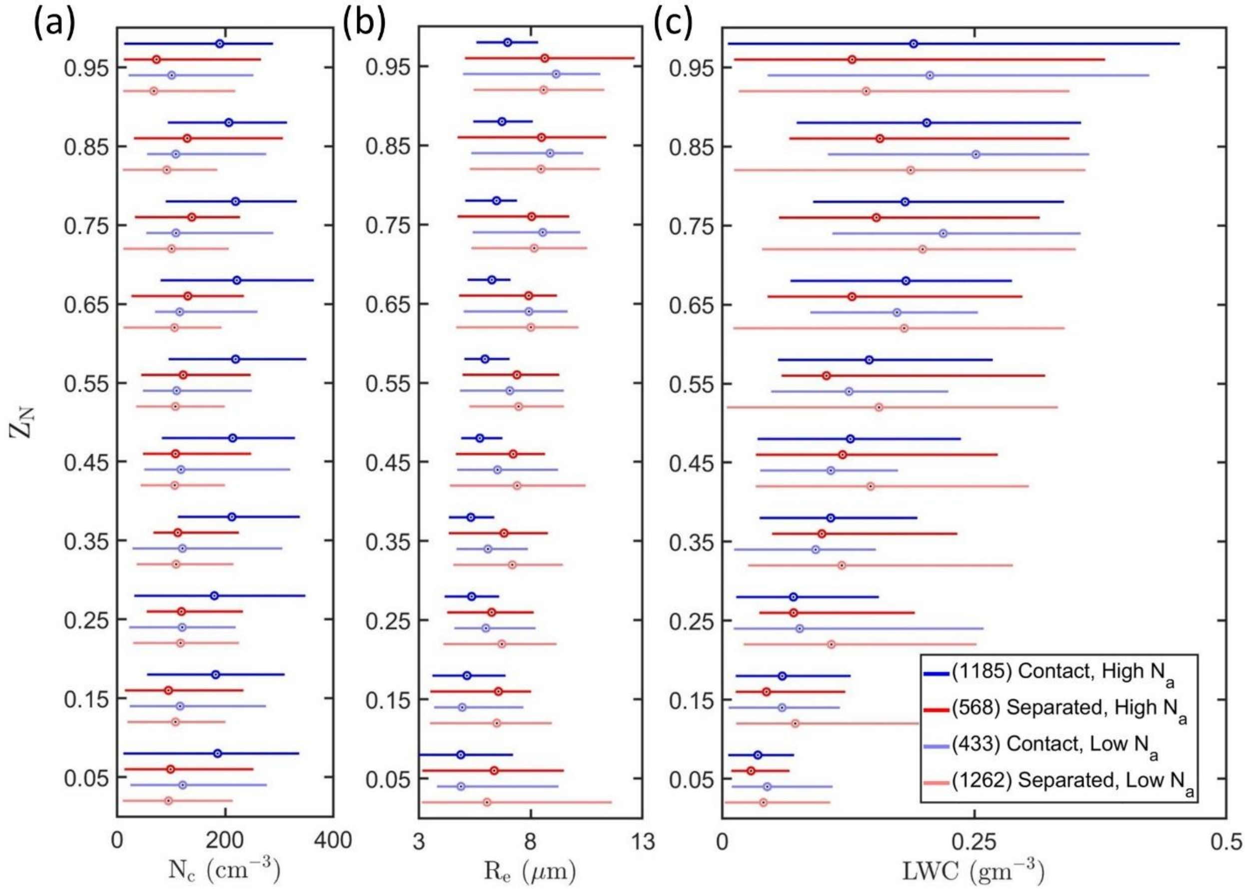

Figure 12: Boxplots representing vertical profiles of (a) N_c, (b) R_e, and (c) LWC as a function of Z_N for contact (blue) and separated (red) profiles within boundary layers with high N_a (> 350 cm^{-3}) (darker) or low N_a (< 350 cm^{-3}) (lighter). The number of 1 Hz measurements within each regime is listed within parentheses.

3 Factors Affecting Precipitation Susceptibility of Marine Stratocumulus with Variable Above and Below-Cloud Aerosol Concentrations over the Southeast Atlantic

3.1. Introduction

Clouds drive the global hydrological cycle with an annual average precipitation rate of 3 mm day^{-1} over the oceans (Behrangi et al., 2014). Marine stratocumulus (MSC) is the most common cloud type with an annual coverage of 22 % over the ocean surface (Eastman et al., 2011). These low-level, boundary layer clouds typically exist over subtropical oceans in regions with large-scale subsidence such as the southeast Atlantic Ocean (Klein and Hartmann, 1993). MSC have higher reflectivity (albedo) than the ocean surface which results in a strong, negative shortwave cloud radiative forcing (CRF) with a weak and positive longwave CRF (Oreopoulos and Rossow, 2011).

Low-cloud cover in the subsidence regions is negatively correlated with sea surface temperature (SST) (Eastman et al., 2011; Wood and Hartmann, 2006). CRF is thus sensitive to changes in SST but there is a large spread in model estimates of CRF sensitivity (Bony and Dufresne, 2005). This provides uncertainty in the model estimates of Earth's energy budget in future climate scenarios (Trenberth and Fasullo, 2009). Uncertainty in parameterization of boundary layer aerosol, cloud, and precipitation processes contributes to model uncertainties (Ahlgrimm and Forbes, 2014; Stephens et al., 2010).

MSC CRF is regulated by cloud processes that depend on cloud microphysical properties, like droplet concentration (N_c), effective radius (R_e), and liquid water content (LWC), and macrophysical properties, like cloud thickness (H) and liquid water path (LWP). These cloud properties can depend on the concentration, composition, and size distributions of aerosols which act as cloud condensation nuclei. Under conditions of constant LWC, increases in aerosol concentration (N_a) can increase N_c and decrease R_e, strengthening the shortwave CRF (Twomey, 1974, 1977). A decrease in droplet sizes in polluted clouds can inhibit droplet growth from collision-coalescence and suppress precipitation intensity, resulting in lower precipitation rate (R_p), higher LWP, and increased cloud lifetime (Albrecht, 1989). In combination, these aerosol-cloud-precipitation interactions (ACIs) and the resulting cloud adjustments lead to an effective radiative forcing termed ERF_{aci} (Boucher et al., 2013).

Satellite retrievals of R_e and cloud optical thickness (τ) can be used to estimate N_c and LWP using the adiabatic assumption (Boers et al., 2006; Wood and Hartmann, 2006; Bennartz, 2007). LWC increases linearly with height in adiabatic clouds and τ is parameterized as a function of N_c and LWP ($\tau \propto N_c^{1/3}$ $\mathrm{LWP}^{5/6}$) (Brenguier et al., 2000). Since τ has greater sensitivity to LWP compared to N_c, assuming constant LWP under different aerosol conditions can lead to underestimation of the cloud albedo susceptibility to aerosol perturbations (Platnick and Twomey, 1994; McComiskey and Feingold, 2012).

LWP can have a positive or negative response to increasing N_c due to aerosols (Toll et al., 2019). The LWP response is regulated by environmental conditions (e.g., lower tropospheric stability (LTS), boundary layer depth (H_{BL}), and relative humidity), cloud particle sizes (e.g., represented by R_e), R_p, and by N_c and LWP themselves (Chen et al., 2014; Gryspeerdt et al., 2019; Toll et al., 2019; Possner et al., 2020). Accurate estimation of the LWP response to aerosol perturbations is important for regional and global estimates of ERF_{aci} (Douglas and L'Ecuyer, 2019; 2020).

Droplet evaporation associated with cloud-top entrainment and precipitation are the two major sinks of LWC in MSC. Smaller droplets associated with higher N_c or N_a evaporate more readily which leads to greater cloud-top evaporative cooling and a negative LWP response (Hill et al., 2008). The LWP response to the evaporation-entrainment feedback (Xue and Feingold, 2006; Small et al., 2009) also depends on above-cloud humidity (Ackerman et al., 2004). Precipitation susceptibility (S_o) to aerosol-induced changes in cloud properties relates the change in R_p due to aerosol-induced changes in N_c and is a function of LWP or H (Feingold and Seibert, 2009).

The magnitude of S_o depends on precipitation formation processes like collision-coalescence which are parameterized in models using mass transfer rates, such as the autoconversion rate (S_{AUTO}) and the accretion rate (S_{ACC}) (Morrison and Gettelman, 2008; Geoffroy et al., 2010). Autoconversion describes the process of collisions between cloud droplets that coalesce to form drizzle drops which initiate precipitation. Accretion refers to collisions between cloud droplets and drizzle drops which lead to larger drizzle drops and greater precipitation intensity. The variability in S_o as a function of LWP or H depends on the cloud type and the ratio of S_{ACC} versus S_{AUTO} (Wood et al., 2009; Jiang et al., 2010; Sorooshian et al., 2010).

Recent field campaigns focused on studying ACIs over the southeast Atlantic Ocean because unique meteorological conditions are present in the region (Zuidema et al., 2016; Redemann et al., 2021). Biomass-burning aerosols from southern Africa are lofted into the free troposphere (Gui et al., 2021) and transported over the southeast Atlantic by mid-tropospheric winds where the aerosols overlay an extensive MSC deck that exists off the coast of Namibia and Angola (Adebiyi and Zuidema, 2016; Devasthale and Thomas, 2011). In situ observations of cloud and aerosol properties were collected over the southeast Atlantic during the NASA ObseRvations of Aerosols above CLouds and their intEractionS (ORACLES) field campaign during three Intensive Observation Periods (IOPs) in September 2016, August 2017, and October 2018 (Redemann et al., 2021). The above-cloud aerosol plume was associated with elevated water vapor content (Pistone at al., 2021) which influenced cloud-top humidity and dynamics following the mechanisms discussed by Ackerman et al. (2004).

During ORACLES, the aerosol layer was comprised of shortwave-absorbing aerosols (500 nm single-scattering albedo of about 0.83) with above-cloud aerosol optical depth up to 0.42 (Pistone et al., 2019; LeBlanc et al., 2020). The sign of the forcing due to shortwave absorption by the aerosol layer depends on the location of aerosols in the vertical column and the albedo of the underlying clouds (Cochrane et al., 2019). Warming aloft due to aerosol absorption of solar radiation strengthens the temperature inversion which decreases dry air entrainment into clouds, increases LWP and cloud albedo, and decreases the shortwave CRF (Wilcox, 2010). The net radiative forcing due to the aerosol and cloud layers thus depends on aerosol-induced changes in N_c, R_e, and LWP and the resulting changes in τ. Sinks of N_c and LWP like precipitation and entrainment mixing lead to uncertainties in satellite retrievals of N_c which pose the biggest challenge in the use of satellite retrievals to study the aerosol impact on N_c (Quaas et al., 2020). This motivates observational studies of ACIs that examine N_c and LWP under different aerosol and meteorological conditions.

During the 2016 IOP, variable vertical displacement (0 to 2000 m) was observed between above-cloud aerosols and the MSC (see Chapter 2). Instances of contact and separation between the aerosol and cloud layers were associated with differences in the above- and below-cloud N_a, water vapor mixing ratio (w_v), and cloud-top entrainment processes. These differences led to changes in N_c, R_e, and LWC, and their vertical profiles (Chapter 2). In this study, the response of the MSC to above- and below-cloud aerosols is further examined using data from all three ORACLES IOPs, and precipitation formation and S_o are evaluated as a function of H.

The chapter is organized as follows. In Section 3.2, the ORACLES observations are discussed along with the data quality assurance procedures (additional details are in the appendix). In Section 3.3, the calculation of cloud properties is described. In Section 3.4, the influence of aerosols on N_c, R_e, and LWC is examined by comparing the parameters for MSC in contact or separated from the above-cloud aerosol layer. In Section 3.5, the changes in precipitation formation due to aerosol-induced microphysical changes are examined. In Section 3.6, N_c, R_p, and S_o are examined as a function of H and the above- and below-cloud N_a. In Section 3.7, the meteorological conditions are examined using reanalysis data. In Section 3.8, the conclusions are summarized with directions for future work.

3.2. Observations

The ORACLES IOPs were based at Walvis Bay, Namibia (23° S, 14.6° E) in September 2016, and at São Tomé and Príncipe (0.3° N, 6.7° E) in August 2017 and October 2018. The data analyzed in this study were collected during the three IOPs (Table 6 and Fig. 13): six P-3 research flights (PRFs) from 6 to 25 September 2016 with cloud sampling conducted between 1° W to 12° E and 9° S to 20° S; seven PRFs from 12 to 28 August 2017 with cloud sampling conducted between 8°

W to 6° E and 2° S to 15° S; and 11 PRFs from 27 September to 23 October 2018 with cloud sampling conducted between 3° W to 9° E and 1° N to 15° S. These PRFs were selected because in situ cloud sampling was conducted during at least three vertical profiles through the cloud layer (Table 6).

Three PRFs from the 2016 IOP had overlapping tracks when the P-3B aircraft flew north-west from 23˚ S, 13.5˚ E toward 10˚ S, 0˚ E, and returned along the same track (Fig. 13). The 2017 and 2018 IOPs had 10 PRFs with overlapping flight tracks when the aircraft flew south from 0˚ N, 5˚ E toward 15˚ S, 5˚ E, and returned along the same track. PRFs with overlapping tracks acquired statistics for model evaluation (Doherty et al., 2021) while the other PRFs targeted specific locations based on meteorological conditions (Redemann et al., 2021).

During ORACLES, the NASA P-3B aircraft was equipped with in situ probes. The data analyzed in this study were collected using Cloud Droplet Probes (CDPs) (Lance et al., 2010), a Cloud and Aerosol Spectrometer (CAS) on the Cloud, Aerosol and Precipitation Spectrometer (Baumgardner et al., 2001), a Phase Doppler Interferometer (PDI) (Chuang et al., 2008), a Two-Dimensional Stereo Probe (2D-S) (Lawson et al., 2006), a High Volume Precipitation Sampler (HVPS-3) (Lawson et al., 1998), a King hot-wire (King et al., 1978), and a Passive Cavity Aerosol Spectrometer Probe (PCASP) (Cai et al., 2013). A single CDP was used during the 2016 IOP (hereafter CDP-A), a second CDP (hereafter CDP-B) was added for the 2017 and 2018 IOPs, and CDP-A was replaced by a different CDP (hereafter CDP-C) for the 2018 IOP.

The CAS, CDP, King hot-wire, and PCASP data were processed at the University of North Dakota using the Airborne Data Processing and Analysis processing package (Delene, 2011). The *PDI* data were processed at the University of Hawaii. The 2D-S and HVPS-3 data were processed using the University of Illinois/Oklahoma Optical Array Probe Processing Software (McFarquhar et al., 2018). The data processing procedures followed to reject artifacts were summarized in Chapter 2. Comparisons between the cloud probe data sets are described in the appendix.

The King hot-wire was used to sample LWC (hereafter King LWC). The PCASP was used to sample the accumulation-mode aerosols sized from 0.1 to 3.0 μm. The CAS, CDP, PDI, 2D-S, and HVPS-3 collectively sampled the number distribution function *N(D)* for particles with diameter *D* from 0.5 to 19200 μm. The size distribution covering the complete droplet size range was determined by merging the *N(D)* for 3 < *D* < 50 μm with the *N(D)* for 50 < *D* < 1050 μm from the 2D-S and the *N(D)* for 1050 < *D* < 19200 μm from the HVPS-3. The HVPS-3 sampled droplets with *D* > 1050 μm for a single 1 Hz data sample across the PRFs analyzed in this study. Measurement uncertainties in droplet sizes were expected to be within 20 % for droplets with *D* > 5 μm from the CAS and the CDP, *D* > 50 μm from the 2D-S, and *D* > 750 μm from the HVPS-3 (Baumgardner et al., 2017).

During each PRF, at least two independent measurements of *N(D)* were made for 3 < *D* < 50 μm using the CAS, the PDI or a CDP (Table 6). The differences between the N_c and LWC derived from the CAS, PDI and CDP *N(D)* were quantified to determine if these differences were within measurement uncertainties. The LWC estimates from the CAS, PDI, and CDP were compared with the adiabatic LWC (LWC_{ad}) which represents the theoretical maximum for LWC (Brenguier et al., 2000). The *N(D)* for droplets with *D* < 50 μm was determined using the probe which consistently had the LWC with better agreement with the LWC_{ad} during each IOP (see appendix). LWC_{ad} can be used to compare LWC from different probes since it is derived using environmental conditions and does not depend on the cloud probe datasets. The relative differences between the LWC_{ad}

and the LWC estimates from cloud probes provide a measure of the uncertainty associated with using one probe over the other for data analysis.

The differences between in-cloud data sets from different instruments were determined using a two-sample t-test. The 95 % confidence intervals (CIs) between parameter means were reported if the differences were statistically significant. During the 2017 IOP, the CAS and the CDP-B sampled droplets with $D < 50$ µm. The CDP-B LWC was higher than the CAS LWC (95 % CIs: 0.11 to 0.12 g m^{-3} higher), and the average CDP-B LWC (0.18 g m^{-3}) had better agreement with the average LWC_{ad} (0.24 g m^{-3}) compared to the average CAS LWC (0.08 g m^{-3}). Thus, the CDP-B *N(D)* was used to represent the *N(D)* for droplets with $D < 50$ µm for the 2017 IOP.

Similar results were obtained when the CAS LWC and the CDP-B LWC were compared with the LWC_{ad} for the 2018 IOP. During the 2018 IOP, the CDP-C was mounted at a different location relative to the aircraft wing compared to the CAS and CDP-B, and the positions of CDP-B and CDP-C were switched after 10 October 2018. O'Brien et al. (2021, in prep) found the CDP mounting positions had only a 6 % impact on the calculation of N_c and the average CDP-B LWC and CDP-C LWC were within 0.02 g m^{-3}. To maintain consistency with the 2017 IOP, data from the CDP mounted next to the CAS were used for droplets with $D < 50$ µm for the 2018 IOP (except on 15 October 2018 when the CDP-C had a voltage issue).

During the 2016 IOP, measurements from the CDP-A were unusable for all PRFs due to an optical misalignment issue. Nevertheless, the CAS and the PDI sampled droplets with $3 < D < 50$ µm. On average, the PDI LWC was higher than the CAS LWC (95 % CIs: 0.20 to 0.21 g m^{-3} higher). Since the PDI LWC was greater than the LWC_{ad} (95 % CIs: 0.04 to 0.06 g m^{-3} higher), it was hypothesized that the PDI LWC was an overestimate of the actual LWC. Thus, the *CAS N(D)* was used to represent the *N(D)* for droplets with $D < 50$ µm for the 2016 IOP.

The *2D-S* has two channels which concurrently sample the cloud volume. N_c and LWC were derived using data from the horizontal channel (N_H and LWC_H) and the vertical channel (N_V and LWC_V). N_H and LWC_H were used for the 2016 IOP because N_V and LWC_V were not available due to soot deposition on the inside of the receive-side mirror of the vertical channel. N_H and N_V as well as LWC_H and LWC_V were strongly correlated for the 2017 and 2018 IOPs with Pearson's correlation coefficient $R \geq 0.92$ and the best-fit slope ≥ 0.90. The high correlation values suggest that little difference would have resulted from using the average of the two 2D-S channels. To maintain consistency with the 2016 *IOP*, N_H and LWC_H were used for all three IOPs.

3.3. Cloud properties

The *N(D)* from the merged droplet size distribution was integrated to calculate N_c. The 1 Hz data samples with $N_c > 10$ cm^{-3} and King *LWC* > 0.05 g m^{-3} were defined as in-cloud measurements (Chapter 2). The PCASP *N(D)* was used to determine the out-of-cloud N_a. In situ cloud sampling during ORACLES included flight legs when the P-3B aircraft ascended or descended through the cloud layer (hereafter cloud profiles). Data from 329 cloud profiles with just under four hours of cloud sampling were examined (Table 6).

For every cloud profile, the cloud top height (Z_T) was defined as the highest altitude with $N_c > 10$ cm^{-3} and King LWC > 0.05 g m^{-3} (Table 7). The average Z_T during ORACLES was 1038 ± 270 m, where the uncertainty estimate refers to the standard deviation. The cloud base height (Z_B) was defined as the lowest altitude with $N_c > 10$ cm^{-3} and King LWC > 0.05 g m^{-3}. In decoupled boundary layers, a layer of cumulus can be present below the stratocumulus layer with a gap between the cloud layers (Wood, 2012). Measurements from stratocumulus were used in this study and Z_B for the stratocumulus layer was identified as the altitude above which the King LWC increased without gaps greater than 25 m in the cloud sampling up to Z_T.

The difference between Z_T and Z_B was defined as H. Due to aerosol-induced changes in entrainment and boundary layer stability, the aerosol impact on H and Z_T can have the strongest influence on LWP adjustments associated with ACIs (Toll et al., 2019). Thus, the influence of ACIs on precipitation formation and S_o was examined as a function of H. Data collected during incomplete profiles of the stratocumulus or while sampling open-cell clouds (for example, on 2nd October 2018) were excluded because of difficulties with estimating H for such profiles.

For each 1 Hz in-cloud data sample, the droplet size distribution was used to calculate R_e following Hansen and Travis (1974), where,

$$R_e\,(h) = \int_3^{\infty} D^3\, N(D,h)\, dD \Big/ \int_3^{\infty} 2\, D^2\, N(D,h)\, dD\,. \qquad (1)$$

Based on the aircraft speed, 1 Hz data samples corresponded to roughly 5 m intervals in the vertical direction. LWC was calculated as

$$LWC\,(h) = \pi\, \rho_w/6 \int_3^{\infty} D^3\, N(D,h)\, dD\,, \qquad (2)$$

where ρ_w is the density of liquid water and h is height in cloud above cloud base. LWC and King LWC were integrated over h from Z_B to Z_T to calculate LWP and King LWP, respectively. τ was calculated as

$$\beta_{ext}\,(h) = \int_3^{\infty} Q_{ext}\, \pi/4\, D^2\, N(D,h)\, dD\,,\ \tau = \int_{Z_B}^{Z_T} \beta_{ext}\,(h)\, dh\,, \qquad (3)$$

where β_{ext} is the cloud extinction and Q_{ext} is the extinction coefficient (approximately 2 for cloud droplets assuming geometric optics apply for visible wavelengths) (Hansen and Travis, 1974). The integrals in Eq. (1) to (3) were converted to discrete sums for D > 3 μm to consider the contributions of cloud drops, and not aerosols.

According to the adiabatic model (Brenguier et al., 2000), LWC_{ad} and LWP_{ad} are functions of H (the subscript 'ad' added to represent the adiabatic equivalents). These relationships help parameterize τ_{ad} as

$$LWC_{ad}(h) \propto h\,,\; LWP_{ad} \propto H^2\,,\; \tau_{ad} \propto (N_c)^{1/3}\, LWP^{5/6}\,, \qquad (4)$$

3.4. Aerosol Influence on cloud microphysics

The MSC over the southeast Atlantic were overlaid by biomass-burning aerosols from southern Africa (Adebiyi and Zuidema, 2016; Redemann et al., 2021) with instances of contact and separation between the MSC cloud tops and the base of the biomass burning aerosol layer (Chapter 2). Across the three IOPs, 173 profiles were conducted at locations where an extensive aerosol plume with N_a > 500 cm^{-3} was located within 100 m above Z_T (hereafter, contact profiles) (Table 6). 156 profiles were conducted at locations where the level of N_a > 500 cm^{-3} was located at least 100 m above Z_T (hereafter, separated profiles). About 50 % of the in situ cloud sampling across the three IOPs was conducted during contact profiles (Table 6). Due to inter-annual variability, contact profiles accounted for about 42 %, 91 %, and 39 % of the in situ cloud sampling during the 2016, 2017, and 2018 IOPs, respectively.

The average N_c and R_e for all cloud profiles across the three IOPs were 157 ± 96 cm^{-3} and 8.2 ± 2.7 μm, respectively (Table 8). The high proportion of contact profiles during the 2017 IOP was associated with higher average N_c and lower average R_e (229 cm^{-3} and 6.9 μm) compared to the 2016 IOP (150 cm^{-3} and 7.0 μm) and the 2018 IOP (132 cm^{-3} and 9.8 μm). It is possible that the use of CDP-B data for the 2017 IOP contributed to the increase in average N_c relative to the

2016 IOP. However, the difference between the average CAS N_c and the average CDP-B N_c for the 2017 IOP (12 cm^{-3}) was lower than the difference between the average N_c for the 2016 and 2017 IOPs (79 cm^{-3}). The difference between the N_c for these IOPs were thus primarily due to the conditions at the cloud sampling locations. The microphysical differences between the 2016 and 2017 IOPs were associated with differences in surface precipitation. Based on the W-band retrievals from the Jet Propulsion Laboratory Airborne Precipitation Radar Version 3 (APR-3), the 2017 IOP had fewer profiles with precipitation reaching the surface (13 %) compared to the 2016 IOP (34 %) (Dzambo et al., 2019).

On average, contact profiles had significantly higher N_c (95 % CIs: 84 to 90 cm^{-3} higher) and lower R_e (95 % CIs: 1.4 to 1.6 μm lower) compared to separated profiles (throughout the study, the term “significant” is exclusively used to represent statistical significance). The significant differences in N_c and R_e were associated with significantly higher τ (95 % CIs: 0.04 to 3.06 higher) for contact profiles, in accordance with the Twomey effect (Twomey, 1974; 1977). These results were consistent with the 2016 IOP when the contact profiles had higher N_c (95 % CIs: 60 to 68 cm^{-3} higher), lower R_e (95 % CIs: 1.1 to 1.3 μm lower), and higher τ (95 % CIs: 1.1 to 4.3 higher) (Chapter 2).

Figure 14 shows violin plots for cloud properties as a function of normalized height (Z_N), defined as $Z_N = Z - Z_B / Z_T - Z_B$. The violin plots include box plots and illustrate the distribution of the data (Hintze and Nelson, 1998). The median N_c increased with Z_N for $Z_N \leq 0.25$, consistent with droplet nucleation (Fig. 14a). The median N_c decreased near cloud top for $Z_N \geq 0.75$ from 204 to 154 cm^{-3} for contact and from 104 to 69 cm^{-3} for separated profiles. This is consistent with droplet evaporation associated with cloud-top entrainment (Chapter 2). The median R_e increased with Z_N consistent with condensational growth (Fig. 14b). There was a greater increase in the median R_e from cloud base to cloud top for separated profiles (from 7.1 to 9.5 μm) compared to contact profiles (from 6.1 to 7.9 μm). This is consistent with previous observations of stronger droplet growth in cleaner conditions as a function of Z_N (Braun et al., 2018; Chapter 2) and LWP (Rao et al., 2020). Statistically insignificant differences between the average H for contact and separated profiles suggest that the differential droplet growth was associated with differences in cloud processes like collision-coalescence (further discussed in Section 5).

The LWC and LWP responses to changes in aerosol conditions were examined because the adiabatic model suggests $\tau \propto \mathrm{LWP}^{5/6}$ (Eq. 4) (Brenguier et al., 2000). Contact profiles had significantly higher LWC, but the relative increase was less than 10 % (Table 9). LWC was divided into rainwater content (RWC) and cloud water content (CWC) based on droplet size. Droplets with $D > 50$ μm were defined as drizzle (Abel and Boutle, 2012; Boutle et al., 2014) and the total drizzle mass was defined as RWC. The droplet mass for $D < 50$ μm was defined as CWC. RWP and CWP were defined as the vertical integrals of RWC and CWC, respectively. The median CWC increased with Z_N but decreased over the top 10 % of the cloud layer for contact profiles and over the top 20 % of the cloud layer for separated profiles consistent with cloud-top entrainment (Fig. 14c). For contact profiles, the median RWC increased with Z_N before decreasing for $Z_N \geq 0.75$. The median RWC for separated profiles varied with Z_N. The bottom half of the cloud layer had higher median values (up to 8.7×10^{-3} g m^{-3}) compared to the top half (up to 7.0×10^{-3} g m^{-3}) (Fig. 14d).

For contact profiles, there was a significant increase in the average CWC (10 %) and a significant decrease in the average RWC (60 %) compared to separated profiles (Table 9). Contact profiles also had significantly lower average RWP with insignificant differences for average CWP

(Table 9). Contact profiles were located in deeper boundary layers with significantly higher Z_B and Z_T compared to separated profiles. However, the decrease in RWC cannot be attributed to differences in *H* or LWP (Kubar et al., 2009) because of statistically similar *H* and LWP for contact and separated profiles, on average (Table 9). These results show that instances of contact between above-cloud aerosols and the MSC were associated with more numerous and smaller cloud droplets and weaker droplet growth compared to instances of separation between the above-cloud aerosols and the MSC.

3.5. Precipitation formation and *H*

Precipitation rate R_p was calculated using the drizzle water content and fall velocity *u(D)* following Abel and Boutle (2012),

$$R_p = \pi/6 \int_{50\ \mu m}^{\infty} n(D) D^3 u(D) dD \quad (5)$$

with fall velocity relationships from Rogers and Yau (1989) used in the computation.

Contact profiles had significantly lower R_p compared to separated profiles (95 % CIs: 0.03 to 0.05 mm h^{-1} lower). This suggests contact between the MSC and above-cloud biomass burning aerosols was associated with precipitation suppression. LWP and *H* impact the sign and magnitude of the precipitation changes in response to changes in aerosol conditions (Kubar et al., 2009; Christensen and Stephens, 2012). Thus, cloud and precipitation properties were evaluated as a function of *H* to examine the aerosol-induced changes in precipitation formation.

The 95th percentile was used to represent the maximum value of a variable. For example, the 95th percentile of R_p (denoted by R_{p95}) represents the maximum R_p during a cloud profile. Although more numerous contact profiles were drizzling compared to separated profiles, the latter had more numerous profiles with high precipitation intensity. For instance, 114 out of 173 contact and 95 out of 156 separated profiles were drizzling with R_{p95} > 0.01 mm h^{-1}, out of which 36 contact and 40 separated profiles had R_{p95} > 0.1 mm h^{-1}, and only 1 contact and 9 separated profiles had R_{p95} > 1 mm h^{-1} (Fig. 15a). This is consistent with radar retrievals of surface R_p < 1 mm h^{-1} for over 93 % of the radar profiles from 2016 and 2017 (Dzambo et al., 2019).

3.5.1. Microphysical properties

On average, separated profiles had greater R_{p95} (0.22 mm h^{-1}) compared to contact profiles (0.07 mm h^{-1}). R_{p95} was positively correlated with H as thicker profiles had higher precipitation intensity (Fig. 15a). The average R_{p95} increased from thin (H < 175 m) to thick clouds (H > 175 m) from 0.04 to 0.10 mm h^{-1} for contact and 0.13 to 0.29 mm h^{-1} for separated profiles. Precipitation intensity thus decreased from separated to contact profiles for both thin and thick profiles. The average R_{p95} for thin and thick contact profiles were 32 % and 37 % of the average R_{p95} for thin and thick separated profiles, respectively.

CWC_{95} was positively correlated with H as thicker clouds had higher droplet mass (Fig. 15b). This was consistent with condensational and collision-coalescence growth continuing to occur with greater height above cloud base (Fig. 14b, c), and greater cloud depth allowing for greater droplet growth. N_{c95} and R_{e95} were negatively and positively correlated with H, respectively (Fig. 15c, d). The trends in N_c and R_e versus H were consistent with the process of collision-coalescence resulting in fewer and larger droplets.

On average, contact profiles had higher N_{c95} and lower R_{e95} (311 cm^{-3} and 8.6 μm) compared to separated profiles (166 cm^{-3} and 10.8 μm). It can be inferred that the presence of more numerous and smaller droplets during contact profiles decreased the efficiency of collision-coalescence. Alternatively, there may not have been sufficient time for the updraft to produce the few large droplets needed to broaden the size distribution and initiate collision-coalescence. Since contact and separated profiles had statistically similar *H* (Table 9), the following discussion examines the link between precipitation suppression and the aerosol-induced changes in N_c, R_e, and *LWC* and their impact on precipitation.

3.5.2. Precipitation properties

Precipitation formation process rates were estimated using equations used in numerical models to compare precipitation formation between contact and separated profiles. Precipitation development in models is parameterized using bulk microphysical schemes. GCMs or LES models parameterize precipitation formation using S_{AUTO} and S_{ACC} (e.g., Penner et al., 2006; Morrison and Gettelman, 2008; Gordon et al., 2018). The most commonly used parameterizations were used to estimate equivalent rates of precipitation formation from models. S_{AUTO} and S_{ACC} were calculated following Khairoutdinov and Kogan (2000),

$$S_{AUTO} = (dw_r)_{AUTO} / dt = 1350\, w_c^{2.47} N_c^{-1.79} \tag{6}$$

and

$$S_{ACC} = (dw_r)_{ACC}/dt = 67\, (w_c w_r)^{1.15} \tag{7}$$

where w_c and w_r are cloud water and rainwater mixing ratios, respectively, and equal to the *CWC* and *RWC* divided by the density of air (ρ_a).

Contact profiles had significantly lower S_{AUTO} and S_{ACC} compared to separated profiles (Table 9). This is consistent with significantly lower RWC and R_p for contact profiles and the association of S_{AUTO} and S_{ACC} with precipitation onset and precipitation intensity, respectively. S_{AUTO95} and S_{ACC95} were positively correlated with *H* (Fig. 16a, b). Separated profiles had higher S_{AUTO95} and S_{ACC95} (9.6×10^{-10} s^{-1} and 2.2×10^{-8} s^{-1}) compared to contact profiles (2.9×10^{-10} s^{-1} and 1.2×10^{-8} s^{-1})

associated with the inverse relationship between S_{AUTO} and N_c (Eq. 6). Faster autoconversion resulted in higher drizzle water content and greater accretion of droplets on drizzle drops.

The sampling of lower N_{c95} and higher R_{e95} compared to thinner profiles suggests that collision-coalescence was more effective in profiles with higher H (Fig. 15c, d). Thin contact profiles had the lowest S_{AUTO95} (1.4 x 10^{-10} s^{-1}) followed by thick contact (4.5 x 10^{-10} s^{-1}), thin separated (4.7 x 10^{-10} s^{-1}), and thick separated profiles (1.4 x 10^{-9} s^{-1}). High N_c and low CWC for thin contact profiles (Fig. 15b, c) are consistent with increased competition for cloud water leading to weaker autoconversion. It is hypothesized that these microphysical differences resulted in the lower S_{AUTO95} and R_{p95} for thin contact profiles compared to other profiles. The differences between R_p for contact and separated profiles thus varied with H in addition to N_c, R_e, and CWC. N_c, R_e, and CWC varied with N_a (Section 4) and ACIs were examined in Sections 6 and 7.

3.6. Aerosol influence on precipitation

3.6.1. Below-cloud N_a

Polluted boundary layers in the southeast Atlantic are associated with entrainment mixing between the free troposphere and the boundary layer (Diamond et al., 2018). Ground-based observations from Ascension Island have shown clean boundary layers can have elevated biomass burning trace gas concentrations during the burning season (Pennypacker et al., 2020). This suggests boundary layers could be clean in terms of N_a despite the entrainment of biomass-burning aerosols into the boundary layer due to precipitation scavenging of below-cloud aerosols. Carbon monoxide (CO) concentrations were examined since CO acts as a biomass burning tracer that is unaffected by precipitation scavenging (Pennypacker et al., 2020). For the

2016 IOP, contact profiles were located in boundary layers with significantly higher N_a (95 % *CIs*: 93 to 115 cm^{-3} higher) and CO (95 % *CIs*: 13 to 16 ppb higher) compared to separated profiles (Chapter 2). This is consistent with data from all three IOPs when contact profiles were located in boundary layers with higher N_a (95 % CIs: 231 to 249 cm^{-3} higher) and CO (95 % CIs: 27 to 29 ppb higher).

Following Chapter 2, 171 contact and 148 separated profiles from the IOPs were classified into four regimes, Contact, high N_a (C-H), Contact, low N_a (C-L), Separated, high N_a (S-H), and Separated, low N_a (S-L), where "low N_a" meant the profile was in a boundary layer with N_a < 350 cm^{-3} up to 100 m below cloud base. Boundary layer CO concentration above 100 ppb was sampled during 107 contact and 31 separated profiles, respectively. Contact profiles were more often located in high N_a boundary layers (131 out of 171 profiles classified as C-H) while separated profiles were more often located in low N_a boundary layers (108 out of 148 profiles classified as S-L). This suggests contact between MSC cloud tops and above-cloud biomass burning aerosols was associated with the entrainment of biomass-burning aerosols into the boundary layer. It is possible the aerosol layer was entrained into the boundary layer before cloud formation.

Contact profiles had significantly higher N_c and significantly lower R_e relative to separated profiles in both high N_a (C-H relative to S-H) and low N_a (C-L relative to S-L) boundary layers (Fig. 17, Table 10). This was associated with significantly higher above- and below-cloud N_a for the contact profiles. The differences in N_c and R_e were higher in high N_a boundary layers where the differences in above- and below-cloud N_a were also higher compared to low N_a boundary layers (Table 10). This is consistent with previous observations of MSC cloud properties (Diamond et al., 2018; Mardi et al., 2019) and similar analysis for data from the 2016 IOP (Chapter 2).

C-L profiles had significantly higher N_c (95 % CIs: 5 to 14 cm^{-3} higher) compared to S-H profiles despite having significantly lower below-cloud N_a (95 % CIs: 69 to 85 cm^{-3} lower). Significantly higher above-cloud N_a for C-L profiles (95 % CIs: 321 to 361 cm^{-3} higher) suggests that this was associated with the influence of above-cloud N_a on N_c. However, the smaller difference in N_c compared to the differences between C-H and S-H or C-L and S-L profiles suggests the combined impact of above- and below-cloud N_a was stronger than the impact of above-cloud N_a alone. These comparisons were qualitatively consistent when thresholds of 300 cm^{-3} or 400 cm^{-3} were used to define a low N_a boundary layer.

3.6.2. N_c and R_p versus H

The cloud profiles were divided into four populations based on H to compare N_c and R_p between different aerosols conditions while H was constrained. The populations were divided at H = 129, 175, and 256 m to ensure similar sample sizes (Table 11). For each population, contact profiles had higher N_c and lower R_p (Fig. 18a, b) consistent with comparisons averaged over all profiles (Table 9). Due to collision-coalescence, the average N_c decreased and the average R_p increased with H (Fig. 18a, b). For contact profiles, the average N_c decreased with H from 221 to 191 cm^{-3} and the average R_p increased from 0.03 to 0.07 mm h^{-1}. For separated profiles, the average N_c decreased from 149 to 92 cm^{-3} and the average R_p increased from 0.06 to 0.21 mm h^{-1} over the same range of H. C-H profiles had the highest average N_c and the lowest average R_p among the four regimes due to high above- and below-cloud N_a (Fig. 18c, d). C-H profiles had the smallest increase in the average R_p with H (0.02 to 0.04 mm h^{-1}). Conversely, low above- and below-cloud N_a for S-L profiles were associated with the lowest average N_c, the highest average

R_p, and the highest increase in the average R_p with H (0.12 to 0.29 mm h^{-1}). For each regime, the average N_c decreased with H (except C-L) and the average R_p increased with H (Fig. 18c, d).

3.6.3. Precipitation susceptibility S_o

S_o was used to evaluate the dependence of R_p on N_c under the different aerosol conditions. S_o, defined as the negative slope between the natural logarithms of R_p and N_c (Feingold and Seibert, 2009), is given by

$$S_o = -\,d\ln(R_p)/d\ln(N_c)\,, \tag{8}$$

where a positive value indicates decreasing R_p with increasing N_c, in accordance with the "lifetime effect" (Albrecht, 1989). The average S_o across all profiles was 0.88 ± 0.03 with lower S_o for contact profiles (0.87 ± 0.04) compared to separated profiles (1.08 ± 0.04) (Table 11). This is consistent with the hypothesis of lower values for S_o analogues (where N_c in Eq. (8) is replaced by N_a) in the presence of above-cloud aerosols (Duong et al., 2011). S_o depends on the ratio of S_{ACC} to S_{AUTO} because S_{ACC} is independent of N_c and higher S_{ACC}/S_{AUTO} represents weaker dependence of R_p on N_c (Wood et al., 2009; Jiang et al., 2010). Lower S_o for contact profiles was associated with higher S_{ACC}/S_{AUTO} compared to separated profiles (Table 9).

S_o was calculated as a function of H using N_c and R_p for the four populations of cloud profiles (Fig. 19). The sensitivity of S_o to the number of populations is discussed in Appendix 3.1. Averaged over all profiles, S_o had minor variations with H (e.g., 0.67, 0.68, and 0.54 as H increased) before increasing to 1.13 for H > 256 m (Table 11). This trend in S_o versus H is consistent with previous analyses of S_o (Sorooshian et al., 2009; Jung et al., 2016). However, different trends emerged when S_o was calculated for contact and separated profiles.

The largest difference between S_o for contact and separated profiles was observed for thin clouds with $H < 129$ m. The 30 separated profiles with $H < 129$ m had the highest S_o (1.47 ± 0.10) because of strong dependence of R_p on N_c. For these profiles, measurements with low N_c (< 100 cm^{-3}) had higher R_p (0.18 mm h^{-1}) compared to measurements with higher N_c (0.01 mm h^{-1}) (Fig. 20a). In contrast, the 52 contact profiles with $H < 129$ m had a low and statistically insignificant value for S_o (-0.06 ± 0.11) due to poor (and statistically insignificant) correlation (R = -0.03). Poor correlation between N_c and R_p for contact profiles was associated with precipitation suppression and weaker droplet growth (Section 5). These factors resulted in $R_p < 0.03$ mm h^{-1} independent of the N_c measurement (Fig. 20a).

For separated profiles, S_o decreased with H from 1.47 ± 0.10 for $H < 129$ m to 0.53 ± 0.09 for $129 < H < 175$ m and to 0.34 ± 0.07 for $175 < H < 256$ m (Fig. 19a). This was due to the increase in average R_p for high N_c measurements as a function of H from 0.01 mm h^{-1} to 0.05 and 0.04 mm h^{-1}, respectively. R_p increased with H due to stronger collision-coalescence as droplet mass increased with H. Separated profiles with $H > 256$ m had lower N_c and higher R_p compared to the populations with lower H (Fig. 18a, b). For measurements with low N_c, collision-coalescence and stronger autoconversion (following Eq. 6) resulted in higher R_p (0.26 mm h^{-1}) compared to measurements with higher N_c (0.13 mm h^{-1}). This led to a strong gradient R_p as a function of N_c (Fig. 20d) and S_o increased to 1.45 ± 0.07 for separated profiles with $H > 256$ m.

For contact profiles with $H > 129$ m, the average R_p increased with H with a larger increase for measurements with low N_c (0.028 to 0.12 mm h^{-1}) compared to measurements with high N_c (0.03 to 0.06 mm h^{-1}). It is hypothesized collision-coalescence was hindered by the presence of more numerous droplets for the latter. With droplet growth and collision-coalescence for higher

H, the limiting factor for R_p changed from H to N_c. The dependence of R_p on N_c thus increased with H and, as a result, S_o increased with H from 0.88 ± 0.06 to 1.15 ± 0.06 (Fig. 19a).

Among the four regimes defined based on the above- and below-cloud N_a, S-L profiles had the highest S_o (1.12) (Table 12). This was associated with S-L profiles having the lowest N_c and the highest R_p among the regimes (Fig. 18c, d). In descending order of S_o, S-L profiles were followed by C-L (0.86), S-H (0.50), and C-H profiles (0.33). Profiles in low N_a boundary layers (S-L and C-L) had higher S_o compared to profiles in high N_a boundary layers (S-H and C-H) consistent with wet scavenging of below-cloud aerosols (Duong et al., 2011; Jung et al., 2016).

C-L and C-H profiles had similar trends in S_o except for profiles with H < 129 m (Fig. 19b). C-L profiles had an insignificant value for S_o due to low sample size (4) and C-H profiles had negative S_o. These were thin profiles with little cloud water (Fig. 16b), high N_c (Fig. 18c), and low R_p (Fig. 18d). It is hypothesized that increasing N_c would provide the cloud water required for precipitation initiation and aid collision-coalescence. 107 out of 148 separated profiles were classified as S-L profiles. As a result, separated and S-L profiles had similar trends in S_o versus H (Fig. 19). On average, S-L profiles had higher S_o than S-H profiles which could be associated with wet scavenging resulting in the lower below-cloud N_a for S-L profiles. For S-H profiles, S_o was constant with H at about 0.45 (except 175 < H < 256 m when the value for S_o was insignificant).

The sensitivity of S_o to removal of clouds based on R_p was examined in Appendix 3.2. The removal of clouds with low R_p and high N_c or with high R_p and low N_c resulted in lower average S_o consistent with previous work (Duong et al., 2011). The S_o comparisons between profiles located in high N_a or low N_a boundary layers varied with the sample sizes of the populations. The sample sizes varied based on the threshold used to define a low N_a boundary layer which is discussed in Appendix 3.3.

3.6.4. S_o discussion

Figure 21 shows how S_o varied with perturbations (Δ) in N_c or R_p. Previous studies hypothesized that increasing above-cloud N_a or precipitation scavenging of below-cloud N_a would lead to changes in S_o (Fig. 4, Duong et al., 2011; Fig. 11, Jung et al., 2016). Thus, ΔN_c and ΔR_p for clouds with variable above- and below-cloud N_a were quantified in this study (Table 10). Higher N_c and lower R_e for contact profiles led to precipitation suppression along with lower S_{AUTO}, S_{ACC}, and R_p which were associated with lower S_o compared to separated profiles. As a result, polluted clouds were 20 % less susceptible to precipitation suppression than cleaner clouds. Figure 21 shows the impact of ΔN_c or ΔR_p on S_o depends on the original values for N_c and R_p as the same ΔN_c or ΔR_p would have an opposing effect on S_o at point 1 compared to point 2.

Both average and maximum N_c and R_p varied with H due to increasing aerosols (Section 4) and droplet growth due to collision-coalescence, autoconversion, and accretion (Section 5). Further, co-variability between droplet growth processes and ACIs meant aerosol-induced ΔN_c and ΔR_p varied with H (Section 6.2). Consequently, the differences between S_o for clean and polluted clouds varied with H. The change in S_o was highest for thin polluted clouds due to poor correlation between N_c and R_p as limited droplet growth led to low R_p regardless of the N_c. Future work must examine the co-variability between ΔN_c or ΔR_p from cloud processes such as droplet growth, entrainment, invigoration, precipitation, and ΔN_c or ΔR_p due to ACIs. Model parameterizations with power-law relationships between R_p, N_c, and H (Geoffroy et al., 2008) must account for changes in the dependence of R_p on N_c/H due to increasing aerosols or H.

The trends in S_o were only compared with studies analyzing airborne data due to the variability in S_o depending on whether aircraft, remote sensing, or modeling data were examined (Sorooshian et al., 2019). Consistent with Terai et al. (2012), S_o decreased with H for separated profiles with H < 256 m. The results from Section 5 suggest droplet growth with H decreased the susceptibility to aerosols because R_p was limited by droplet growth instead of N_a or N_c. In comparison, S_o increased with H for contact profiles consistent with Jung et al. (2016). The low S_o for thin contact profiles was consistent with the low S_o (0.06) for thin MSC over the southeast Pacific (Jung et al., 2016). This was attributed to insufficient cloud water for precipitation initiation (as noted in Section 5).

Jung et al. (2016) analyzed MSC sampled farther east and away from South America compared to Terai et al. (2012). They argued a westward increase in precipitation frequency and intensity, along with a decrease in aerosols and N_c, led to the differences between the two studies. This same attribution on the role of aerosols can be made for the ORACLES data as there were differences between contact and separated profiles because the MSC sampled during these profiles were located in similar geographical locations with different aerosol conditions. Modeling studies (e.g., Wood et al., 2009; Gettelman et al., 2013) have shown that S_o increases with H when S_{AUTO} dominates S_{ACC} (typically for R_e < 14 μm, the critical radius for precipitation initiation). Maximum R_e < 14 μm was sampled during all but 23 separated and 3 contact profiles (Fig. 16d). This would explain the increase in S_o with H for both contact (for H > 129 m) and separated profiles (for H > 256 m).

3.7. Meteorological Influence on LWP

The relationships between LWP or H and N_c, R_e, and LWC depend on meteorological conditions in addition to aerosol properties. The MSC LWP and cloud cover can vary with LTS (Klein and Hartmann, 1993; Mauger and Norris, 2007), estimated inversion strength (EIS) (Wood and Bretherton, 2006), and SST (Wilcox, 2010; Sakaeda et al., 2011). The correlations between LWP/H and these parameters are examined using the European Centre for Medium-Range Weather Forecasts (ECMWF) atmospheric reanalysis (ERA5) (Hersbach et al., 2020) to define the meteorological conditions.

ERA5 provides hourly output with a horizontal resolution of 0.25° x 0.25° for 37 pressure (p) levels (up to 1 hPa). The cloud sampling for most flights was conducted within three hours of 12:00 UTC (Table 7). ERA5 data at 12:00 UTC were thus used for the grid box nearest to the profile (Dzambo et al., 2019). The low cloud cover (LCC), SST, H_{BL}, total column liquid water (ERA5 LWP) and rainwater (ERA5 RWP), mean sea level pressure (p_o), 2 m temperature (T_o), and 2 m dew point temperature (T_d) were examined (Table 13).

The difference between potential temperatures at 700 hPa and the surface was defined as LTS (Klein and Hartmann, 1993). EIS was calculated following Wood and Bretherton (2006),

$$EIS = LTS - \Gamma_m^{850}(z_{700} - LCL),\ LCL = 125\ (T_o - T_d)\ , \tag{9}$$

where Γ_m is the moist adiabatic potential temperature gradient, z_{700} is the height at 700 mb, and LCL is the lifting condensation level (Lawrence, 2005). Γ_m^{850} is Γ_m for 850 hPa and calculated following Wood and Bretherton (2006).

LCC refers to cloud fraction for $p > 0.8\ p_o$, corresponding to $p > 810$ hPa, where most profiles were sampled (Table 7). The ECMWF model used a threshold of EIS > 7 K to distinguish between well-mixed boundary layers topped by stratocumulus and decoupled boundary layers with cumulus clouds (ECMWF IFS Documentation, 2016). This distinction improved the agreement between the model LCC and LWP and observations (Köhler et al., 2011). LCC was proportional to EIS/LTS, and LCC < 0.8 was mostly observed for EIS < 7 K (Fig. 22a). Decoupled boundary layers can be topped by MSC (Chapter 2; Wood, 2012). Profiles with EIS < 7 K were included in the analysis if ERA5 had LCC > 0.95. This included 64 contact and 88 separated profiles from the three IOPs. For the 2016, 2017, and 2018 IOPs, 50, 20, and 76 profiles, respectively, had LCC > 0.95 out of which, 0, 4, and 44 profiles, respectively, had EIS < 7 K. The average ERA5 H_{BL} (599 ± 144 m) was lower than the average Z_T (932 ± 196 m). This underestimation of H_{BL} by ERA5 has been observed for stratocumulus over the southeast and northeast Pacific (Ahlgrimm et al., 2009; Hannay et al., 2009).

On average, the ERA5 LWP (51 ± 21 g m^{-2}) was slightly greater than LWP (46 ± 41 g m^{-2}), but the differences were statistically insignificant. There was a significant but weak correlation between LWP and ERA5 LWP (R = 0.18) (Fig. 22b). On average, the ERA5 RWP (0.48 ± 1.07 g m^{-2}) was lower than RWP (1.19 ± 2.76 g m^{-2}). There were insignificant differences between ERA5 LWP/LWP for contact and separated profiles with LCC > 0.95 (Table 13). Contact profiles with LCC > 0.95 had significantly higher ERA5 RWP (Table 13). While this is counter-intuitive, given the precipitation suppression, it was due to selection of profiles with LCC > 0.95. Contact profiles with LCC > 0.95 also had higher in situ RWP (95 % CIs: 0.32 to 2.08 g m^{-2} higher) compared to separated profiles with LCC > 0.95.

LWP was positively correlated with SST and T_o and negatively correlated with LTS and EIS with weak but statistically significant correlations (Fig. 23). On average, separated profiles had significantly higher SST (95 % CIs: 0.01 to 1.48 K higher) compared to contact profiles with insignificant differences between the average T_o, EIS, and LTS. Since the correlation between LWP/H and SST was weak, it is unlikely the differences between contact and separated profiles were driven by SST differences alone. When all profiles (irrespective of LCC) were considered, there were insignificant differences between the average ERA5 RWP, SST, T_o, EIS, and LTS for contact and separated profiles. This suggests the differences between contact and separated profiles found during the ORACLES IOPs were primarily associated with ACIs instead of meteorological effects.

3.8. Conclusions

In situ measurements of stratocumulus over the southeast Atlantic Ocean were collected during the NASA ORACLES field campaign. The microphysical (N_c and R_e), macrophysical (LWP and H), and precipitation properties (R_p and S_o) of the stratocumulus were analyzed. 173 "contact" profiles with N_a > 500 cm^{-3} within 100 m above cloud tops were compared with 156 "separated" profiles with N_a < 500 cm^{-3} up to at least 100 m above cloud tops. Contact between above-cloud aerosols and the stratocumulus was associated with,

1. More numerous and smaller droplets with weaker droplet growth with height.

Contact profiles had significantly higher N_c (84 to 90 cm^{-3} higher) and lower R_e (1.4 to 1.6 μm lower) compared to separated profiles. The median R_e had a smaller increase from cloud base to cloud top for contact (6.1 to 7.9 μm) compared to separated profiles (7.1 to 9.5 μm). The profiles had similar LWP and H, and it is hypothesized the differences in droplet growth were associated with collision-coalescence.

2. Aerosol-induced cloud microphysical changes in both clean and polluted boundary layers.

Contact profiles had 25 to 31 cm^{-3} higher N_c and 0.2 to 0.5 μm lower R_e in clean and 98 to 108 cm^{-3} higher N_c and 1.6 to 1.8 μm lower R_e in polluted boundary layers compared to separated profiles. Contact profiles were more often located in polluted boundary layers and had higher below-cloud CO concentration (27 to 29 ppb higher) which suggests more frequent entrainment of biomass-burning aerosols into the boundary layer compared to separated profiles or pre-existing polluted boundary layers.

3. Precipitation suppression with significantly lower precipitation intensity and precipitation formation process rates.

Separated profiles had R_p up to 0.22 mm h^{-1} while contact profiles had R_p up to 0.07 mm h^{-1}. S_{AUTO} and S_{ACC} had higher maxima for separated (up to 9.6 x 10^{-10} s^{-1} and 2.2 x 10^{-8} s^{-1}) compared to contact profiles (up to 2.9 x 10^{-10} s^{-1} and 1.2 x 10^{-8} s^{-1}).

4. Lower precipitation susceptibility with the strongest impact in thin clouds (H < 129 m).

Contact profiles had lower S_o (0.87 ± 0.04) compared to separated profiles (1.08 ± 0.04). Thin clouds had the highest difference in S_o (-0.06 ± 0.11 for contact and 1.47 ± 0.10 for separated). Lower S_o for thin contact profiles was associated with poor correlation between N_c and R_p (R = -0.03). For separated profiles, S_o decreased with H before increasing for H > 256 m. In comparison, S_o increased with H for contact profiles for H > 129 m.

5. Statistically insignificant differences in meteorological parameters that influence LWP/H.

Based on ERA5 reanalysis data, LWP was correlated with SST (R = 0.22), T_o (R = 0.27), LTS (R = - 0.29), and EIS (R = - 0.31). Contact profiles with ERA5 LCC > 0.95 had lower SST (0.01 to 1.48

K lower) with similar T_o, LTS, and EIS compared to separated profiles. The SST differences were insignificant when profiles with LCC < 0.95 were included in the comparison.

The ORACLES dataset addresses the "lack of long-term data sets needed to provide statistical significance for a sufficiently large range of aerosol variability influencing specific cloud regimes over a range of macrophysical conditions" (Sorooshian et al., 2010). Three important factors affecting S_o were discussed (Sorooshian et al., 2019): above-cloud N_a, below-cloud N_a, and meteorological conditions. This study analyzed ORACLES data from all three IOPs and the first two conclusions were consistent with the analysis of ORACLES 2016 (Chapter 2). Future work will compare in situ data with R_p retrievals from APR-3 (Dzambo et al., 2021) to evaluate the sensitivity of S_o to the use of satellite retrievals of R_p (Bai et al., 2018). Vertical profiles of MSC cloud properties will be used to evaluate satellite retrievals (Painemal and Zuidema, 2011; Zhang and Platnick, 2011) to address the uncertainties associated with satellite-based estimates of ACIs (Quaas et al., 2020).

Appendix 3.1 – Sensitivity studies on dependence of S_o on H

The base analysis examined how cloud properties varied with H by separating cloud profiles into four populations of H using the following endpoints: 28, 129, 175, 256, and 700 m. Two sensitivity studies determine if trends describing the variation of N_c, R_p, and S_o with H were sensitive to the endpoints used to sort cloud profiles into different populations.

First, cloud profiles were classified into two populations using the median H (175 m) to divide the populations (Table 14). The average N_c decreased and the average R_p increased with H for both contact (211 to 186 cm^{-3} and 0.03 to 0.07 mm h^{-1}) and separated profiles (129 to 104 cm^{-3} and 0.07 to 0.15 mm h^{-1}). S_o increased with H for contact profiles from 0.53 to 1.06 and slightly decreased with H for separated profiles from 1.05 to 1.02 (Table 14). The difference between S_o for contact and separated profiles was greater for thin profiles (H < 175 m) compared to thick profiles (H > 175 m). These results are consistent with trends using four populations but provide less detail about how S_o varies with H (Fig. 24).

Second, cloud profiles were classified into three populations using the terciles of H (145 and 224 m) (Table 14). The average N_c decreased and the average R_p increased from the lowest to the highest H for contact (231 to 187 cm^{-3} and 0.03 to 0.07 mm h^{-1}) and separated profiles (138 to 95 cm^{-3} and 0.06 to 0.18 mm h^{-1}). For separated profiles, S_o first decreased with H from 1.15 to 0.25 before increasing to 1.45 for the highest H (Fig. 24). Contact profiles had insignificant S_o for the lowest H followed by S_o increasing from 0.95 to 1.08 with H. The results presented here are robust as relates to the number of populations used.

Appendix 3.2 – Sensitivity studies on dependence of S_o on R_p

Another sensitivity study examined the R_p threshold used for cloud profiles included while calculating S_o. The average S_o decreased if weakly precipitating clouds with low R_p were excluded (Fig. 25, Table 15). It is possible that this was due to the higher N_a and N_c associated with weakly precipitating clouds. The exclusion of weakly-precipitating clouds provides biased trends in S_o since these clouds could have undergone precipitation suppression already. Conversely, strongly precipitating clouds were associated with cleaner conditions and lower N_a and N_c. The exclusion of strongly precipitating clouds also leads to a decrease in the average S_o (Fig. 26, Table 15).

The occurrence of wet scavenging below strongly precipitating clouds (Duong et al., 2011) results in lower below-cloud N_a (and subsequently N_c). Higher susceptibility to precipitation suppression for cleaner, strongly precipitating clouds would explain the increase in the average

S_o. This is consistent with observations of S_o using different R_p thresholds (c.f. Fig 11, Jung et al., 2016) and hypotheses regarding the impact of different N_a on S_o (Duong et al., 2011; Fig. 11, Jung et al., 2016).

Appendix 3.3 – Dependence of S_o on the definition of clean and polluted boundary layers

The number of cloud profiles classified into the S-L, C-L, S-H, and C-H regimes varied depending on the below-cloud N_a threshold used to define a low N_a or clean boundary layer. For the threshold used in the base analysis (350 cm^{-3}), contact profiles were more often located in polluted boundary layers (131 out of 171 profiles classified as C-H) while separated profiles were more often located in clean boundary layers (108 out of 148 profiles classified as S-L). The comparisons between S_o in clean and polluted boundary layers varied with the threshold used.

As a sensitivity study, a lower threshold was used to define a clean boundary layer (300 cm^{-3}). For this case, the C-L regime had no profiles in the population with the lowest H (H < 129 m) when four populations of profiles were used to examine the dependence of S_o on H. Two out of the other three populations had an insignificant value for S_o due to poor and statistically insignificant correlations between N_c and R_p (Table 16). This was associated with a low sample size for the populations (6 each). A second sensitivity study used a higher threshold to define a clean boundary layer (400 cm^{-3}). For this case, the S-H regime has insignificant S_o for three out of the four populations of H and the remaining population had a small sample size (3 profiles) (Table 16). The base analysis using a threshold of 350 cm^{-3} to define a clean boundary layer was used to compare S_o values that represent a larger number of cloud profiles.

TABLES AND FIGURES

Table 6: The number of cloud profiles (n) for P-3 research flights (PRFs) analyzed in the study, number of contact and separated profiles with sampling time in parentheses, and instruments that provided valid samples of droplets with *D* < 50 µm (instrument used for analysis is in bold).

PRF number and date	n	Contact	Separated	Instruments
PRF05Y16: Sep. 06	24	13 (857 s)	11 (470 s)	**CAS**, PDI
PRF07Y16: Sep. 10	9	0 (0 s)	9 (461 s)	**CAS**, PDI
PRF08Y16: Sep. 12	8	1 (32 s)	7 (472 s)	**CAS**, PDI
PRF09Y16: Sep. 14	8	0 (0 s)	8 (574 s)	**CAS**, PDI
PRF11Y16: Sep. 20	13	13 (669 s)	0 (0 s)	**CAS**, PDI
PRF13Y16: Sep. 25	9	3 (148 s)	6 (363 s)	**CAS**, PDI
PRF01Y17: Aug. 12	15	14 (499 s)	1 (25 s)	CAS, **CDP-B**
PRF02Y17: Aug. 13	17	17 (754 s)	0 (0 s)	CAS, **CDP-B**
PRF03Y17: Aug. 15	12	12 (272 s)	0 (0 s)	CAS, **CDP-B**
PRF04Y17: Aug. 17	7	7 (127 s)	0 (0 s)	CAS, **CDP-B**
PRF07Y17: Aug. 21	13	9 (188 s)	4 (76 s)	CAS, **CDP-B**
PRF08Y17: Aug. 24	9	9 (324 s)	0 (0 s)	CAS, **CDP-B**
PRF10Y17: Aug. 28	11	7 (496 s)	4 (168 s)	CAS, **CDP-B**
PRF01Y18: Sep. 27	21	0 (0 s)	21 (933 s)	CAS, **CDP-B**, CDP-C
PRF02Y18: Sep. 30	13	7 (337 s)	6 (183 s)	CAS, **CDP-B**, CDP-C
PRF04Y18: Oct. 03	5	0 (0 s)	5 (137 s)	CAS, **CDP-B**, CDP-C
PRF05Y18: Oct. 05	4	4 (109 s)	0 (0 s)	CAS, **CDP-B**, CDP-C
PRF06Y18: Oct. 07	10	10 (337 s)	0 (0 s)	CAS, **CDP-B**, CDP-C
PRF07Y18: Oct. 10	13	11 (472 s)	2 (153 s)	**CDP-B**, CDP-C
PRF08Y18: Oct. 12	19	0 (0 s)	19 (773 s)	CDP-B, **CDP-C**
PRF09Y18: Oct. 15	30	17 (766 s)	13 (365 s)	**CDP-B**, CDP-C
PRF11Y18: Oct. 19	12	0 (0 s)	12 (731 s)	CDP-B, **CDP-C**
PRF12Y18: Oct. 21	18	0 (0 s)	18 (833 s)	CDP-B, **CDP-C**
PRF13Y18: Oct. 23	29	19 (777 s)	10 (366 s)	CDP-B, **CDP-C**
Total (2016)	**71**	**30 (1,706 s)**	**41 (2,340 s)**	
Total (2017)	**84**	**75 (2,660 s)**	**9 (269 s)**	
Total (2018)	**174**	**68 (2,798 s)**	**106 (4,474 s)**	
Total	**329**	**173 (7,164 s)**	**156 (7,083 s)**	

Table 7: Range of time, latitude, longitude, Z_T and cloud top pressure (P_T) for PRFs in Table 6.

PRF	Time (UTC)	Latitude (°S)	Longitude (°E)	Z_T (m)	P_T (mb)
PRF05Y16: Sep. 06	08:46 - 12:35	10.2 - 19.7	9.00 - 11.9	359 - 1002	904 - 976
PRF07Y16: Sep. 10	09:09 - 12:36	14.1 - 18.7	4.00 - 8.60	990 - 1201	885 - 908
PRF08Y16: Sep. 12	11:16 - 12:26	9.70 - 12.9	-0.30 - 3.00	1146 - 1226	881 - 890
PRF09Y16: Sep. 14	09:36 - 14:16	16.4 - 18.1	7.50 - 9.00	635 - 824	922 - 945
PRF11Y16: Sep. 20	08:44 - 13:11	15.7 - 17.3	8.90 - 10.5	432 - 636	941 - 966
PRF13Y16: Sep. 25	10:59 - 13:51	10.9 - 14.3	0.80 - 4.30	729 - 1124	890 - 934
PRF01Y17: Aug. 12	11:30 - 15:01	2.41 - 13.0	4.84 - 5.13	748 - 1379	866 - 933
PRF02Y17: Aug. 13	10:15 - 13:07	7.20 - 9.00	4.50 - 5.00	779 - 1384	865 - 928
PRF03Y17: Aug. 15	11:26 - 13.32	9.08 - 15.0	4.96 - 5.00	536 - 1148	887 - 954
PRF04Y17: Aug. 17	12:03 - 16:14	7.99 - 9.43	-7.0 - -12.8	1547 - 1782	827 - 848
PRF07Y17: Aug. 21	13:20 - 16:37	7.96 - 8.05	-8.16 - 3.32	1061 - 1491	855 - 897
PRF08Y17: Aug. 24	11:28 - 14:58	4.90 - 14.8	4.97 - 5.15	911 - 2015	801 - 916
PRF10Y17: Aug. 28	11:46 - 13:18	7.84 - 11.0	4.89 - 5.01	1070 - 1216	881 - 897
PRF01Y18: Sep. 27	10:07 - 13:11	5.66 - 12.1	4.87 - 5.03	819 - 1169	885 - 922
PRF02Y18: Sep. 30	09:50 - 12:24	6.85 - 8.18	4.94 - 5.13	747 - 840	920 - 930
PRF04Y18: Oct. 03	13:17 - 14:41	-1.05 - 4.61	5.00 - 5.06	1137 - 2151	790 - 888
PRF05Y18: Oct. 05	07:22 - 10:09	9.50 - 9.63	5.79 - 6.66	780 - 892	915 - 928
PRF06Y18: Oct. 07	11:04 - 11:29	10.1 - 11.8	5.00 - 5.00	863 - 928	913 - 918
PRF07Y18: Oct. 10	10:16 - 13:31	4.46 - 13.1	4.88 - 5.09	926 - 1329	866 - 912
PRF08Y18: Oct. 12	13:02 - 16:19	1.02 - 4.58	5.50 - 6.96	1073 - 1905	813 - 895
PRF09Y18: Oct. 15	10:27 - 13:09	5.25 - 14.1	4.91 - 5.00	693 - 1547	849 - 937
PRF11Y18: Oct. 19	11:58 - 13:00	6.50 - 7.70	8.00 - 9.06	701 - 1276	873 - 932
PRF12Y18: Oct. 21	10:21 - 13:07	4.91 - 13.5	4.88 - 5.00	675 - 983	902 - 936
PRF13Y18: Oct. 23	10:28 - 13:38	3.07 - 5.00	-2.65 - 5.00	873 - 1281	873 - 915

Table 8: Average values for cloud properties measured during cloud profiles from the PRFs listed in Table 6 for each *IOP*. Error estimates represent one standard deviation. *R* between LWP estimates and *H* in parentheses.

Parameter	2016	2017	2018	All
Profile count	71	84	174	329
N_c (cm^{-3})	150 ± 73	229 ± 108	132 ± 87	157 ± 96
R_e (μm)	7.0 ± 1.9	6.9 ± 1.6	9.8 ± 3.3	8.2 ± 2.7
LWC ($g\ m^{-3}$)	0.15 ± 0.09	0.21 ± 0.15	0.26 ± 0.17	0.22 ± 0.16
King LWC ($g\ m^{-3}$)	0.29 ± 0.15	0.23 ± 0.17	0.24 ± 0.14	0.25 ± 0.15
τ	7.2 ± 3.6	7.2 ± 8.9	9.0 ± 7.7	8.8 ± 7.7
H (m)	244 ± 83	148 ± 92	212 ± 116	201 ± 108
LWP ($g\ m^{-2}$)	34 ± 17 (0.75)	37 ± 43 (0.88)	59 ± 54 (0.83)	48 ± 47 (0.78)
King LWP ($g\ m^{-2}$)	68 ± 30 (0.80)	37 ± 35 (0.84)	52 ± 40 (0.89)	52 ± 38 (0.87)
LWP_{ad} ($g\ m^{-2}$)	77 ± 57 (0.97)	51 ± 55 (0.96)	93 ± 97 (0.94)	79 ± 82 (0.93)

R_p (mm h^{-1})	0.02 ± 0.05	0.02 ± 0.08	0.10 ± 0.33	0.06 ± 0.25

Table 9: Average and standard deviation for cloud properties measured during contact and separated profiles with 95 % confidence intervals (CIs) from a two-sample t-test applied to contact and separated profile data. Positive CIs indicate higher average for contact profiles and "insignificant" indicates statistically similar averages for contact and separated profiles.

Parameter	**Contact**	**Separated**	**95 % CIs**
N_c (cm^{-3})	200 ± 103	113 ± 63	84 to 90
R_e (μm)	7.5 ± 2.1	9 ± 3	-1.6 to -1.4
τ	8.8 ± 8.3	7 ± 5	0.04 to 3.06
LWC (g m^{-3})	0.23 ± 0.17	0.21 ± 0.14	0.01 to 0.02
CWC (g m^{-3})	0.22 ± 0.16	0.20 ± 0.14	0.01 to 0.02
RWC (x 10^{-3} g m^{-3})	11 ± 15	18 ± 31	-8 to -6
H (m)	194 ± 109	208 ± 106	insignificant
LWP (g m^{-2})	46 ± 49	46 ± 41	insignificant
CWP (g m^{-2})	45 ± 50	46 ± 44	Insignificant
RWP (g m^{-2})	1.8 ± 3.3	3.0 ± 7.1	-2.4 to -0.01
Z_T (m)	1069 ± 267	1004 ± 271	6 to 123
Z_B (m)	874 ± 294	796 ± 274	16 to 140
R_p (mm h^{-1})	0.04 ± 0.09	0.08 ± 0.33	-0.05 to -0.03
S_{AUTO} (x 10^{-10} s^{-1})	1.6 ± 3.0	4.9 ± 12.6	-3.6 to -3.1
S_{ACC} (x 10^{-8} s^{-1})	0.8 ± 1.6	1.7 ± 4.3	-1.1 to -0.8
S_{ACC}/S_{AUTO} (x 10^2)	0.7 ± 1.1	0.5 ± 0.9	0.2 to 0.3

Table 10: 95 % CIs from statistical comparisons between cloud regimes defined in text.

Parameter	**C-H relative to S-H**	**C-L relative to S-L**
Above-cloud N_a (cm^{-3})	852 to 948	387 to 413
Below-cloud N_a (cm^{-3})	194 to 226	45 to 53
N_c (cm^{-3})	98 to 108	25 to 31
R_e (μm)	-1.6 to -1.8	-0.2 to -0.5
R_p (mm h^{-1})	-0.03 to -0.04	0 to -0.04

Table 11: S_o ± standard error for contact, separated, and all profiles, with sample size and *R* in parentheses. S_o is statistically insignificant if underlined.

H	**Contact**	**Separated**	**All Profiles**
All	0.87 ± 0.04 (173, 0.30)	1.08 ± 0.04 (156, 0.36)	0.88 ± 0.03 (329, 0.33)
28 to 129 m	<u>-0.06 ± 0.11 (52, -0.03)</u>	1.47 ± 0.10 (30, 0.55)	0.67 ± 0.07 (82, 0.28)
129 to 175 m	0.88 ± 0.06 (38, 0.42)	0.53 ± 0.09 (42, 0.20)	0.68 ± 0.05 (80, 0.32)
175 to 256 m	0.92 ± 0.08 (41, 0.27)	0.34 ± 0.07 (44, 0.13)	0.54 ± 0.05 (85, 0.20)
256 to 700 m	1.15 ± 0.06 (42, 0.36)	1.45 ± 0.07 (40, 0.41)	1.13 ± 0.04 (82, 0.40)

Table 12: S_o ± standard error with sample size and R in parenthesis for cloud regimes defined in text. S_o is statistically insignificant if underlined.

H	S-L	S-H
All	1.29 ± 0.06 (107, 0.40)	0.50 ± 0.06 (41, 0.19)
28 to 129 m	1.12 ± 0.15 (21, 0.42)	0.43 ± 0.14 (8, 0.27)
129 to 175 m	0.66 ± 0.12 (25, 0.25)	0.48 ± 0.18 (11, 0.17)
175 to 256 m	0.66 ± 0.09 (34, 0.22)	0.07 ± 0.10 (9, 0.03)
256 to 700 m	1.89 ± 0.09 (27, 0.52)	0.45 ± 0.11 (13, 0.14)

H	C-L	C-H
All	0.86 ± 0.07 (40, 0.30)	0.33 ± 0.05 (131, 0.11)
28 to 129 m	0.04 ± 0.42 (4, 0.01)	-0.33 ± 0.11 (48, -0.14)
129 to 175 m	0.50 ± 0.12 (9, 0.25)	0.26 ± 0.08 (27, 0.13)
175 to 256 m	1.06 ± 0.13 (14, 0.34)	0.61 ± 0.11 (27, 0.17)
256 to 700 m	0.72 ± 0.11 (13, 0.24)	0.59 ± 0.09 (29, 0.17)

Table 13: Meteorological and cloud properties from ERA5 reanalysis for contact and separated profiles with *LCC* > 0.95 (LCC is reported for all profiles), 95 % CIs from a two-sample t-test applied to contact and separated profile data, and *R* between each parameter and *LWP* (R_{LWP}) or *H* (R_H) with statistically significant R_H and R_{LWP} in bold.

Parameter	Contact	Separated	95 % CIs	R_H, R_{LWP}
LCC	0.75 ± 0.29	0.83 ± 0.26	-0.14 to -0.02	**0.24**, 0.04
SST (K)	293 ± 2	294 ± 3	-1.5 to -0	**0.16, 0.22**
H_{BL} (m)	566 ± 164	624 ± 124	-103 to -11	-0.05, -0.11
ERA5 LWP (g m^{-2})	53 ± 18	51 ± 23	insignificant	**0.31, 0.18**
ERA5 RWP (g m^{-2})	0.71 ± 1.56	0.32 ± 0.40	0.05 to 0.73	**0.19**, -0.01
P_o (mb)	1015 ± 1	1014 ± 2	1 to 2	-0.09, -0.07
T_o (K)	293 ± 2	293 ± 3	insignificant	**0.16**, **0.27**
LTS (K)	23 ± 2	22 ± 3	insignificant	-0.10, **-0.29**
EIS (K)	8.1 ± 1.9	7.8 ± 3.1	insignificant	-0.13, **-0.31**

Table 14: S_o ± standard error with sample size and R in parentheses for contact, separated, and all profiles classified into a different number of populations.

H Bin	Contact	Separated	All Profiles
2 populations			
28 to 175 m	0.53 ± 0.05 (90, 0.24)	1.05 ± 0.07 (72, 0.39)	0.69 ± 0.04 (162, 0.30)
175 to 700 m	1.06 ± 0.05 (83, 0.33)	1.02 ± 0.05 (84, 0.33)	0.93 ± 0.03 (167, 0.33)
3 populations			
28 to 145 m	0.08 ± 0.08 (67, 0.04)	1.15 ± 0.09 (41, 0.45)	0.60 ± 0.05 (108, 0.26)
145 to 224 m	0.95 ± 0.07 (51, 0.34)	0.25 ± 0.06 (60, 0.11)	0.60 ± 0.04 (111, 0.25)
224 to 700 m	1.08 ± 0.05 (55, 0.34)	1.45 ± 0.06 (55, 0.41)	1.05 ± 0.04 (110, 0.37)

Table 15: S_o ± standard error with sample size and R in parentheses for contact, separated, and all profiles with R_p above a certain threshold.

H Bin	Contact	Separated	All Profiles
$R_p > 10^{-3}$ mm h^{-1}			
All	0.88 ± 0.03 (173, 0.34)	0.95 ± 0.04 (156, 0.36)	0.84 ± 0.02 (329, 0.37)
28 to 129 m	0.03 ± 0.10 (52, 0.02)	1.41 ± 0.09 (30, 0.61)	0.71 ± 0.07 (82, 0.33)
129 to 175 m	0.94 ± 0.05 (38, 0.49)	0.64 ± 0.09 (42, 0.27)	0.78 ± 0.04 (80, 0.40)
175 to 256 m	0.78 ± 0.07 (41, 0.30)	0.21 ± 0.06 (44, 0.10)	0.38 ± 0.04 (85, 0.18)
256 to 700 m	1.11 ± 0.06 (42, 0.38)	1.18 ± 0.07 (40, 0.39)	1.06 ± 0.04 (82, 0.42)
$R_p > 10^{-2}$ mm h^{-1}			
All	0.49 ± 0.03 (173, 0.27)	0.76 ± 0.03 (156, 0.38)	0.61 ± 0.02 (329, 0.35)
28 to 129 m	0.01 ± 0.08 (52, 0.01)	0.97 ± 0.10 (30, 0.57)	0.48 ± 0.06 (82, 0.36)
129 to 175 m	0.70 ± 0.04 (38, 0.53)	0.53 ± 0.08 (42, 0.29)	0.66 ± 0.04 (80, 0.44)
175 to 256 m	0.62 ± 0.06 (41, 0.31)	0.48 ± 0.05 (44, 0.31)	0.47 ± 0.04 (85, 0.28)
256 to 700 m	0.37 ± 0.05 (42, 0.19)	0.78 ± 0.06 (40, 0.33)	0.60 ± 0.03 (82, 0.32)

Table 16: S_o ± standard error with sample size and R in parenthesis for regimes defined in text and different thresholds to define a low N_a boundary layer (300 cm^{-3} or 400 cm^{-3}). S_o is statistically insignificant if underlined. H1 represents 28 < H < 129 m, H2 represents 129 < H < 175 m, H3 represents 175 < H < 256 m, and H4 represents 256 < H < 700 m.

H	S-L	S-H
300 cm^{-3}		
All	1.37 ± 0.06 (96, 0.42)	0.45 ± 0.06 (52, 0.17)
H1	1.20 ± 0.16 (19, 0.44)	0.38 ± 0.13 (10, 0.25)
H2	0.68 ± 0.13 (21, 0.26)	0.56 ± 0.16 (15, 0.20)
H3	0.70 ± 0.10 (31, 0.24)	<u>0.07 ± 0.10 (12, 0.03)</u>
H4	2.03 ± 0.10 (25, 0.55)	0.40 ± 0.10 (15, 0.12)
400 cm^{-3}		
All	1.12 ± 0.05 (125, 0.36)	0.37 ± 0.09 (23, 0.16)
H1	1.04 ± 0.13 (23, 0.43)	<u>-0.20 ± 0.21 (6, -0.11)</u>
H2	0.81 ± 0.11 (30, 0.30)	<u>0.02 ± 0.19 (6, 0.01)</u>
H3	0.53 ± 0.09 (35, 0.19)	<u>0.12 ± 0.12 (8, 0.06)</u>
H4	1.42 ± 0.07 (37, 0.41)	1.10 ± 0.42 (3, 0.25)

H	C-L	C-H
300 cm^{-3}		
All	0.29 ± 0.10 (21, 0.10)	0.84 ± 0.04 (150, 0.29)
H1	NaN (0, NaN)	-0.06 ± 0.11 (52, -0.03)
H2	0.02 ± 0.15 (6, 0.01)	0.86 ± 0.07 (30, 0.41)
H3	0.44 ± 0.17 (9, 0.15)	1.04 ± 0.10 (32, 0.30)
H4	-0.09 ± 0.17 (6, -0.03)	1.13 ± 0.07 (36, 0.36)
400 cm^{-3}		
All	1.11 ± 0.05 (64, 0.39)	0.25 ± 0.06 (107, 0.08)
H1	0.51 ± 0.22 (11, 0.21)	-0.33 ± 0.13 (41, -0.14)
H2	0.90 ± 0.10 (12, 0.43)	0.22 ± 0.09 (24, 0.10)
H3	0.84 ± 0.09 (24, 0.30)	0.53 ± 0.19 (17, 0.12)
H4	1.52 ± 0.08 (17, 0.50)	0.47 ± 0.09 (25, 0.13)

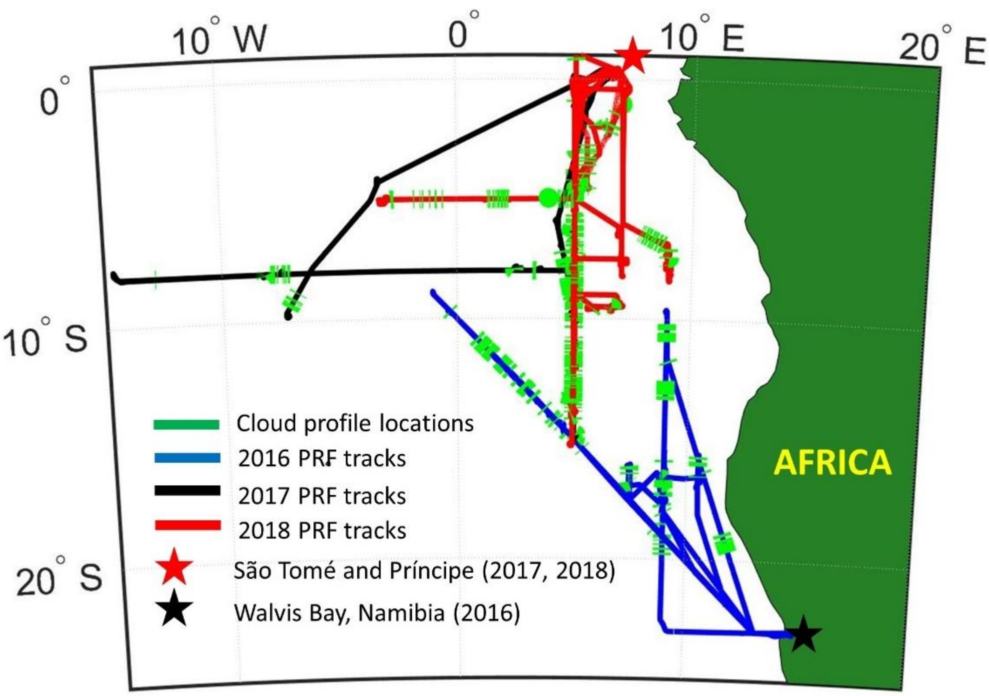

Figure 13: PRF tracks from ORACLES IOPs with base of operations and cloud sampling locations (tracks for multiple 2017 and 2018 PRFs overlap along 5° E).

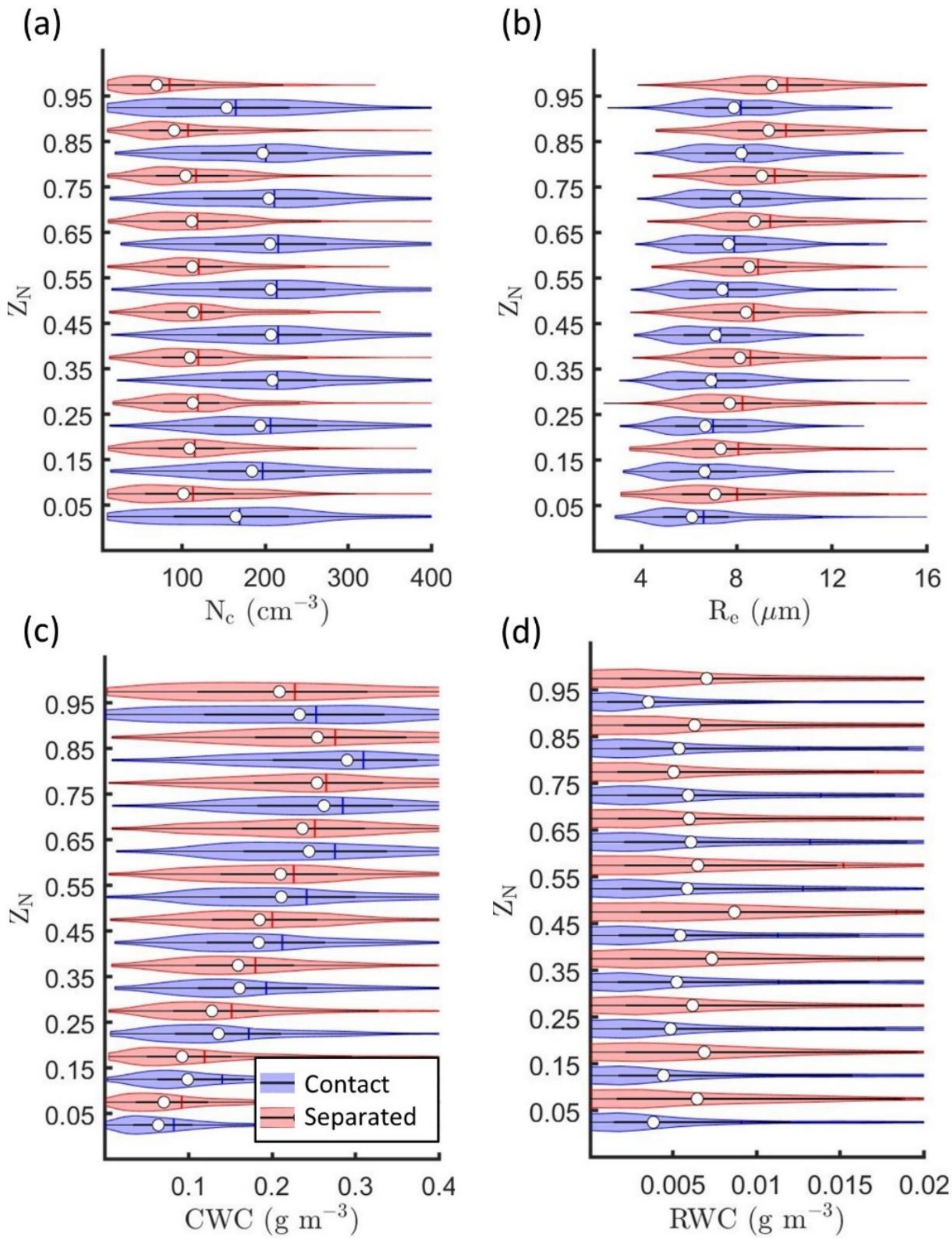

Figure 14: Kernel density estimates (indicated by the width of shaded area) and boxplots showing the 25th, 50th (white circle), and 75th percentiles for (a) N_c, (b) R_e, (c) CWC, and (d) RWC as a function of Z_N for contact and separated profiles.

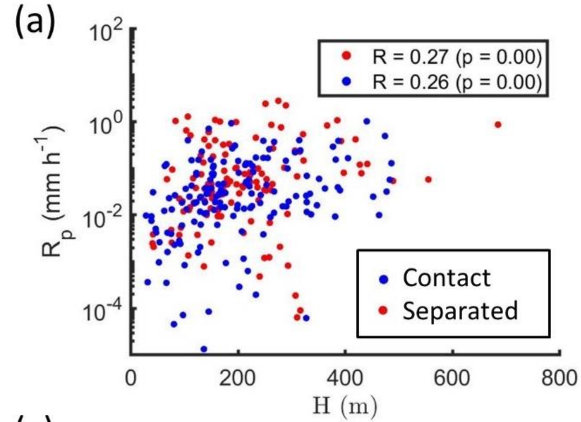

Figure 15: The 95th percentile for (a) R_p, (b) CWC, (c) N_c, and (d) R_e as a function of H. Each dot represents the 95th percentile from the 1 Hz measurements for a single cloud profile. Pearson's correlation coefficient (R) and p-value for the correlation indicated in legend.

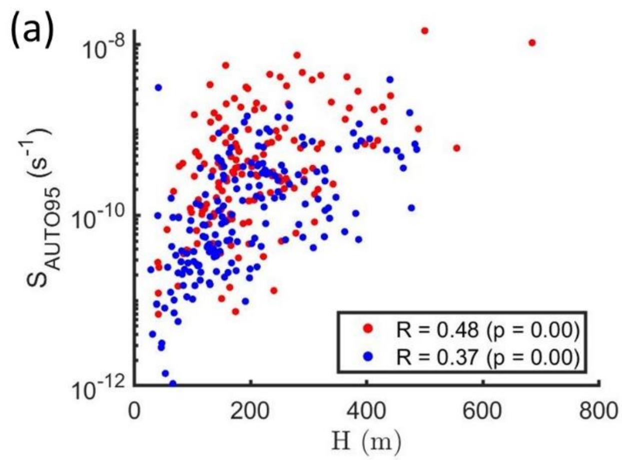

Figure 16: The 95th percentile for (a) S_{AUTO} and (b) S_{ACC} as a function of H. Each dot represents the 95th percentile from the 1 Hz measurements for a single cloud profile. R and p-value for the correlation indicated in legend.

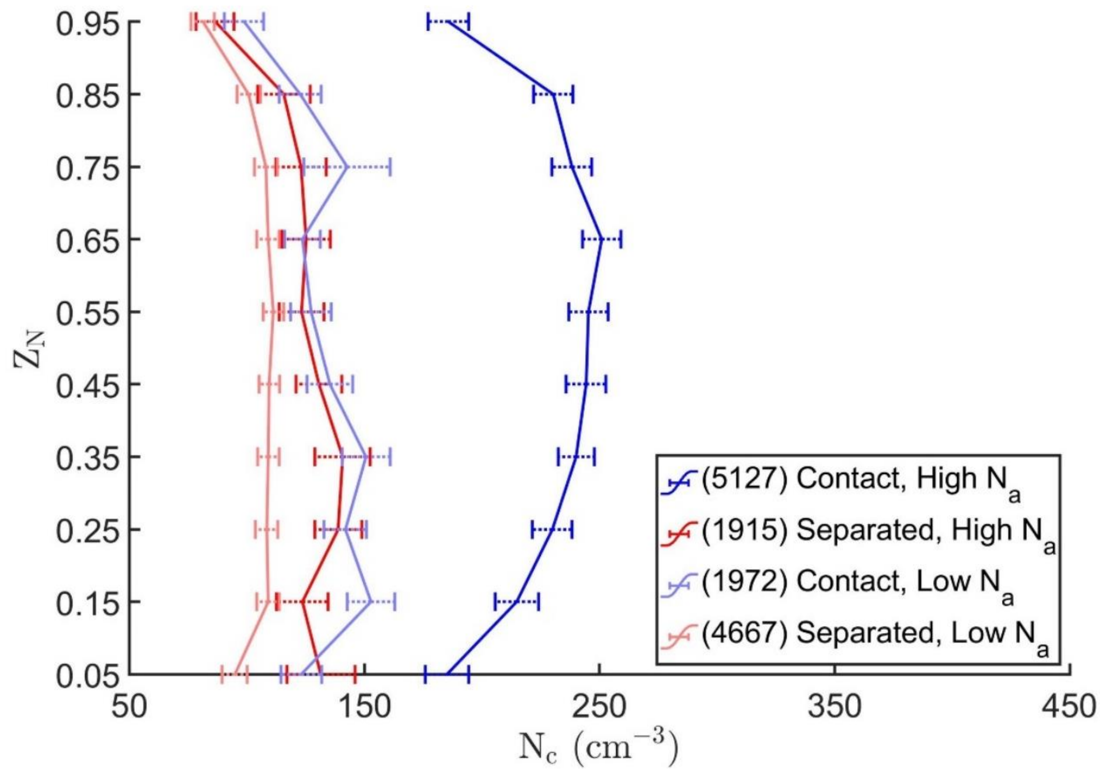

Figure 17: Average N_c (error bars extend to 95 % CIs) as a function of Z_N. Number of 1 Hz data points and corresponding regimes indicated in legend.

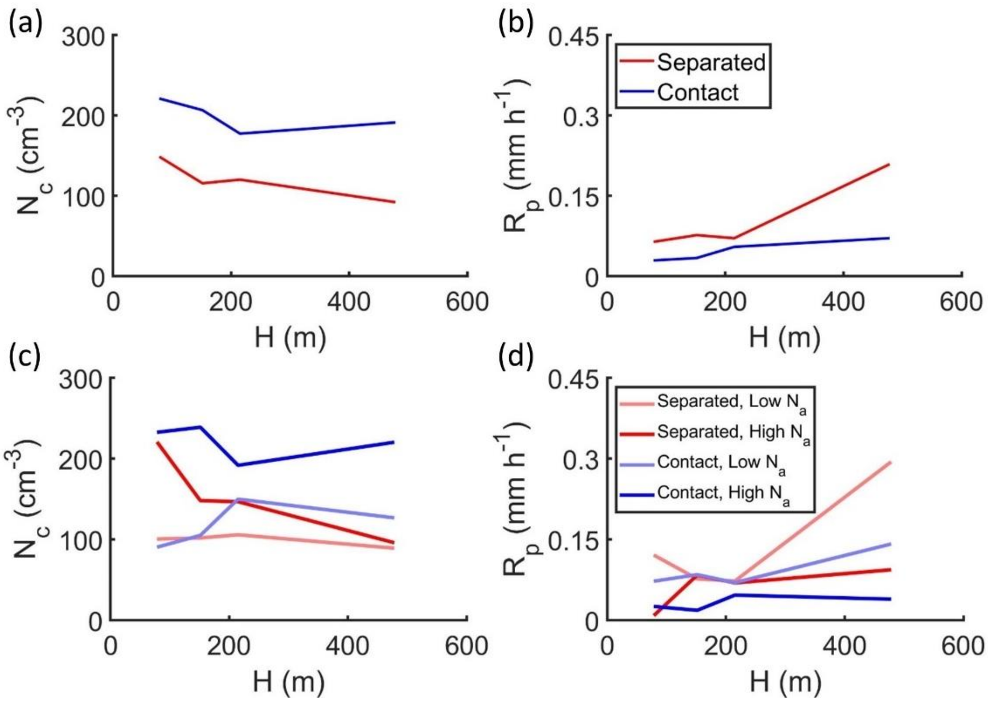

Figure 18: The average (a, c) N_c and (b, d) R_p as a function of H for (a, b) contact and separated profiles, and (c, d) the regimes indicated in legend.

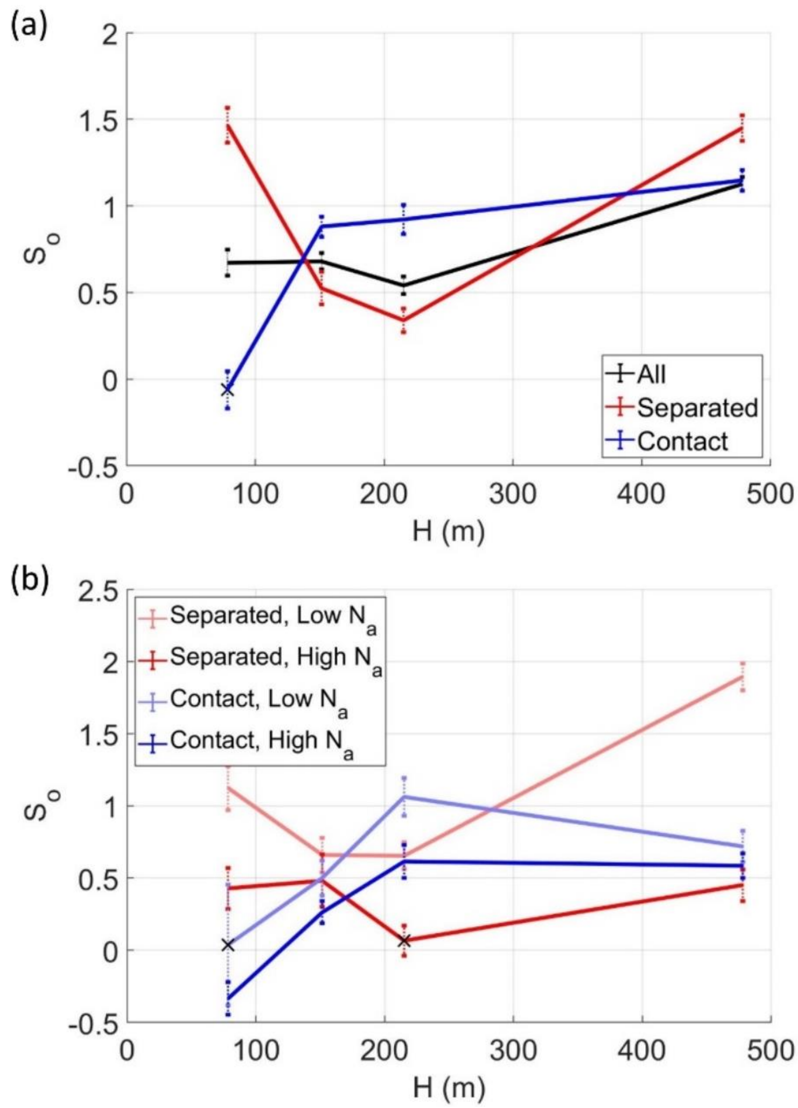

Figure 19: S_o as a function of H (error bars extend to standard error from the regression model) for (a) contact, separated, and all profiles, and (b) the regimes indicated in legend. S_o was statistically insignificant when marked with a cross.

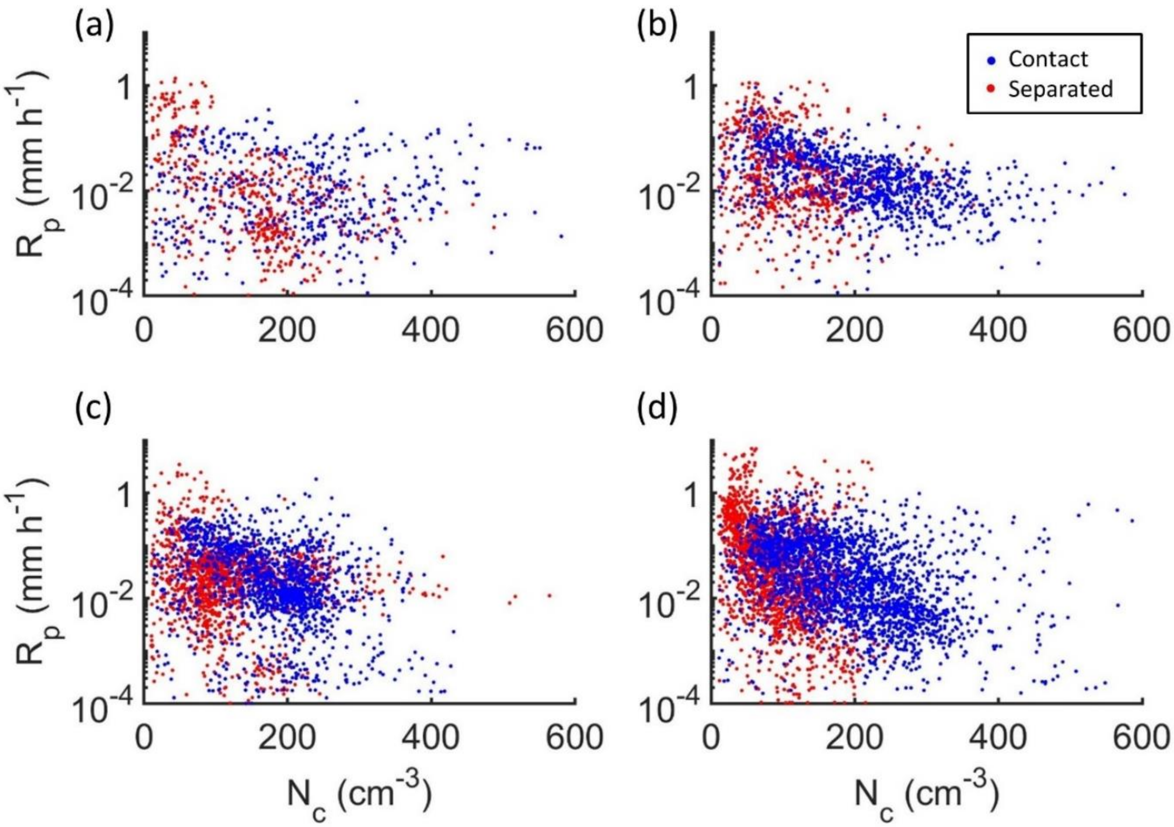

Figure 20: Scatter plots of R_p and N_c for 1 Hz data points from contact and separated profiles with (a) 28 < H < 129 m, (b) 129 < H < 175 m, (c) 175 < H < 256 m, and (d) 256 < H < 700 m.

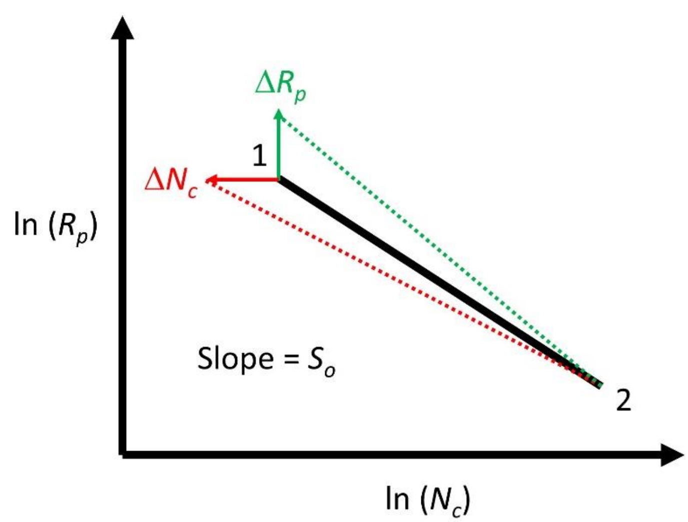

Figure 21: An illustration of the dependence of S_o on N_c, R_p, and perturbations (Δ) in N_c or R_p.

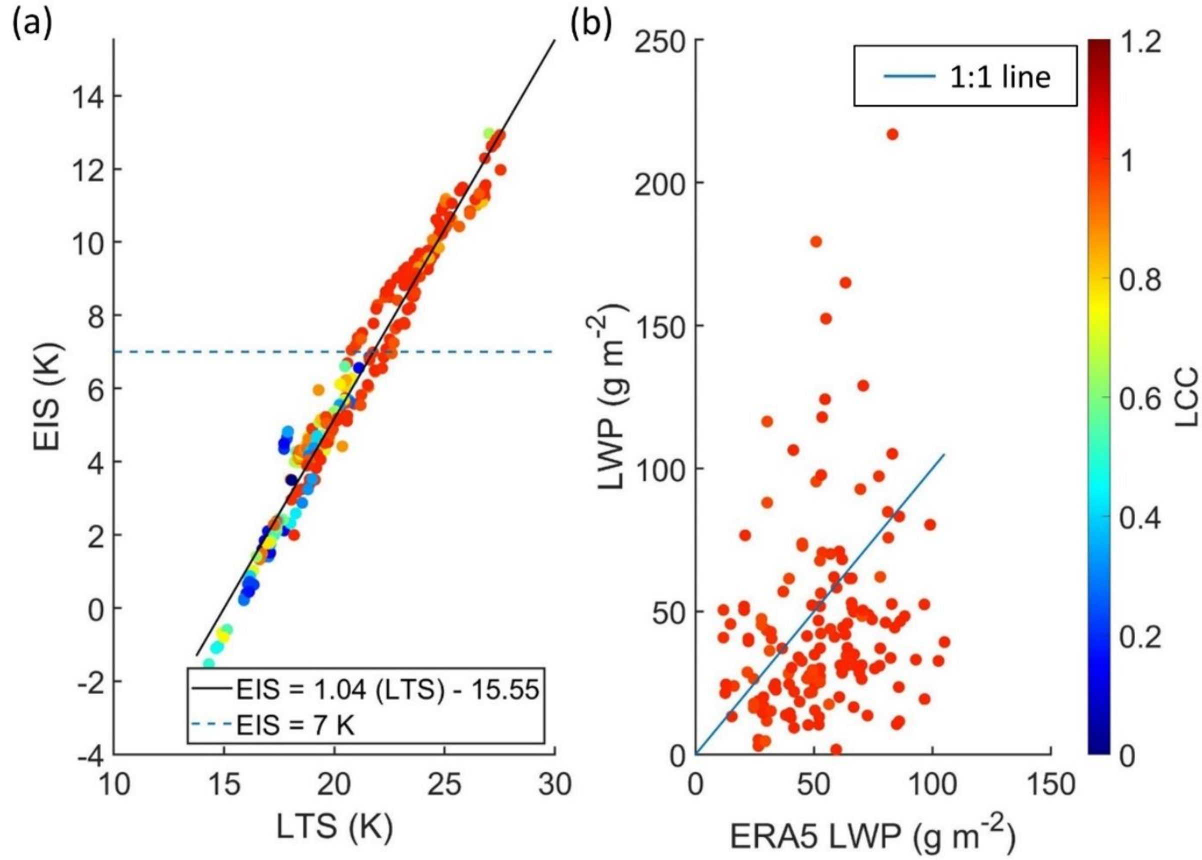

Figure 22: (a) LTS versus EIS with regression coefficients in legend (*R* = 0.98) and (b) LWP from size-resolved probes versus LWP from the ERA5 reanalysis (*R* = 0.18) where each dot represents a single cloud profile. LTS, EIS, ERA5 LWP, and LCC for each cloud profile taken from the nearest ERA5 grid box (within 0.25˚ of latitude and longitude) at 12:00 UTC. Panel (a) shows all cloud profiles and panel (b) shows cloud profiles with LCC > 0.95.

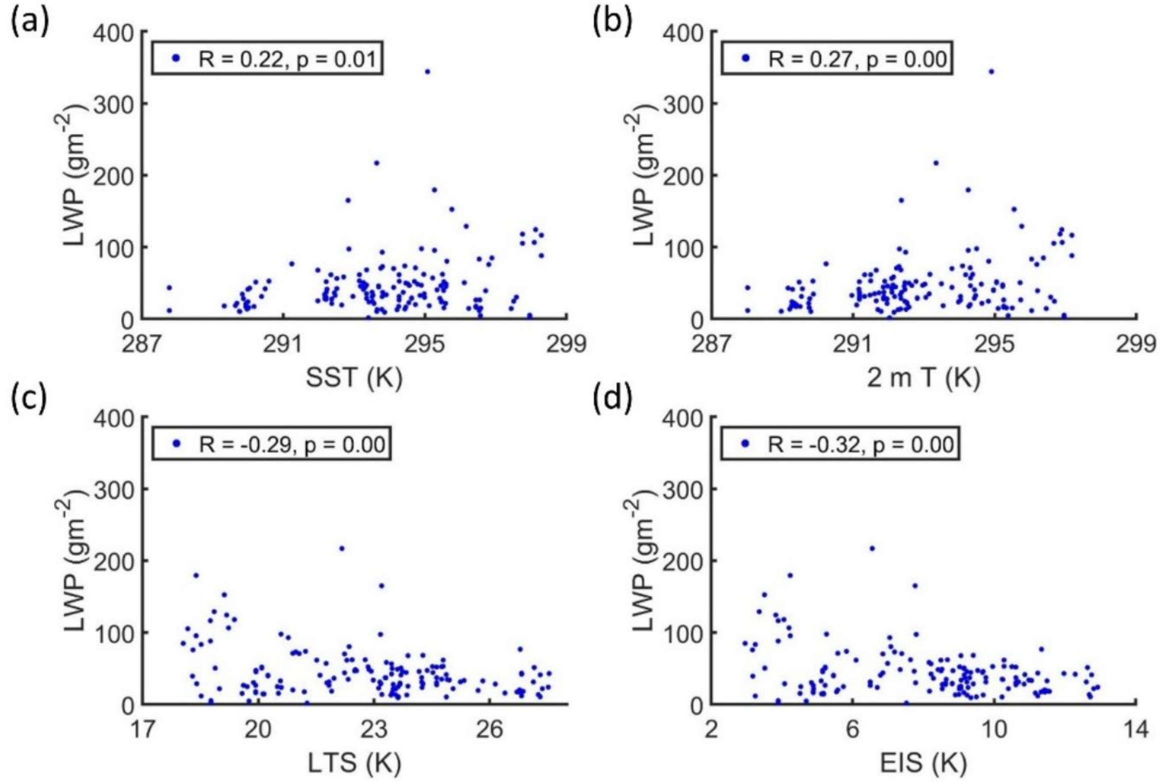

Figure 23: LWP from size-resolved probes as a function of (a) SST, (b) 2 m *T*, (c) LTS, and (d) EIS. Each dot represents a single cloud profile with LCC > 0.95 and SST, 2 m *T*, LTS, and EIS taken from the nearest ERA5 grid box (within 0.25˚ of latitude and longitude) at 12:00 UTC.

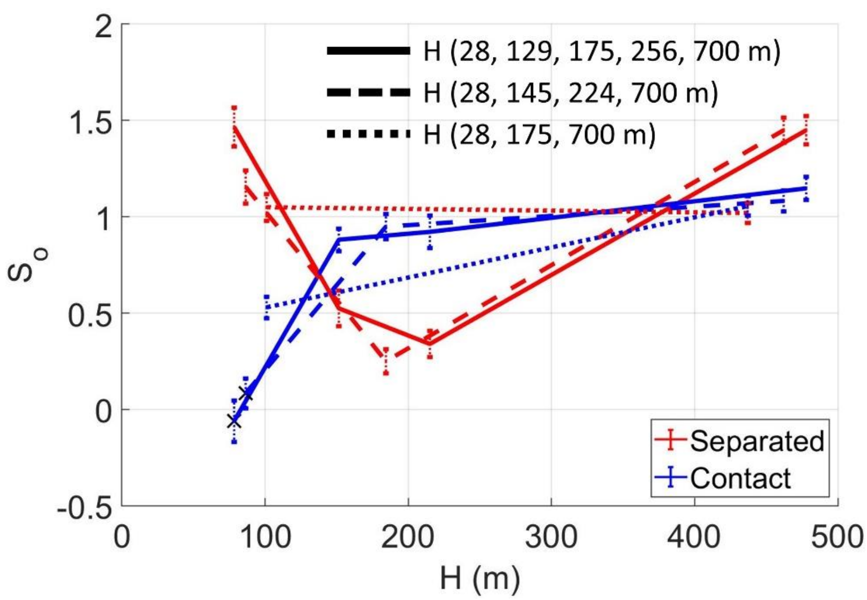

Figure 24: S_o as a function of *H* for contact and separated profiles classified into different populations using the end points indicated in legend. S_o was statistically insignificant when marked with a cross.

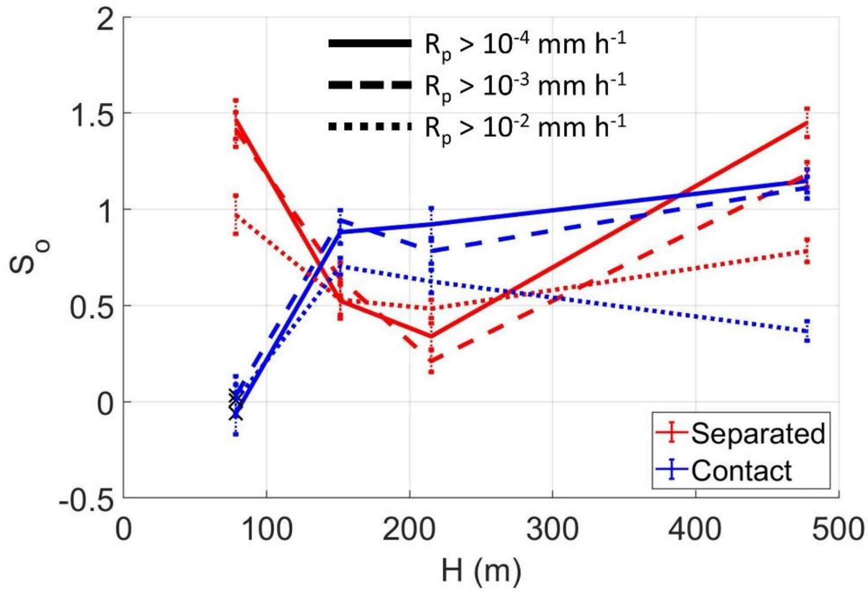

Figure 25: S_o as a function of H for contact and separated profiles with R_p greater than the thresholds indicated in legend. S_o was statistically insignificant when marked with a cross.

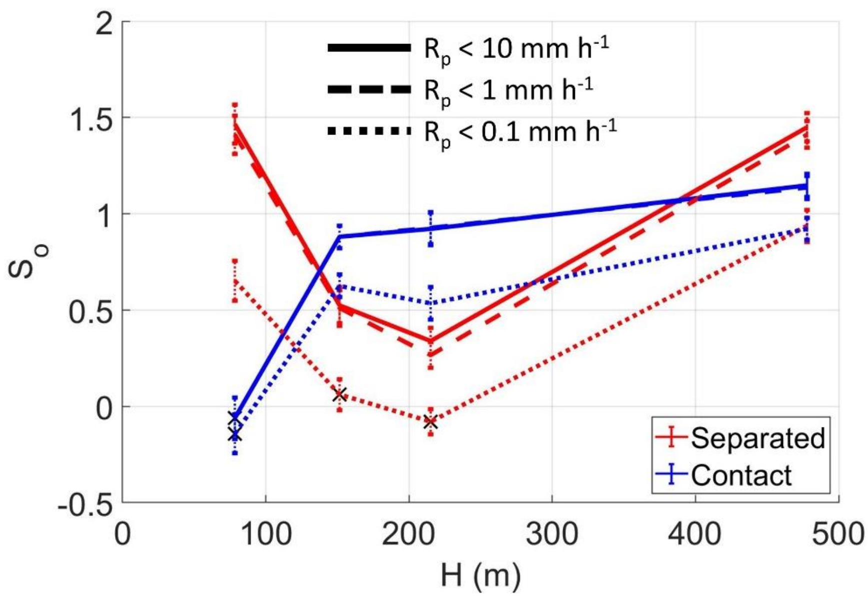

Figure 26: S_o as a function of H for contact and separated profiles with R_p less than the thresholds indicated in legend. S_o was statistically insignificant when marked with a cross.

4 In Situ and MODIS Estimates of Cloud Microphysical Properties and Aerosol-Cloud Interactions over the Southeast Atlantic Ocean

4.1. Introduction

Uncertainties in the effective radiative forcing due to aerosol-cloud interactions (ACI) lead to variability in climate model estimates of Earth's energy budget in future climate scenarios (e.g., Boucher et al., 2013). The ACI for warm, low-level clouds are particularly important due to their dominating impact on the aerosol indirect forcing (Christensen et al., 2016). Further, the shortwave cloud radiative forcing of - 17.1 W m^{-2} (Loeb et al., 2009) is largely driven by the ubiquitous low-level clouds (Hartmann et al., 1992). Marine stratocumulus is the most common type of low-level cloud with an annual mean coverage of 23 % of Earth's ocean surface (Wood, 2012). The radiative forcing due to well-mixed greenhouse gases (+ 2.83 W m^{-2}) (Myhre et al., 2013) or the doubling of CO_2 concentration (about + 2.5 W m^{-2}) could be offset by the radiative forcing from just a 15 to 20 % reduction in droplet sizes for low clouds (Slingo, 1990). Low-level clouds are thus strong modulators of planetary albedo and global climate.

ACI lead to changes in the cloud radiative forcing through processes that impact cloud extinction (β) and optical thickness (τ) which are closely related to microphysical properties like cloud droplet concentration (N_c), effective radius (R_e), and liquid water content (LWC). Cloud reflectance is a strong function of R_e, which represents the mean droplet size retrieved from radiative transfer calculations for the measured cloud reflectance (Hansen and Travis, 1974). An increase in aerosol concentration (N_a) can increase the number of cloud condensation nuclei and lead to higher N_c and lower R_e when LWC remains constant. These aerosol-induced changes in N_c

and R_e lead to clouds with higher reflectance or τ (Twomey, 1974; 1977). However, ACI are often masked by meteorological conditions (Mauger and Norris, 2007), other cloud responses to increasing N_a like invigoration (Douglas and L'Ecuyer, 2021), or changes in cloud properties due to the vertical profile of radiative heating (Johnson et al., 2004; McFarquhar and Wang, 2006).

Uncertainties in estimating the impact of ACI on cloud albedo are driven by differences between process scales for ACI and the resolution of climate models or satellite retrievals (McComiskey and Feingold, 2012). This inconsistency is addressed by combining satellite retrievals with airborne observations for specific regimes. A regime of interest for ACI exists over the southeast Atlantic Ocean where an extensive stratocumulus deck is overlaid by biomass burning aerosols from southern Africa (Haywood et al., 2004; Adebiyi and Zuidema, 2016). Climate models struggle to simulate the aerosol radiative forcing and the altitude of the above-cloud aerosol layer over the southeast Atlantic leading to biases in model estimates of low-cloud feedbacks and ACI (Das et al., 2020; Mallet et al., 2021). Multiple airborne campaigns have been conducted over the southeast Atlantic since 2016 to understand the ACI in this region and their impact on global climate (Zuidema et al., 2016; Formenti et al., 2019; Haywood et al., 2021).

During the NASA ObseRvations of Aerosols above CLouds and their intEractionS (ORACLES) field campaign (Redemann et al., 2021), in situ measurements of cloud droplet size distributions, from which N_c, R_e, and τ can be estimated, were collected over the southeast Atlantic at locations with contact or separation between the base of the aerosol layer and stratocumulus cloud tops. Variable vertical separation between the aerosol and cloud layers was associated with aerosol-induced changes in N_c, R_e, and τ (Chapter 2) and precipitation suppression (Chapter 3). Accurate satellite retrievals of N_c, R_e, and τ, and the aerosol-induced changes in N_c, R_e, and τ could enable such investigations over a larger domain and longer timescales than possible using in situ measurements alone.

The Earth Observing System Terra and Aqua satellites provide global coverage of cloud microphysical properties using the Moderate Resolution Imaging Spectroradiometer (MODIS). MODIS acquires solar reflectance for 36 atmospheric bands including a non-absorbing band (0.86 μm) which provides information on τ and a water absorbing band (1.6, 2.1, or 3.7 μm) which provides information on R_e (Platnick et al., 2003). The reflectance pair from these bands allows simultaneous retrievals of R_e and τ (Nakajima and King, 1990). In the absence of direct retrievals, MODIS N_c is estimated assuming adiabatic LWC (Brenguier et al., 2000; Szczodrak et al., 2001).

MODIS retrievals can have biases relative to in situ N_c, R_e, and τ depending on the occurrence of drizzle (Zinner et al., 2010), width and shape of droplet size distributions (Chang and Li, 2002; Brenguier et al., 2011), vertical profile of R_e (McFarquhar and Heymsfield, 1998; Platnick, 2000), and cloud adiabaticity (Min et al., 2012; Braun et al., 2018). Results from comparisons of MODIS retrievals with in situ data also depend on the cloud probes used for in situ measurements (King et al., 2013; Witte et al., 2018) and the spatiotemporal co-location of MODIS retrievals with in situ measurements (Painemal and Zuidema, 2011, hereafter PZ11).

Based on a review of N_c from satellite retrievals, Grosvenor et al. (2018) concluded airborne datasets were under-utilized for satellite retrieval evaluation. This study compares in situ N_c, R_e, and τ from ORACLES with MODIS retrievals of R_e and τ (Platnick et al., 2017) and the MODIS derived N_c based on the adiabatic assumption. Previous work comparing MODIS retrievals with in situ observations of marine stratocumulus (PZ11; Min et al., 2012; Noble and Hudson, 2015; Braun et al., 2018; Witte et al., 2018) is extended by using a larger in situ dataset from different aerosol-cloud conditions. Biases in MODIS retrievals of cloud properties are quantified as a function of time gap between MODIS retrievals and in situ data. The biases in MODIS Aqua are compared with biases in MODIS Terra and MODIS estimates of aerosol-induced changes in N_c, R_e, and τ are compared against in situ estimates.

The chapter is organized as follows. In situ observations and satellite retrievals used in the study are described in Section 4.2 along with the methodology for spatiotemporal co-location of the datasets. In Section 4.3, the MODIS R_e, τ, and N_c are compared with in situ R_e, τ, and N_c, potential sources of biases are discussed, and uncertainties and errors were quantified. In Section 4.4, MODIS estimates of aerosol-induced changes in R_e, τ, and N_c over the southeast Atlantic are compared with in situ estimates. Implications for studies of ACI over the southeast Atlantic are discussed in Section 4.5. Finally, the conclusions are presented in Section 4.6.

4.2. Data and Methodology

4.2.1. In situ observations

In situ observations of marine stratocumulus clouds over the southeast Atlantic Ocean were collected during ORACLES using the NASA P-3B aircraft (Redemann et al., 2021). In situ cloud sampling was conducted during vertical profiles through the stratocumulus layer (hereafter, cloud profiles) between 10˚ W to 15˚ E and 5˚ N to 20˚ S in September 2016, August 2017, and October 2018 (Chapter 3). At least three cloud profiles were obtained during 24 of the research flights, of which all but three (12 September 2016, 17 August 2017, and 5 October 2018) had at least one cloud profile with a co-located satellite retrieval (Table 17) based on the criteria described in Section 2.3.

Data from in situ cloud probes were used to derive the number distribution function (*n(D)*) for droplets with diameter (*D*) between 3 to 19200 μm. The cloud probes used included a Cloud and Aerosol Spectrometer (CAS) (Baumgardner et al., 2001), Cloud Droplet Probes (CDP) (Lance et al., 2010), a Two-Dimensional Stereo probe (2D-S) (Lawson et al., 2006), a Phase Doppler Interferometer (PDI) (Chuang et al., 2008), and a High Volume Precipitation Sampler (HVPS-3) (Lawson et al., 1998). A King hot-wire probe (King et al., 1978) was used to measure LWC (hereafter, King LWC). A Passive Cavity Aerosol Spectrometer Probe (PCASP) (Cai et al., 2013) measured *n(D)* for accumulation-mode aerosols (0.1 < *D* < 3 μm). The Airborne Data Processing and Analysis processing package (Delene, 2011) was used to process the CAS, CDP, King hot-wire, and PCASP data. The University of Illinois/Oklahoma Optical Array Probe Processing Software (McFarquhar et al., 2018) was used to process the 2D-S and HVPS-3 data.

A merged droplet size distribution was calculated using the CAS or CDP dataset for 3 < *D* < 50 μm, the 2D-S dataset for 50 < *D* < 1050 μm, and the HVPS-3 dataset for *D* > 1050 μm. N_c was calculated by integrating the droplet *n(D)* from the merged size distribution. Each 1 Hz data sample with $N_c > 10$ cm^{-3} and King LWC > 0.05 g m^{-3} was identified as in-cloud. N_a was calculated by integrating the PCASP *n(D)* for out of cloud data samples. Due to overlapping measurement ranges, the CAS, the CDPs, and the PDI provided at least two independent measurements of *n(D)* for 3 < *D* < 50 μm during each flight (Chapter 3). Data from one probe was chosen for inclusion in the merged size distribution based on availability of valid measurements from the CAS, CDP or PDI and through comparison of N_c and LWC from the CAS, CDP, and PDI datasets. The CAS was used to represent droplets with 3 < *D* < 50 μm for research flights from ORACLES 2016 and the CDP for research flights from ORACLES 2017 and 2018 (see Chapter 3 for justification and more details). The CAS *n(D)* for ORACLES 2016 was scaled using the King LWC due to a potential sizing bias in the CAS dataset based on the LWC comparisons. The methodology for scaling the 2016 CAS *n(D)* using the King LWC is described in Appendix 4.1 along with its impact on the results from this study.

For each profile, cloud top height (Z_T) and cloud base height (Z_B) were defined as the highest and the lowest altitude, respectively, with N_c > 10 cm^{-3} and King LWC > 0.05 g m^{-3} (Chapter 2). Cloud thickness (H) was defined as the difference between Z_T and Z_B. R_e and the effective variance (V_e) for the merged size distribution were calculated following Hansen and Travis (1974) as

$$R_e\ (h) = \int_0^\infty D^3\ N(D,h)\ dD \Big/ \int_0^\infty 2\ D^2\ N(D,h)\ dD$$

and

$$V_e(h) = \int_0^\infty (D - 2R_e\ (h))^2\ D^2\ N(D,h)\ dD \big/ (2R_e(h))^2 \int_0^\infty\ D^2\ N(D,h)\ dD \quad (1)$$

R_e can also be defined in terms of R_v (mean volume radius) as

$$R_e\ = k^{-1/3}\ R_v\ ,\ \ k = (1 + d^2)^3/(ad^3 + 1 + 3\ d^2)^2\ , \quad (2)$$

where k is the droplet spectral width which is a function of the skewness (a) and dispersion (d) of the droplet size distribution (Martin et al., 1994). Previous work has shown k varies with aerosol conditions, occurrence of drizzle, cloud adiabaticity, and height in cloud (McFarquhar and Heymsfield, 2001; Brenguier et al., 2011). LWC was calculated as

$$LWC\ (h) = \ \pi\ \rho_w/6 \int_0^\infty D^3\ N(D,h)\ dD = \ 4/3\ \pi\ \rho_w\ N_c(h)\ R_v(h)^3 \quad (3)$$

where h is height above Z_B and p_w is the liquid water density. At a height h in cloud, LWC is a function of the average N_c and R_v following Eq. (3). Liquid water path (LWP) and King LWP were calculated by integrating LWC and King LWC over h from Z_B to Z_T. τ was calculated as

$$\beta_{ext}\,(h) = \int_0^\infty Q_{ext}\,\pi/4\,D^2\,N(D,h)\,dD\,,\ \tau = \int_{Z_B}^{Z_T} \beta_{ext}\,(h)\,dh\,, \qquad (4)$$

where β_{ext} is the cloud extinction and the extinction coefficient (Q_{ext}) for cloud droplets is assumed to be 2 (Hansen and Travis, 1974) in the limit of geometric optics. The integrals in Eq. (1), (3), and (4) were converted to discrete sums corresponding to the cloud probe size bins for D > 3 μm with a maximum drop size of 19200 μm.

4.2.2. Satellite retrievals

The MODIS instrument onboard Terra and Aqua acquired passive retrievals of the radiance at non-absorbing and liquid water absorbing spectral bands (Platnick et al., 2003). The bispectral retrieval method was used to calculate R_e and τ using the 0.86 μm band paired with the 1.6, 2.1, or 3.7 μm band (Nakajima and King, 1990). R_e and τ at 1 km resolution from the MODIS Collection 6/6.1 Level 2 product (C6) (Platnick et al., 2017) were used. The wavelength dependence of MODIS τ was not examined since τ is mainly determined by the reflectance from the non-absorbing band (King et al., 1998). The C6 product included three retrievals for R_e, namely R_{e16}, R_{e21}, and R_{e37}, which were made using the 1.6, 2.1, and 3.7 μm band, respectively. Consistent with previous studies (e.g., PZ11), R_{e21} was used as the primary retrieval and MODIS R_e hereafter refers to R_{e21}.

R_{e16}, R_{e21}, and R_{e37} represent R_e at 2 to 4 optical depths below cloud top depending on liquid water absorption and a weighting function based on vertical penetration of photons into cloud (McFarquhar and Heymsfield, 1998; Platnick, 2000). R_{e37} corresponds to the level closest to cloud top followed by R_{e21} and R_{e16} in order of increasing distance from cloud top. In an upgrade from the MODIS Collection 5.1 (C5) product which reported R_{e21}, R_{e21} - R_{e16}, and R_{e21} - R_{e37}, the MODIS C6 product reports R_{e16}, R_{e21}, and R_{e37} separately. Thus, biases in R_{e16} and R_{e37} associated with the condition of a successful R_{e21} retrieval are removed (Platnick et al., 2017) and R_{e16}, R_{e21}, and R_{e37} can be compared (Section 3). For the ORACLES sampling domain (10˚ W to 15˚ E and 5˚ N to 20˚ S; Fig. 27), R_{e16}, R_{e21}, and R_{e37} from the C6 product were up to 2 μm lower than the corresponding retrievals from the C5 product (Rausch et al., 2017).

The MODIS retrievals are integrated quantities which do not describe a cloud's vertical structure. In the absence of in situ data, the vertical profile of LWC and R_v can be approximated using the adiabatic model (Brenguier et al., 2000). The adiabatic model was used to parameterize N_c and LWP as a function of τ and R_e (Szczodrak et al., 2001). The adiabatic LWC was defined as

$$LWC_{ad}(h) = C_w\, h \; = \; 4/3\ \pi\, \rho_w\, N_{ad}(h)\, R_{vad}(h)^3\ , \tag{5}$$

where C_w is the condensation rate, and the subscript 'ad' represents the adiabatic equivalent of a variable. Equations (1) to (4) were combined with Eq. (5) to determine τ_{ad} and LWP_{ad} following Brenguier et al. (2000) and Szczodrak et al. (2001), respectively, as

$$\tau_{ad} = 3/5\, \pi\, Q_{ext}\, (3\, C_w / 4\, \pi\, \rho_w)^{2/3}\, (kN_c)^{1/3}\, H^{5/3} \text{ and}$$

$$LWP_{ad} = 1/2\, C_w\, H^2 \; = 5/9\, \rho_w\, \tau\, R_e\ . \tag{6}$$

Using Equation (5), N_c was parameterized in terms of τ and R_e (Szczodrak et al., 2001) as

$$N_c = \sqrt{10}/4\, \pi\, k\ \ (\alpha\, C_w\, \tau\ /\ \rho_w\, R_e^5\ )^{1/2}\ , \tag{7}$$

where α is the adiabaticity defined as LWP divided by LWP_{ad}. The MODIS N_c was calculated using the MODIS R_e and τ in Eq. (7).

4.2.3. Co-location methodology

MODIS data with valid retrievals within the ORACLES sampling domain (10˚ W to 15˚ E and 5˚ N to 20˚ S; Fig. 27) were used. The Terra and Aqua satellites pass over the Equator at about 10:30 and 13:30 local time (+ 0 UTC), respectively. Most cloud profiles from ORACLES were flown within 1 to 2 hours of 12:00 UTC (Table 17). The time gap between the MODIS scan and the in situ sampling for a cloud profile was designated as ΔT. The analysis was limited to cloud profiles with a co-located MODIS retrieval with ΔT < 3600 s. This assumes the cloud layer did not undergo significant changes within one hour. This assumption was tested by comparing MODIS retrievals against in situ measurements for different upper bounds of ΔT (Section 3).

MODIS retrievals were co-located with in situ data following the criteria outlined by PZ11. The pixel closest to the cloud top latitude and longitude during a cloud profile was identified. The location of the selected pixel was adjusted to account for advection of the cloud field using the mean wind speed and direction from the Turbulent Air Motion Measurement System (Thornhill et al., 2003) on the P-3 aircraft. The wind speed was between 5 to 10 m s^{-1} which meant the pixel location was adjusted by a distance of up to 18 to 36 km, on average. The MODIS data were rejected if the corrected pixel was less than 3 pixels from the edge of the MODIS scan. The MODIS R_e and τ were averaged over a 5 km x 5 km domain centered on the corrected pixel to account for spatial inhomogeneity. The MODIS data were rejected if more than 10 % of the retrievals within the 5 km x 5 km domain, i.e., at least three out of the 25 pixels, were invalid.

There were 74 cloud profiles with co-located MODIS Terra retrievals and 75 cloud profiles with co-located MODIS Aqua retrievals with ΔT < 3600 s (Table 18). The ΔT for these profiles was evenly distributed with 10 to 15 cloud profiles within every 300 s bin from 0 to 3600 s (except

1500 to 1800 s) (Fig. 28a). For 101 out of the 149 cloud profiles, the distance between the cloud profile location and the MODIS pixel after adjusting for advection was below 12 km (Fig. 28b). The distance was greater than 36 km for three profiles.

4.3. MODIS versus in situ

4.3.1. R_e comparisons

MODIS R_e was compared with the in situ R_e averaged over the top 10 % of the cloud layer for 149 cloud profiles with a co-located MODIS retrieval with $\Delta T < 3600$ s (Fig. 29a). The difference between MODIS R_e and in situ R_e for a cloud profile was termed ΔR_e, with positive ΔR_e indicating MODIS R_e was greater than in situ R_e. The average MODIS R_e (11.4 μm) was 1.7 μm higher than the average in situ R_e (9.7 μm) with Pearson's correlation coefficient (R) = 0.78. The difference between the average MODIS R_e and in situ R_e was statistically significant. MODIS R_e was greater than the in situ R_e for all but 13 profiles. There were 106 profiles with ΔR_e less than ± 2 μm and 10 outliers had $\Delta R_e > 5$ μm (Fig. 30).

The ΔR_e was well correlated with MODIS R_e (R = 0.62) and poorly correlated with in situ R_e (R = 0.02). There were 14 profiles with MODIS $R_e > 15$ μm with an average ΔR_e of 4.5 μm and eight of the profiles had $\Delta R_e > 5$ μm (Fig. 30a). The MODIS R_e retrieval uncertainty was between 5 and 15 % and poorly correlated with ΔR_e (Fig. 30b). The average ΔR_e decreased and the correlation between MODIS R_e and in situ R_e was higher for profiles with lower ΔT (Table 19). The 43 cloud profiles with a co-located MODIS retrieval with $\Delta T < 900$ s had only three outliers with $\Delta R_e > 5$ μm (Fig. 29b). All three outliers were associated with MODIS $R_e > 15$ μm. These results were consistent with previous comparisons between aircraft measurements and MODIS retrievals. For example, PZ11 compared MODIS R_e and in situ R_e for 20 profiles of marine stratocumulus over the southeast Pacific with co-located MODIS retrievals having ΔT < 3600 s. They reported a higher average ΔR_e (2.1 μm) with higher correlation between MODIS R_e and in situ R_e (R = 0.98). Painemal et al. (2021) compared MODIS R_e and in situ R_e for liquid clouds over the North Atlantic (ΔT < 1500 s) with an average ΔR_e of 1.7 μm.

Retrievals from MODIS Aqua had higher average ΔR_e and weaker correlation with in situ R_e compared to MODIS Terra (Table 19). The MODIS R_e for seven out of the 10 outliers with ΔR_e > 5 μm was retrieved from MODIS Aqua and resulted in higher average ΔR_e compared to MODIS Terra (Table 19). This was despite the MODIS Aqua retrievals having lower ΔT (1630 s) compared to MODIS Terra retrievals (2020 s), on average. The impact of solar (μ_o) and sensor (μ) zenith angles on the relative performance of MODIS Aqua and MODIS Terra was examined. For co-located MODIS retrievals with ΔT < 3600 s, the average μ_o and μ were 26.9˚ and 41.5˚, respectively. The average μ_o and μ for MODIS Terra (24.0˚ and 43.0˚) were 5.7˚ lower and 3.0˚ higher than the average μ_o and μ for MODIS Aqua (29.7˚ and 40.0˚) (Fig. 31). The MODIS R_e and ΔR_e had weak correlations with μ_o (R = 0.18 and 0.16) and μ (R = -0.05 and -0.09) which suggests μ_o and μ had little impact on the performance of MODIS Terra relative to MODIS Aqua.

R_{e16}, R_{e21}, and R_{e37} were compared to determine if the average ΔR_e was dependent on the use of R_{e21} as the primary retrieval (Fig. 32). Co-located MODIS retrievals with ΔT < 3600 s had an average R_{e16}, R_{e21}, and R_{e37} of 10.5, 11.4, and 11.6 μm, respectively. The average R_{e16} and R_{e21} had statistically significant differences while the average R_{e21} and R_{e37} had statistically insignificant differences. The latter was consistent with global analyses that found R_{e37} minus R_{e21} depends on cloud regime with positive values (0 to 0.6 μm) for homogeneous marine stratocumulus (Zhang and Platnick, 2011; Fu et al., 2019).

The differences between R_{e16}, R_{e21}, and R_{e37} were associated with differences in the vertical penetration of photons into the cloud. The penetration depth decreases from R_{e16} to R_{e21} to R_{e37} (Platnick, 2000) and an increase in R_e with height in cloud (Chapter 3) resulted in $R_{e16} < R_{e21} < R_{e37}$. Although R_{e21} minus R_{e37} depends on μ_o, the average μ_o for ORACLES (24.0˚) was lower than the range of μ_o (65 to 70˚) for which R_{e37} minus R_{e21} exceeds 1 μm (Grosvenor and Wood, 2014). Consistent with Zhang and Platnick (2011), the correlation between R_{e21} and R_{e16} or R_{e37} decreased for values above 15 μm (Fig. 32). For values below 15 μm, R_{e16}, R_{e21}, and R_{e37} had an average of 9.7, 10.6, and 11.0 μm, respectively, and improved correlation between R_{e16} and R_{e21} (R = 0.92) and R_{e21} and R_{e37} (R = 0.95). MODIS R_e would have a positive bias regardless of the retrieval chosen. On average, R_{e21} had lower retrieval uncertainty (0.9 μm) compared to R_{e16} (1.9 μm) and R_{e37} (1.1 μm) which suggests R_{e21} gives a robust estimate of the average ΔR_e.

Since each MODIS R_e retrieval penetrated a certain optical depth into cloud, the altitude and in situ R_e at the level of 2 optical depths below cloud top ($Z_{\tau 2}$ and $R_{e\tau 2}$) were compared with the altitude and in situ R_e averaged over the top 10 % of the cloud (R_{e10} and Z_{10}). For profiles with a co-located MODIS retrieval with ΔT < 3600 s, $R_{e\tau 2}$ and R_{e10} were strongly correlated (R = 0.86) with average values of 9.5 and 9.7 μm, respectively (Fig. 33a). $R_{e\tau 2}$ was less than R_{e10} because $Z_{\tau 2}$ was 18 m lower than Z_{10}, on average (Fig. 33b), and R_e increased with height (Chapter 3). When seven outliers with R_e > 15 μm were removed, $R_{e\tau 2}$ and R_{e10} had average values of 9.3 and 9.4 μm, respectively, with improved correlation (R = 0.95). The average difference between $R_{e\tau 2}$ and R_{e10} (0.1 to 0.2 μm) was lower than the average ΔR_e between MODIS R_e and R_{e10} (1.7 μm). Thus, the choice of R_{e10} did not have a large impact on the average ΔR_e. In fact, MODIS R_e had weaker correlation with $R_{e\tau 2}$ (R = 0.67) compared to R_{e10} (R = 0.78).

4.3.2. τ comparisons

For profiles with a co-located MODIS retrieval with ΔT < 3600 s, the average MODIS τ (11.7) was 2.4 optical depths greater than the average in situ τ (R = 0.72) (Fig. 34a). $\Delta\tau$ was defined as the difference between MODIS τ and in situ τ for a profile with positive $\Delta\tau$ indicating that MODIS τ was higher. The biases in MODIS τ can be associated with spatial heterogeneity of the cloud field or retrieval uncertainties associated with MODIS τ. The average 5 km x 5 km MODIS τ standard deviation ($\sigma(\tau)$) was 2.2 and the average MODIS τ retrieval uncertainty (reported in C6 product) was 0.6. $\sigma(\tau)$ was correlated with MODIS τ (R = 0.72) and $\Delta\tau$ (R = 0.66). There were 84 profiles with $\Delta\tau$ > 2, 18 profiles with $\Delta\tau$ < -2, 32 profiles with $\Delta\tau$ > 5 and six profiles with $\Delta\tau$ < -5. An increase in the magnitude of $\Delta\tau$ with MODIS τ (Fig. 35a) was due to higher retrieval uncertainty at higher MODIS τ (Fig. 35b). The latter was expected given the sensitivity of MODIS τ to the non-absorbing reflectance decreases as τ increases (King et al., 1998).

The nine profiles with MODIS τ > 25 had an average $\Delta\tau$ of 8.1. Seven of these profiles had $\Delta\tau$ > 5 and one profile had $\Delta\tau$ < -5. The average $\Delta\tau$ decreased and the correlation between MODIS τ and in situ τ improved for profiles with lower ΔT (Table 19). This was consistent with the time-dependent improvement in correlations between τ from the MODIS C6 product and the airborne Solar Spectral Flux Radiometer used during ORACLES (Chang et al., 2021). Profiles with a co-located MODIS retrieval with ΔT < 900 s had an average $\Delta\tau$ of 1.5 with $\sigma(\tau)$ = 2.1 and the average MODIS τ uncertainty = 0.6. About 60 % of the profiles with a co-located MODIS retrieval with ΔT

< 900 s had $\Delta\tau > \pm 2$ (Fig. 34b). A single profile with $\Delta T < 900$ s and MODIS $\tau > 25$ had $\Delta\tau = -14.6$. MODIS Terra τ had lower $\Delta\tau$ and better correlation with in situ τ compared to MODIS Aqua τ (Table 19). The closest agreement between MODIS τ and in situ τ was observed for the 20 profiles with a co-located MODIS Terra retrieval with $\Delta T < 900$ s (Table 19).

4.3.3. N_c comparisons

N_c calculated using MODIS R_e and τ in Eq. (7) (hereafter, MODIS N_c) was compared with in situ N_c. Figure 36 shows cloud properties as a function of normalized height above cloud base (Z_N) where $Z_N = Z - Z_B$ divided by $Z_T - Z_B$. The in situ N_c was averaged over the top half of the cloud layer since entrainment mixing led to lower N_c over the top 10 % of the cloud height (Fig. 36a). Cloud-top entrainment did not affect the R_e near cloud top (Fig. 36b), indicative of inhomogeneous mixing, and did not affect the R_e comparisons. Nine profiles with MODIS $\tau < 5$ were removed from the N_c comparisons to avoid the impact of higher variability in MODIS retrievals for optically thin clouds (Zhang and Platnick, 2011). The exclusion of these profiles did not lead to significant changes in the R_e or τ comparisons.

ΔN_c was defined as the difference between MODIS N_c and in situ N_c for a profile with positive ΔN_c indicating that MODIS N_c was higher. For 140 profiles with a co-located MODIS retrieval with $\Delta T < 3600$ s and MODIS $\tau > 5$, there was good agreement between the average MODIS N_c (150.3 cm^{-3}) and the average in situ N_c (150.2 cm^{-3}) with $R = 0.90$ (Fig. 37). This was consistent with an average ΔN_c of - 4 cm^{-3} ($R = 0.94$) for stratocumulus over the southeast Pacific (PZ11). For 50 % of the profiles, ΔN_c was below ± 20 cm^{-3} which highlights the validity of the adiabatic assumption (Brenguier et al., 2000; Szczodrak et al., 2001) and the precision of the in situ estimates of k, C_w, and α (0.76, 2.94 g m^{-3} km^{-1}, and 0.74, respectively).

For 17 profiles, ΔN_c was greater than ± 50 cm^{-3}. This was due to higher variability in the in situ N_c for these profiles with an average standard deviation of 64 cm^{-3}. The average ΔN_c for these profiles was low (about 2 cm^{-3}) because nine profiles had $\Delta N_c > 0$ and eight profiles had $\Delta N_c < 0$. For three outliers with $\Delta N_c > \pm$ 100 cm^{-3}, the in situ N_c had an average standard deviation of 86 cm^{-3}. When the three outliers were removed, profiles with $\Delta T < 3600$ s and MODIS $\tau > 5$ had an average ΔN_c of 1 cm^{-3} ($R = 0.93$). Unlike the R_e or τ comparisons, lower ΔT was not associated with lower ΔN_c or better correlation between MODIS and in situ N_c. Further, MODIS Aqua N_c and MODIS Terra N_c had similar performance relative to in situ N_c (Table 19). The high level of agreement between MODIS N_c and in situ N_c was driven by compensating uncertainties associated with the parameters used in Eq. (7). These uncertainties were examined along with their impact on MODIS N_c.

4.3.3.1. Uncertainties with k, C_w, and α

MODIS does not retrieve the vertical profile of LWC, and the estimated rate of condensation with height in cloud (C_w) and the ratio of the vertical integrals of LWC and LWC_{ad} (α) provide the largest sources of error in MODIS N_c (Janssen et al., 2011; Min et al., 2012). Based on the range of estimates in the existing literature, C_w and α contribute a factor ranging from 0.9 to 1.5 in Eq. (7) (Merk et al., 2016, and references therein). For example, PZ11 assumed $C_w = 2$ g m^{-3} km^{-1} and $\alpha = 1$ with C_w and α contributing a factor of 1.41. α was negatively correlated with H (Fig. 38) (Min et al., 2012; Braun et al., 2018) and C_w was a function of cloud base pressure and temperature (Brenguier et al., 2000). For 142 profiles with a co-located MODIS retrieval with $\Delta T < 3600$ s and $LWP_{ad} > 5$ g m^{-2}, the average C_w and α were 2.94 ± 0.21 g m^{-3} km^{-1} and 0.74 ± 0.26, respectively, contributing a factor of 1.47 in Eq. (7). The uncertainty estimates represent one standard deviation. The use of C_w = 2 and α = 1 in Eq. (7) would lead to lower MODIS N_c and the average ΔN_c for profiles with ΔT < 3600 s and MODIS τ > 5 would change to - 6 cm^{-3} (from 0.1 cm^{-3} when C_w = 2.94 and α = 0.74 were used).

k represents spectral width which decreases when droplet size distributions get narrower. Consistent with PZ11, *k* averaged over the top 10 % of the cloud layer (0.76 ± 0.12) was higher than *k* averaged over the entire cloud layer (0.70 ± 0.15) (Fig. 39). The uncertainty estimates represent one standard deviation. Since MODIS R_e and τ correspond to values near cloud top, *k* = 0.76 was used in Eq. (7). Using *k* = 0.70 would increase MODIS N_c and the average ΔN_c for profiles with ΔT < 3600 s and MODIS τ > 5 would change to 13 cm^{-3} (from 0.1 cm^{-3} when *k* = 0.76 was used). The value of cloud top *k* (0.76) was consistent with that calculated by Brenguier et al. (2011) for marine clouds with entrainment mixing where *k* decreased when α decreased. In contrast, Martin et al. (1994) examined marine clouds without entrainment mixing with higher *k* (0.8). The decrease in N_c and LWC near cloud top with increasing R_e was indicative of inhomogeneous mixing (Fig. 36) and spectral broadening due to entrainment or drizzle (Sinclair et al., 2021) would explain the higher values for *k* near cloud top (Fig. 39).

4.3.3.2. Uncertainties with MODIS R_e and τ retrievals

The MODIS algorithm assumes vertically homogeneous R_e and LWC (King et al., 1998) but R_e and LWC increased almost linearly with height (LWC decreased near cloud top due to entrainment mixing) (Fig. 36b, c). The impact of this inconsistency was examined by quantifying the ΔN_c for profiles with large MODIS biases in R_e or τ. The average ΔN_c for nine profiles with MODIS τ > 25 (average $\Delta\tau$ = 5.3) and 14 profiles with MODIS R_e > 15 μm (average ΔR_e = 4.5 μm) was 8 and 29 cm^{-3}, respectively. The magnitude of ΔN_c was greater than 50 cm^{-3} for only two profiles with MODIS $\tau > 25$ and one profile with MODIS $R_e > 15$ μm. This suggests a large bias in MODIS R_e or τ did not necessarily result in a large bias in MODIS N_c.

The MODIS algorithm used a modified gamma distribution function to represent the droplet spectrum assuming V_e (Eq. 1) to be 10 % (Platnick et al., 2017). For such size distributions, k is related to V_e as $k = (1-V_e) \times (1-2V_e)$ and $V_e = 10$ % corresponds to $k = 0.72$ (Grosvenor et al., 2018). For ORACLES, V_e decreased with height (Fig. 36d) with a median cloud top V_e of 8.4 % corresponding to $k = 0.76$. The a priori assumption of $V_e = 10$ % could lead to biases of up to 1 μm for MODIS R_e (Chang and Li, 2002). Radiative transfer simulations to quantify the MODIS R_e bias associated with V_e were beyond the scope of this study. Further, it is assumed the uncertainties associated with instrument error and atmospheric corrections were included in the retrieval uncertainties in the MODIS C6 product.

The occurrence of drizzle could introduce biases in MODIS R_e or N_c due to lower k associated with spectral broadening (Sinclair et al., 2021), higher V_e for a bimodal size distribution (Nakajima et al., 2010), or lower α due to cloud water removal through precipitation (Braun et al., 2018). However, the average rain rate for ORACLES was too low (0.06 mm h^{-1}) (Chapter 3) for drizzle to have a major impact on the R_e retrievals (Zinner et al., 2010; PZ11). This was supported by the positive values for R_{e37} minus R_{e21} which represent size distributions without a significant drizzle mode (Nakajima et al., 2010). The impact of cloud water removal through precipitation was included by using the in situ α (0.74) in Eq. (7).

4.3.3.3. MODIS N_c error analysis

The total error for MODIS N_c from Eq. (7) was quantified using propagation of measurement uncertainties associated with k, C_w, and α and retrieval uncertainties associated with MODIS R_e and τ. Assuming the covariances were normally distributed and random, the total error can be calculated using Gaussian error propagation as

$$\left(\frac{\delta N_c}{N_c}\right)^2 = \left(\frac{1}{2}\frac{\delta\tau}{\tau}\right)^2 + \left(\frac{5}{2}\frac{\delta R_e}{R_e}\right)^2 + \left(\frac{1}{2}\frac{\delta C_W}{C_W}\right)^2 + \left(\frac{1}{2}\frac{\delta\alpha}{\alpha}\right)^2 + \left(\frac{\delta k}{k}\right)^2, \quad (8)$$

where δ represents the error for each variable.

For MODIS R_e and τ, the error was defined as the average retrieval uncertainty from the MODIS C6 product (7.5 and 5 %, respectively). For k, C_w, and α, the error was defined as one standard deviation (16, 7.1, and 35 % of the respective averages). Based on Eq. (8), MODIS N_c had an error of 30.5 %. This was smaller than previous estimates of 38 % (Janssen et al., 2011) and 78 % (Grosvenor et al., 2018). Consistent with Grosvenor et al. (2018), uncertainties in R_e had the largest contribution to the total error (since $N_c \propto R_e^{-5/2}$) followed by α and k. Profiles with MODIS R_e > 15 μm and average ΔR_e = 4.5 μm had an average ΔN_c of 28 cm^{-3} which shows the impact of the R_e uncertainty was compensated by the uncertainties for other parameters in Eq. (7).

MODIS N_c calculated using in situ estimates of k, C_w, and α from ORACLES was higher than MODIS N_c calculated using a priori assumptions for k, C_w, and α. For example, using C_w = 2 g m^{-3} km^{-1} and $\alpha = 1$ (PZ11) and k = 0.8 (Martin et al., 1994) introduced a factor of 0.91 in Eq. (7) relative to using C_w = 2.94 g m^{-3} km^{-1}, α = 0.74, and k = 0.76. The MODIS N_c based on the a priori assumptions had an average ΔN_c of -14, 6, and 5 cm^{-3} for profiles with a co-located MODIS retrieval with MODIS $\tau > 5$ and ΔT < 3600, 1800, and 900 s, respectively.

4.4. Aerosol-cloud interactions

During the ORACLES research flights, variable vertical separation was observed between biomass burning aerosols from southern Africa and marine stratocumulus over the southeast

Atlantic (Redemann et al., 2021). Cloud profiles were conducted at locations of both contact and separation between the base of the aerosol layer and the top of the cloud layer. The cloud profiles with aerosol concentration (N_a) greater than 500 cm^{-3} within 100 m above cloud tops were termed "contact profiles" and cloud profiles with N_a < 500 cm^{-3} up to 100 m above cloud tops were termed "separated profiles" (see Chapter 2).

Across the ORACLES campaigns, 173 contact profiles were conducted with 84 to 90 cm^{-3} higher in situ N_c, 1.4 to 1.6 μm lower in situ R_e, and 0.04 to 3.06 higher in situ τ compared to 156 separated profiles (Chapter 3). These differences were attributed to ACI given the similar sea surface temperature, lower tropospheric stability, and estimated inversion strength at the locations of contact and separated profiles, on average (Chapter 3). The differences in the in situ N_c, R_e, and τ for contact and separated profiles were statistically significant ($p < 0.02$) unless otherwise stated. The differences were reported using the 95 % confidence intervals from a two-sample t-test which represent the range of the difference between the average values for two parameters determined with 95 % confidence.

Differences in the in situ N_c, R_e, and τ for contact and separated profiles were compared with the corresponding differences in MODIS N_c, R_e, and τ. A co-located MODIS retrieval with ΔT less than 3600 s was available for 67 contact and 82 separated profiles (Table 17). These contact profiles had 85 to 92 cm^{-3} higher in situ N_c, 1.5 to 1.7 μm lower in situ R_e, and 0.67 to 4.82 higher in situ τ compared to the separated profiles. When the in situ N_c and R_e were averaged over the top 50 % and top 10 % of the cloud, respectively, contact profiles had 88 to 98 cm^{-3} higher in situ N_c and 1.5 to 2.2 μm lower in situ R_e compared to separated profiles.

The average MODIS R_e for contact profiles (9.9 μm) was 1.4 μm larger than the average in situ R_e (R = 0.76) (Fig. 40). In comparison, for separated profiles, the average MODIS R_e (12.7 μm) was 2 μm larger than the average in situ R_e (R = 0.72). Separated profiles had a larger positive bias in MODIS R_e compared to contact profiles because 13 out of the 14 profiles with MODIS R_e > 15 μm, with high average ΔR_e (4.5 μm) (Fig. 29a), were classified as separated profiles. The MODIS R_e estimate (2.8 μm) for the aerosol-induced increase in R_e from contact to separated profiles was thus greater than the in situ R_e estimate (2.2 μm). If profiles with MODIS R_e > 15 μm were removed, the estimates from MODIS R_e (1.8 μm) and in situ R_e (1.6 μm) were closer. This was because MODIS R_e had a similar positive bias for contact and separated profiles with MODIS R_e < 15 μm (1.3 and 1.6 μm, respectively). The number of profiles with MODIS R_e > 15 μm was lower for MODIS Terra compared to MODIS Aqua. Thus, closer agreement was observed between the in situ R_e and MODIS R_e estimates of the aerosol-induced change in R_e for MODIS Terra compared to MODIS Aqua (Table 20).

The average MODIS τ for contact profiles (13.3) was 2.5 optical depths greater than the average in situ τ (R = 0.75) (Fig. 41). For separated profiles, the average MODIS τ (10.3) was 2.3 optical depths greater than the average in situ τ (R = 0.60). As a result, there was good agreement between the MODIS τ estimate (3.0) and the in situ τ estimate (2.8) for the aerosol-induced increase in τ from separated to contact profiles. Contact profiles with co-located MODIS Aqua retrievals had lower in situ τ compared to separated profiles. The MODIS Aqua τ reproduced the sign and magnitude of this change (Table 20). The MODIS Terra τ underestimated the in situ τ increase from separated to contact profiles (Table 20) due to the profile with MODIS τ > 25 and $\Delta\tau$ = - 14.6 (Fig. 41). The estimate for the aerosol-induced change in τ was underestimated by

MODIS τ compared to in situ τ (Table 20). All nine profiles with MODIS $\tau > 25$ were classified as contact profiles (Fig. 41). These profiles were removed given the large average $\Delta\tau$ (8.1) for these profiles. For the remaining 58 contact profiles, MODIS τ (10.8) was 1.6 optical depths greater than in situ τ (R = 0.74), on average. The MODIS τ estimate (0.5) for the aerosol-induced increase in τ from separated to contact profiles was less than the in situ τ estimate (1.2). However, for lower ΔT, the estimates showed better agreement with average values within 0.4 optical depths.

The average MODIS N_c for contact profiles (203 cm^{-3}) was 2 cm^{-3} lower than the average in situ N_c (R = 0.86) (Fig. 42). For separated profiles, the average MODIS N_c (104 cm^{-3}) was 2 cm^{-3} greater than the average in situ N_c (R = 0.81). The estimate for the aerosol-induced increase in N_c (from separated to contact profiles) from MODIS N_c (99 cm^{-3}) was similar to the estimate from in situ N_c (103 cm^{-3}). The three outliers with $\Delta N_c > \pm$ 100 cm^{-3} were classified as contact profiles. When these outliers were removed, the MODIS N_c estimate (95 cm^{-3}) and the in situ N_c estimate (95 cm^{-3}) for the aerosol-induced increase in N_c from separated to contact profiles were similar. For MODIS Terra retrievals, underestimation of the increase in in situ N_c from separated to contact profiles (Table 20) was driven by the profile with $\Delta\tau$ = - 14.6 and MODIS $\tau > 25$ (Fig. 41). When this profile was removed, the MODIS N_c and in situ N_c estimates were within 5 cm^{-3}. The MODIS N_c calculated using a priori assumptions for k, C_w, and α underestimated the in situ N_c for contact profiles (by 20 cm^{-3}) and separated profiles (by 8 cm^{-3}). The a priori MODIS N_c estimate (91 cm^{-3}) for the increase in N_c from separated to contact profiles was slightly lower than the in situ N_c estimate (103 cm^{-3}).

4.5. Discussion

Differences between climate model and observational estimates of the effective radiative forcing due to ACI are largely driven by uncertainties in observational estimates of the radiative forcing due to aerosol effects on cloud albedo (RF_{aci}) (Gryspeerdt et al., 2020). Issues with satellite estimates of RF_{aci} persist due to biases in satellite retrievals of N_c (Grosvenor et al., 2018), above-cloud aerosol properties (Painemal et al., 2020; Chang et al., 2021), and aerosol perturbations of N_c (Quaas et al., 2020). Factors that frequently result in biases in MODIS retrievals of cloud properties include subpixel heterogeneity (Zhang and Platnick, 2011), solar and satellite viewing geometry (Grosvenor and Wood, 2014; Painemal et al., 2021), and cloud thermodynamic phase (Ahn et al., 2018). The impact of these factors on MODIS retrievals over the southeast Atlantic was limited given the low latitude and observations of homogeneous, warm, closed cell marine stratocumulus with low precipitation rates (Chapter 2, 3).

Results from Sections 3 and 4 suggest satellite estimates of N_c and aerosol perturbations of N_c over the southeast Atlantic have low biases (below 10 %) relative to in situ estimates. Good agreement between the MODIS and in situ estimates of aerosol-induced changes in N_c, R_e, and τ was also associated with similar biases in MODIS retrievals of clouds in different aerosol regimes. Differences between the estimates were lowered by removing profiles with large biases in MODIS retrievals (i.e., when MODIS R_e > 15 μm or MODIS τ > 25). This retrieval-based screening led to MODIS estimates of aerosol-induced changes in N_c, R_e, and τ within 5 cm^{-3}, 0.5 μm, and 0.7 of the in situ estimates. Such agreement suggests ACI for horizontally homogeneous, warm, closed cell marine stratocumulus can be studied using MODIS retrievals in the absence of in situ datasets.

Future work will evaluate attenuation-corrected retrievals of marine stratocumulus (Meyer et al., 2015) using polarimetric retrievals that operate without the assumptions required for passive satellite retrievals (Alexandrov et al., 2012). Polarimetric retrievals will help address the biases and errors in satellite retrievals of low-level clouds with stronger precipitation and bimodal size distributions (Sinclair et al., 2021) or complicated solar and viewing geometry (e.g., Painemal et al., 2021). It must be noted that improved estimates of both cloud and aerosol properties are needed for reducing the uncertainties in satellite estimates of RF_{aci} over the southeast Atlantic (Douglas and L'Ecuyer, 2020). Issues associated with satellite estimates of the placement or optical and microphysical properties of above-cloud aerosols must be addressed (e.g., Rajapakshe et al., 2017; Painemal et al., 2020; Chang et al., 2021; Peers et al., 2021).

4.6. Conclusions

In situ measurements of N_c, R_e, and τ for marine stratocumulus over the southeast Atlantic were collected during the NASA ORACLES field campaign. In situ data from 149 cloud profiles were co-located with MODIS retrievals from the Terra and Aqua satellites with a time gap (ΔT) below 1 hour. On average, MODIS R_e and τ (11.4 μm and 11.7) were 1.7 μm and 2.4 optical depths higher than in situ R_e and τ (R = 0.78 and 0.72). For over 70 % of the profiles, the biases in MODIS R_e and τ relative to in situ R_e and τ were below 2 μm and 5, respectively. The biases in MODIS retrievals decreased for lower ΔT and for retrievals from MODIS Terra compared to MODIS Aqua. Profiles with MODIS R_e > 15 μm had larger biases in MODIS R_e (average bias = 4.5 μm) and profiles with MODIS τ > 25 had larger biases in MODIS τ (average bias = 8.1). MODIS N_c (150.3 cm^{-3}) showed good agreement with in situ N_c (150.2 cm^{-3}) (R = 0.90) despite an error of 30.5 %. The retrieval uncertainty for MODIS R_e provided the largest source of error in calculating

MODIS N_c but compensating uncertainties for τ, k, C_w, and α resulted in the agreement between MODIS N_c and in situ N_c. For 50 % of the profiles, the bias in MODIS N_c was below 20 cm^{-3}. Profiles with biases above 50 cm^{-3} were associated with higher variability in the in situ N_c.

Changes in N_c, R_e, and τ for marine stratocumulus due to variable vertical separation with overlying biomass burning aerosols were estimated. For 67 “contact” profiles with N_a > 500 cm^{-3} within 100 m above cloud tops, in situ N_c and τ were 103 cm^{-3} and 2.8 higher and in situ R_e was 2.2 μm lower compared to 82 “separated” profiles with N_a < 500 cm^{-3} up to 100 m above cloud tops. In comparison, contact profiles had 99 cm^{-3} and 3.0 higher MODIS N_c and τ, and 2.8 μm lower MODIS R_e compared to separated profiles. The MODIS retrievals estimated the sign of the aerosol-induced changes in N_c, R_e, and τ with small differences in the magnitude of these changes compared to in situ estimates. The MODIS estimates were within 5 cm^{-3}, 0.5 μm, and 0.7 of the in situ estimates when profiles with larger biases (MODIS R_e > 15 μm or MODIS τ > 25) were removed. When k, C_w, and a from on a priori assumptions were used, the MODIS N_c decreased by 9 % and the MODIS estimate for change in N_c was within 12 cm^{-3} of the in situ estimate.

Good agreement between MODIS estimates and in situ estimates of aerosol-induced changes in cloud properties over the southeast Atlantic was associated with similar biases in MODIS retrievals relative to in situ data for clean and polluted clouds. MODIS retrievals can thus be used to study ACI for homogeneous and warm marine stratocumulus over the southeast Atlantic. Combined with lidar estimates of the vertical separation between aerosol and cloud layers and underlying cloud properties (Zeng et al., 2014; Rajapakshe et al., 2017; Painemal et al., 2020), MODIS retrievals with low biases will enable investigations of ACI over a larger domain of the southeast Atlantic over longer timescales than is possible using in situ data.

Appendix 4.1 – Scaling the CAS/CDP *n(D)* based on King LWC

For ORACLES 2016, CAS data were used in the study since CDP measurements were invalid due to an instrument misalignment issue. Chapter 3 showed there were statistically significant differences between the average CAS LWC of 0.15 ± 0.09 g m^{-3} (± one standard deviation) and the average King LWC of 0.28 ± 0.15 g m^{-3} (R = 0.80). The LWC comparison provides an estimate of the uncertainties in the CAS data due to known issues like droplet co-incidence in the CAS sample volume (Lance et al., 2012). For the six flights selected for data analysis, the King LWC and CAS LWC had a best fit slope (a) between 0.46 and 0.63 and R = 0.71 to 0.93 (Table 21). Based on the LWC differences, it was hypothesized the CAS was under-sizing the droplets passing through the CAS sample volume. The methodology outlined by PZ11 was used to account for the sizing bias wherein the CAS *n(D)* was scaled by adjusting the CAS size bins using the King LWC as

$$CAS\ LWC = a\ x\ King\ LWC,\ \ D_i^* = a^{-1/3}\ D_i\ , \qquad \text{(A1)}$$

where D_i is the midpoint diameter for the ith size bin and D_i* is the scaled midpoint diameter for the ith size bin. The D_i used to calculate LWC using Eq. 2 was replaced by D_i^*. The CAS size bin midpoints were increased by up to 30 % since $R_i^* > R_i$ for $a < 1$ and each flight had $a < 1$. The average in situ R_e for the 34 profiles from ORACLES 2016 with a co-located MODIS retrieval (Table 17) increased from 8.6 μm for unscaled CAS *n(D)* to 10.6 μm for CAS *n(D)* scaled using Eq. (A1).

The average MODIS R_e (12.4 μm) overestimated the average in situ R_e from both the unscaled and scaled CAS *n(D)*. When the CAS *n(D)* was scaled, the number of profiles having in situ R_e > MODIS R_e increased from 0 to 2 and the average ΔR_e decreased from 3.8 μm (R = 0.83) to 1.8 μm (R = 0.86), relative to using the unscaled CAS *n(D)*. These changes were consistent with the hypothesis of CAS under sizing the droplets passing through the CAS sample volume. Since the average ΔR_e for scaled CAS *n(D)* was consistent with previous studies (PZ11; Painemal et al., 2021), the scaled CAS *n(D)* was used in the study.

Valid CDP measurements were available for ORACLES 2017 and 2018. For the research flights from ORACLES 2017 and 2018, the average CDP LWC was 0.18 ± 0.16 g m^{-3} and 0.21 ± 0.14 g m^{-3}, the average King LWC was 0.21 ± 0.15 g m^{-3} and 0.20 ± 0.12 g m^{-3}, and the average CAS LWC was 0.09 ± 0.07 g m^{-3} and 0.10 ± 0.07 g m^{-3}, respectively (Chapter 3). These differences are within the typical uncertainties of these in situ cloud probes (Baumgardner et al., 2017). Given the closer agreement between CDP LWC and King LWC, it is unlikely the CDP had a sizing bias like the CAS and thus, the CDP measurements were used. In the absence of a sizing bias, the unscaled CDP *n(D)* was used in the study. Nevertheless, CDP *n(D)* was scaled using Eq. (A1) to determine if this would lead to qualitative changes in the results presented in the study.

For 14 out of 18 flights from ORACLES 2017 and 2018, the King LWC and CDP LWC had $0.7 < a < 1.4$ and the CDP size bin midpoints were adjusted by less than 13 % using Eq. (A1). When the CDP *n(D)* was scaled for the 42 profiles from ORACLES 2017 (Table 17), the average CDP R_e increased from 7.6 μm to 8.7 μm, the number of profiles having in situ R_e > MODIS R_e increased from 2 to 21, and the average ΔR_e decreased from 1.4 μm (R = 0.57) to 0.3 μm (R = 0.43), relative to using the unscaled CDP *n(D)*. Scaling the CDP *n(D)* led to a decrease in the best fit slope for MODIS R_e as a function of in situ R_e (0.73 to 0.50) along with an increase in the intercept (3.5 to 4.7 μm). These changes suggest the in situ R_e might be overestimated when the CDP *n(D)* is scaled, and the unscaled CDP *n(D)* was thus used in the study for ORACLES 2017.

When the CDP *n(D)* was scaled for the 73 profiles from ORACLES 2018 (Table 17), the average CDP R_e increased from 10.5 μm to 10.8 μm, the number of profiles having in situ R_e > MODIS R_e increased from 9 to 15, and the average ΔR_e decreased from 1.9 μm (R = 0.68) to 1.6 μm (R = 0.62), relative to using the unscaled CDP *n(D)*. The use of scaled CDP *n(D)* led to small changes in the best fit slope for MODIS R_e as a function of in situ R_e (0.77 to 0.73) and the intercept (4.3 to 4.5 μm). Scaling the CDP *n(D)* for ORACLES 2018 did not have a major impact on the CDP dataset. To remain consistent with the use of unscaled CDP data for ORACLES 2017, unscaled CDP data were used in the study for ORACLES 2018, as well.

When MODIS R_e was compared with in situ R_e calculated using unscaled *n(D)* for all three campaigns, the average ΔR_e was 2.2 μm with R = 0.72 and a best-fit slope and intercept of 0.86 and 3.5 μm, respectively (Fig. 43a). In comparison, when MODIS R_e was compared with in situ R_e calculated using scaled *n(D)* for all three campaigns, the average ΔR_e was 1.3 μm with R = 0.70 and a best-fit slope and intercept of 0.90 and 2.4 μm, respectively (Fig. 43b). Comparing Fig. 43 with Fig. 29a shows the use of either scaled or unscaled *n(D)* for all three campaigns did not lead to qualitative changes in the results presented in the study. MODIS R_e always had a positive bias greater than 1 μm relative to in situ R_e. It must be noted that the quantitative changes highlight the uncertainties associated with in situ data which must be considered when validating satellite retrievals using airborne datasets (Witte et al., 2018).

TABLES AND FIGURES

Table 17: List of research flights analyzed and the time range, number, sampling duration, and cloud top height (Z_T) for profiles with a co-located MODIS retrieval with time gap (ΔT) less than 3600 s. Number and duration listed for profiles classified by above-cloud aerosol location.

Flight Date	Time (UTC)	Separated	Contact	Z_T (m)
06 Sep 2016	09:36 – 12:35	6 (256 s)	9 (606 s)	509 - 1002
10 Sep 2016	10:08 – 12:36	5 (255 s)	0 (0 s)	1151 - 1201
14 Sep 2016	09:36 – 13:02	3 (148 s)	0 (0 s)	635 - 814
20 Sep 2016	12:57 – 13:11	0 (0 s)	2 (61 s)	580 - 583
25 Sep 2016	11:00 – 13:51	6 (363 s)	3 (148 s)	729 - 1124
12 Aug 2017	11:53 – 13:46	0 (0 s)	8 (327 s)	1148 - 1193
13 Aug 2017	10:15 – 11:33	0 (0 s)	15 (718 s)	1334 - 1384
15 Aug 2017	12:55 – 13:27	0 (0 s)	6 (169 s)	1108 - 1148
21 Aug 2017	13:34 – 13:35	1 (18 s)	0 (0 s)	1447
24 Aug 2017	12:39 – 12:40	0 (0 s)	1 (10 s)	1099
28 Aug 2017	11:46 – 13:18	4 (168 s)	7 (496 s)	1070 - 1230
27 Sep 2018	10:07 – 13:11	10 (366 s)	0 (0 s)	819 - 1169
30 Sep 2018	09:50 – 12:24	6 (183 s)	7 (337 s)	747 - 840
03 Oct 2018	13:30 – 14:41	2 (45 s)	0 (0 s)	1157 - 2151
07 Oct 2018	11:03 – 11:14	0 (0 s)	3 (136 s)	845 - 928
10 Oct 2018	10:16 – 13:31	2 (153 s)	1 (42 s)	991 - 1329
12 Oct 2018	13:02 – 14:19	6 (165 s)	0 (0 s)	1431 - 1905
15 Oct 2018	10:28 – 13:09	4 (125 s)	0 (0 s)	693 - 1547
19 Oct 2018	12:36 – 13:00	9 (661 s)	0 (0 s)	959 - 1276
21 Oct 2018	10:21 – 12.25	10 (504 s)	0 (0 s)	675 - 812
23 Oct 2018	10:28 – 13:08	8 (286 s)	5 (317 s)	873 - 1281
Total (2016)		**20 (1,022 s)**	**14 (815 s)**	
Total (2017)		**5 (186 s)**	**37 (1,720 s)**	
Total (2018)		**57 (2,488 s)**	**16 (832 s)**	
Total		**82 (3,696 s)**	**67 (3,367 s)**	

Table 18: Number of cloud profiles during ORACLES deployments with a co-located MODIS Terra or Aqua retrieval for ΔT less than 3600, 1800, or 900 s.

ΔT	Terra (2016, 2017, 2018)	Aqua (2016, 2017, 2018)	Total
3600 s	20, 15, 39	14, 27, 34	149
1800 s	9, 3, 17	12, 13, 15	69
900 s	9, 1, 10	8, 7, 8	43

Table 19: Pearson's correlation coefficient (R) and average bias (Δ) in MODIS (Terra, Aqua, and combined) retrievals relative to in situ measurements of R_e, τ, and N_c for different ΔT.

Parameter	**ΔT (s)**	**Terra Δ (R)**	**Aqua Δ (R)**	**Combined Δ (R)**
R_e (μm)	3600	1.5 (0.82)	1.9 (0.76)	1.7 (0.78)
	1800	1.4 (0.95)	2.1 (0.80)	1.8 (0.83)
	900	1.3 (0.91)	1.7 (0.81)	1.5 (0.83)
τ	3600	2.8 (0.70)	2.1 (0.71)	2.4 (0.72)
	1800	1.7 (0.90)	2.1 (0.70)	2.0 (0.84)
	900	1.3 (0.91)	1.6 (0.54)	1.5 (0.86)
N_c (cm^{-3})	3600	0.5 (0.87)	0.6 (0.93)	0.1 (0.90)
	1800	11 (0.82)	6.1 (0.95)	8.1 (0.90)
	900	9.1 (0.74)	10 (0.96)	9.6 (0.87)

Table 20: Differences between the average R_e, τ, and N_c for contact and separated profiles based on MODIS retrievals (Terra, Aqua, and combined) and in situ measurements. Positive values indicate contact profiles had a higher value.

Parameter	**ΔT (s)**	**Terra (In situ)**	**Aqua (In situ)**	**Terra & Aqua (In situ)**
R_e (μm)	3600	-1.7 (-1.4)	-3.7 (-2.9)	-2.8 (-2.2)
	1800	-0.9 (-0.7)	-5.8 (-3.8)	-3.6 (-2.5)
	900	-0.3 (-0.4)	-5.6 (-3.4)	-3.0 (-2.0)
τ	3600	6.0 (6.1)	-0.9 (-1.1)	3.0 (2.8)
	1800	7.1 (10.1)	-0.1 (-0.5)	2.4 (3.3)
	900	7.3 (10.5)	-2.2 (-2.5)	1.7 (2.9)
N_c (cm^{-3})	3600	83 (87)	115 (118)	99 (103)
	1800	80 (91)	161 (151)	115 (115)
	900	43 (77)	159 (131)	99 (101)

Table 21: ORACLES 2016 flight dates with the best fit slope (a) and intercept (c) between the average CAS LWC and King LWC from the flight.

Flight date	**$a + c$ (R)**
September 06	0.51 + 0.01 (0.71)
September 10	0.63 - 0.02 (0.93)
September 12	0.47 + 0.00 (0.88)
September 14	0.55 - 0.04 (0.85)
September 20	0.60 + 0.01 (0.88)
September 25	0.46 + 0.04 (0.74)

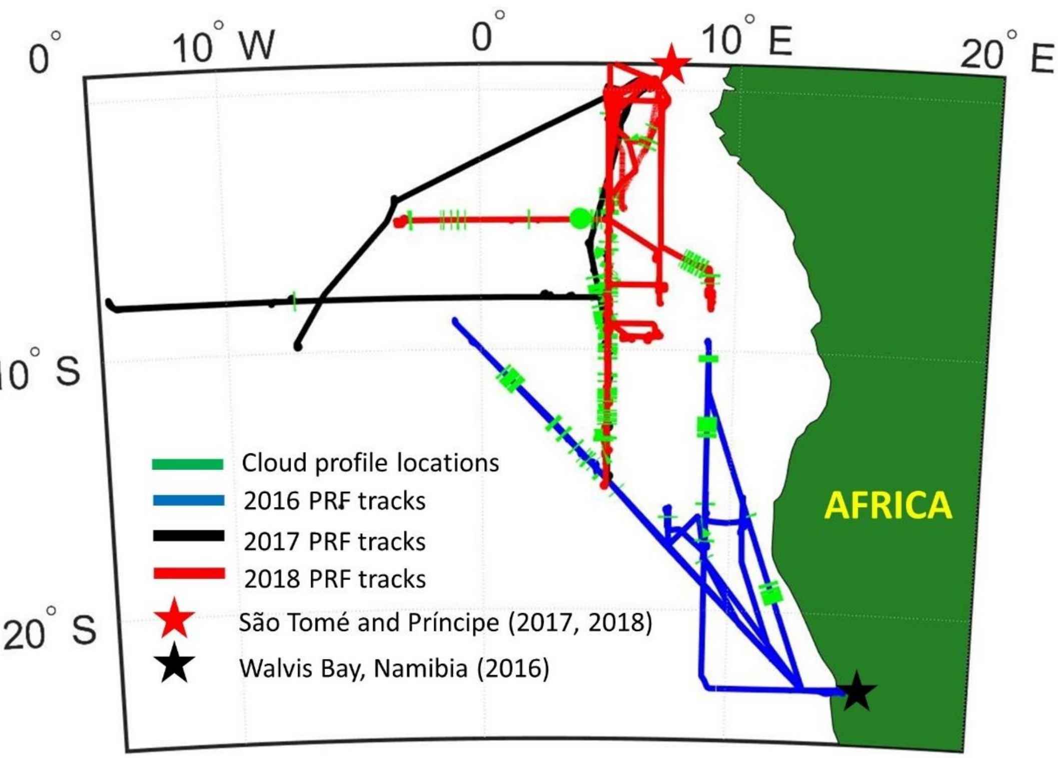

Figure 27: ORACLES flight tracks, base of operations, and sampling locations for profiles with a MODIS retrieval co-located with in situ data for ∆T less than 3600 s.

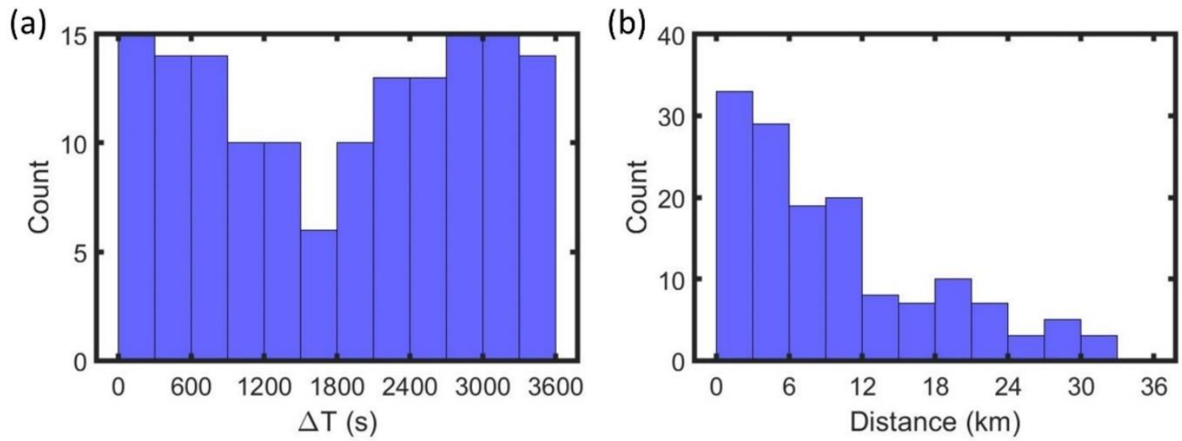

Figure 28: Histograms of (a) time gap between profiles and the co-located MODIS scan (∆T) and (b) distance between profiles and the co-located MODIS pixel after adjusting for advection.

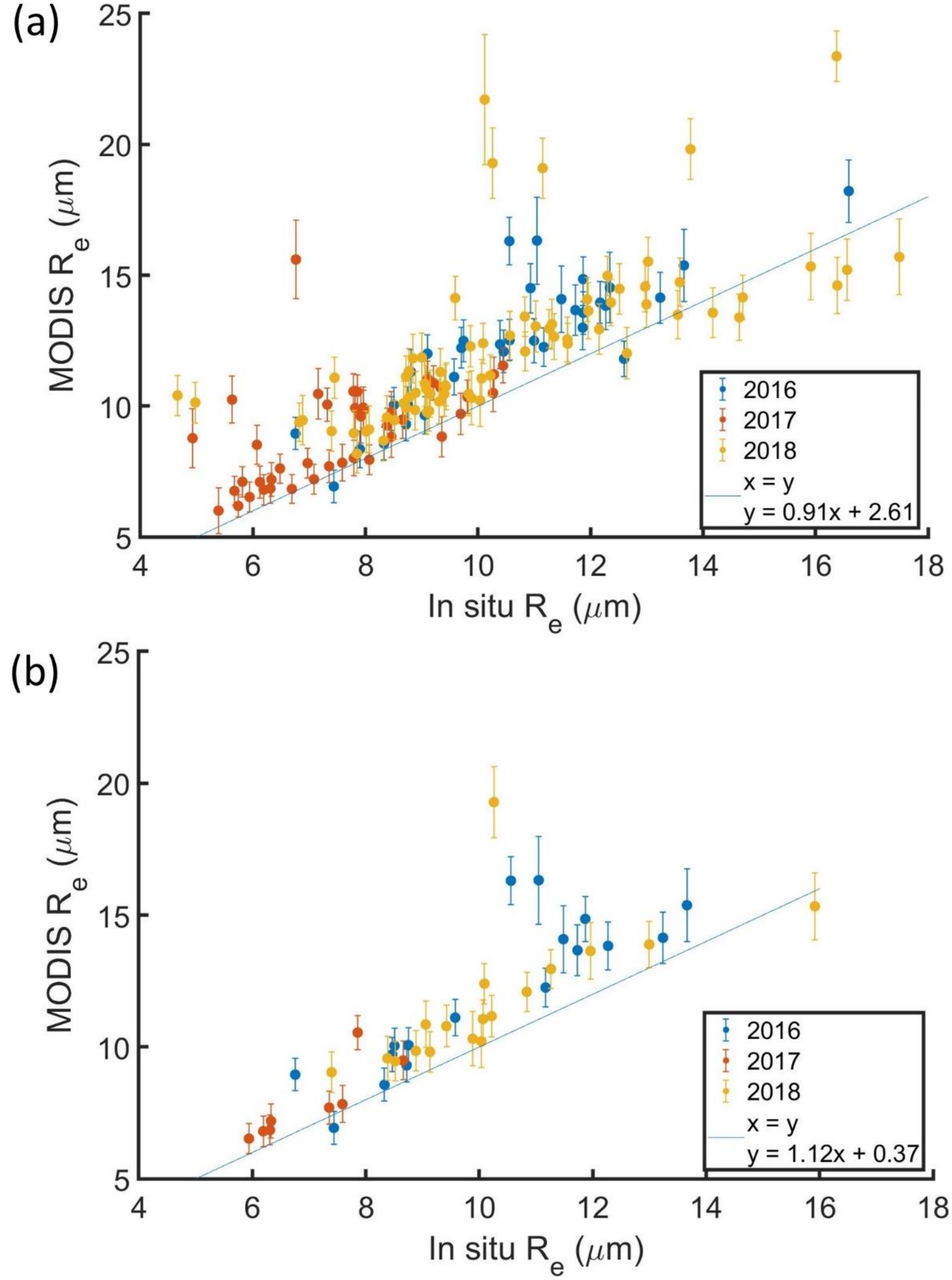

Figure 29: MODIS R_e versus in situ R_e for profiles with a MODIS retrieval co-located with in situ data for ΔT (a) less than 3600 s and (b) less than 900 s colored by ORACLES deployment year. Each point represents a cloud profile with the in situ R_e averaged over the top 10 % of the cloud and MODIS R_e averaged over a 5 km x 5 km domain centered at the cloud profile's location.

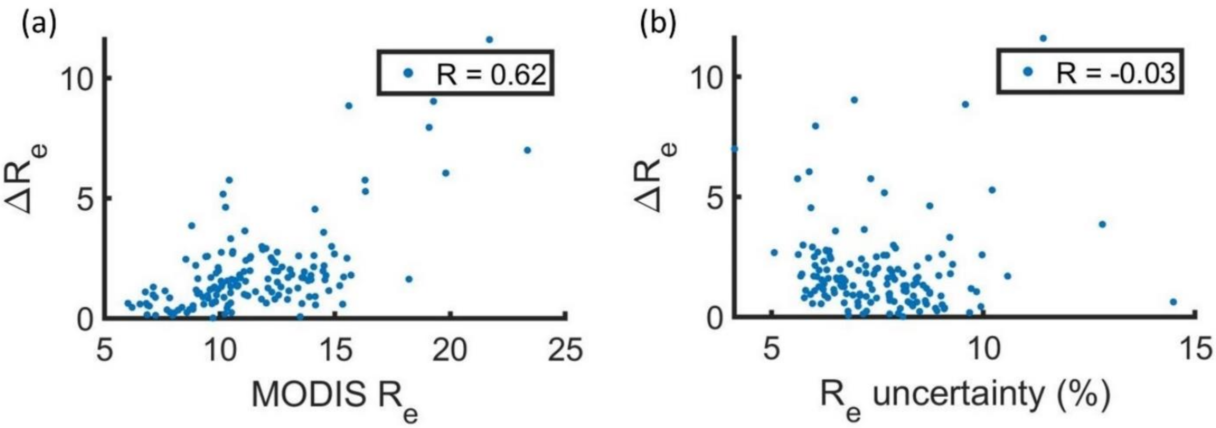

Figure 30: Magnitude of the difference between MODIS R_e and in situ R_e (ΔR_e) for profiles with a MODIS retrieval co-located with in situ data for ΔT less than 3600 s as a function of (a) MODIS R_e and (b) MODIS R_e uncertainty. Each point represents average values over a 5 km x 5 km domain centered at the corresponding cloud profile's location.

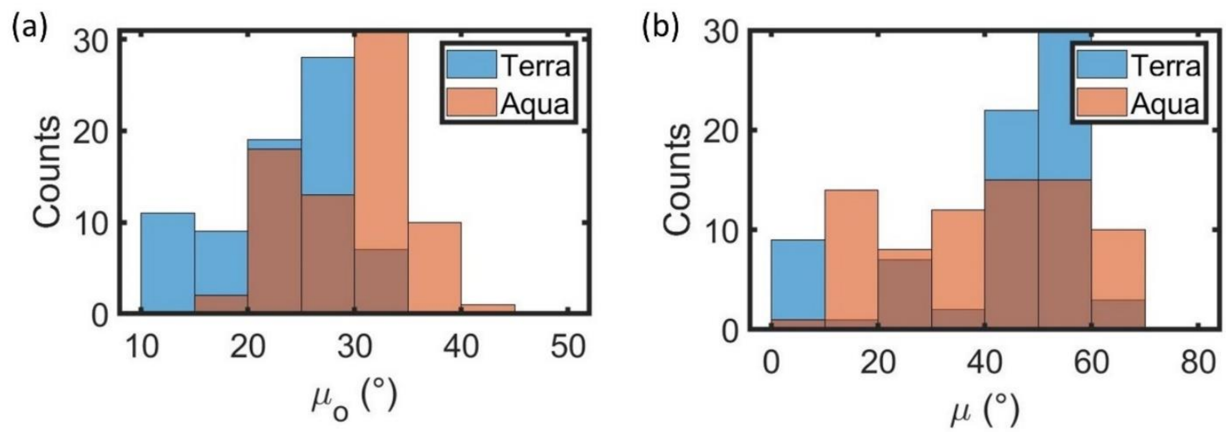

Figure 31: Histograms of (a) solar zenith angle (μ_o) and (b) sensor zenith angle (μ)for MODIS retrievals co-located with in situ data for ΔT less than 3600 s.

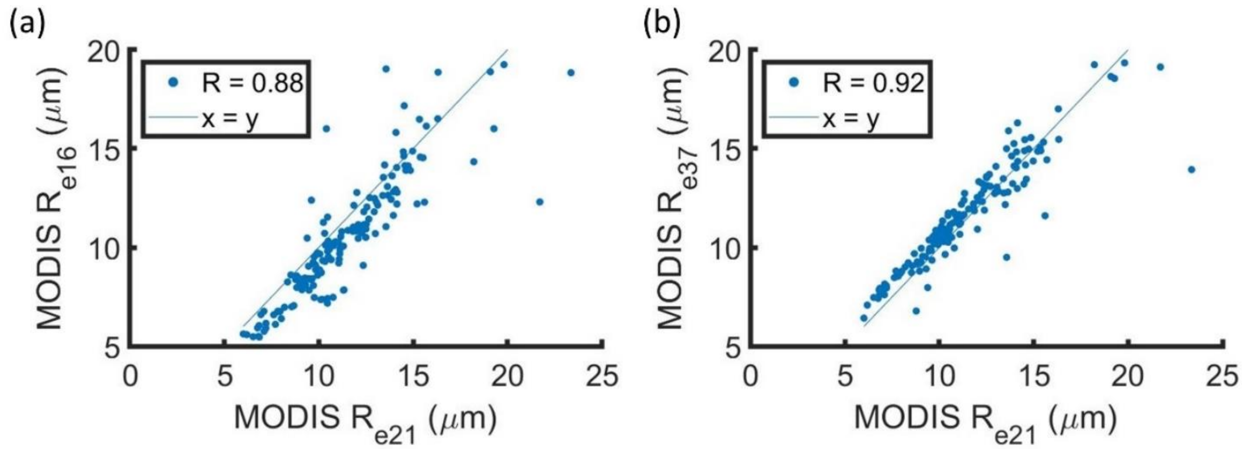

Figure 32: (a) R_{e16} and (b) R_{e37} as a function of R_{e21} for MODIS retrievals co-located with in situ data for ΔT less than 3600 s. Each point represents average values over a 5 km x 5 km domain centered at the corresponding cloud profile's location.

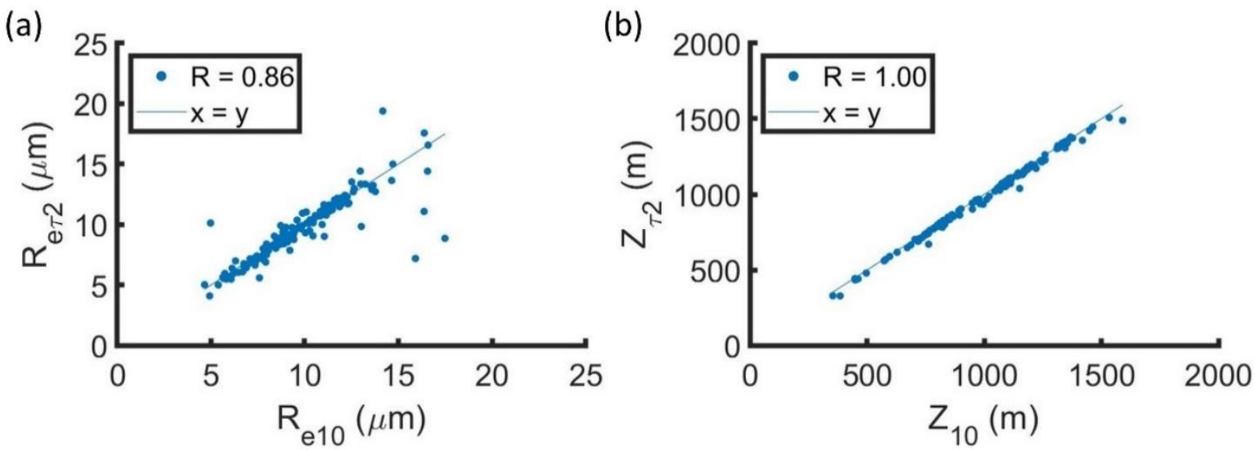

Figure 33: (a) R_e and (b) Z at two optical depths below cloud top ($R_{e\tau 2}$ and $Z_{e\tau 2}$) against those averaged over top 10 % of cloud layer (R_{e10} and Z_{10}) for profiles with a MODIS retrieval co-located with in situ data for ΔT less than 3600 s.

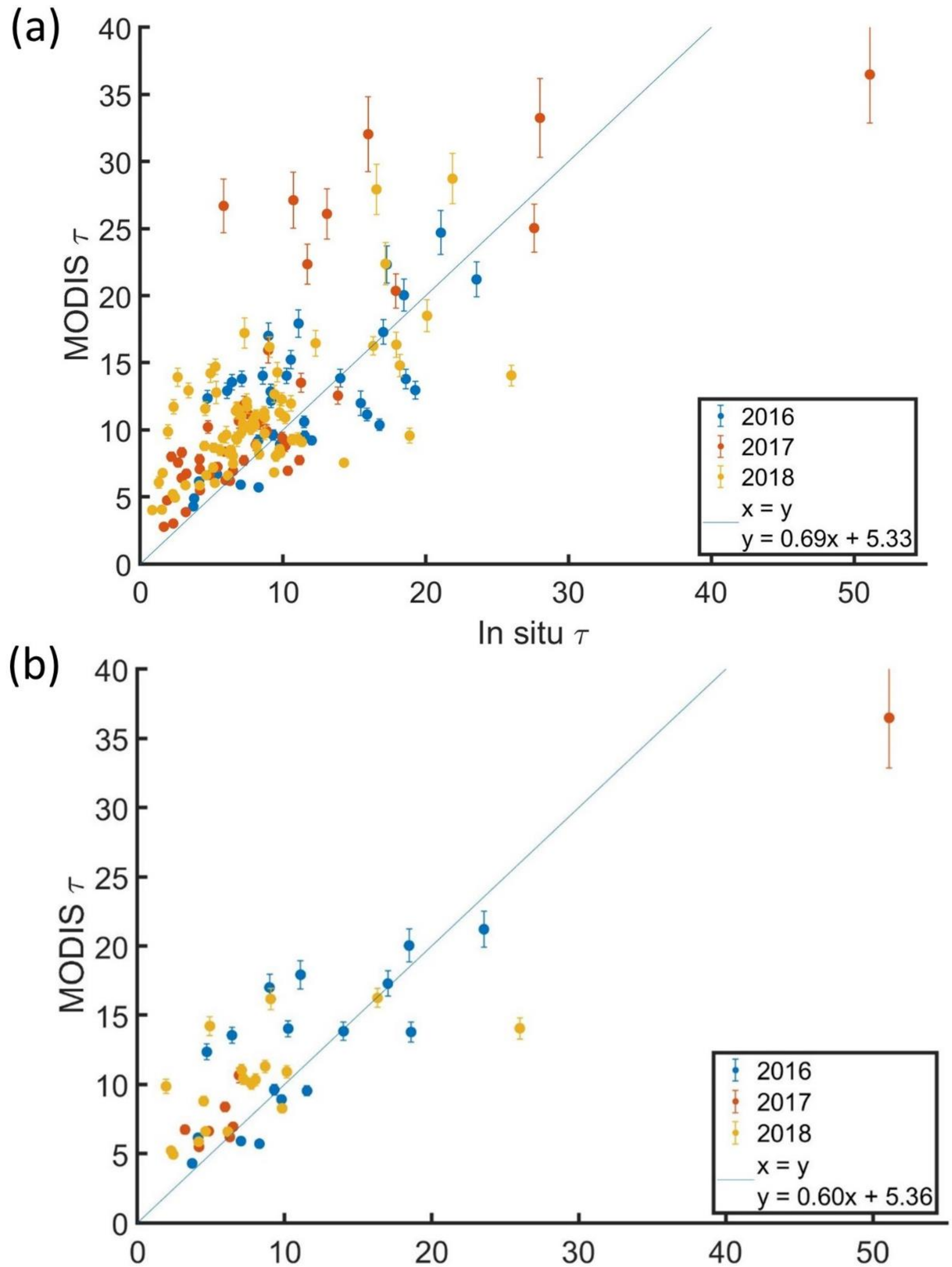

Figure 34: MODIS τ versus in situ τ for profiles with a MODIS retrieval co-located with in situ data for ΔT (a) less than 3600 s and (b) less than 900 s colored by ORACLES deployment year. Each point represents a cloud profile with the MODIS τ averaged over a 5 km x 5 km domain centered at the cloud profile's location.

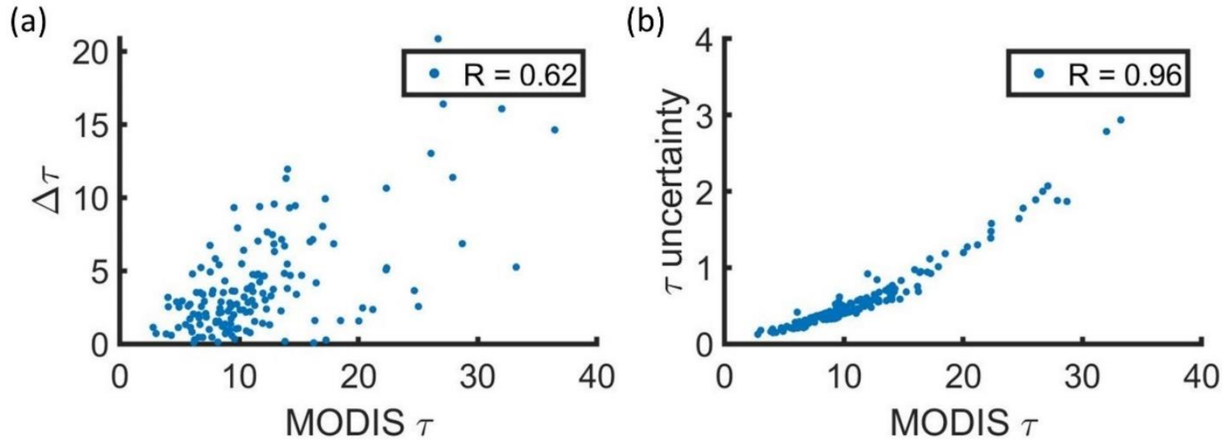

Figure 35: MODIS τ versus (a) magnitude of the difference between MODIS τ and in situ τ (Δ) and (b) MODIS τ retrieval uncertainty for profiles with a MODIS retrieval co-located with in situ data for ΔT less than 3600 s. Each point represents average values over a 5 km x 5 km domain centered at the corresponding cloud profile's location.

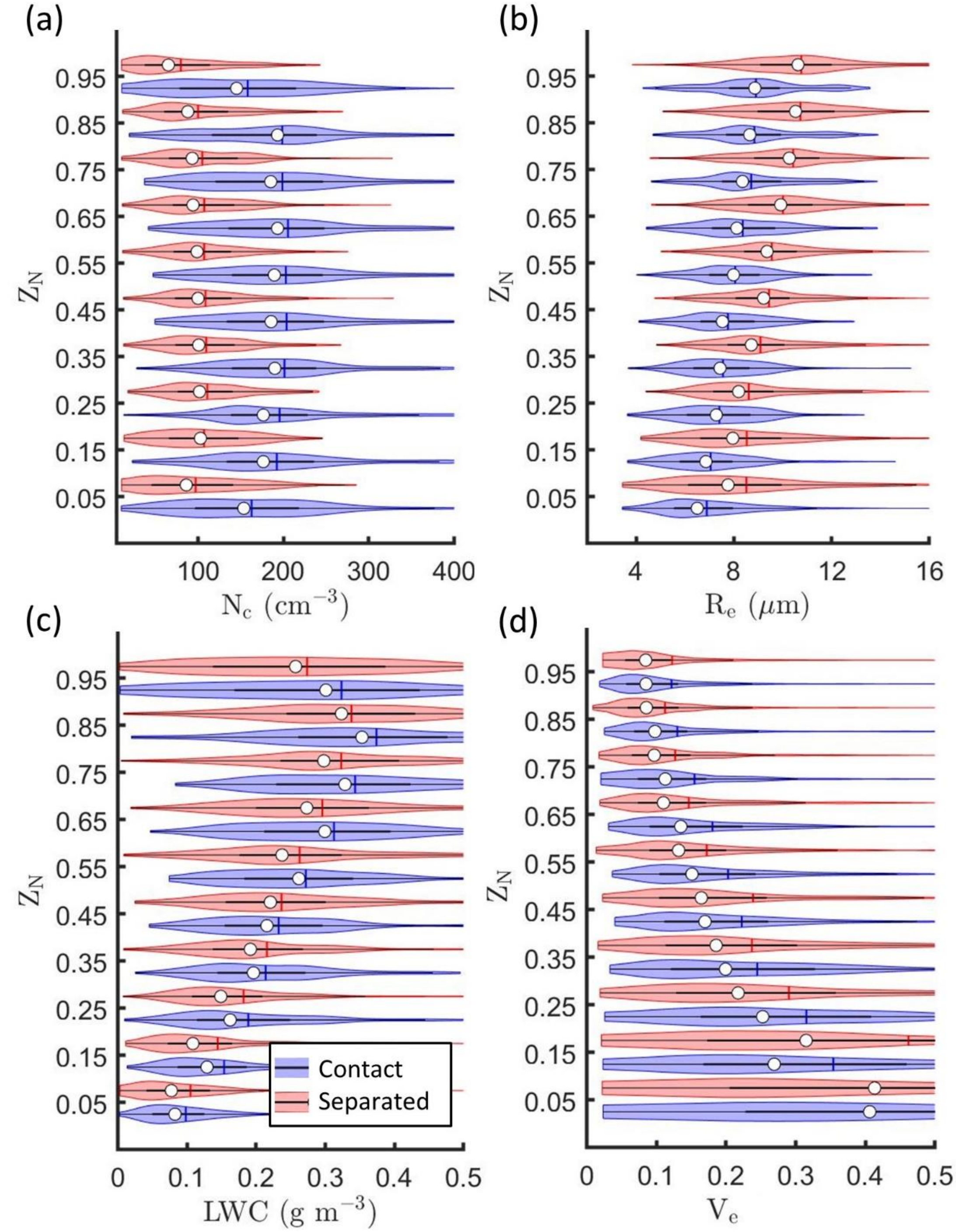

Figure 36: Kernel density estimates (indicated by width of shaded area) and boxplots showing mean (vertical line) and median (white circle) for (a) N_c, (b) R_e, (c) LWC, and (d) V_e versus normalized height in cloud (Z_N) for profiles with a MODIS retrieval co-located with in situ data for ΔT less than 3600 s.

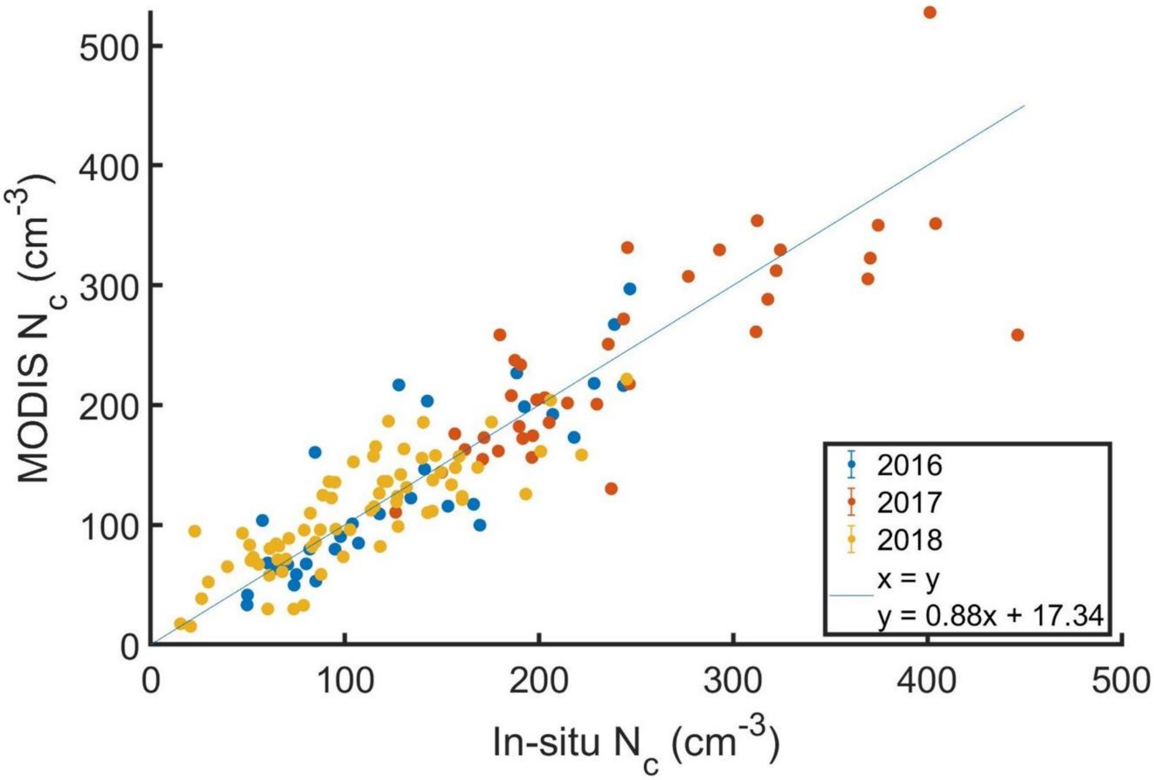

Figure 37: MODIS N_c versus in situ N_c for with a MODIS retrieval co-located with in situ data for ΔT less than 3600 s colored by ORACLES deployment year. Each point represents a cloud profile with the in situ N_c averaged over the top half of the cloud and MODIS N_c calculated using MODIS R_e and τ averaged over a 5 km x 5 km domain centered at the cloud profile's location.

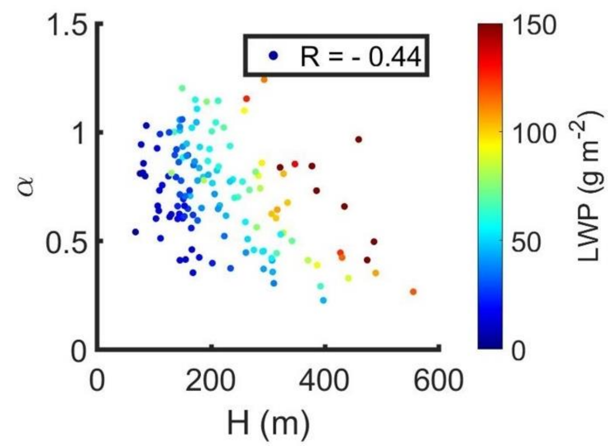

Figure 38: Cloud adiabaticity (α) versus cloud thickness (H) colored by liquid water path (LWP) for with a MODIS retrieval co-located with in situ data for ΔT less than 3600 s.

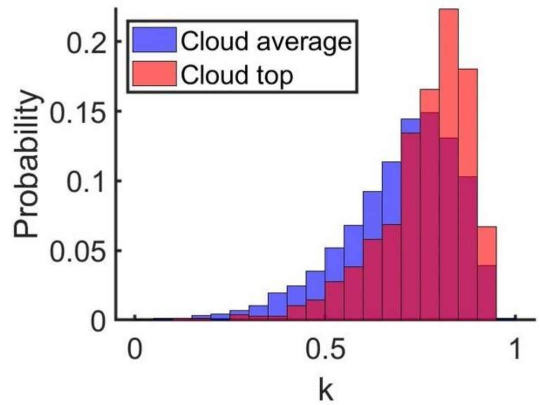

Figure 39: Probability density function for *k* averaged over entire cloud layer (blue) or top 10 % of cloud (red) for profiles with a MODIS retrieval co-located with in situ data for ∆T less than 3600 s.

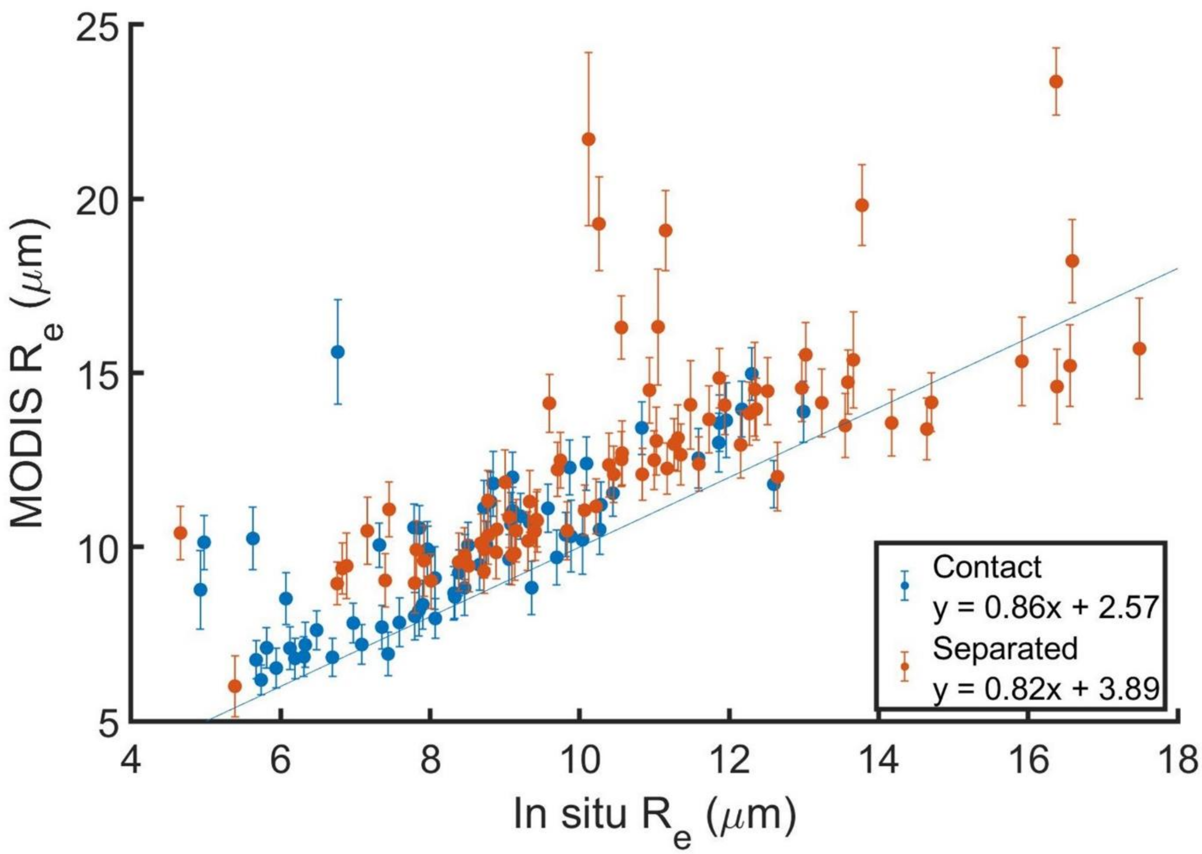

Figure 40: Same as Fig. 29a with cloud profiles colored based on regime classification.

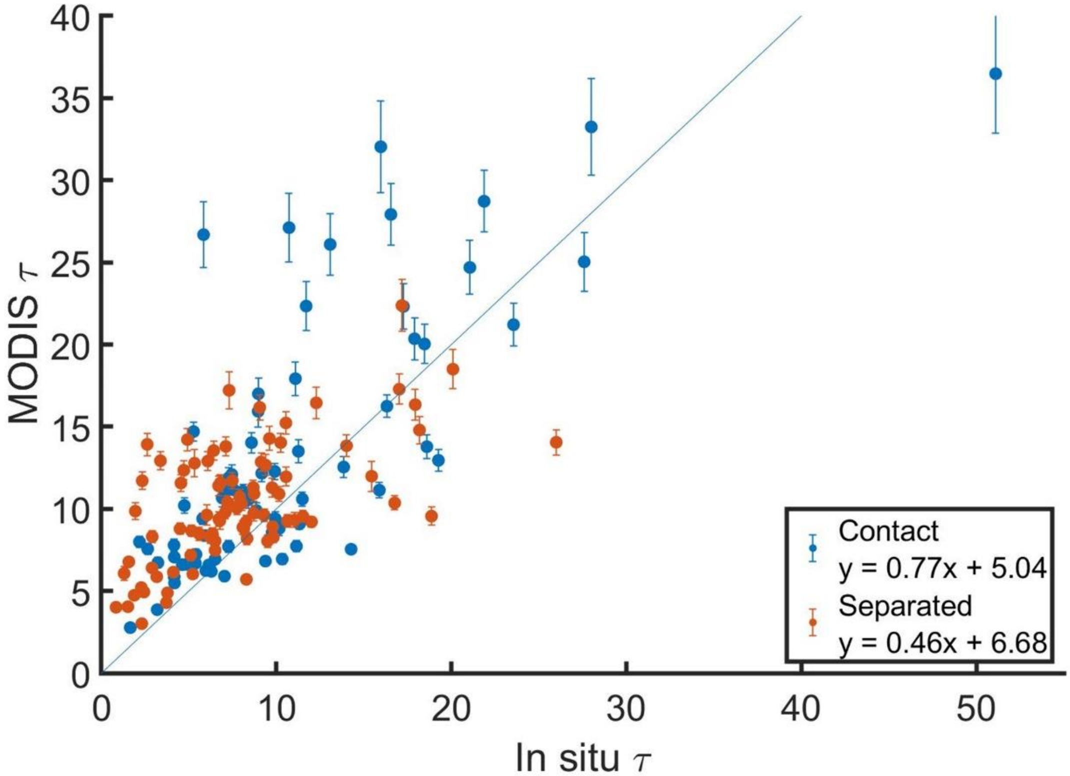

Figure 41: Same as Fig. 34a with cloud profiles colored based on regime classification.

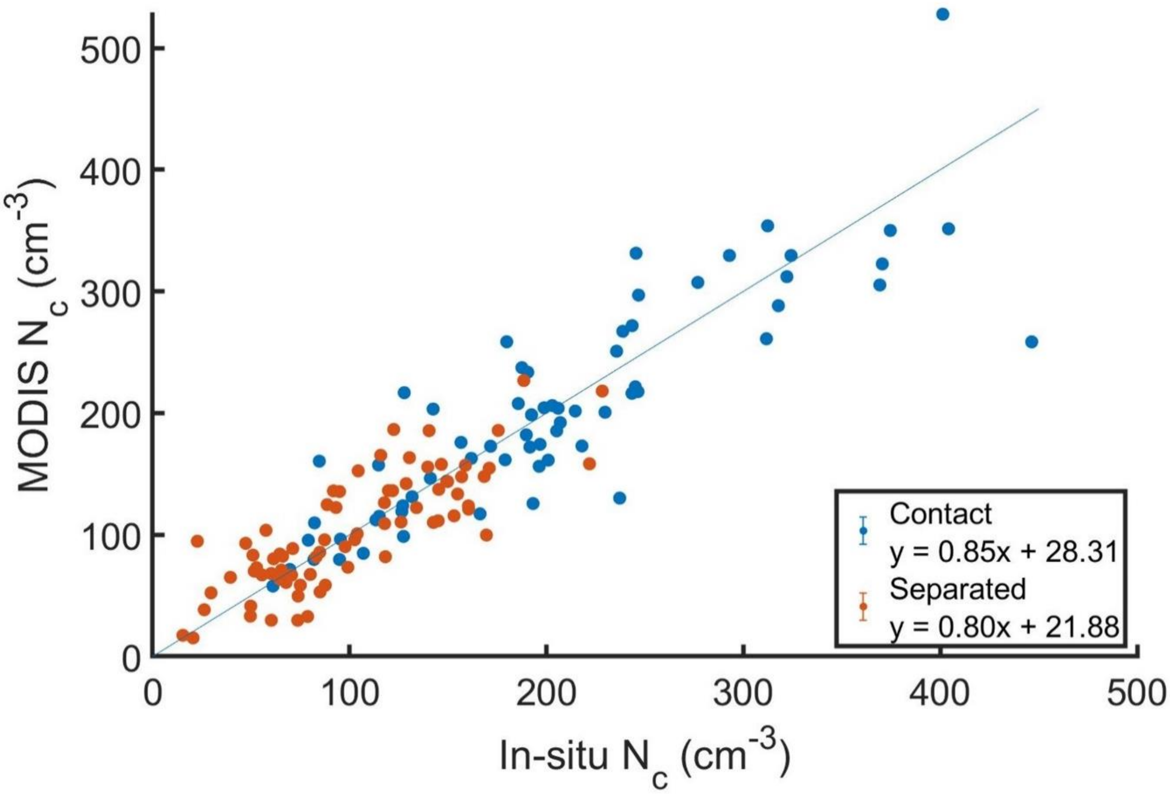

Figure 42: Same as Fig. 37 with cloud profiles colored based on regime classification.

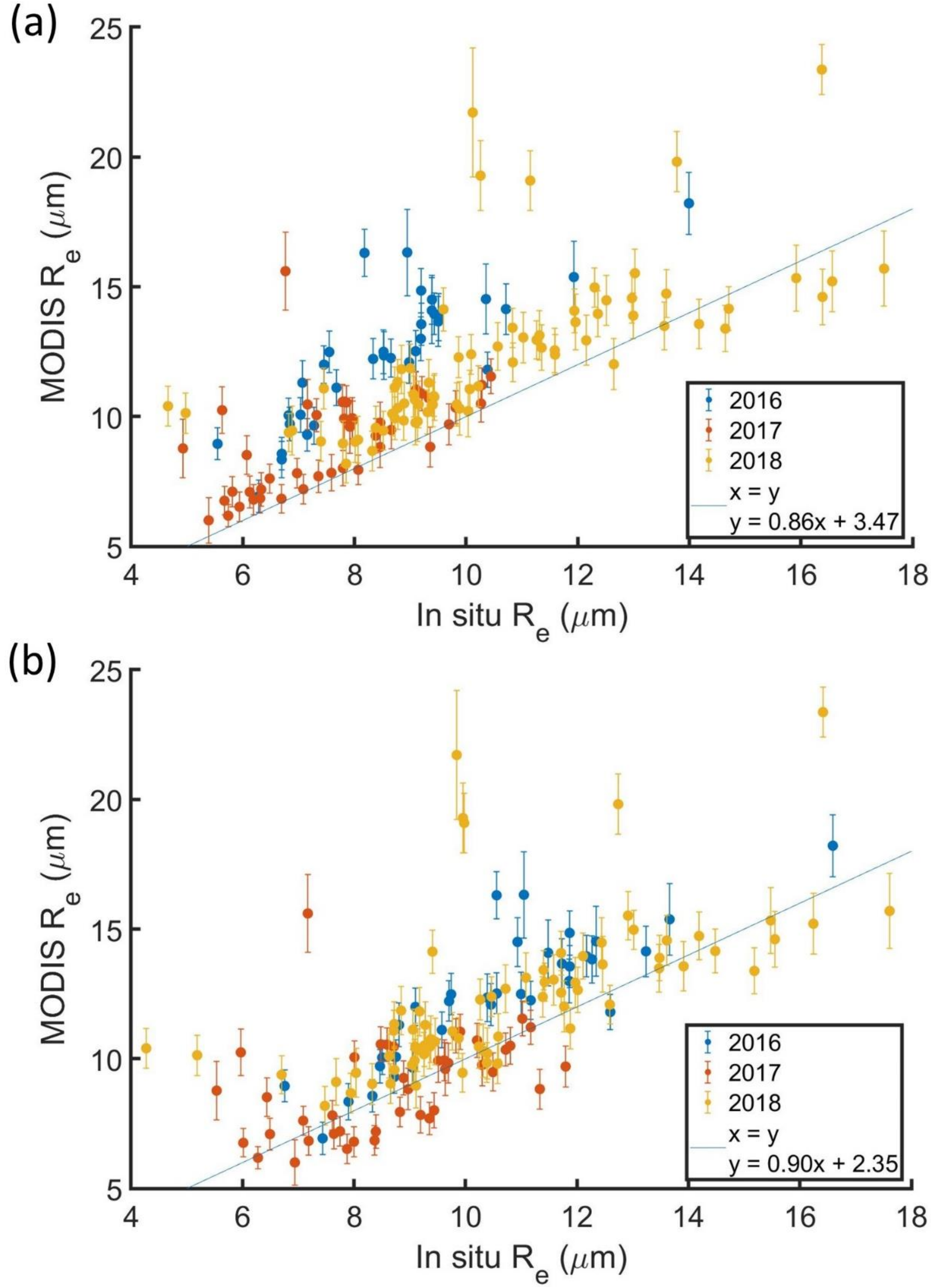

Figure 43: Same as Fig. 29a with in situ R_e calculated (a) unscaled CAS and CDP *n(D)* and (b) CAS and CDP *n(D)* scaled based on King LWC.

5 CONCLUSIONS

Biomass burning aerosols from southern Africa overlay marine stratocumulus clouds over the southeast Atlantic Ocean with variable vertical separation (0 to 2000 m) from the cloud tops. In this dissertation, aerosol-cloud interactions between aerosol and clouds over the southeast Atlantic were studied. In situ data from the NASA ORACLES field campaign were used to estimate cloud microphysical (N_c, R_e, and LWC), macrophysical (LWP and H), and precipitation properties (R_p and S_o) for regimes defined based on N_a. In situ estimates of N_c, R_e, and τ, and aerosol-induced changes in N_c, R_e, and τ were compared with MODIS retrievals co-located with in situ data. During 173 "contact" profiles, the biomass burning aerosol layer with N_a > 500 cm^{-3} was located within 100 m above cloud tops. The level of N_a > 500 cm^{-3} was vertically separated from cloud tops by at least 100 m during 156 "separated" profiles. Relative to separated profiles, the presence of biomass burning aerosols near cloud tops during contact profiles was associated with,

1. More numerous and smaller cloud droplets and weaker droplet growth with height.

Contact profiles had significantly higher N_c and τ (87 cm^{-3} and 1.8 higher) and lower R_e (1.5 μm lower) than separated profiles. There was a smaller increase in median R_e from Z_B to Z_T for contact profiles (6.1 to 7.9 μm) compared to separated profiles (7.1 to 9.5 μm).

2. A smaller decrease in q_T and positive buoyancy across cloud tops.

Free-tropospheric humidity was higher in the presence of biomass burning aerosols. For contact profiles, this led to a smaller decrease in median N_c and LWC near cloud top (25% and 12%) compared to separated profiles (33% and 18%). The latter had negative buoyancy across cloud tops which led to forced descent of drier free-tropospheric air into the clouds.

3. Changes in N_c and R_e within both clean and polluted boundary layers.

Contact profiles were more often located in high N_a boundary layers with higher CO concentration (28 ppb higher) which suggests biomass burning aerosols were more frequently entrained into the boundary layer at these locations. There were larger differences between N_c and R_e for contact and separated profiles in high N_a boundary layers (108 cm^{-3} and 1.8 μm) compared to low N_a boundary layers (31 cm^{-3} and 0.5 μm).

4. Lower precipitation intensity and precipitation formation process rates.

Changes in N_c and R_e for contact profiles led to precipitation suppression with 50% lower R_p compared to separated profiles, on average. Lower values of R_p, S_{AUTO}, and S_{ACC} were observed during contact profiles (up to 0.07 mm h^{-1}, 2.9 x 10^{-10} s^{-1}, and 1.2 x 10^{-8} s^{-1}) compared to separated profiles (up to 0.22 mm h^{-1}, 9.6 x 10^{-10} s^{-1}, and 2.2 x 10^{-8} s^{-1}).

5. Lower precipitation susceptibility with the strongest impact in thin clouds (H < 129 m).

Contact profiles had lower average S_o (0.87) than separated profiles (1.08). S_o depends on N_c and R_p, both of which varied with H due to droplet growth. The differences between S_o for contact and separated profiles varied with H due to the co-variability between changes in N_c and R_p due to droplet growth and increasing N_a. Thin clouds had the highest difference in S_o (-0.06 versus 1.47) as poor correlation between N_c and R_p for thin contact profiles led to lower S_o.

6. Statistically insignificant differences in meteorological parameters affecting LWP or H.

Based on ERA5 reanalysis data, LWP was correlated with SST (R = 0.22), T_o (R = 0.27), LTS (R = - 0.29), and EIS (R = - 0.31). Contact profiles with ERA5 low-cloud cover > 0.95 had lower SST

(0.01 to 1.48 K lower) and statistically similar T_o, LTS, and EIS compared to separated profiles. The SST differences were insignificant when profiles with ERA5 low-cloud cover < 0.95 were included.

In situ data from 67 contact and 82 separated profiles were co-located with a MODIS retrieval from Terra or Aqua with a time gap (ΔT) below 1 hour. On average, the MODIS R_e, τ, and N_c (11.4 μm, 11.7, and 150.3 cm^{-3}) were 1.7 μm, 2.4, and less than 1 cm^{-3} higher than the in situ R_e, τ, and N_c with R = 0.78, 0.72, and 0.90, respectively. For the contact profiles, in situ N_c and τ were 103 cm^{-3} and 2.8 higher and in situ R_e was 2.2 μm lower compared to the separated profiles. In comparison, contact profiles had 99 cm^{-3} and 3.0 higher MODIS N_c and τ, and 2.8 μm lower MODIS R_e compared to separated profiles. The MODIS retrievals estimated the sign of the aerosol-induced changes in N_c, R_e, and τ with small biases in the magnitude relative to in situ estimates. The MODIS estimates were within 5 cm^{-3}, 0.5 μm, and 0.7 of the in situ estimates when profiles with larger biases (MODIS R_e > 15 μm or MODIS τ > 25) were removed.

Uncertainties in ERF$_{aci}$ exist due to the inconsistency between process scales and analysis scales (McComiskey and Feingold, 2012). This can be addressed using airborne and satellite observations on a regional basis. The ORACLES dataset allows such analyses for the southeast Atlantic region by addressing the “lack of long-term data sets needed to provide statistical significance for a sufficiently large range of aerosol variability influencing specific cloud regimes over a range of macrophysical conditions” (Sorooshian et al., 2010).

Future work should be aimed at improved understanding of ACIs at both the process scale and the analysis scale. At the process scale, in-cloud aerosol samples collected using the counterflow virtual impactor inlet should be analyzed to examine the extent of entrainment mixing of biomass-burning aerosols into stratocumulus clouds. Case studies of cloud profiles can be used to investigate cloud-top entrainment and evaporative cooling using water isotope measurements. Data from constant altitude in-cloud flight legs can be used to study the scales at which droplet clustering can occur and the horizontal heterogeneity of stratocumulus clouds affected by ACIs. Modeling studies should examine the impact of precipitation suppression on cloud lifetime and boundary layer dynamics. Model parameterizations of R_p should be adjusted to account for changes in relationships between N_c, R_p, and H under different aerosol conditions.

At the analysis scale, the in situ LWC and R_p can be compared with W-band radar retrievals from APR-3 (Dzambo et al., 2021) and the sensitivity of S_o estimates based on remote sensing retrievals could be quantified (Bai et al., 2018). Based on the agreement between MODIS and in situ estimates of ACIs, MODIS retrievals can be used to study ACIs for warm, homogeneous marine stratocumulus over the southeast Atlantic. Combined with lidar estimates of the vertical separation between aerosol and cloud layers and underlying cloud properties (Zeng et al., 2014; Rajapakshe et al., 2017; Painemal et al., 2020), MODIS retrievals with low biases could enable studies of ACI over a larger domain of the southeast Atlantic and over longer timescales than possible using in situ data alone. For example, the High Spectral Resolution LIDAR used during ORACLES could be used to estimate the vertical separation between the aerosol and cloud layers and ACIs could be estimated using co-located MODIS retrievals.

APPENDIX A – Intercomparisons between datasets from in situ cloud probes

The NASA P-3B aircraft was equipped with in situ probes during the NASA ObseRvations of Aerosols above CLouds and their intEractionS (ORACLES) field campaign. The probes included a Cloud and Aerosol Spectrometer (CAS), Cloud Droplet Probes (CDP), a Phase Doppler Interferometer (PDI, serial number 0491), a 2-Dimensional Stereo Probe (2D-S, serial number 012), and a King hot-wire probe (model KLWC-5, serial number SN-PMI-1058-0704-86). The CAS was a part of the Cloud, Aerosol, and Precipitation Spectrometer (CAPS, model AAA-0009, serial number 5). The P-3 carried a single CDP (CDP-A, serial number 0901-48) during the 2016 Intensive Observation Period (IOP). A second CDP (CDP-B) was added to the P-3 for the 2017 and 2018 (serial number 1206-070) IOPs. CDP-A was replaced by a different CDP (CDP-C, serial number 0604-006) for the 2018 IOP.

The probes were calibrated by the manufacturers before and after each ORACLES IOP. Instrument performance was monitored during the IOPs using calibration tests and auxiliary data, such as temperature and sensor voltages, were monitored during the research flights. Flight legs through aerosol plumes with high (greater than 1000 cm^{-3}) aerosol concentration (N_a) were conducted during ORACLES. These plumes contained soot particles that could adversely affect the quality of measurements, especially for the 2D-S. This was addressed by cleaning the optical lenses of the probes with isopropyl before each flight. In Chapter 2, the 2D-S measurements and data processing techniques used to identify and remove data artefacts were discussed.

The objective of this appendix was to compare data sets created using measurements from different cloud probes used during ORACLES. The focus was on droplets with diameter (*D*) between 3 and 50 μm since the CAS, CDP, and PDI measured droplets over this size range. The differences between droplet concentration (N_c) and liquid water content (*LWC*) from the CAS, CDP, and PDI data sets were determined. While they may, or may not, be within the uncertainties (Baumgardner et al., 2017), the differences between the data sets were quantified to illustrate that using one instrument versus another could affect the data analysis.

The CAS, CDP, and PDI measurements were compared for each IOP when measurements were available (Table 22). The *CAS* measurements were invalid before 6 September 2016 and after 7 October 2018 due to an electronics issue. The CDP-A measurements were invalid for the 2016 and 2017 IOPs due to a misalignment of the optical system. The PDI measurements were invalid for the 2017 and 2018 IOPs due to electrical interference on the aircraft, which affected data transfer between the instrument and onboard computers. Hence, the following sections present analyses comparing measurements from the CAS and the PDI for the 2016 IOP, the CAS and the CDP-B for the 2017 and 2018 IOPs, and the CDP-B and the CDP-C for the 2018 IOP. The measurements collected by the horizontal and vertical channels of the 2D-S, which concurrently sample the cloud volume, were compared for the 2017 and 2018 IOPs.

2016 IOP - CAS versus PDI

Nine research flights between 6 and 27 September 2016 were used to create data sets for comparing measurements from the CAS and the PDI (Table 22). N_c and LWC were calculated for in-cloud measurements, defined as 1 Hz samples with CAS $N_c > 10$ cm^{-3}, PDI $N_c > 10$ cm^{-3}, and King LWC > 0.05 g m^{-3}. The range of the difference between the CAS and PDI data set parameters was defined using the 95 % confidence intervals (CIs) from a two-sample t-test (Table 23 and Table 24). For example, the difference between N_c for in-cloud CAS and PDI data sets was determined to be between 9 to 12 cm^{-3} with 95 % confidence. The average PDI N_c was 164 ± 90 cm^{-3} and the average CAS N_c was 153 ± 72 cm^{-3}, where the error estimates represent the standard deviation. The PDI N_c and the CAS N_c were well correlated with Pearson's correlation coefficient (R) = 0.88 but their averages had statistically significant differences (Table 23). The PDI more frequently sampled N_c > 300 cm^{-3} and LWC > 0.5 g m^{-3} (1,353 and 3158 1 Hz measurements) compared to the CAS (302 and 25 1 Hz measurements) (Fig. 44).

The average PDI LWC was 0.35 ± 0.19 g m^{-3}, and the average CAS LWC was 0.15 ± 0.09 g m^{-3}. The CAS LWC and PDI LWC were well correlated with R = 0.84 but their averages had statistically significant differences (Table 24). The King LWC had an average of 0.28 ± 0.15 g m^{-3} for the in-cloud data. The average PDI LWC was higher than the average King LWC (95 % CIs: 0.06 to 0.07 g m^{-3} higher, R = 0.78) while the average CAS LWC was lower than the average King LWC (95 % CIs: 0.13 to 0.14 g m^{-3} lower, R = 0.80).

Vertical profiles of CAS LWC, PDI LWC, and King LWC were compared against the adiabatic LWC (hereafter LWC_{ad}) (Fig. 45) for in-cloud measurements from cloud profiles flown on the six 2016 research flights used for data analysis (Table 22). The average CAS LWC and King LWC were lower than the average LWC_{ad} (95 % CIs: 0.16 to 0.17 g m^{-3} lower for CAS LWC and 0.01 to 0.03 g m^{-3} lower for King LWC). However, the average PDI LWC was higher than the average LWC_{ad} (95 % CIs: 0.04 to 0.06 g m^{-3} higher). The PDI LWC exceeded LWC_{ad} over the entire cloud layer except the top 10 %, the CAS LWC exceeded LWC_{ad} for the bottom 10 %, and the King LWC exceeded LWC_{ad} for the bottom 40 % of the cloud layer. Marine stratocumulus are typically sub-adiabatic due to cloud-top entrainment and droplet evaporation (Chapter 2) or cloud water removal by precipitation. Since the LWC_{ad} represents the theoretical maximum for LWC based on the adiabatic model (Section 3), these results suggest the PDI LWC was an overestimate.

The CAS N_c and the PDI N_c had larger differences (with lower R) when the CAS N_c and PDI N_c both exceeded 200 cm^{-3} (Table 23). On the other hand, for about 65 % of the measurements with CAS N_c and PDI N_c < 200 cm^{-3}, the CAS N_c and PDI N_c had insignificant differences while the CAS LWC and PDI LWC had significant differences for the measurements (Table 24). No obvious trends were observed for these differences as a function of altitude or pitch angle (not shown).

The skewness (α) and mean radius (r_1) were calculated for the CAS and PDI in-cloud measurements. r_1 and α were negatively correlated for each probe with R = - 0.59 for the CAS and R = - 0.65 for the PDI (Fig. 46). Over 60 % of the samples had $\alpha_{PDI} < 2$, CAS N_c < 200 cm^{-3}, and PDI N_c < 200 cm^{-3} (Table 23). For these samples, there were insignificant differences between the average CAS N_c and PDI N_c (Table 24), but the PDI LWC was significantly higher than CAS LWC (Table 24). This was because the average PDI r_1 was 2.1 μm higher than the average CAS r_1. The data samples with PDI N_c > 200 cm^{-3} were associated with r_1 < 10 μm and $\alpha_{PDI} > 1$ (Fig. 46). Higher PDI LWC compared to the CAS LWC, King LWC, and LWC_{ad} with statistically significant differences suggests the PDI could be oversampling droplets with $D > r_1$ since LWC is dominated by the contribution of larger droplets. This would explain the statistically significant differences between the CAS LWC and the PDI LWC despite smaller or statistically insignificant differences between the CAS N_c and the PDI N_c. Based on these comparisons, measurements from the CAS were used to characterize droplets with 3 < D < 50 μm for the 2016 IOP in the absence of measurements from the CDP-A.

2017 IOP - CAS versus CDP-B

The CAS and the CDP-B data sets were created using in-cloud measurements defined as 1 Hz samples with CAS N_c > 10 cm^{-3}, CDP-B N_c > 10 cm^{-3}, and King LWC > 0.05 g m^{-3}. For in-cloud measurements collected over 12 research flights during the 2017 IOP, the average CDP-B N_c (192 ± 123 cm^{-3}) and CDP-B LWC (0.18 ± 0.16 g m^{-3}) were greater than the average CAS N_c (181 ± 96 cm^{-3}) and CAS LWC (0.09 ± 0.07 g m^{-3}) (Fig. 47). The average King LWC (0.21 ± 0.15 g m^{-3}) was higher than the average CDP-B LWC (95 % CIs: 0.01 to 0.02 g m^{-3} higher, R = 0.68) and the average CAS LWC (95 % CIs: 0.10 to 0.11 g m^{-3} higher, R = 0.78).

For the research flights flown on 30 and 31 August 2017, the average CDP-B N_c (109 ± 39 cm^{-3}) and CDP-B LWC (0.05 ± 0.04 g m^{-3}) were 96 cm^{-3} and 0.16 g m^{-3} lower than the CDP-B N_c and CDP-B LWC averaged over the other flights. The average CAS N_c (146 ± 46 cm^{-3}) and CAS LWC (0.11 ± 0.05 g m^{-3}) for these two flights were 41 cm^{-3} lower and 0.02 g m^{-3} higher than their corresponding averages. The average King LWC for these flights (0.18 ± 0.10 g m^{-3}) was 0.03 g m^{-3} lower than the average King LWC for other flights. Since the relative changes in King LWC and CAS LWC compared to other flights were much smaller, it is unlikely the CDP-B measurements from 30 and 31 August 2017 were accurate. The CDP-B measurements from 30 and 31 August did not impact the results presented in this study since these flights were not included in the data analysis (Table 22) because few cloud profiles were conducted during these flights. However, the data from these flights were excluded from data sets created for comparing the in-cloud CAS and CDP-B measurements for the 2017 IOP.

The 10 research flights between 12 August and 2 September 2017 were used to create data sets for comparing N_c and LWC from the CAS and the CDP-B in-cloud measurements (Fig.

47). 95 % CIs between the N_c and LWC from the CAS and the CDP-B are listed in Table 25 and Table 26, respectively. The CDP-B more frequently sampled N_c > 300 cm^{-3} (2536 1 Hz measurements) than the CAS (1623 1 Hz measurements). The average CDP-B N_c was higher than the average CAS N_c with R = 0.91 (Table 25). For 75 % of the samples with *CDP-B* N_c < 300 cm^{-3}, CAS N_c and CDP-B N_c had small differences (95 % CIs: 1 to 5 cm^{-3}) but the average CDP-B LWC and CAS LWC had statistically significant differences (Table 26). This was because the average CDP-B r_1 was higher than the average CAS r_1 (95 % CIs: 1.4 to 1.5 μm higher).

The average King LWC (0.19 ± 0.13 g m^{-3}) was comparable to the average CDP-B LWC (0.18 ± 0.13 g m^{-3}) while the average CAS LWC (0.08 ± 0.06 g m^{-3}) was lower than CDP-B LWC and King LWC. The CAS LWC, CDP-B LWC, and King LWC were compared against LWC_{ad} (Fig. 48) for in-cloud measurements from cloud profiles flown on the seven research flights from the 2017 IOP used for data analysis (Table 22). The average LWC_{ad} was greater than each LWC estimate but the differences with CAS LWC (95 % CIs: 0.17 to 0.19 g m^{-3} higher) were higher than with CDP-B LWC (95 % CIs: 0.05 to 0.07 g m^{-3} higher). Thus, measurements from the CDP-B were used to characterize droplets with 3 < D < 50 μm for the 2017 IOP.

2018 IOP - CAS versus CDP-B

For the 2018 IOP, N_c and LWC from the CAS and the CDP-B were compared using data sets created from the in-cloud measurements on six research flights until the CAS was operational (Table 22). These comparisons were consistent with the CAS versus CDP-B comparisons for the 2017 IOP. The average CDP-B N_c (125 ± 92 cm^{-3}) was higher than the average CAS N_c (106 ± 67 cm^{-3}) with statistically significant differences (95 % CIs: 15 to 21 cm^{-3} higher, R = 0.88) (Fig. 49). The average CDP-B LWC (0.21 ± 0.14 g m^{-3}) was closer to the average King LWC (0.20 ± 0.12 g m^{-}

^{3}) compared to the average CAS LWC (0.10 ± 0.07 g m^{-3}). The average LWC_{ad} was closer to the average CDP-B LWC (95 % CIs: 0.04 to 0.06 g m^{-3} higher) and the average King LWC (95 % CIs: 0.07 to 0.08 g m^{-3} higher) compared to the average CAS LWC (95 % CI: 0.18 to 0.19 g m^{-3} higher). It was hypothesized that the CDP-B provided better estimates of *N(D)* for droplets with $3 < D < 50$ μm compared to the CAS for the first six research flights from the 2018 *IOP*.

Based on these comparisons, the CAS could be under-sizing droplets or under-sampling certain droplets during the 2017 and 2018 IOPs. The differences between the data sets from the CAS and the other instruments could be due to droplet co-incidence in the CAS sample volume. It is possible the air flow into the CAS inlet tube could have affected the droplets entering the CAS sample volume compared to the CDP-B sample volume (which had a more open path for droplets). The differences between the estimates of N_c and LWC from the CAS and CDP-B for the 2017 IOP increased slightly when the absolute value of pitch angle exceeded 0.5˚ (Table 25 and Table 26). However, this was not observed for data collected during the 2018 IOP. No obvious trends were observed for these differences as a function of altitude or the skewness from the CAS and the CDP-B *N(D)* (not shown).

2018 IOP - CDP-B versus CDP-C

During the 2016 IOP, cloud probes were installed on newly designed pylons that placed the instruments directly underneath the wing rather than slightly ahead of its leading edge as commonly regarded as best practice (McFarquhar et al. 2007; Afchine et al. 2018). There was concern that the air flow into a probe sample volume could have been affected by airflow perturbations induced by the wing (Weigel et al. 2016), potentially affecting the size distributions and the calculation of N_c, LWC, and other microphysical parameters. To investigate this, a new pylon was designed at the NASA Wallops Flight Facility and installed on one wing for the 2017 and 2018 IOPs. This pylon placed the CAS and the CDP-B slightly lower and ahead of the leading edge of the aircraft wing, compared to other probes. Therefore, the CDP-B and CDP-C were mounted at different locations relative to the aircraft wing.

The mounting locations of the CDP-B and CDP-C were switched halfway through the 2018 IOP to isolate instrument differences caused by the pylons from those caused by the CDP probes. O'Brien et al. (2021, in prep.) compared the in-cloud measurements from CDP-B and CDP-C and found the mounting position of the probes had only a 6 % impact on the calculation of N_c with the average CDP-B LWC and CDP-C LWC being within 0.02 g m^{-3}. To maintain consistency with the 2017 IOP, in-cloud measurements from the CDP mounted on the new pylon (next to the CAS) were used for data analysis (Table 22) except for 15 October 2018 when the CDP-C, placed on the new pylon, erroneously sampled large N_c due to a qualifier voltage issue. However, the use of measurements from the CDP mounted on the old pylon is unlikely to have a significant impact on the data analysis.

2017 and 2018 IOPs - 2D-S horizontal and vertical channel

N_c and LWC were derived using the in-cloud measurements from the horizontal (N_H and LWC$_H$) and vertical (N_V and LWC$_V$) channels of the 2D-S. N_H, N_V, LWC$_H$, and LWC$_V$ were computed for 3,966 and 7,612 1 Hz in-cloud measurements with LWC$_H$ and LWC$_V$ between 0.001 to 1 g m^{-3} collected during 7 and 12 research flights from the 2017 and 2018 IOPs, respectively. Based on a linear regression model, N_H and N_V (Fig. 50) as well as LWC$_H$ and LWC$_V$ (Fig. 51) were highly correlated for the 2017 and 2018 IOPs. Only N_H and LWC_H were available for the 2016 IOP because of soot deposition on the inside of the receive-side mirror of the 2D-S vertical channel. To maintain consistency between the three IOPs, N_H and LWC_H were used in this study despite the availability of N_v and LWC_V for the 2017 and 2018 *IOPs*. The high correlations suggest little difference would have resulted in the data analysis from using the average of the 2D-S channels.

TABLES AND FIGURES:

Table 22: P-3 research flights (PRFs) from ORACLES used for data analysis along with instruments that provided valid samples of droplets with 3 < *D* < 50 μm during the PRF (primary instrument for data analysis in bold).

PRF date	PRF used	Instruments
Aug 30 2016	No	Aborted flight
Aug 31 2016	No	PDI
Sept 02 2016	No	PDI
Sept 04 2016	No	PDI
Sept 06 2016	Yes	CAS, PDI
Sept 08 2016	No	CAS, PDI
Sept 10 2016	Yes	CAS, PDI
Sept 12 2016	Yes	CAS, PDI
Sept 14 2016	Yes	CAS, PDI
Sept 18 2016	No	CAS, PDI
Sept 20 2016	Yes	CAS, PDI
Sept 24 2016	No	CAS, PDI
Sept 25 2016	Yes	CAS, PDI
Aug 12 2017	Yes	CAS, CDP-B
Aug 13 2017	Yes	CAS, CDP-B
Aug 15 2017	Yes	CAS, CDP-B
Aug 17 2017	Yes	CAS, CDP-B
Aug 18 2017	No	CAS, CDP-B
Aug 19 2017	No	Aborted flight
Aug 21 2017	Yes	CAS, CDP-B
Aug 24 2017	Yes	CAS, CDP-B
Aug 26 2017	No	CAS, CDP-B
Aug 28 2017	No	CAS, CDP-B
Aug 30 2017	No	CAS, CDP-B
Aug 31 2017	No	CAS, CDP-B
Sept 02 2017	No	CAS, CDP-B
Sept 27 2018	Yes	CAS, CDP-B, CDP-C
Sept 30 2018	Yes	CAS, CDP-B, CDP-C
Oct 02 2018	No	CAS, CDP-B, CDP-C

Oct 03 2018	Yes	CAS, CDP-B, CDP-C
Oct 05 2018	Yes	CAS, CDP-B, CDP-C
Oct 07 2018	Yes	CAS, CDP-B, CDP-C
Oct 10 2018	Yes	CDP-B, CDP-C
Oct 12 2018	Yes	CDP-B, CDP-C
Oct 15 2018	Yes	CDP-B, CDP-C
Oct 17 2018	No	CDP-B, CDP-C
Oct 19 2018	Yes	CDP-B, CDP-C
Oct 21 2018	Yes	CDP-B, CDP-C
Oct 23 2018	Yes	CDP-B, CDP-C

Table 23: 95 % confidence intervals (CIs) for differences between CAS and PDI N_c (positive when average PDI N_c higher) determined using a two-sample t-test. Number of 1 Hz measurements (n), correlation co-efficient (*R*) and p-value (p) listed for various criteria applied to the CAS and the CDP *N(D)*, where α refers to skewness. Best-fit slope (M_o) and intercept (C_o) were determined using linear regression for CAS data as a function of PDI data.

Criteria	**n**	**CIs (cm^{-3})**	***R***	**p**	**M_o**	**C_o (cm^{-3})**
All data	16559	9 to 12	0.88	0	0.70	38
CAS and PDI N_c > 300 cm^{-3}	243	67 to 90	0.46	0	0.12	273
CAS and PDI N_c < 300 cm^{-3}	15147	2 to 5	0.88	0	0.81	24
CAS and PDI N_c > 200 cm^{-3}	4076	32 to 37	0.64	0	0.32	156
CAS and PDI N_c < 200 cm^{-3}	10832	-2 to 1	0.83	0.32	0.82	21
α_{PDI} < 2	14311	4 to 7	0.89	0	0.76	31
α_{PDI} > 2	2248	37 to 48	0.85	0	0.58	60
α_{PDI} < 2, CAS & PDI N_c < 200 cm^{-3}	10066	-3 to 0	0.83	0.06	0.82	21

Table 24: Same as Table 23, but the parameters correspond to comparisons between CAS and PDI LWC. The CIs were positive when the average PDI LWC was higher.

Criteria	**n**	**CIs (g m^{-3})**	***R***	**p**	**M_o**	**C_o (g m^{-3})**
All data	16559	0.20 to 0.20	0.84	0	0.40	0.01
CAS and PDI N_c > 300 cm^{-3}	243	0.25 to 0.31	0.92	0	0.36	0.02
CAS and PDI N_c < 300 cm^{-3}	15147	0.19 to 0.20	0.84	0	0.42	0.01
CAS and PDI N_c > 200 cm^{-3}	4076	0.23 to 0.25	0.93	0	0.38	0.01
CAS and PDI N_c < 200 cm^{-3}	10832	0.19 to 0.19	0.81	0	0.41	0.01
α_{PDI} < 2	14311	0.21 to 0.21	0.83	0	0.40	0.01
α_{PDI} > 2	2248	0.15 to 0.16	0.92	0	0.35	0.01
α_{PDI} < 2, CAS & PDI N_c < 200 cm^{-3}	10066	0.19 to 0.20	0.79	0	0.41	0.01

Table 25: Same as Table 23, but the parameters correspond to comparisons between CAS N_c and CDP-B N_c from 10 research flights during 2017 IOP (positive CIs when the average CDP N_c was higher and linear regression coefficients listed for CAS data as function of CDP-B data).

Criteria	**n**	**CIs (cm^{-3})**	***R***	**p**	**M_o**	**C_o (cm^{-3})**
All data (excluding 08/30, 31)	11438	16 to 22	0.91	0	0.73	37
CDP N_c > 300 cm^{-3}	2536	73 to 80	0.62	0	0.54	102
CDP N_c < 300 cm^{-3}	8902	1 to 5	0.87	0.01	0.84	20
pitch < - 0.5° or pitch > 0.5°	8445	18 to 25	0.90	0	0.70	42
- 0.5° < pitch < 0.5°	2961	8 to 20	0.91	0	0.80	23

Table 26: Same as Table 25, but parameters correspond to comparisons between CAS LWC and CDP-B LWC.

Criteria	**n**	**CI (g m^{-3})**	***R***	**p**	**M_o**	**C_o (g m^{-3})**
All data (excluding 08/30, 31)	11438	0.11 to 0.12	0.82	0	0.37	0.01
CDP N_c > 300 cm^{-3}	2536	0.17 to 0.19	0.85	0	0.40	0.00
CDP N_c < 300 cm^{-3}	8902	0.09 to 0.10	0.80	0	0.37	0.02
pitch < - 0.5° or pitch > 0.5°	8445	0.12 to 0.12	0.83	0	0.37	0.01
- 0.5° < pitch < 0.5°	2961	0.10 to 0.11	0.79	0	0.39	0.02

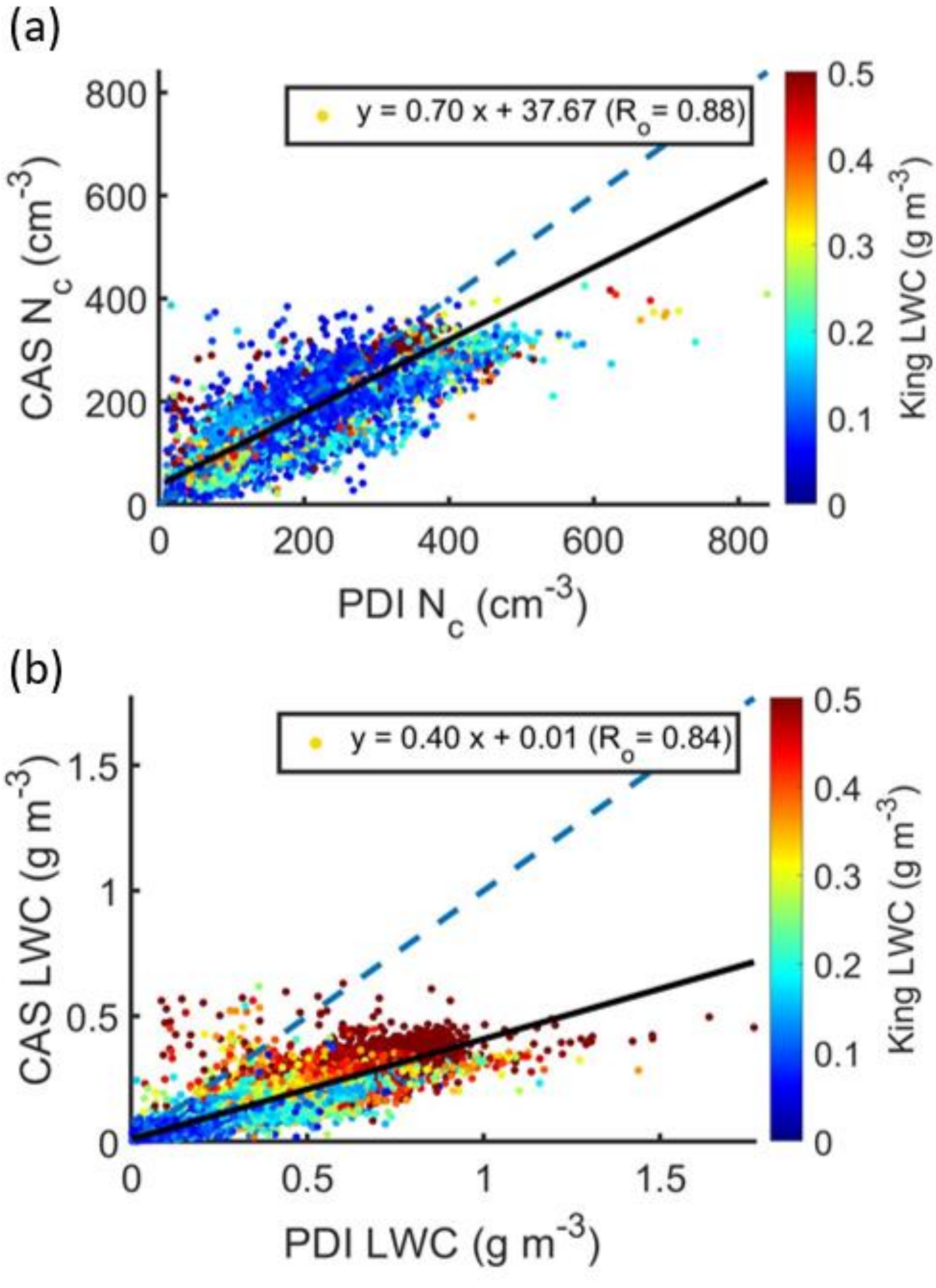

Figure 44: (a) N_c and (b) LWC measured by CAS against that measured by PDI during 2016 IOP. Each dot represents a 1 Hz data sample colored by King LWC. Linear regression coefficients indicated in legend.

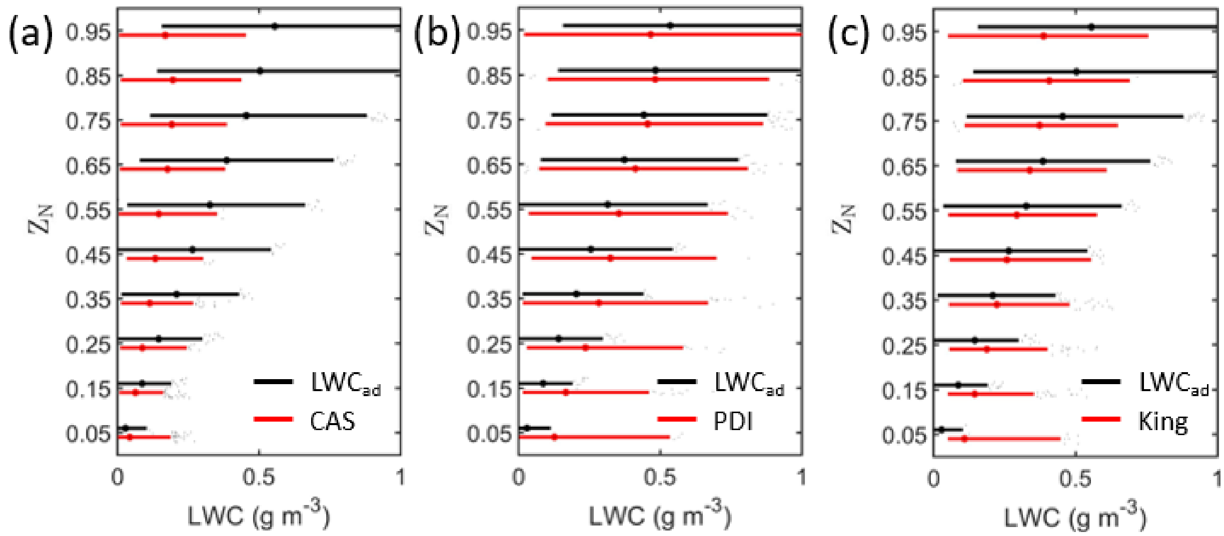

Figure 45: Boxplots representing profiles of (a) CAS LWC, (b) PDI LWC, and (c) King LWC with adiabatic LWC (LWC_{ad}) as function of normalized height above cloud base (Z_N). These data represent cloud samples from cloud profiles flown during the six research flights from 2016 IOP used for data analysis.

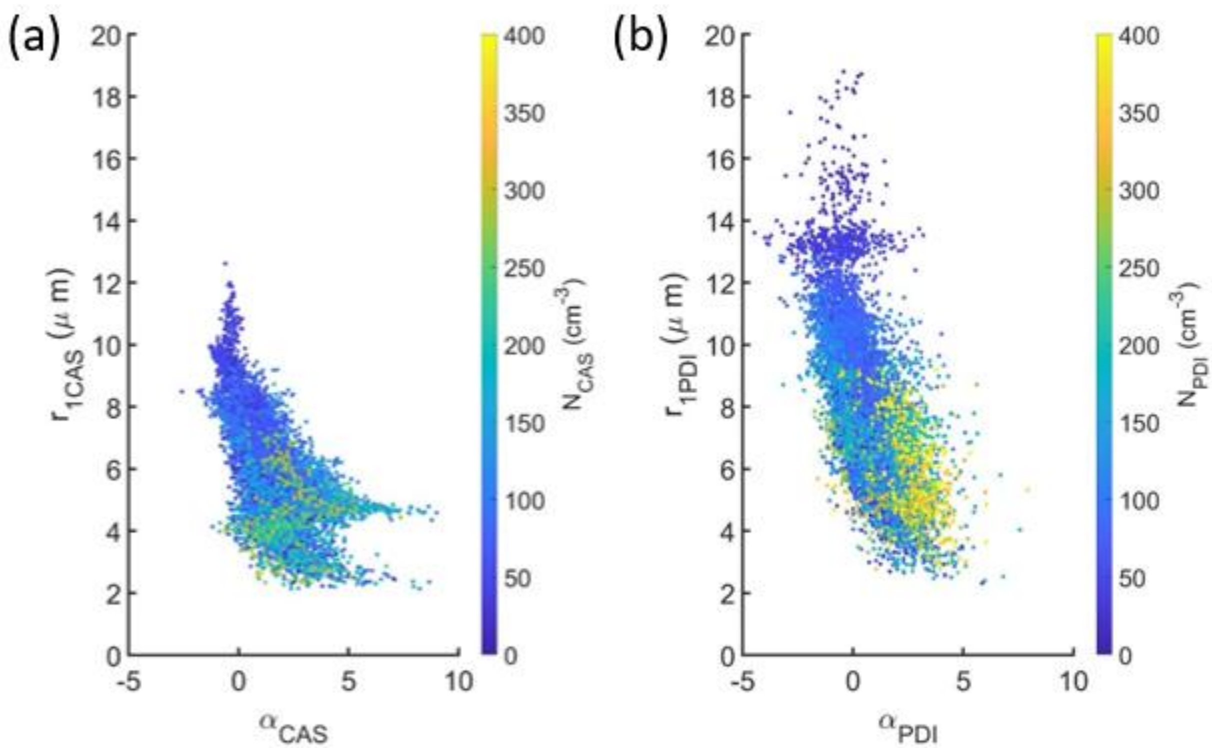

Figure 46: Mean radius (r_1) versus skewness (α) for (a) CAS and (b) PDI droplet size distributions. Each dot represents a 1 Hz sample colored by the corresponding droplet concentration.

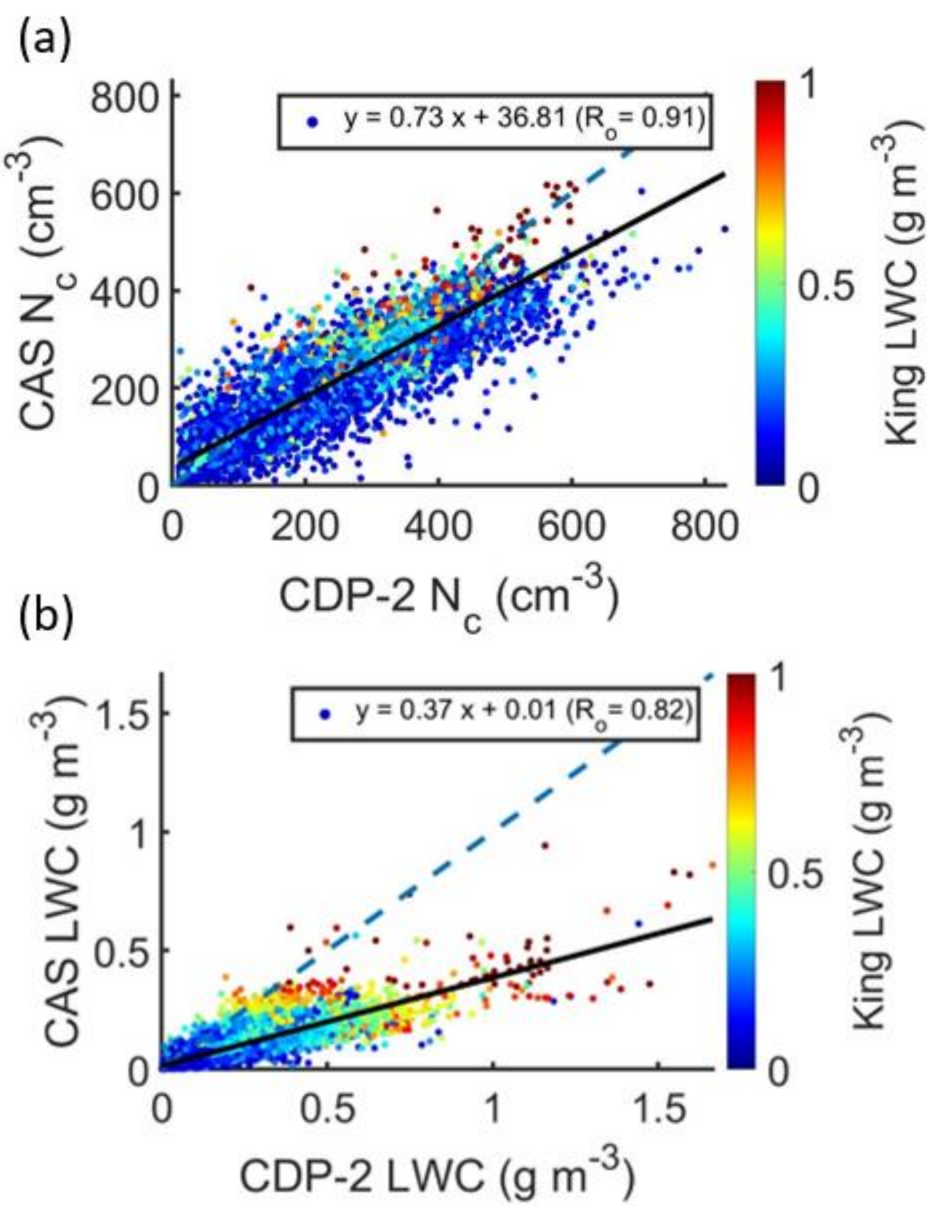

Figure 47: Scatter plots comparing (a) N_c and (b) LWC measured by CAS and CDP-B during 2017 IOP excluding data from 30 and 31 August 2017. Each dot represents a 1 Hz data sample colored by King LWC. Linear regression coefficients indicated in legend.

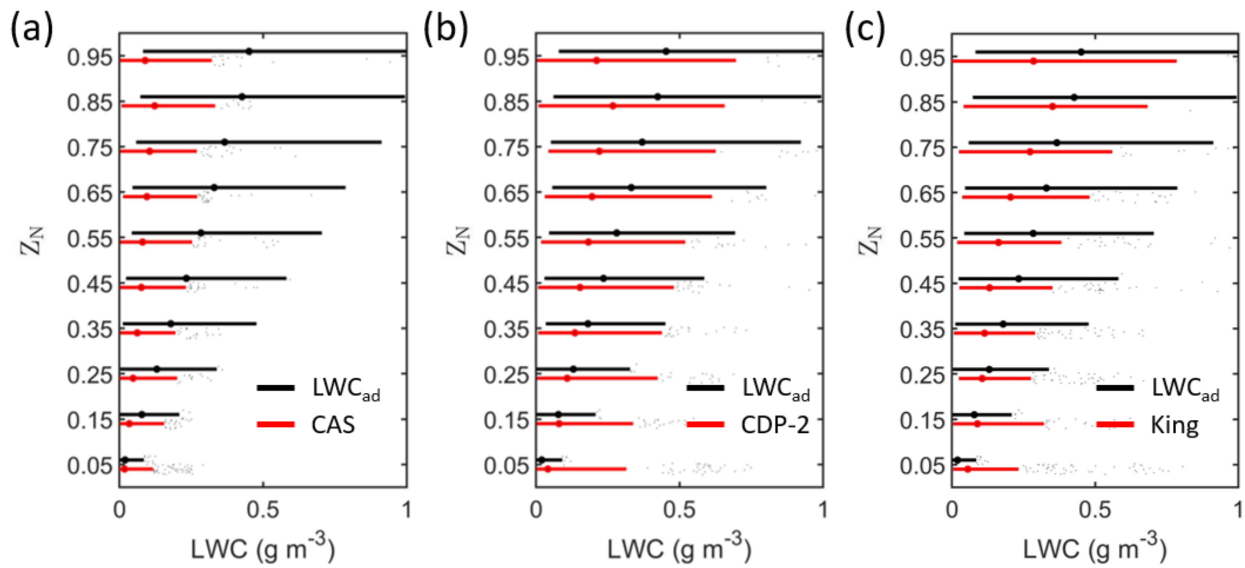

Figure 48: Boxplots representing the vertical profiles of (a) CAS LWC, (b) CDP-B LWC, and (c) King LWC with LWC_{ad} as function of Z_N. These data represent cloud samples from cloud profiles flown during the seven research flights from 2017 IOP used for data analysis.

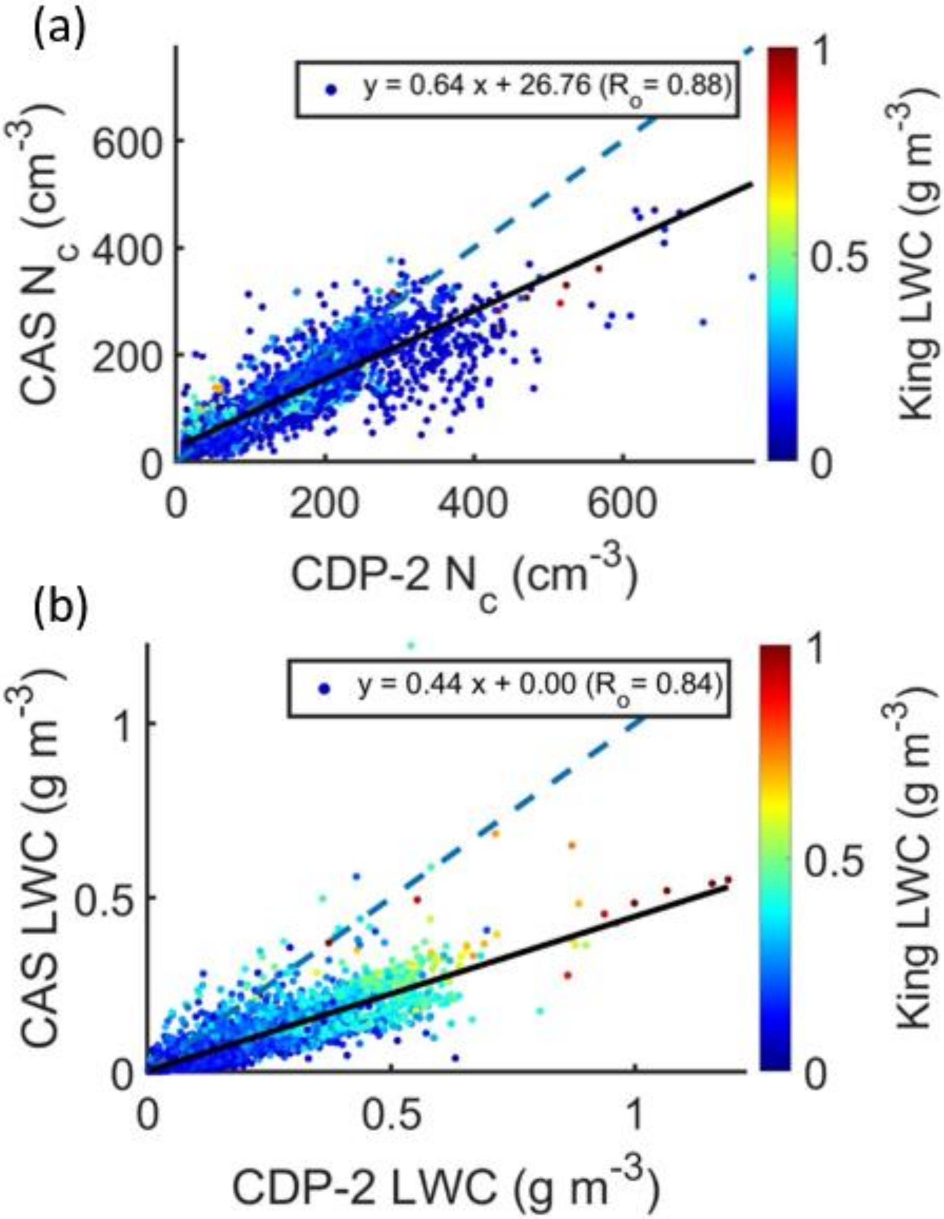

Figure 49: Scatter plots comparing (a) N_c and (b) LWC measured by CAS and CDP-B during 2018 IOP for six research flights when CAS was operational. Each dot represents a 1 Hz data sample colored by King LWC. Linear regression coefficients indicated in legend.

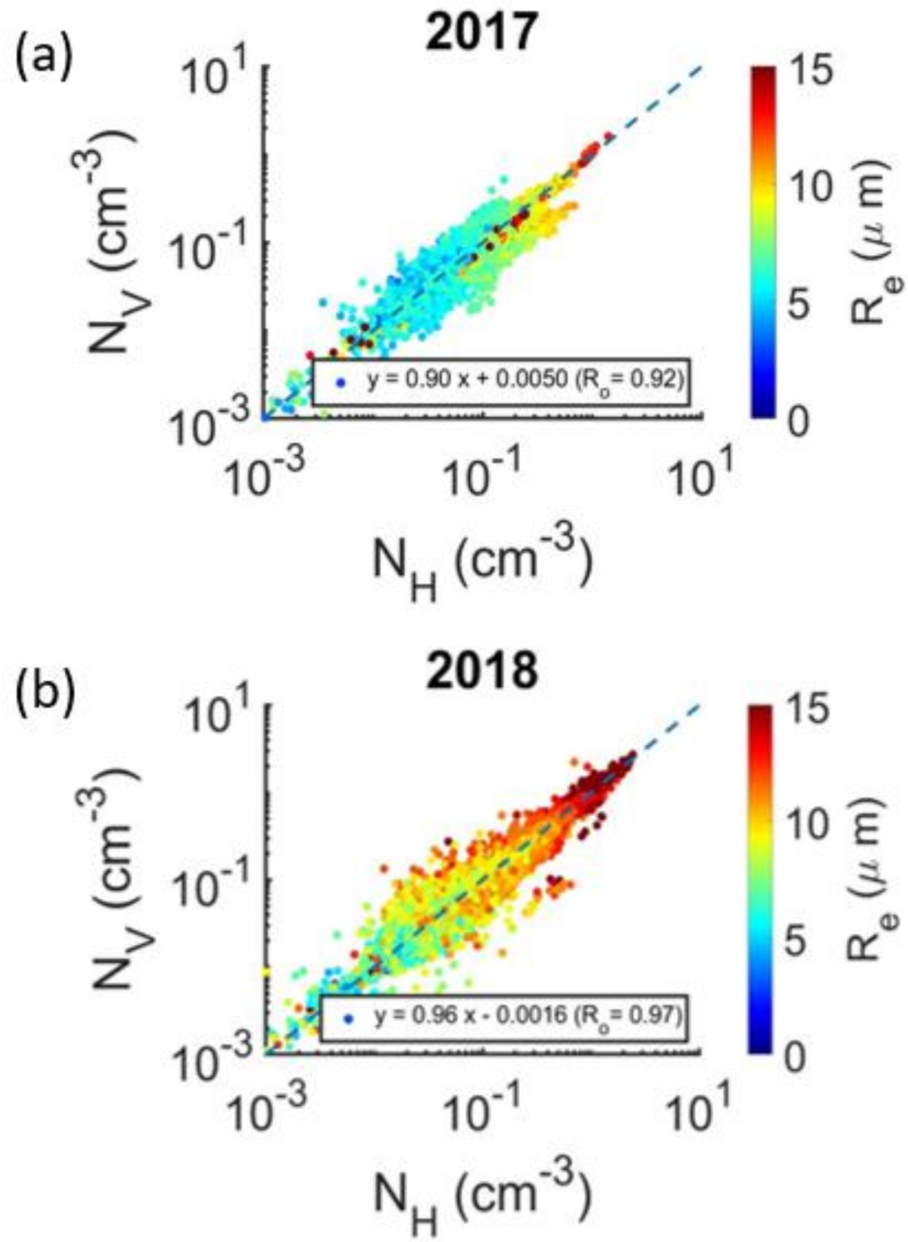

Figure 50: Droplet concentration measured by vertical array of 2D-S (N_V) as function of droplet concentration measured by horizontal array of 2D-S (N_H) for (a) 2017 and (b) 2018 IOP. Each data point represents a 1 Hz sample colored by R_e for cloud profiles flown during the research flights from 2017 and 2018 IOP used for data analysis. Linear regression coefficients indicated in legend.

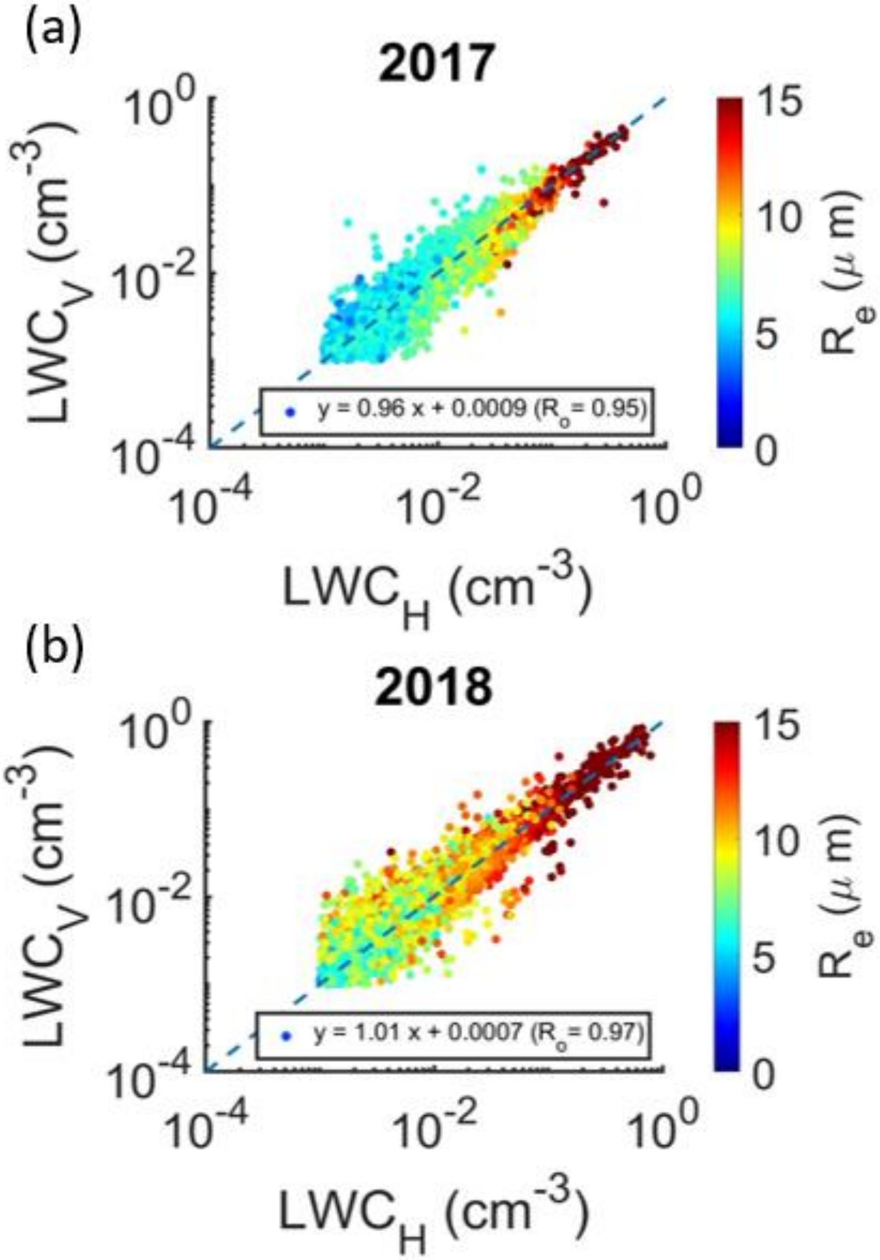

Figure 51: Same as Fig. 50, comparing LWC_H and LWC_V for (a) 2017 and (b) 2018 IOP.

APPENDIX B – Data processing codes and tools developed

The University of Illinois/Oklahoma Optical Array Probe Processing Software (UIOOPS) (McFarquhar et al., 2018) was used to process the 2D-S and HVPS-3 data. The software was modified to address data quality issues due to soot deposition on the optical lenses (Fig. 52) during flight legs through aerosol plumes. In this section, the modifications are described, and scripts developed for the modifications are provided. The scripts previously available online before the conduct of this research and used without modifications are not provided here.

UIOOPS includes three processing steps: file decompression, image processing, and final product creation (Fig. 53). Step 1 converts different types of raw data files into the NetCDF format. Step 2 processes images for individual particles, determines the inter-arrival time for the particles, and retrieves morphological properties like maximum dimension, area ratio, and aspect ratio from the binary images. Step 3 sorts the particles into size bins for each unit of time in order to calculate the particle size distributions. Particle rejection based on inter-arrival time (shatter removal) or image shape (aspect ratio, area ratio, etc.) is also done during step 3. No changes were made to Step 1. Two changes were made to Step 2:

1. Modification of the inter-arrival time analysis.

The inter-arrival time analysis is done before step 3 to determine the threshold for particle rejection. For the 2-DS data files, particles with inter-arrival time < 6 μs, indicative of intermittently stuck diodes, were rejected. The threshold was determined using the peaks of a bimodal distribution of inter-arrival times (Field et al., 2006). For the HVPS-3 data files, a wide range of thresholds were determined for different flights. Thus, a dynamic threshold was used.

The analysis was conducted using the script "IntArrAnalysis_time.m". This script provided histograms of inter-arrival times for populations of particles sampled within a specific time period (Fig. 54). The script was written by Wei Wu, modified by Joe Finlon, and modified again for ORACLES. The final version is provided along with "IntArr_time.m" which specifies the inputs.

2. "Shadow diode" analysis to identify diodes affected by soot deposition.

A diode that is stuck or occluded by soot deposition would be "shadowed" for a longer duration compared to diodes shadowed by particles crossing the probe sample volume. The impact of soot deposition on the particles imaged by the photodiode array was examined by comparing the illumination counts across the photodiode array. Diodes shadowed for more than 20% of the average count across the array were identified as "shadow diodes" (Fig. 55). Step 2 was then re-run by forcibly illuminating the shadow diodes. The script "find_shadow_diodes.m" was written to conduct this analysis. This script provides a list of the shadow diodes for the data file which is used as an input to re-run Step 2.

The thresholds used for particle rejection in Step 3 were changed according to the artifacts observed within particle images from ORACLES (Fig. 56). Particles with aspect ratio > 4 or area ratio < 0.5 were rejected and hollow particles were accepted.

In addition to the scripts mentioned above, the following scripts are provided:

1. Retrieving the true air speed from 2D-S or HVPS-3 data files: "loadTASinfo_2DS.m"
2. Running all three steps for either HVPS-3 or 2D-S data files: "steps_script_1.m"
3. Combining the output files from Step 2: "combine_pbp.m" (originally written by Joe Finlon and modified for ORACLES).

4. Combining the output files from Step 3 and adding a time sync with ORACLES data files: “combine_sizedist.m”
5. Step 2 script: “imgProc_sm.m” (written and modified by various group members).
6. Step 3 script: “sizeDist.m” (written and modified by various group members).
7. Another script required for the inter-arrival time analysis is available here: https://svn.oss.deltares.nl/repos/openearthtools/tags/xbeach_release_02Nov2011/_externals/general/time_fun/time2datenum.m

The following naming convention was followed:

baseYYmmDDhhMMss.2DS or baseYYmmDDhhMMss.HVPS (raw data file),

baseYYmmDDhhMMss.H.cdf and BaseYYmmDDhhMMss.V.cdf (step 1 output),

baseYYmmDDhhMMss.H_1.cdf and BaseYYmmDDhhMMss.V_1.cdf (step 2 output), and

baseYYmmDDhhMMss.H.2DS.cdf and BaseYYmmDDhhMMss.H.2DS.cdf (step 3 output).

TABLES AND FIGURES:

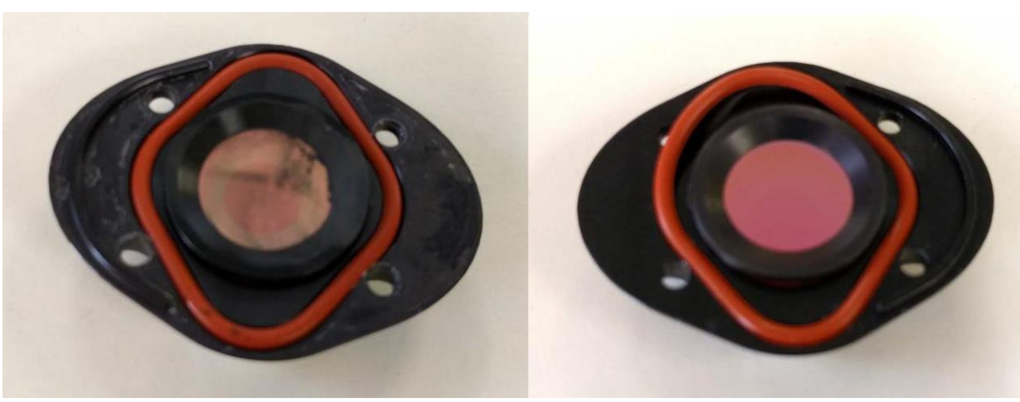

Figure 52: Aerosol deposition on the inside of the receive side mirror for 2D-S vertical channel with the cleaned mirror on the right. (courtesy: Joe O’Brien).

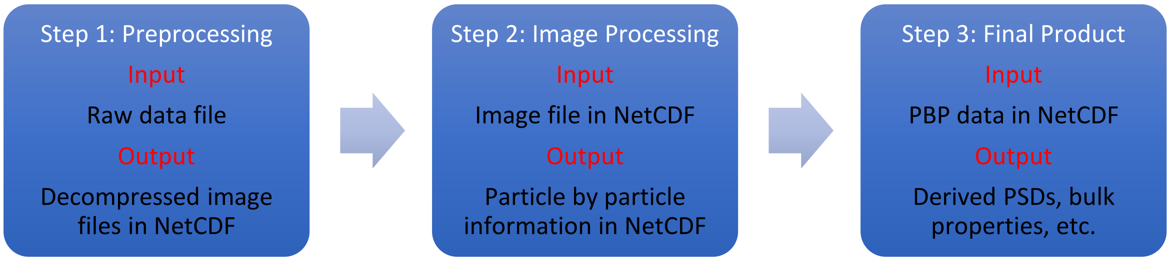

Figure 53: UIOOPS software structure and processing steps (courtesy: Wei Wu).

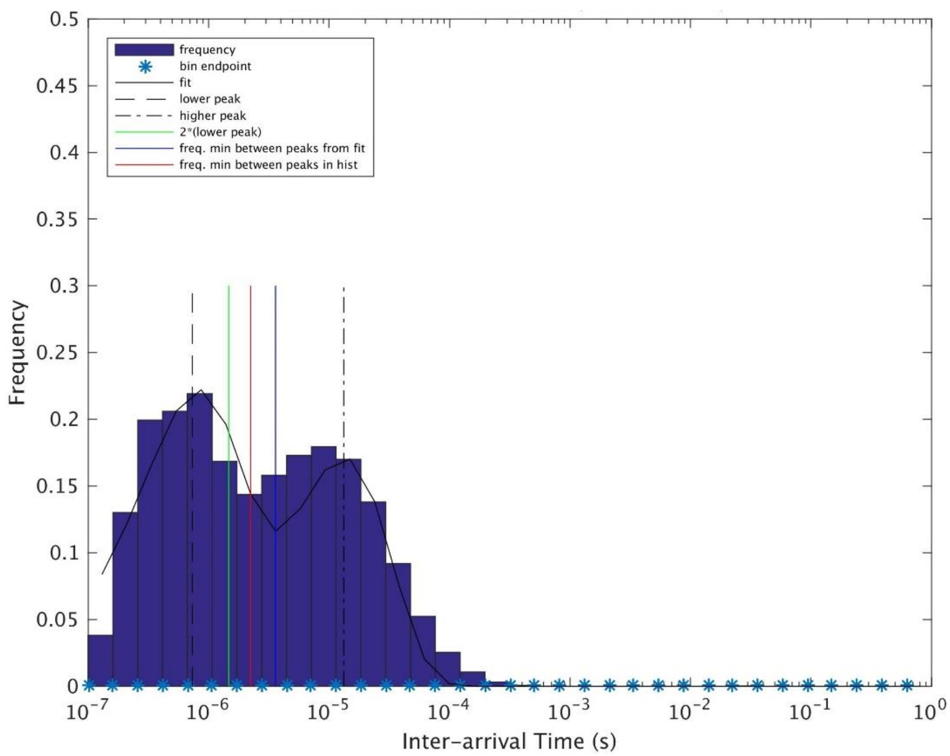

Figure 54: Inter-arrival time distribution for particles sampled by 2D-S between 10:50:20 and 10:50:46 UTC on 6 September 2016. The lines indicate values at different points of interest from the peaks of the bimodal distribution (minima between modes from fit/histogram, etc.)

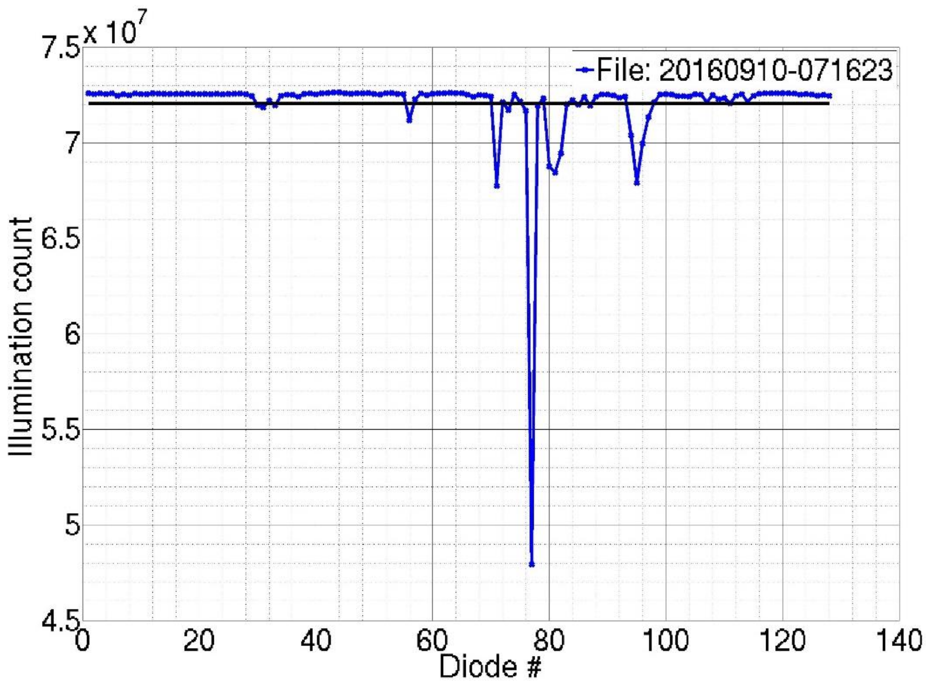

Figure 55: Illumination counts for the 2D-S photodiode array from 10 September 2016. The black line is average illumination count with diode #77 identified as a shadow diode.

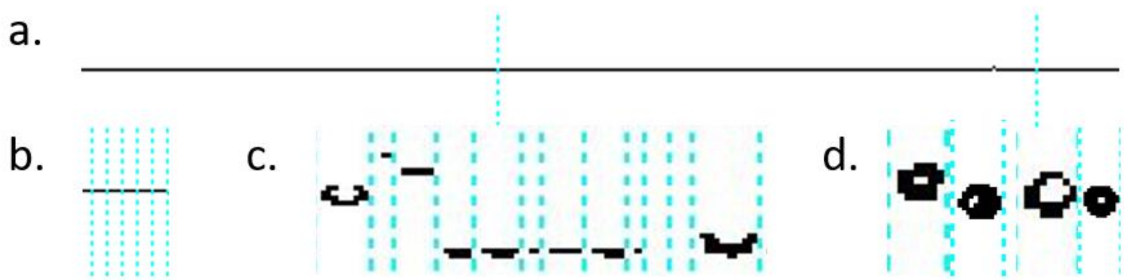

Figure 56: (a-c) Different types of data artifacts and (d) hollow particles from the 2D-S during ORACLES. The vertical dotted lines (blue) separate individual particles.

LOADTASINFO_2DS.M

```
function [timehhmmss,tas] = loadTASinfo_2DS(filename, startRow, endRow)
%IMPORTFILE Import numeric data from a text file as column vectors.
%   [VARNAME1,VARNAME2] = IMPORTFILE(FILENAME) Reads data from text file
%   FILENAME for the default selection.
%
%   [VARNAME1,VARNAME2] = IMPORTFILE(FILENAME, STARTROW, ENDROW) Reads data
%   from rows STARTROW through ENDROW of text file FILENAME.
%
% Example:
%   [VarName1,VarName2] = importfile('base160906075333.tas.csv',1, 2799);
%
%    See also TEXTSCAN.

% Auto-generated by MATLAB on 2016/11/09 23:51:10

%% Initialize variables.
delimiter = ',';
if nargin<=2
    startRow = 1;
    endRow = inf;
end

%% Format string for each line of text:
%   column1: double (%f)
%             column2: double (%f)
% For more information, see the TEXTSCAN documentation.
formatSpec = '%f%f%*s%*s%*s%*s%*s%*s%*s%*s%[^\n\r]';

%% Open the text file.
fileID = fopen(filename,'r');

%% Read columns of data according to format string.
% This call is based on the structure of the file used to generate this
% code. If an error occurs for a different file, try regenerating the code
% from the Import Tool.
dataArray = textscan(fileID, formatSpec, endRow(1)-startRow(1)+1, 'Delimiter', delimiter, 'EmptyValue' ,NaN,'HeaderLines', startRow(1)-1, 'ReturnOnError', false);
for block=2:length(startRow)
    frewind(fileID);
    dataArrayBlock = textscan(fileID, formatSpec, endRow(block)-startRow(block)+1, 'Delimiter', delimiter, 'EmptyValue' ,NaN,'HeaderLines', startRow(block)-1, 'ReturnOnError', false);
    for col=1:length(dataArray)
        dataArray{col} = [dataArray{col};dataArrayBlock{col}];
    end
end

%% Close the text file.
fclose(fileID);

%% Post processing for unimportable data.
% No unimportable data rules were applied during the import, so no post
% processing code is included. To generate code which works for
% unimportable data, select unimportable cells in a file and regenerate the
% script.
```

```
%% Allocate imported array to column variable names
timehhmmss = dataArray{:, 1};
tas = dataArray{:, 2};
```

STEPS_SCR_1.M

```
% Run all steps at once

flight='181017';
file='064304';
probe='2DS';
diodes=0; % 0 unless diode re-analysis being performed

% path=['/scratch/sid/oracles/oracles_20' flight];
path=['/condo/mcfarq/sid/b/oracles/oracles_20' flight];
filename=[path '/base' flight file];
orientation1='H';
orientation2='V';
campaign='ORACLES';

switch probe
   case '2DS'
% 2DS Step 1
if diodes==0
read_binary_SPEC([filename '.' probe],filename)
else
end

% 2DS Step 2 - H
nChucks=1; % 48;         % Number of chucks (seperate files)
nEvery =1000000;         % Size of every chucks.
numb=11:10+nChucks;      % Start from 11 to avoid sigle numbers in file name for later convinience
for iii=1:nChucks %3:4    % iiith chuck will be processed
   infile  = [filename '.' orientation1 '.cdf'];  % Input file
   if diodes==0
   outfile = [filename '.' orientation1 '_1.cdf'];                  % Output image autoanalysis file
   else
   outfile = [filename '.' orientation1 '_2.cdf'];                  % Output image autoanalysis file
   end
   imgProc_sm(infile,outfile, probe, iii, nEvery,campaign,path,flight,file);  % See imgprocdm documentation for more information
end

% 2DS Step 2 - V
nChucks=1; % 48;         % Number of chucks (seperate files)
nEvery =1000000;         % Size of every chucks.
numb=11:10+nChucks;      % Start from 11 to avoid sigle numbers in file name for later convinience
for iii=1:nChucks %3:4    % iiith chuck will be processed
   infile  = [filename '.' orientation2 '.cdf'];  % Input file
   if diodes==0
   outfile = [filename '.' orientation2 '_1.cdf'];                  % Output image autoanalysis file
   else
   outfile = [filename '.' orientation2 '_2.cdf'];                  % Output image autoanalysis file
   end
   imgProc_sm(infile,outfile, probe, iii, nEvery,campaign,path,flight,file);  % See imgprocdm documentation for more information
end

% 2DS Step 3 - H
```

```
[timehhmmss,tas]=loadTASinfo_2DS([filename '.tas.csv']);
pres=tas;
pres(:)=9e5;
temp=tas;
temp(:)=15;
if diodes==0
inFile =  [filename '.' orientation1 '_1.cdf'];
outFile = [filename '.' orientation1 '.' probe '.cdf'];
else
inFile =  [filename '.' orientation1 '_2.cdf'];
outFile = [filename '.' orientation1 '.' probe '_2.cdf'];
end
ds=0.010;
IntArrFile=[probe '_intArrThreshold_base' flight file '.' orientation1 '_1.cdf'];
sizeDist(inFile,outFile, tas, floor(timehhmmss),probe, 6, 0,pres,temp,campaign,['20' flight ' ' file],IntArrFile);

%sizeDist(inFile,outFile, tas, floor(timehhmmss),probe, 6, 0,pres,temp,campaign,0);

% 2DS Step 3 - V
[timehhmmss,tas]=loadTASinfo_2DS([filename '.tas.csv']);
pres=tas;
pres(:)=9e5;
temp=tas;
temp(:)=15;
outFile = [filename '.' orientation2 '.' probe '.cdf'];
if diodes==0
inFile =  [filename '.' orientation2 '_1.cdf'];
outFile = [filename '.' orientation2 '.' probe '.cdf'];
else
inFile =  [filename '.' orientation2 '_2.cdf'];
outFile = [filename '.' orientation2 '.' probe '_2.cdf'];
end
ds=0.010;
IntArrFile=[probe '_intArrThreshold_base' flight file '.' orientation2 '_1.cdf'];
sizeDist(inFile,outFile, tas, floor(timehhmmss),probe, 6, 0,pres,temp,campaign,['20' flight ' ' file],IntArrFile);

%sizeDist(inFile,outFile, tas, floor(timehhmmss),probe, 6, 0,pres,temp,campaign,0);

   case 'HVPS'
% HVPS Step 1
if diodes==0
read_binary_hvps([filename '.' probe],filename)
else
end

% HVPS Step 2
nChucks=1; % 48;         % Number of chucks (seperate files)
nEvery =1000000;         % Size of every chucks.
numb=11:10+nChucks;      % Start from 11 to avoid sigle numbers in file name for later convinience
for iii=1:nChucks %3:4    % iiith chuck will be processed
   infile  = [filename '.' orientation2 '.cdf'];  % Input file
   if diodes==0
   outfile = [filename '.' orientation2 '_1.cdf'];                    % Output image autoanalysis file
   else
   outfile = [filename '.' orientation2 '_1.cdf'];                    % Output image autoanalysis file
   end
   imgProc_sm(infile,outfile, probe, iii, nEvery,campaign,path,flight,file);  % See imgprocdm documentation for more information
end
```

```
% HVPS Step 3
[timehhmmss,tas]=loadTASinfo_2DS([filename '.tas.csv']);
pres=tas;
pres(:)=9e5;
temp=tas;
temp(:)=15;
if diodes==0
outFile = [filename '.' orientation2 '.' probe '.cdf'];
inFile =  [filename '.' orientation2 '_1.cdf'];
else
outFile = [filename '.' orientation2 '.' probe '.cdf'];
inFile =  [filename '.' orientation2 '_1.cdf'];
end
ds=0.150;
IntArrFile=[probe '_intArrThreshold_base' flight file '.' orientation2 '_1.cdf'];
sizeDist(inFile,outFile, tas, floor(timehhmmss),probe, 6, 0,pres,temp,campaign,['20' flight ' ' file],IntArrFile);

%sizeDist(inFile,outFile, tas, floor(timehhmmss),probe, 6, 0,pres,temp,campaign,0);

   case 'CIP'
% CIP Step 1
filename=[path '/' flight(1:2) '_' flight(3:4) '_' flight(5:6) '_' file(1:2) '_' file(3:4) '_' file(5:6) '.sea'];
read_binary_SEA(filename,[path '/base' flight file])
filename=[path '/base' flight file];

% CIP Step 2
nChucks=1; % 48;         % Number of chucks (seperate files)
nEvery =1000000;         % Size of every chucks.
numb=11:10+nChucks;      % Start from 11 to avoid sigle numbers in file name for later convinience
for iii=1:nChucks %3:4    % iiith chuck will be processed
   infile  = [filename '.' probe '.cdf'];  % Input file
   outfile = [filename '.' probe '_1.cdf'];                              % Output image autoanalysis file
   imgProc_sm(infile,outfile, probe, iii, nEvery,campaign,path,flight,file);  % See imgprocdm documentation for more information
end

% CIP Step 3
loadTASinfo_CIP;
%clearvars -except flight file path timehhmmss tas
pres=tas;
pres(:)=9e5;
temp=tas;
temp(:)=15;
outFile = [filename '.' orientation2 '.' probe '.cdf'];
inFile =  [filename '.' probe '_1.cdf'];
ds=0.025;
IntArrFile=[probe '_intArrThreshold_base' flight file '.' orientation2 '_1.cdf'];
sizeDist(inFile,outFile, tas, floor(timehhmmss),probe, 6, 0,pres,temp,campaign,['20' flight ' ' file],IntArrFile);

%sizeDist(inFile,outFile, tas, floor(timehhmmss),probe, 6, 0,pres,temp,campaign,0);

End
```

COMBINE_PBP.M

```
% function combine_pbp(campaign, inputDate)
campaign='oracles';
```

```
inputDate='20181003';
orientation='V';
%%%%%%%%%%%%%%%%%%%%%%%%%%%%%%%%%%%%%%%%%%%%%%%%%%%%%%%%%%%%%%%%%%%%%%%%%%%%%%%
%%%
% This code is property of Joseph Finlon. Univ of Illinois. Copyright 2016.
% Modified for ORACLES: Siddhant Gupta - 10/03/2017
%
% This script combines processed particle data into 1 file if more than one
% data file exists for that day.
%
% Inputs:
%   campaign - 'olympex', 'gcpex', 'mc3e'
%   inputDate - date to process in 'yyyymmdd' format
%   probeType - '2DC', '2DP', '2DS', 'HVPS'
%
%%%%%%%%%%%%%%%%%%%%%%%%%%%%%%%%%%%%%%%%%%%%%%%%%%%%%%%%%%%%%%%%%%%%%%%%%%%%%%%
%%%
%% Grab processed file names for the input date

% path = '/scratch/sid/';


path = sprintf('/condo/mcfarq/sid/b/%s/%s_%s/', campaign,campaign,inputDate);
% path = sprintf('/scratch/sid/%s/%s_%s/', campaign,campaign,inputDate);
% path = [pwd '/'];
addpath(path);
infile = dir(fullfile(path,sprintf('base%s*.%s_1.cdf', inputDate(3:8),orientation))); % grab files to process

%% Loop through each file to append data for each variable

if size(infile,1)>1
  %% Load data from each processed file into a structure array

  for i=1:size(infile,1)
    disp(['Combining file ', num2str(i), ' of ', num2str(size(infile,1))])
    infilename = sprintf('%s%s',path,infile(i).name);

    data(i).Time = ncread(infilename,'Time');
    data(i).Date = ncread(infilename,'Date');
    data(i).msec = ncread(infilename,'msec');
    data(i).Time_in_seconds = ncread(infilename,'Time_in_seconds');
    data(i).SliceCount = ncread(infilename,'SliceCount');
    data(i).DMT_DOF_SPEC_OVERLOAD = ncread(infilename,'DMT_DOF_SPEC_OVERLOAD');
    data(i).Particle_number_all = ncread(infilename,'Particle_number_all');
    data(i).position = ncread(infilename,'position');
    data(i).particle_time = ncread(infilename,'particle_time');
    data(i).particle_millisec = ncread(infilename,'particle_millisec');
    data(i).particle_microsec = ncread(infilename,'particle_microsec');
    data(i).parent_rec_num = ncread(infilename,'parent_rec_num');
    data(i).particle_num = ncread(infilename,'particle_num');
    data(i).image_length = ncread(infilename,'image_length');
    data(i).image_width = ncread(infilename,'image_width');
    data(i).image_area = ncread(infilename,'image_area');
    data(i).image_longest_y = ncread(infilename,'image_longest_y');
    data(i).image_diam_minR = ncread(infilename,'image_diam_minR');
    data(i).image_diam_AreaR = ncread(infilename,'image_diam_AreaR');
    data(i).image_perimeter = ncread(infilename,'image_perimeter');
%     data(i).image_RectangleL = ncread(infilename,'image_RectangleL');
```

```
%       data(i).image_RectangleW = ncread(infilename,'image_RectangleW');
%       data(i).image_RectangleAngle = ncread(infilename,'image_RectangleAngle');
%       data(i).image_EllipseL = ncread(infilename,'image_EllipseL');
%       data(i).image_EllipseW = ncread(infilename,'image_EllipseW');
%       data(i).image_EllipseAngle = ncread(infilename,'image_EllipseAngle');
        data(i).percent_shadow_area = ncread(infilename,'percent_shadow_area');
        data(i).edge_at_max_hole = ncread(infilename,'edge_at_max_hole');
        data(i).max_hole_diameter = ncread(infilename,'max_hole_diameter');
        data(i).part_z = ncread(infilename,'part_z');
        data(i).size_factor = ncread(infilename,'size_factor');
        data(i).holroyd_habit = ncread(infilename,'holroyd_habit');
        data(i).area_hole_ratio = ncread(infilename,'area_hole_ratio');
        data(i).inter_arrival = ncread(infilename,'inter_arrival');
        data(i).bin_stats = ncread(infilename,'bin_stats');
    end

    %% Combine structures into 1 array

    arrayIndex = 0;

    for i=1:size(infile,1)
        Date(arrayIndex+1:arrayIndex+length(data(i).Date),1) = data(i).Date;
        Time(arrayIndex+1:arrayIndex+length(data(i).Time),1) = data(i).Time;
        msec(arrayIndex+1:arrayIndex+length(data(i).msec),1) = data(i).msec;
        Time_in_seconds(arrayIndex+1:arrayIndex+length(data(i).Time_in_seconds),1) = data(i).Time_in_seconds;
        SliceCount(arrayIndex+1:arrayIndex+length(data(i).SliceCount),1) = data(i).SliceCount;
        DMT_DOF_SPEC_OVERLOAD(arrayIndex+1:arrayIndex+length(data(i).DMT_DOF_SPEC_OVERLOAD),1)                    =
data(i).DMT_DOF_SPEC_OVERLOAD;
        Particle_number_all(arrayIndex+1:arrayIndex+length(data(i).Particle_number_all),1) = data(i).Particle_number_all;
        position(:,arrayIndex+1:arrayIndex+length(data(i).position)) = data(i).position;
        particle_time(arrayIndex+1:arrayIndex+length(data(i).particle_time),1) = data(i).particle_time;
        particle_millisec(arrayIndex+1:arrayIndex+length(data(i).particle_millisec),1) = data(i).particle_millisec;
        particle_microsec(arrayIndex+1:arrayIndex+length(data(i).particle_microsec),1) = data(i).particle_microsec;
        parent_rec_num(arrayIndex+1:arrayIndex+length(data(i).parent_rec_num),1) = data(i).parent_rec_num;
        particle_num(arrayIndex+1:arrayIndex+length(data(i).particle_num),1) = data(i).particle_num;
        image_length(arrayIndex+1:arrayIndex+length(data(i).image_length),1) = data(i).image_length;
        image_width(arrayIndex+1:arrayIndex+length(data(i).image_width),1) = data(i).image_width;
        image_area(arrayIndex+1:arrayIndex+length(data(i).image_area),1) = data(i).image_area;
        image_longest_y(arrayIndex+1:arrayIndex+length(data(i).image_longest_y),1) = data(i).image_longest_y;
        image_diam_minR(arrayIndex+1:arrayIndex+length(data(i).image_diam_minR),1) = data(i).image_diam_minR;
        image_diam_AreaR(arrayIndex+1:arrayIndex+length(data(i).image_diam_AreaR),1) = data(i).image_diam_AreaR;
        image_perimeter(arrayIndex+1:arrayIndex+length(data(i).image_perimeter),1) = data(i).image_perimeter;
%       image_RectangleL(arrayIndex+1:arrayIndex+length(data(i).image_RectangleL),1) = data(i).image_RectangleL;
%       image_RectangleW(arrayIndex+1:arrayIndex+length(data(i).image_RectangleW),1) = data(i).image_RectangleW;
%      image_RectangleAngle(arrayIndex+1:arrayIndex+length(data(i).image_RectangleAngle),1) = data(i).image_RectangleAngle;
%       image_EllipseL(arrayIndex+1:arrayIndex+length(data(i).image_EllipseL),1) = data(i).image_EllipseL;
%       image_EllipseW(arrayIndex+1:arrayIndex+length(data(i).image_EllipseW),1) = data(i).image_EllipseW;
%       image_EllipseAngle(arrayIndex+1:arrayIndex+length(data(i).image_EllipseAngle),1) = data(i).image_EllipseAngle;
        percent_shadow_area(arrayIndex+1:arrayIndex+length(data(i).percent_shadow_area),1) = data(i).percent_shadow_area;
        edge_at_max_hole(arrayIndex+1:arrayIndex+length(data(i).edge_at_max_hole),1) = data(i).edge_at_max_hole;
        max_hole_diameter(arrayIndex+1:arrayIndex+length(data(i).max_hole_diameter),1) = data(i).max_hole_diameter;
        part_z(arrayIndex+1:arrayIndex+length(data(i).part_z),1) = data(i).part_z;
        size_factor(arrayIndex+1:arrayIndex+length(data(i).size_factor),1) = data(i).size_factor;
        holroyd_habit(arrayIndex+1:arrayIndex+length(data(i).holroyd_habit),1) = data(i).holroyd_habit;
        area_hole_ratio(arrayIndex+1:arrayIndex+length(data(i).area_hole_ratio),1) = data(i).area_hole_ratio;
        inter_arrival(arrayIndex+1:arrayIndex+length(data(i).inter_arrival),1) = data(i).inter_arrival;
        bin_stats(:,i) = data(i).bin_stats;
```

```
    arrayIndex = length(Date);
  end

  %% Create variables for new output file

  disp(['Saving ', num2str(arrayIndex), ' particles to file'])

%    outfile = sprintf('%sbase1609%s%s.H_1.cdf', path, inputDate(7:8), infile(1).name(end-13:end-8));
%    outpath = sprintf('/data/pecan/a/sgupta92/%s/%s_%s/IntArrAnalysis/', campaign,campaign,inputDate);
   outpath = path;
%   outpath = [pwd '/'];
  outfile = sprintf('%sbase%s%s.combined.%s_1.cdf', outpath, inputDate(3:8), infile(1).name(end-13:end-8),orientation);
%        path, inputDate(7:8)); % define combined file name
  f = netcdf.create(outfile, '64BIT_OFFSET');
%    dimid0 = netcdf.defDim(f,'time',netcdf.getConstant('NC_UNLIMITED'));
  dimid0 = netcdf.defDim(f,'time',arrayIndex);
  dimid1 = netcdf.defDim(f,'pos_count',2);
  dimid2 = netcdf.defDim(f,'bin_count',size(bin_stats, 1));
  dimid3 = netcdf.defDim(f,'files_stitched',size(infile,1));

  varid0  = netcdf.defVar(f,'Time','double',dimid0);
  varid1 = netcdf.defVar(f,'Date','double',dimid0);
  varid2  = netcdf.defVar(f,'msec','double',dimid0);
  varid101 = netcdf.defVar(f,'Time_in_seconds','double',dimid0);
  varid102 = netcdf.defVar(f,'SliceCount','double',dimid0);
  varid103 = netcdf.defVar(f,'DMT_DOF_SPEC_OVERLOAD','double',dimid0);
  varid104 = netcdf.defVar(f,'Particle_number_all','double',dimid0);
  varid4  = netcdf.defVar(f,'position','double',[dimid1 dimid0]);
  varid5  = netcdf.defVar(f,'particle_time','double',dimid0);
  varid6  = netcdf.defVar(f,'particle_millisec','double',dimid0);
  varid7  = netcdf.defVar(f,'particle_microsec','double',dimid0);
  varid8  = netcdf.defVar(f,'parent_rec_num','double',dimid0);
  varid9  = netcdf.defVar(f,'particle_num','double',dimid0);
  varid10 = netcdf.defVar(f,'image_length','double',dimid0);
  varid11 = netcdf.defVar(f,'image_width','double',dimid0);
  varid12 = netcdf.defVar(f,'image_area','double',dimid0);
  varid13 = netcdf.defVar(f,'image_longest_y','double',dimid0);
  varid26 = netcdf.defVar(f,'image_diam_minR','double',dimid0);
  varid27 = netcdf.defVar(f,'image_diam_AreaR','double',dimid0);
  varid45 = netcdf.defVar(f,'image_perimeter','double',dimid0);
%   varid46 = netcdf.defVar(f,'image_RectangleL','double',dimid0);
%   varid47 = netcdf.defVar(f,'image_RectangleW','double',dimid0);
%   varid67 = netcdf.defVar(f,'image_RectangleAngle','double',dimid0);
%   varid48 = netcdf.defVar(f,'image_EllipseL','double',dimid0);
%   varid49 = netcdf.defVar(f,'image_EllipseW','double',dimid0);
%   varid69 = netcdf.defVar(f,'image_EllipseAngle','double',dimid0);
  varid28 = netcdf.defVar(f,'percent_shadow_area','double',dimid0);
  varid29 = netcdf.defVar(f,'edge_at_max_hole','double',dimid0);
  varid30 = netcdf.defVar(f,'max_hole_diameter','double',dimid0);
  varid31 = netcdf.defVar(f,'part_z','double',dimid0);
  varid32 = netcdf.defVar(f,'size_factor','double',dimid0);
  varid33 = netcdf.defVar(f,'holroyd_habit','double',dimid0);
  varid34 = netcdf.defVar(f,'area_hole_ratio','double',dimid0);
  varid35 = netcdf.defVar(f,'inter_arrival','double',dimid0);
  varid36 = netcdf.defVar(f,'bin_stats','double',[dimid2 dimid3]);
  netcdf.endDef(f)

  %% Save the combined variables
```

```
   netcdf.putVar ( f, varid0, Time );
   netcdf.putVar ( f, varid1, Date );
   netcdf.putVar ( f, varid2, msec );
   netcdf.putVar ( f, varid101,  Time_in_seconds );
   netcdf.putVar ( f, varid102,  SliceCount );
   netcdf.putVar ( f, varid103,  DMT_DOF_SPEC_OVERLOAD );
   netcdf.putVar ( f, varid104,  Particle_number_all );
   netcdf.putVar ( f, varid4, position' );
   netcdf.putVar ( f, varid5, particle_time );
   netcdf.putVar ( f, varid6, particle_millisec );
   netcdf.putVar ( f, varid7, particle_microsec );
   netcdf.putVar ( f, varid8, parent_rec_num );
   netcdf.putVar ( f, varid9, particle_num );
   netcdf.putVar ( f, varid10, image_length);
   netcdf.putVar ( f, varid11, image_width);
   netcdf.putVar ( f, varid12, image_area);
   netcdf.putVar ( f, varid13, image_longest_y);
   netcdf.putVar ( f, varid26, image_diam_minR);
   netcdf.putVar ( f, varid27, image_diam_AreaR);
   netcdf.putVar ( f, varid45, image_perimeter);
%    netcdf.putVar ( f, varid46, image_RectangleL);
%    netcdf.putVar ( f, varid47, image_RectangleW);
%    netcdf.putVar ( f, varid67, image_RectangleAngle);
%    netcdf.putVar ( f, varid48, image_EllipseL);
%    netcdf.putVar ( f, varid49, image_EllipseW);
%    netcdf.putVar ( f, varid69, image_EllipseAngle);
   netcdf.putVar ( f, varid28, percent_shadow_area);
   netcdf.putVar ( f, varid29, edge_at_max_hole);
   netcdf.putVar ( f, varid30, max_hole_diameter);
   netcdf.putVar ( f, varid31, part_z);
   netcdf.putVar ( f, varid32, size_factor);
   netcdf.putVar ( f, varid33, holroyd_habit);
   netcdf.putVar ( f, varid34, area_hole_ratio);
   netcdf.putVar ( f, varid35, inter_arrival);
   netcdf.putVar ( f, varid36, bin_stats);
   netcdf.close(f);
end
% end
```

COMBINE_SIZEDIST.M

```
%-----Script to combine multiple size distribution files from one flight-----%
%-----Remove duplicate time steps, append for breaks and time sync with .campaign file-----%

%-----Written by Siddhant Gupta - 10/01/2017-----%
%-----MODIFIED: Removed input of file #, faster time vector conversion - 10/05/2017-----%
%-----MODIFIED: Sync with summary file even if it starts after 2DS file - 06/11/2018-----%
%-----MODIFIED: If time ends with '60', e.g. 155060, it is corrected to 155100 - 06/25/2018-----%

flightdate='20181017';
campaign='oracles';
orientation='V';
current_year='21'; % 20 is for 2020

%%%%%%%%%%%%%%%%%%%%%%%%%%%%%%%%%%%%%%%%%%%%%%%%%%%%%%%%%
%    Input:
```

```
%       1. Size distribution files: baseYYMMDDHHMMSS.H.2DS.cdf
%       2. .campaign summary file (in same directory)
%       Flight date: 'YYMMDD'
%       Campaign:    'oracles'
%
%    Output:
%       baseYYMMDDHHMMSS.combined.H.2DS.cdf
%       'conc_dmax' saved as 'twods_Nd' in cm-3
%%%%%%%%%%%%%%%%%%%%%%%%%%%%%%%%%%%%%%%%%%%%%%%%%%%%%%%%%%%%%%%%%%%%%%%%%%%%%%%%%%%%%%%%%%%%%%%%%%%

path = sprintf('/condo/mcfarq/sid/b/%s/%s_%s/', campaign,campaign,flightdate);
% path = sprintf('/scratch/sid/%s/%s_%s/', campaign,campaign,flightdate);
% path = [pwd '/'];

addpath(path);
infile = dir(fullfile(path,sprintf('base%s*.%s.2DS.cdf', flightdate(3:8),orientation))); % grab files to process
summaryfile = dir(fullfile(path,sprintf('%s_%s_%s*.%s',flightdate(3:4),flightdate(5:6),flightdate(7:8),campaign)));
summary=summaryfile(1).name;

%-----Create variables with input file data-----%

for k=1:size(infile,1);
disp(['Reading file ', num2str(k), ' of ', num2str(size(infile,1))])
eval(sprintf('filename_%d=infile(%d).name;',k,k));
eval(sprintf('ncid_%d=netcdf.open(filename_%d);',k,k));
eval(sprintf('time_%d=netcdf.getVar(ncid_%d,0);',k,k));
eval(sprintf('bin_min_%d=netcdf.getVar(ncid_%d,1);',k,k));
eval(sprintf('bin_max_%d=netcdf.getVar(ncid_%d,2);',k,k));
eval(sprintf('bin_mid_%d=netcdf.getVar(ncid_%d,3);',k,k));
eval(sprintf('bin_dD_%d=netcdf.getVar(ncid_%d,4);',k,k));
eval(sprintf('bin_dD__%d=repmat(bin_dD_%d'',length(time_%d),1);',k,k,k));
eval(sprintf('conc_dmax_%d=netcdf.getVar(ncid_%d,5)''/10^1;',k,k)); % cm-3 um-1
eval(sprintf('conc_dmax_%d=conc_dmax_%d.*bin_dD__%d;',k,k,k)); % cm-3
eval(sprintf('conc_darea_%d=netcdf.getVar(ncid_%d,7)''/10^4;',k,k)); % cm-3 um-1
eval(sprintf('conc_darea_%d=conc_darea_%d.*bin_dD__%d;',k,k,k)); % cm-3
eval(sprintf('twods_Nt_%d=netcdf.getVar(ncid_%d,8);',k,k));
eval(sprintf('count_%d=netcdf.getVar(ncid_%d,20);',k,k));
eval(sprintf('mean_area_ratio_%d=netcdf.getVar(ncid_%d,21);',k,k));
eval(sprintf('reject_ratio_%d=netcdf.getVar(ncid_%d,15);',k,k));
end

%-----Combine variable data from multiple files into one big variable-----%

arrayindex=0;

for i=1:size(infile,1);
bin_min=bin_min_1;
bin_mid=bin_mid_1;
bin_max=bin_max_1;
bin_dD=bin_dD_1;
eval(sprintf('time(arrayindex+1:arrayindex+length(time_%d),1) = time_%d;',i,i));
eval(sprintf('twods_Nd(arrayindex+1:arrayindex+length(conc_dmax_%d),:) = conc_dmax_%d;',i,i));
eval(sprintf('conc_darea(arrayindex+1:arrayindex+length(conc_darea_%d),:) = conc_darea_%d;',i,i));
eval(sprintf('twods_Nt(arrayindex+1:arrayindex+length(twods_Nt_%d),1) = twods_Nt_%d;',i,i));
eval(sprintf('count(arrayindex+1:arrayindex+length(count_%d),:) = count_%d'';',i,i));
eval(sprintf('mean_area_ratio(arrayindex+1:arrayindex+length(mean_area_ratio_%d),:)=mean_area_ratio_%d'';',i,i));
eval(sprintf('reject_ratio(arrayindex+1:arrayindex+length(reject_ratio_%d),1)=reject_ratio_%d;',i,i));
arrayindex=length(time);
```

```
end

%-----Remove extra variables with data from each file-----%

for k=1:size(infile,1);
eval(sprintf('clearvars *_%d',k));
end

%-----Remove duplicate time steps-----%

k_1=find(diff(time)==0);
time(k_1+1)=[];
twods_Nd(k_1+1,:)=[];
count(k_1+1,:)=[];
mean_area_ratio(k_1+1,:)=[];
reject_ratio(k_1+1)=[];
twods_Nt(k_1+1)=[];
conc_darea(k_1+1,:)=[];

%-----Convert time to time vector-----%

if time(end)<100000
time_1=num2str(time,'%06.f');
else
time_1=num2str(time);
end
time_mod=zeros(1,1);
for k=1:length(time_1)
if time_1(k,5:6)=='60'
   time_mod(end+1)=k;
   time_1(k,5:6)='00';
else
end
end
% timevec=zeros(length(time_1),1);
timevec=datenum(str2double(flightdate(3:4)),str2double(flightdate(5:6)),...
      str2double(flightdate(7:8)))+datenum(time_1,'HHMMSS')-datenum(str2double(current_year),0,1,0,0,0);
% for k=1:length(time);
%     timevec(k)=datenum(str2double(flightdate(1:2)),str2double(flightdate(3:4)),...
%        str2double(flightdate(5:6)))+datenum(time_1(k,:),'HHMMSS')-datenum(17,0,1,0,0,0);
% end
for k=1:length(time_1)
   if ismember(k,time_mod)==1
      timevec(k)=timevec(k)+datenum(0,0,0,0,1,0);
   else
   end
end

%-----Append missing time steps-----%

timevec_new=(timevec(1):datenum(0,0,0,0,0,1):timevec(end))';
time_new=NaN(length(timevec_new),1);
twods_Nt_new=NaN(length(timevec_new),1);
twods_Nd_new=NaN(length(timevec_new),length(bin_mid));
count_new=NaN(length(timevec_new),length(bin_mid));
mean_area_ratio_new=NaN(length(timevec_new),length(bin_mid));
reject_ratio_new=NaN(length(timevec_new),1);
conc_darea_new=NaN(length(timevec_new),length(bin_mid));
```

```
%-----Sync data to appended indices-----%
for k=1:length(timevec);
   index(k)=find(abs(timevec_new-timevec(k))<datenum(0,0,0,0,0,0.3));
   time_new(index(k))=time(k);
   twods_Nt_new(index(k))=twods_Nt(k);
   twods_Nd_new(index(k),:)=twods_Nd(k,:);
   count_new(index(k),:)=count(k,:);
   mean_area_ratio_new(index(k),:)=mean_area_ratio(k,:);
   reject_ratio_new(index(k))=reject_ratio(k);
   conc_darea_new(index(k),:)=conc_darea(k,:);
   for j=1000:1000:length(timevec);
      if k==j;
   fprintf('%d of %d time steps combined. \n',k, length(timevec));
      end
   end
end

%-----Sync with summary file [YY_MM_DD_HH_MM_SS.oracles]-----%

timevec_summary=datenum(2000,0,0,0,0,0)+datenum(str2double(summary(1:2)),str2double(summary(4:5)),...
   str2double(summary(7:8)),str2double(summary(10:11)),str2double(summary(13:14)),...
   str2double(summary(16:17)));

if timevec_new(1)>timevec_summary(1)==1;
x=timevec_summary:datenum(0,0,0,0,0,1):timevec_new(1)-datenum(0,0,0,0,0,1);
disp(['Sync with summary file: Adding ', num2str(length(x)), ' time steps at the top to combined file.'])

timevec=vertcat(x',timevec_new);
time=vertcat(NaN(length(x),1),time_new);
twods_Nt=vertcat(NaN(length(x),1),twods_Nt_new);
twods_Nd=vertcat(NaN(length(x),length(bin_mid)),twods_Nd_new);
count=vertcat(NaN(length(x),length(bin_mid)),count_new);
mean_area_ratio=vertcat(NaN(length(x),length(bin_mid)),mean_area_ratio_new);
reject_ratio=vertcat(NaN(length(x),1),reject_ratio_new);
conc_darea=vertcat(NaN(length(x),length(bin_mid)),conc_darea_new);

elseif timevec_new(1)>timevec_summary(1)==0;
y=int16((timevec_new(1)-timevec_summary(1))/datenum(0,0,0,0,0,1));
x=num2str(y);
disp(['Sync with summary file: Removing ',x, ' time steps at the top from combined file.'])

timevec_new(1:y,:)=[];timevec=timevec_new;
time_new(1:y,:)=[];time=time_new;
twods_Nt_new(1:y,:)=[];twods_Nt=twods_Nt_new;
twods_Nd_new(1:y,:)=[];twods_Nd=twods_Nd_new;
count_new(1:y,:)=[];count=count_new;
mean_area_ratio_new(1:y,:)=[];mean_area_ratio=mean_area_ratio_new;
reject_ratio_new(1:y,:)=[];reject_ratio=reject_ratio_new;
conc_darea_new(1:y,:)=[];conc_darea=conc_darea_new;
end

timevec_twods=timevec; clearvars timevec;
count_twods=count; clearvars count;
mean_area_ratio_twods=mean_area_ratio; clearvars mean_area_ratio;
reject_ratio_twods=reject_ratio; clearvars reject_ratio;
conc_darea_twods=conc_darea; clearvars conc_darea;
bin_dD_twods=bin_dD; clearvars bin_dD;
```

```
bin_min_twods=bin_min; clearvars bin_min;
bin_mid_twods=bin_mid; clearvars bin_mid;
bin_max_twods=bin_max; clearvars bin_max;

disp(['Saving ', num2str(length(timevec_twods)), ' time steps to the file.'])

%-----Create output file-----%
% outpath = path;
outpath = [pwd '/'];
outfile = sprintf('%sbase%s%s%s%s.combined.%s.2DS_2.cdf', outpath,...
   flightdate(3:8),summaryfile(1).name(10:11),summaryfile(1).name(13:14),summaryfile(1).name(16:17),orientation);

f = netcdf.create(outfile, 'clobber');

%-----Create dimensions and variables-----%
   dimid0 = netcdf.defDim(f,'time',length(timevec_twods));
   dimid1 = netcdf.defDim(f,'bin_count',size(bin_min_twods,1));
   dimid3 = netcdf.defDim(f,'files_stitched',size(infile,1));
   varid0 = netcdf.defVar(f,'Time Vector','double',dimid0);
   varid1 = netcdf.defVar(f,'Bin Minimum','double',dimid1);
   varid2 = netcdf.defVar(f,'Bin Maximum','double',dimid1);
   varid3 = netcdf.defVar(f,'Bin Midpoints','double',dimid1);
   varid4 = netcdf.defVar(f,'Bin Width','double',dimid1);
   varid5 = netcdf.defVar(f,'Mean Area Ratio','double',[dimid0 dimid1]);
   varid6 = netcdf.defVar(f,'Counts','double',[dimid0 dimid1]);
   varid7 = netcdf.defVar(f,'Size Distribution cm-3','double',[dimid0 dimid1]);
   varid8 = netcdf.defVar(f,'Number Concentration cm-3','double',dimid0);
   varid9 = netcdf.defVar(f,'Reject Ratio','double',dimid0);
   netcdf.endDef(f)

%-----Put variables into output file-----%
   netcdf.putVar ( f, varid0, timevec_twods );
   netcdf.putVar ( f, varid1, bin_min_twods );
   netcdf.putVar ( f, varid2, bin_max_twods );
   netcdf.putVar ( f, varid3, bin_mid_twods );
   netcdf.putVar ( f, varid4, bin_dD_twods );
   netcdf.putVar ( f, varid5, mean_area_ratio_twods );
   netcdf.putVar ( f, varid6, count_twods );
   netcdf.putVar ( f, varid7, twods_Nd );
   netcdf.putVar ( f, varid8, twods_Nt );
   netcdf.putVar ( f, varid9, reject_ratio_twods );
   netcdf.close(f);
```

INTARRANALYSIS_TIME.M

```
function IntArrAnalysis_time(campaign,filedate,filetime,startTime,endTime,fileNum,probeName,orientation)
%% Preamble
%  This script determines the inter-arrival time between peaks in a bimodal
%  distribution for each population of particles. Follows Field et al.
%  (2006) technique.
%
%  Original code by Wei Wu, Univ. Illinois.
%  Significant modifications by Joe Finlon, Univ. Illinois 2017.
%  Modified to run over defined time period, for combined PBP file - Siddhant Gupta
%  Modified for ORACLES - Siddhant Gupta
%
```

```
%     **************************
%     *** Modification Notes ***
%     **************************
%
% Usage:
%
%  infile : the particle-by-particle file containing inter-arrival times
%          directory: file path to save plots and threshold data
%          probeName : for handling SPEC probes (2DS & HVPS) differently
%          ianalysis: 1 to start inter-arrival analysis; 0 indicate only plotting
%  numparticles: population size belonging to each bimodal fit
%          dateString: yyyymmdd if not using parallel processing, otherwise
%     yyyymmdd_varargin format
%  fileNum: Number of files with bimodal fit
%          varargin: {n chunks to be processed in parallel}{optional input for nth
%     chunk to be processed} -- length(varargin)==1 means parallel
%     processing is ignored
%
%%%%%%%%%%%%%%%%%%%%%%%%%%%%%%%%%%%%%%%%%%%%%%%%%%%%%%%%%%%%%%%%%%%%%%%%%%%
%%%

%-----Inputs-----%
% campaign =   'oracles';
% filedate =   '20160908';
% filetime =   '064343';
% startTime=   '075000';
% endTime  =   '075500';
% fileNum  =   '5';
% probeName=   '2DS';
% orientation= 'H';

cd (sprintf('/condo/mcfarq/sid/b/%s/%s_%s/',campaign,campaign,filedate))
directory='';
directory_2='';
%directory=sprintf('/condo/mcfarq/sid/b/%s/%s_%s/',campaign,campaign,filedate);
%directory_2=sprintf('/condo/mcfarq/sid/b/%s/%s_%s/',campaign,campaign,filedate);

%file = dir(fullfile(directory,sprintf('base%s*.combined.%s_1.cdf', filedate(3:8),orientation)));
file = dir(fullfile(directory,sprintf('base%s%s.%s_1.cdf', filedate(3:8),filetime,orientation)));

infile = file(1).name;
ianalysis=1;
% % numparticles=ceil(length(intarr)/2);
% % numparticles=200;
dateString=filedate;
varargin=0;
%% Import file variables

disp(['File: ', infile])
% ncid=netcdf.open(infile,'nowrite');
ncid=netcdf.open(infile);

%%%%%
timehhmmss_full=netcdf.getVar(ncid,netcdf.inqVarID(ncid,'Time'));
startT=find(timehhmmss_full>=str2double(startTime));
endT=find(timehhmmss_full<=str2double(endTime));
timehhmmss=timehhmmss_full(startT(1):endT(end));
```

```
if strcmp(probeName,'2DS') || strcmp(probeName,'HVPS')
		tempTime_full=netcdf.getVar(ncid,netcdf.inqVarID(ncid,'Time_in_seconds'));
   tempTime = tempTime_full(startT(1):endT(end));
%    tempTime=time_in_seconds;
		intarr(1) = 0; % sets inter arrival time of first particle equal to 0
		intarr(2:length(tempTime)) = diff(tempTime); % subtract time between particles
		clear tempTime;
else
		intarr_full=netcdf.getVar(ncid,netcdf.inqVarID(ncid,'inter_arrival'));
   intarr=intarr_full(startT(1):endT(end));
end

% Read other particle variables

% timehhmmss=time;
% date=date;
date_full = netcdf.getVar(ncid, netcdf.inqVarID(ncid,'Date'));
date = date_full(startT(1):endT(end));
Dmax_full = netcdf.getVar(ncid, netcdf.inqVarID(ncid,'image_diam_minR')); % Joe Finlon
Dmax = Dmax_full(startT(1):endT(end));
% Dmax = image_diam_minR; % Joe Finlon
netcdf.close(ncid)
intarr(intarr<=0)=NaN;
int_arr=intarr;

numparticles=ceil(length(intarr)/str2double(fileNum));

% Trim infile variable if processing will take too long
if length(varargin)==2 % two arguments, # CPUs and the nth chunk to process
   nChunks = varargin{1}; % number of chunks being processed in parallel
   fileNum = varargin{2}; % nth chunk to be processed
   startInd = 1000000*ceil(length(intarr)/(nChunks*1000000))*(fileNum-1)+1;
   endInd = min(1000000*ceil(length(intarr)/(nChunks*1000000))*fileNum,length(int_arr));

   timehhmmss = timehhmmss(startInd:endInd);
   date = date(startInd:endInd);
   int_arr = int_arr(startInd:endInd);
end

if (ianalysis==0)
   return
end

%% Start analyzing if prompted

clear hist2dc NEWdate2dc NEWtime2dc
n=1;
int_arr(int_arr<0)=0;
int_arr(int_arr>0.1)=0;
bins = logspace(-7, 0, 35);		% Specify range of normalized frequency histogram
width = log(bins(2))-log(bins(1));

% Determine # particles to factor into bimodal fit
if numel(find(timehhmmss==mode(timehhmmss)))<numparticles
   num_particles = numparticles; % mininum # of particles to factor into fit
else % # of particles to factor into fit to nearest 25k
   num_particles = (numparticles/4)*...
      ceil(numel(find(timehhmmss==mode(timehhmmss)))/(numparticles/4));
```

```
end
disp(['  ', num2str(num_particles), ' particles will be factored into the bimodal distribution fit.'])

% Initialize bimodal fitting function
%bimodalfit = @(tau, dt) (dt/tau(1)).*exp(-dt/tau(1)); % Equation from Chapter 2+3 for bimodal fit
bimodalfit = @(tau, dt) (1-tau(3)).*(dt/tau(1)).*exp(-dt/tau(1))+(tau(3)).*(dt/tau(2)).*exp(-dt/tau(2));
tau_std=[1e-2 1e-6 0.5];

hist2dc = NaN(ceil(length(int_arr)/num_particles), length(bins)-1);
NEWtime2dc = NaN(1, ceil(length(int_arr)/num_particles));
NEWdate2dc = NaN(1, ceil(length(int_arr)/num_particles));

% Loop through sample populations and determine threshold
for i=1:num_particles:length(int_arr)
   disp(['  Current Progress: ', num2str(i), '/', num2str(length(int_arr)),...
      ' Time: ', datestr(now)])

            indicies = i:min([i+num_particles-1 length(int_arr)]);
            arr = int_arr(indicies);
            [h,~] = histcounts(arr, bins);
   binsCenter = bins(1:end-1)+diff(bins)/2;
   hist2dc(n,:) = h;
   NEWtime2dc(n) = timehhmmss(i);
   NEWdate2dc(n) = date(i);

   beta0 = [1e-2 1e-6 0.5]; % initial parameter guesses
   [tau_std] = abs(nlinfit(binsCenter,h./sum(h)./width,bimodalfit,beta0,...
      statset('Robust', 'on', 'FunValCheck', 'off', 'MaxIter', 1000)));

   if sum(isnan(tau_std))>0 % bimodal fit still isn't achieved (nlinfit returns NaN) -- added by Joe Finlon
      threshhold(i:min([i+num_particles-1 length(int_arr)])) = 1.3494e-6; % use a default inter-arrival time
   else
      threshhold(i:min([i+num_particles-1 length(int_arr)]))=min(tau_std(1:2))*2;
   end

   for j=i:min([i+num_particles-1 length(int_arr)])
     tau_all(j,:)=tau_std;
   end

   dt = binsCenter;
   tau = tau_std;
   hfit = (1-tau(3)).*(dt/tau(1)).*exp(-dt/tau(1))+(tau(3)).*(dt/tau(2)).*exp(-dt/tau(2));

   % Determine thresholds using 3 different techniques
   tau1 = max(tau_std(1:2)); tau2 = min(tau_std(1:2));
   newDT = dt(dt<tau1 & dt >tau2);

   if isempty(newDT) %% JOE FINLON
      newDT = dt([find(dt<tau1 , 1, 'last'), find(dt>tau2, 1, 'first')]);
      [minFit, indexFit] = min( hfit([find(dt<tau1 , 1, 'last'), find(dt>tau2, 1, 'first')]) );
      [minOriginal, indexOriginal] = min( h([find(dt<tau1 , 1, 'last'), find(dt>tau2, 1, 'first')]) );
   else
      [minFit, indexFit] = min( hfit(dt <tau1 & dt >tau2 ) );
      [minOriginal, indexOriginal] = min( h(dt<tau1 & dt >tau2 ) );
   end

   if isempty(newDT) % bimodal fit isn't achieved (nlinfit returns NaN) -- added by Joe Finlon
      disp(['Trouble obtaining a bimodal fit for index ', num2str(i),...
```

```
        '. Setting inter-arrival thresholds to a default value.'])
      threshhold_ww(i:min([i+num_particles-1 length(int_arr)])) = 1.3494e-6; % use a default inter-arrival time
      threshhold_ak(i:min([i+num_particles-1 length(int_arr)])) = 1.3494e-6; % use a default inter-arrival time
    else
      threshhold_ww(i:min([i+num_particles-1 length(int_arr)]))=newDT(indexFit);
      threshhold_ak(i:min([i+num_particles-1 length(int_arr)]))=newDT(indexOriginal);
    end

    % Optionally plot inter-arrival information for current population
    if sum(isnan(tau_std))==0
     figure('visible','off'); set(gcf, 'color', 'w');
     bar(bins(1:end-1), h ./ sum(h) ./ width, 'histc'); hold on;
     plot(dt, hfit, 'k');
     plot(ones(1,length(0:0.01:0.3))*(tau2),0:0.01:0.3,'--k'); % tau2
     plot(ones(1,length(0:0.01:0.3))*(tau1),0:0.01:0.3,'-.k'); % tau1
     plot(ones(1,length(0:0.01:0.3))*(min(tau_std(1:2))*2),0:0.01:0.3,'g'); % threshold
     plot(ones(1,length(0:0.01:0.3))*(newDT(indexFit)),0:0.01:0.3,'b'); % threshold_ww
     plot(ones(1,length(0:0.01:0.3))*(newDT(indexOriginal)),0:0.01:0.3,'r'); % threshold_ak

     ylim([0 0.5]); set(gca, 'xscale', 'log'); set(gca, 'xminortick', 'on');
     %set(gca,'FontSize',16); set(findall(gcf,'type','text'),'FontSize',16);
     title(['Inter-arrival Distribution (', num2str(NEWtime2dc(n)), ' UTC)']);
     xlabel('Inter-arrival Time (s)'); ylabel('Frequency');
     legend({'frequency', 'bin endpoint', 'fit', 'lower peak', 'higher peak',...
        '2*(lower peak)', 'freq. min between peaks from fit', 'freq. min between peaks in hist'},...
        'FontSize', 6, 'Location', 'northwest');
     print([directory_2, probeName, '_IntArrHistogram_', num2str(NEWtime2dc(n)), '.',...
        dateString, '.jpg'],'-djpeg','-r300')
    end

    n=n+1;
end

%% Plotting Routines

bins = logspace(-7, 0, 70);
binsCenter = bins(1:end-1)+diff(bins)/2;

disp(['  ', num2str(num_particles), ' paricles are factored into the contour plot for each time interval.'])
n=1;
for i=1:num_particles:length(int_arr)
          indicies = i:min([i+num_particles-1 length(int_arr)]);
          arr = int_arr(indicies);
          [h,~] = histcounts(arr, bins);
    binsCenter = bins(1:end-1)+diff(bins)/2;
    hist2dc_contour(n,:) = h;
    NEWtime2dc(n) = timehhmmss(i);
    NEWdate2dc(n) = date(i);
    n=n+1;
end
NEWtime2dc(n-1) = timehhmmss(length(int_arr)); % fix end time for contour plot
NEWdate2dc(n-1) = date(length(int_arr)); % fix end date for contour plot

cd /home/sid/b

histsum = sum(hist2dc_contour,2);
histsum = repmat(histsum,1,69);
% time = time2datenum(date,timehhmmss);
```

```
y=num2str(timehhmmss);
for k=1:length(timehhmmss);
if timehhmmss(k)<100000;
time(k)=time2datenum(date(k))+datenum(0,0,0,str2double(y(k,1)),str2double(y(k,2:3)),str2double(y(k,4:5)));
else
time(k)=time2datenum(date(k))+datenum(0,0,0,str2double(y(k,1:2)),str2double(y(k,3:4)),str2double(y(k,5:6)));
end
end
% % ======= Plot the inter-arrival time in dot scatter =======
% figure('visible','off'); set(gcf, 'color', 'w');
% n=1;
% plot(time(1:n:end),intarr(1:n:end),'.','markersize', 0.5);

% ======= Plot the inter-arrival time as a contoured distribution =======
figure('visible','off'); set(gcf, 'color', 'w');
y=num2str(NEWtime2dc');
for k=1:length(NEWtime2dc);
if NEWtime2dc(1,k)<100000;
   if size(y,2)==5
x(k,1)=time2datenum(NEWdate2dc(k))+datenum(0,0,0,str2double(y(k,1)),str2double(y(k,2:3)),str2double(y(k,4:5)));
   elseif size(y,2)==6
x(k,1)=time2datenum(NEWdate2dc(k))+datenum(0,0,0,str2double(y(k,2)),str2double(y(k,3:4)),str2double(y(k,5:6)));
   end
else
x(k,1)=time2datenum(NEWdate2dc(k))+datenum(0,0,0,str2double(y(k,1:2)),str2double(y(k,3:4)),str2double(y(k,5:6)));
end
end
% contourf(time2datenum(NEWdate2dc',NEWtime2dc'),binsCenter,(hist2dc_contour./histsum)',...
contourf(x,binsCenter,(hist2dc_contour./histsum)',...
   0.005:0.005:0.1,'LineColor','none');
%
contourf(time2datenum(NEWdate2dc')+datenum(0,0,0,str2double(NEWtime2dc(1:2)),str2double(NEWtime2dc(3:4)),str2doubl
e(NEWtime2dc(5:6))),binsCenter,(hist2dc_contour./histsum)',...

% contourf(datenum(NEWdate2dc', NEWtime2dc'),binsCenter,(hist2dc_contour./histsum)',...
colormap(jet); colorbar; hold on;
n=1;
plot(time(1:n:length(time)),threshhold(1:n:end),'g','LineWidth',2);
plot(time(1:n:length(time)),threshhold_ww(1:n:end),'b','LineWidth',2);
plot(time(1:n:length(time)),threshhold_ak(1:n:end),'r','LineWidth',2);

ylim([1e-7, 1]); set(gca,'yscale','log'); datetick('x','HH:MM');
title(sprintf('Inter-arrival Time Frequency for %s',dateString));
xlabel('Time'); ylabel('Inter-arrival Time [sec]');
legend({'frequency', '2*lower peak', 'freq. min between peaks from fit',...
   'freq. min between peaks in hist'}, 'FontSize', 6, 'Location', 'northwest');
% set(gca,'FontSize',16); set(findall(gcf,'type','text'),'FontSize',16);

cd (sprintf('/condo/mcfarq/sid/b/%s/%s_%s/',campaign,campaign,filedate))
% savefig([directory, probeName, 'IntArrAnalysis.', dateString, '.fig'])
print([directory_2, probeName, '_IntArrAnalysis.', dateString,filetime, '_', startTime, '_', endTime, '.jpg'],'-djpeg','-r300')

% ======= Box plot of inter-arrival times by size =======
switch probeName
   case '2DS'
dD = 0.01; % bin width for size categories to partition inter-arrival times [mm]
binsMid = 0.05:dD:1.3; % particle size categories to partition inter-arrival times [mm]
   case 'HVPS'
```

```
dD = 0.15; % bin width for size categories to partition inter-arrival times [mm]
binsMid = 0.15:dD:10; % particle size categories to partition inter-arrival times [mm]
end

intArr_copy = int_arr; % copy inter-arrival times for plotting
intArr_sizes = NaN(1, length(int_arr)); % allocate size category for
for iter=1:length(binsMid)
   intArr_sizes(find((Dmax>=binsMid(iter)-dD/2) & (Dmax<binsMid(iter)+dD/2))) = binsMid(iter);
end

intArr_copy(find(isnan(intArr_sizes))) = []; % ignore particles outside of size range
intArr_sizes(find(isnan(intArr_sizes))) = []; % ignore particles outside of size range

figure('visible','off'); set(gcf, 'color', 'w');
intArr_round = NaN(1,ceil(length(int_arr)/num_particles)); % dummy inter-arrival for box plot grouping
for i=1:num_particles:length(int_arr)
   intArr_round(i) = 1000*(ceil(Dmax(i)*10)/10 - 0.05); % round to mid-point of 100 um bin incriments [e.g. 50,150,250]
end

boxplot(intArr_copy, 1000*intArr_sizes, 'PlotStyle',  'compact');
ylim([1e-7 1]); set(gca,'YScale','log');
title(sprintf('Inter-arrival Time by Size for %s',dateString));
xlabel('Size Bin Midpoint (\mum)'); ylabel('Inter-arrival Time [sec]');

% savefig([directory, probeName, 'IntArrSizes.', dateString, '.fig'])
print([directory_2, probeName, '_IntArrSizes.', dateString, filetime, '_', startTime, '_', endTime, '.jpg'],'-djpeg','-r300')

%% Save the Data

fprintf('Now writing ouput to file: %s\n\n', datestr(now));

% Save all variables to Matlab datafile
save([directory_2, probeName, '_IntArrAnalysis.', dateString, '_', startTime, '_', endTime, '.mat'])

% Save only threshold information for sizeDist.m script (may need manual
% intervention if fitting technique is not robust
% f = netcdf.create([directory_2,probeName '_intArrThreshold_', dateString, '_', startTime, '_', endTime, '.cdf'], 'clobber');
f = netcdf.create([directory_2,probeName '_intArrThreshold_', infile], 'clobber');

dimid0 = netcdf.defDim(f,'particleTime',length(time));

NC_GLOBAL = netcdf.getConstant('NC_GLOBAL');
netcdf.putAtt(f, NC_GLOBAL, 'Software', 'UIOOPS/IntArrAnalysis_revised');
netcdf.putAtt(f, NC_GLOBAL, 'Institution', 'Univ. Oklahoma, SoM');
netcdf.putAtt(f, NC_GLOBAL, 'Creation Time', datestr(now, 'yyyy/mm/dd HH:MM:SS'));
netcdf.putAtt(f, NC_GLOBAL, 'Description', ['Contains inter-arrival threshold ',...
   'information for each particle following Field et al. (2006)']);
netcdf.putAtt(f, NC_GLOBAL, 'Flight Date', dateString)
netcdf.putAtt(f, NC_GLOBAL, 'Data Source', infile);
netcdf.putAtt(f, NC_GLOBAL, 'Probe Type', probeName);
netcdf.putAtt(f, NC_GLOBAL, 'Population Size', [num2str(num_particles),...
   ' particles per distribution fit']);

varid0 = netcdf.defVar(f,'particle_time','double',dimid0);
netcdf.putAtt(f, varid0,'units','HHMMSS');
netcdf.putAtt(f, varid0,'name','Time');

varid1 = netcdf.defVar(f,'threshold','double',dimid0);
```

```
netcdf.putAtt(f, varid1,'units','sec');
netcdf.putAtt(f, varid1,'name','Inter-arrival time threshold in n-particle blocks');

netcdf.endDef(f)

netcdf.putVar ( f, varid0, timehhmmss );
netcdf.putVar ( f, varid1, threshhold_ak );

netcdf.close(f) % Close output NETCDF file

disp('Finished determining inter-arrival time thresholds!')
% end

% function [dateValue] = time2datenum(date, timehhmmss)
%
%       secFromMidnight     =     floor(timehhmmss/10000)*3600     +     floor(mod(timehhmmss,10000)/100)*60     +
floor(mod(timehhmmss,100));
% dateVector = [floor(date/10000), floor(mod(date,10000)/100), floor(mod(date,100)) , zeros(length(date),1),...
%    zeros(length(date),1), secFromMidnight];
% dateValue = datenum(dateVector);
%
cd /home/sid/b
end
```

INTARR_TIME.M

```
%-----Call Inter-arrival analysis function for a defined time period-----%
%-----Requires the Combined PBP file (combined.H_1.cdf) to be in the same directory-----%
%-----Written by Siddhant Gupta - 10/26/2017-----%

campaign =   'oracles';            % Name of Campaign
filedate =   '20170818';           % Flight date
filetime =   '150513';             % Flight time
startTime=   '150000';             % Start time for analysis
endTime  =   '173000';             % End time for analysis
fileNum  =   '5';                  % Number of histograms required
probeName=   'HVPS';               % Required for SPEC probes (2DS, HVPS)
orientation= 'V';                  % Required for 2DS

IntArrAnalysis_time(campaign,filedate,filetime,startTime,endTime,fileNum,probeName,orientation);
```

FIND_SHADOW_DIODES.M

```
function find_shadow_diodes(date,time,orientation)
%%%%%%%%%%%%%%%%%%%%%%%%%%%%%%%%%%%%%%%%%%%%%%%%%%%%%%%%%%%%%%%%%%%
%-----Plot illumination/shadow count for diodes from particle by particle image file-----%
%-----Identify diodes with <80% of max count and output them in .mat file-----%
%-----Written by Siddhant Gupta - 10/31/2017-----%
%
%-----MODIFIED: If high counts (20% greater than mean) found from diodes masked
%           in-flight, replace counts with mean from other diodes and
%           mask the diodes with <80% of mean count - 06/20/2018-----%
%
% Input:
%    Date: 'YYMMDD' - Flight date
%    Time: 'HHMMSS' - Start time
```

```
%     Particle-by-particle image file: 'baseYYMMDDHHMMSS.H_1.cdf'
%     IMPORTANT: This script uses 'bin_stats' (# times specified photodiode
%     is shadowed for particles in file).
%
% Output:
%     Figure: Illumination/shadow counts for each diode, with mean count line
%     - diodeYYMMDDHHMMSS.counts.jpeg
%     Figure: If high counts present, new figure with replaced counts
%     - diodeYYMMDDHHMMSS.counts_high.jpeg
%     Mat file with diode # for diodes having <80% of max count
%     Diode # are stored within "shadow_diode" in:
%     diodeYYMMDDHHMMSS.H.mat
%%%%%%%%%%%%%%%%%%%%%%%%%%%%%%%%%%%%%%%%%%%%%%%%%%%%%%%%%%%%%%%%%%%
%%
campaign='oracles';
% path = [pwd '/'];
path=sprintf('/condo/mcfarq/sid/b/%s/%s_20%s/',campaign,campaign,date);

% clear all
% date='170812';
% time='123215';
% % orientation='H';
% orientation='V';
% path = [pwd '/'];

infile=[path 'base' date time '.' orientation '_1.cdf'];
a=ncread(infile,'bin_stats');

%-----Plot Illumination counts for diodes-----%
hold on
g=plot(a);
grid minor
h=line('XData',1:length(a),'YData',ones(length(a),1)*mean(a));
set(g,'LineWidth',5);
set(g,'Marker','x');
set(g,'MarkerSize',10);
set(h,'LineWidth',5);

xlabel('Diode #','FontSize',40);
ylabel('Illumination count','FontSize',40);
ylim([0 1.5*nanmean(a)]);
set(gca,'fontsize',40);
legend(sprintf('File: 20%s-%s-%s',date,time,orientation));

%-----Save figure-----%
fig=gcf;
set(gcf,'PaperUnits','centimeters','PaperPosition',[0 0 60 40])
saveas(gcf,[path sprintf('diode.%s%s.%s_2.counts',date,time,orientation) '.jpeg']);
close all
%% %-----Replace high values (20% greater than mean) from diodes masked in-flight-----%

ill_diode=find(a>1.2*mean(a));
if ~isempty(ill_diode)==1;
a(ill_diode)=NaN;
a(ill_diode)=nanmean(a);

%-----Plot Illumination counts for diodes-----%
hold on
```

```
g=plot(a);
grid minor
h=line('XData',1:length(a),'YData',ones(length(a),1)*mean(a));
set(g,'LineWidth',5);
set(g,'Marker','x');
set(g,'MarkerSize',10);
set(h,'LineWidth',5);

xlabel('Diode #','FontSize',40);
ylabel('Illumination count','FontSize',40);
ylim([0 1.5*nanmean(a)]);
set(gca,'fontsize',40);
legend(sprintf('File: 20%s-%s-%s',date,time,orientation));

%-----Save figure-----%
fig=gcf;
set(gcf,'PaperUnits','centimeters','PaperPosition',[0 0 60 40])
saveas(gcf,[path sprintf('diode.%s%s.%s.counts',date,time,orientation) '_highs.jpeg']);
close all

   diode=find(a<0.80*mean(a));
   shadow_diode=sort(diode);
else
   diode=find(a<0.80*max(a));
   shadow_diode=sort(diode);
end
%%
clearvars -except path orientation shadow_diode date time a
%save(sprintf('diode.%s%s.%s.mat',date,time,orientation));
if isempty(shadow_diode)==0;
save([path sprintf('diode.%s%s.%s.mat',date,time,orientation)]);
elseif isempty(shadow_diode)==1;
save([path sprintf('diode.%s%s.%sempty.mat',date,time,orientation)]);
end
end
```

IMGPROC_SM.M

```
function imgProc_sm(infile, outfile, probename, n, nEvery, projectname,path,flight,file)
%%%%%%%%%%%%%%%%%%%%%%%%%%%%%%%%%%%%%%%%%%%%%%%%%%%%%%%%%%%%%%%%%%%%%%%%%%%%
%%%
%  This function is the image processing part of OAP processing using
%  distributed memory parallisation. The function use one simple interface
%  for all probes.
%
%  Interface:
%    infile   :   The input file name
%    outfile  :   The output file name
%    probetype:   One of the following: '2DC','2DP','CIP','PIP','HVPS' and '2DS'
%    n        :   The nth chuck to be processed.
%    nEvery   :   The individual chuck size. nChuck*nEvery shoudl equal the
%                 total frame number
%    projectname: The name of project so that you can write the specific
%                 code for you data
%
%  Note other important variables used in the program
%    handles:  a structure to store information. It is convinient to use a
```

```
%        struture to store the global information rather than using
%        various varibles
%
%  Update Dates:
%   * Initially Written by Will Wu, 06/24/2013
%        imgprocdm(File,probetype,n)
%   * Updated by Will Wu, 10/11/2013
%        New function interface
%        imgprocdm(infile,outfile,probetype,n, nEvery) and updated documentation.
%        This version is a major update to include all probes and simplify
%        the function interface significantly
%   * Updated by Will Wu, 07/10/2013
%        New function interface imgProc_dm(infile,outfile,probetype,n, nEvery)
%        Output perimeter, rectangle length/width/angle and eclispe
%        length/width/angle
%   * Added by Wei Wu, May 11, 2016
%        Add the project specific code with projectname in the following format:
%          if strcmp(projectname, 'PECAN')  % For example for PECAN dataset
%            ...
%          end
%   * Updated by Will Wu, 07/11/2016
%        New function name with the option to turn CGAL on and off for
%        speed
%%%%%%%%%%%%%%%%%%%%%%%%%%%%%%%%%%%%%%%%%%%%%%%%%%%%%%%%%%%%%%%%%%%%%%%%%%%%%%
%%%

%% Setting probe information according to probe type
%   use ProbeType to indicate three type of probes:
%     0: 2DC/2DP, 32 doides, boundary 85,
%     1: CIP/PIP, 64 doides, boundary 170
%     2: HVPS/2DS, 128 doides, boundary 170


iRectEllipse = 0;  % Set defualt to no Rectangle fit and Ellipse fit
switch probename
   case '2DC'
      boundary=[255 255 255 255];
      boundarytime=85;

      ds = 0.025;                             % Size of diode in millimeters
      handles.diodesize = ds;
      handles.diodenum  = 32;  % Diode number
      handles.current_image = 1;
      probetype=0;

   case '2DP'
      boundary=[255 255 255 255];
      boundarytime=85;

      ds = 0.200;                             % Size of diode in millimeters
      handles.diodesize = ds;
      handles.diodenum  = 32;  % Diode number
      handles.current_image = 1;
      probetype=0;

   case 'CIP'
      boundary=[170, 170, 170, 170, 170, 170, 170, 170];
      boundarytime=NaN;
```

```
        ds = 0.025;                          % Size of diode in millimeters
        handles.diodesize = ds;
        handles.diodenum  = 64;  % Diode number
        handles.current_image = 1;
        probetype=1;

    case 'PIP'
        boundary=[170, 170, 170, 170, 170, 170, 170, 170];
        boundarytime=NaN;

        ds = 0.100;                          % Size of diode in millimeters
        handles.diodesize = ds;
        handles.diodenum  = 64;  % Diode number
        handles.current_image = 1;
        probetype=1;

    case 'HVPS'
        boundary=[43690, 43690, 43690, 43690, 43690, 43690, 43690, 43690];
        boundarytime=0;

        ds = 0.150;                          % Size of diode in millimeters
        handles.diodesize = ds;
        handles.diodenum  = 128; % Diode number
        handles.current_image = 1;
        probetype=2;

    case '2DS'
        boundary=[43690, 43690, 43690, 43690, 43690, 43690, 43690, 43690];
        boundarytime=0;

        ds = 0.010;                          % Size of diode in millimeters
        handles.diodesize = ds;
        handles.diodenum  = 128; % Diode number
        handles.current_image = 1;
        probetype=2;
end

diodenum = handles.diodenum;
byteperslice = diodenum/8;
handles.disagree = 0;

%% Read the particle image files
handles.f = netcdf.open(infile,'nowrite');
[~, dimlen] = netcdf.inqDim(handles.f,2);
[~, handles.img_count] = netcdf.inqDim(handles.f,0);
size_mat = dimlen;
warning off all
diode_stats = zeros(1,diodenum);

if strcmp(projectname, 'PECAN')  % For example for PECAN dataset
    disp('Testing...')  %% Add project specific code if you like
end
%% Create output NETCDF file and variables
f = netcdf.create(outfile, 'clobber');
dimid0 = netcdf.defDim(f,'time',netcdf.getConstant('NC_UNLIMITED'));
dimid1 = netcdf.defDim(f,'pos_count',2);
dimid2 = netcdf.defDim(f,'bin_count',diodenum);
```

```
varid1 = netcdf.defVar(f,'Date','double',dimid0);
varid0  = netcdf.defVar(f,'Time','double',dimid0);
varid2  = netcdf.defVar(f,'msec','double',dimid0);
varid101  = netcdf.defVar(f,'Time_in_seconds','double',dimid0);

varid102  = netcdf.defVar(f,'SliceCount','double',dimid0);
varid103  = netcdf.defVar(f,'DMT_DOF_SPEC_OVERLOAD','double',dimid0);
varid104  = netcdf.defVar(f,'Particle_number_all','double',dimid0);

%varid3 = netcdf.defVar(f,'wkday','double',dimid0);
varid4  = netcdf.defVar(f,'position','double',[dimid1 dimid0]);
varid5  = netcdf.defVar(f,'particle_time','double',dimid0);
varid6  = netcdf.defVar(f,'particle_millisec','double',dimid0);
varid7  = netcdf.defVar(f,'particle_microsec','double',dimid0);
varid8  = netcdf.defVar(f,'parent_rec_num','double',dimid0);
varid9  = netcdf.defVar(f,'particle_num','double',dimid0);
varid10 = netcdf.defVar(f,'image_length','double',dimid0);
varid11 = netcdf.defVar(f,'image_width','double',dimid0);
varid12 = netcdf.defVar(f,'image_area','double',dimid0);
varid13 = netcdf.defVar(f,'image_longest_y','double',dimid0);
varid14 = netcdf.defVar(f,'image_max_top_edge_touching','double',dimid0);
varid15 = netcdf.defVar(f,'image_max_bottom_edge_touching','double',dimid0);
varid16 = netcdf.defVar(f,'image_touching_edge','double',dimid0);
varid17 = netcdf.defVar(f,'image_auto_reject','double',dimid0);
varid18 = netcdf.defVar(f,'image_hollow','double',dimid0);
varid19 = netcdf.defVar(f,'image_center_in','double',dimid0);
varid20 = netcdf.defVar(f,'image_axis_ratio','double',dimid0);
varid21 = netcdf.defVar(f,'image_diam_circle_fit','double',dimid0);
varid22 = netcdf.defVar(f,'image_diam_horiz_chord','double',dimid0);
varid23 = netcdf.defVar(f,'image_diam_horiz_chord_corr','double',dimid0);
varid24 = netcdf.defVar(f,'image_diam_following_bamex_code','double',dimid0);
varid25 = netcdf.defVar(f,'image_diam_vert_chord','double',dimid0);
varid26 = netcdf.defVar(f,'image_diam_minR','double',dimid0);
varid27 = netcdf.defVar(f,'image_diam_AreaR','double',dimid0);
varid45 = netcdf.defVar(f,'image_perimeter','double',dimid0);
if 1==iRectEllipse
   varid46 = netcdf.defVar(f,'image_RectangleL','double',dimid0);
   varid47 = netcdf.defVar(f,'image_RectangleW','double',dimid0);
   varid67 = netcdf.defVar(f,'image_RectangleAngle','double',dimid0);
   varid48 = netcdf.defVar(f,'image_EllipseL','double',dimid0);
   varid49 = netcdf.defVar(f,'image_EllipseW','double',dimid0);
   varid69 = netcdf.defVar(f,'image_EllipseAngle','double',dimid0);
end
varid28 = netcdf.defVar(f,'percent_shadow_area','double',dimid0);
varid29 = netcdf.defVar(f,'edge_at_max_hole','double',dimid0);
varid30 = netcdf.defVar(f,'max_hole_diameter','double',dimid0);
varid31 = netcdf.defVar(f,'part_z','double',dimid0);
varid32 = netcdf.defVar(f,'size_factor','double',dimid0);
varid33 = netcdf.defVar(f,'holroyd_habit','double',dimid0);
varid34 = netcdf.defVar(f,'area_hole_ratio','double',dimid0);
varid35 = netcdf.defVar(f,'inter_arrival','double',dimid0);
varid36 = netcdf.defVar(f,'bin_stats','double',dimid2);
netcdf.endDef(f)

%% Variables initialization
kk=1;
w=-1;
```

```
wstart = 0;

time_offset_hr = 0;
time_offset_mn = 0;
time_offset_sec = 0;
time_offset_ms = 0;
timeset_flag = 0;



%% Processing nth chuck. Every chuck is nEvery frames
%% Analyze each individual particle images and Output the particle by particle information
for i=((n-1)*nEvery+1):min(n*nEvery,handles.img_count) % Start on 1st frame for 1st chuck, nEvery+1 frame for 2nd chuck...

  handles.year     = netcdf.getVar(handles.f,netcdf.inqVarID(handles.f,'year'    ),i-1,1);
  handles.month    = netcdf.getVar(handles.f,netcdf.inqVarID(handles.f,'month'  ),i-1,1);
  handles.day      = netcdf.getVar(handles.f,netcdf.inqVarID(handles.f,'day'  ),i-1,1);
  handles.hour     = netcdf.getVar(handles.f,netcdf.inqVarID(handles.f,'hour'    ),i-1,1);
  handles.minute   = netcdf.getVar(handles.f,netcdf.inqVarID(handles.f,'minute'  ),i-1,1);
  handles.second   = netcdf.getVar(handles.f,netcdf.inqVarID(handles.f,'second'  ),i-1,1);
  handles.millisec = netcdf.getVar(handles.f,netcdf.inqVarID(handles.f,'millisec'),i-1,1);

  if mod(i,100) == 0
    [num2str(i),'/',num2str(handles.img_count), ', ',datestr(now)]
    % Display if diode unmasking is being done - Added by Siddhant Gupta
    if exist([path '/' 'diode.' flight file '.' infile(end-4) '.mat'],'file')==2;
      disp(['Diode unmasking done. See diode' flight file '.' infile(end-4) '.mat file for diode # unmasked']);
    else
    end
  end
  varid = netcdf.inqVarID(handles.f,'data');

  if probetype==0
    temp = netcdf.getVar(handles.f,varid,[0, 0, i-1], [4,1024,1]);
  else
    temp = netcdf.getVar(handles.f,varid,[0, 0, i-1], [8,1700,1]);
  end
  data(:,:) = temp';

  j=1;
  start=0;
  firstpart = 1;

  %c=[dec2bin(data(:,1),8),dec2bin(data(:,2),8),dec2bin(data(:,3),8),dec2bin(data(:,4),8)];
  while data(j,1) ~= -1 && j < size(data,1)
    % Calculate every particles
    if (isequal(data(j,:), boundary) && ( (isequal(data(j+1,1), boundarytime) || probetype==1) ) )
      if start ==0
        if 1 == probetype
          start = 2;
        elseif 0 == probetype
          start = 2;
        else
          start = 1;
        end
      end

        if probetype==0
```

```
        if start+1 > (j-1)  % Remove Corrupted Data
         break;
        end
      else
        if start > (j-1)  % Remove Corrupted Data
         break;
        end
      end

       header_loc = j+1;
       w=w+1;
       %% Create binary image according to probe type

       if probetype==0
          ind_matrix(1:j-start-1,:) = data(start+1:j-1,:);  % 2DC has 3 slices between particles (sync word timing word and end of
particle words)
          c=[dec2bin(ind_matrix(:,1),8),dec2bin(ind_matrix(:,2),8),dec2bin(ind_matrix(:,3),8),dec2bin(ind_matrix(:,4),8)];
       elseif probetype==1
          ind_matrix(1:j-start,:) = data(start:j-1,:);
          c=[dec2bin(ind_matrix(:,1),8), dec2bin(ind_matrix(:,2),8),dec2bin(ind_matrix(:,3),8),dec2bin(ind_matrix(:,4),8), ...
          dec2bin(ind_matrix(:,5),8), dec2bin(ind_matrix(:,6),8),dec2bin(ind_matrix(:,7),8),dec2bin(ind_matrix(:,8),8)];
       elseif probetype==2
          ind_matrix(1:j-start,:) = 65535 - data(start:j-1,:); % I used 1 to indicate the illuminated doides for HVPS
          c=[dec2bin(ind_matrix(:,1),16),   dec2bin(ind_matrix(:,2),16),dec2bin(ind_matrix(:,3),16),dec2bin(ind_matrix(:,4),16),
...
          dec2bin(ind_matrix(:,5),16), dec2bin(ind_matrix(:,6),16),dec2bin(ind_matrix(:,7),16),dec2bin(ind_matrix(:,8),16)];
       end

       % If diode.YYMMDDHHMMSS.H.mat file exists, unmask diodes numbered in 'shadow_diode' variable, added by Siddhant
Gupta
       if exist([path '/' 'diode.' flight file '.' infile(end-4) '.mat'],'file')==2;
       load([path '/' 'diode.' flight file '.' infile(end-4) '.mat'],'shadow_diode');
       c(:,shadow_diode)='1';
       else
       end

       % Just to test if there is bad images, usually 0 area images
       figsize = size(c);
       if figsize(2)~=diodenum
          disp('Not equal to diode number');
          return
       end


       images.position(kk,:) = [start, j-1];
       parent_rec_num(kk)=i;
       particle_num(kk) = mod(kk,66536); %hex2dec([dec2hex(data(start-1,7)),dec2hex(data(start-1,8))]);

       %  Get the particle time
       if probetype==0
          bin_convert = [dec2bin(data(header_loc,2),8),dec2bin(data(header_loc,3),8),dec2bin(data(header_loc,4),8)];
          part_time = bin2dec(bin_convert);       % Interarrival time in tas clock cycles
          tas2d = netcdf.getVar(handles.f,netcdf.inqVarID(handles.f,'tas'),i-1, 1);
          part_time = part_time/tas2d*handles.diodesize/(10^3);
          time_in_seconds(kk) = part_time;

          images.int_arrival(kk) = part_time;
```

```
    if(firstpart == 1)
      firstpart = 0;
      start_hour = handles.hour;
      start_minute = handles.minute;
      start_second = handles.second;
      start_msec = handles.millisec*10;
      % First, we get the hours....
      start_msec = start_msec;
      start_microsec = 0;
      time_offset_hr = 0;
      time_offset_mn = 0;
      time_offset_sec = 0;
      time_offset_ms = 0;

      part_hour(kk) = start_hour;
      part_min(kk) = start_minute;
      part_sec(kk) = start_second;
      part_mil(kk) = start_msec;
      part_micro(kk) = 0;
    else
      frac_time = part_time - floor(part_time);
      frac_time = frac_time * 1000;
      part_micro(kk) = part_micro(kk-1) + (frac_time - floor(frac_time))*1000;
      part_mil(kk) = part_mil(kk-1) + floor(frac_time);
      part_sec(kk) = part_sec(kk-1) + floor(part_time);
      part_min(kk) = part_min(kk-1);
      part_hour(kk) = part_hour(kk-1);
    end

    part_sec(part_mil >= 1000) = part_sec(part_mil >= 1000) + 1;
    part_mil(part_mil >= 1000) = part_mil(part_mil >= 1000) - 1000;

    part_min(part_sec >= 60) = part_min(part_sec >= 60) + 1;
    part_sec(part_sec >= 60) = part_sec(part_sec >= 60) - 60;

    part_hour(part_min >= 60) = part_hour(part_min >= 60) + 1;
    part_min(part_min >= 60) = part_min(part_min >= 60) - 60;
    part_hour(part_hour >= 24) = part_hour(part_hour >= 24) - 24;
  elseif probetype==1
    bin_convert = [dec2bin(data(start-1,2),8),dec2bin(data(start-1,3),8),dec2bin(data(start-1,4),8), ...
      dec2bin(data(start-1,5),8), dec2bin(data(start-1,6),8)];

    part_hour(kk) = bin2dec(bin_convert(1:5));
    part_min(kk) = bin2dec(bin_convert(6:11));
    part_sec(kk) = bin2dec(bin_convert(12:17));
    part_mil(kk) = bin2dec(bin_convert(18:27));
    part_micro(kk) = bin2dec(bin_convert(28:40))*125e-9;

    particle_sliceCount(kk)=bitand(data(start-1,1),127);
    particle_DOF(kk)=bitand(data(start-1,1),128);
    particle_partNum(kk)=bin2dec([dec2bin(data(start-1,7),8),dec2bin(data(start-1,8),8)]);

    time_in_seconds(kk) = part_hour(kk) * 3600 + part_min(kk) * 60 + part_sec(kk) + part_mil(kk)/1000 + part_micro(kk);
    if kk > 1
      images.int_arrival(kk) = time_in_seconds(kk) - time_in_seconds(kk-1);
    else
      images.int_arrival(kk) = time_in_seconds(kk);
    end
```

```
elseif probetype==2

   particle_DOF(kk)=bitand(data(header_loc,4), 32768);
   particle_partNum(kk)=double(data(header_loc,5));
   particle_sliceCount(kk)=double(data(header_loc,6));

   part_time = double(data(header_loc,7))*2^16+double(data(header_loc,8));      % Interarrival time in tas clock cycles
   part_micro(kk) = part_time;
   part_mil(kk)   = 0;
   part_sec(kk)   = 0;
   part_min(kk)   = 0;
   part_hour(kk)  = 0;
   time_in_seconds(kk) = part_time*(handles.diodesize/(10^3)/170);
   if(kk>1)
      images.int_arrival(kk) = part_time-part_micro(kk-1);
   else
      images.int_arrival(kk) = 0;
   end
end

temptimeinhhmmss = part_hour(kk) * 10000 + part_min(kk) * 100 + part_sec(kk);
%if (temptimeinhhmmss<200000 || temptimeinhhmmss>240000)
%    temptimeinhhmmss
%end

slices_ver = length(start:j-1);
rec_time(kk)=double(handles.hour)*10000+double(handles.minute)*100+double(handles.second);
rec_date(kk)=double(handles.year)*10000+double(handles.month)*100+double(handles.day);
rec_millisec(kk)=handles.millisec;
%               rec_wkday(kk)=handles.wkday(i);

%% Determine the Particle Habit
%  We use the Holroyd algorithm here
handles.bits_per_slice = diodenum;
diode_stats = diode_stats + sum(c=='1',1);
csum = sum(c=='1',1);

images.holroyd_habit(kk) = holroyd(handles,c);

%% Determine if the particle is rejected or not
%  Calculate the Particle Length, Width, Area, Auto Reject
%  Status And more... See calculate_reject_unified()
%  funtion for more information

[images.image_length(kk),images.image_width(kk),images.image_area(kk), ...

images.longest_y_within_a_slice(kk),images.max_top_edge_touching(kk),images.max_bottom_edge_touching(kk),...
   images.image_touching_edge(kk),
images.auto_reject(kk),images.is_hollow(kk),images.percent_shadow(kk),images.part_z(kk),...
   images.sf(kk),images.area_hole_ratio(kk),handles]=calculate_reject_unified(c,handles,images.holroyd_habit(kk));

images.max_hole_diameter(kk) = handles.max_hole_diameter;
images.edge_at_max_hole(kk) = handles.edge_at_max_hole;

max_horizontal_length = images.image_length(kk);
max_vertical_length = images.longest_y_within_a_slice(kk);
```

```
        image_area = images.image_area(kk);

        diode_size= handles.diodesize;
        corrected_horizontal_diode_size = handles.diodesize;
        largest_edge_touching  = max(images.max_top_edge_touching(kk), images.max_bottom_edge_touching(kk));
        smallest_edge_touching = min(images.max_top_edge_touching(kk), images.max_bottom_edge_touching(kk));

        %% Calculate more size deciptor using more advanced techniques
        %  See dropsize for more information

[images.center_in(kk),images.axis_ratio(kk),images.diam_circle_fit(kk),images.diam_horiz_chord(kk),images.diam_vert_chord(
kk),...
          images.diam_horiz_mean(kk),
images.diam_spheroid(kk)]=dropsize(max_horizontal_length,max_vertical_length,image_area...
          ,largest_edge_touching,smallest_edge_touching,diode_size,corrected_horizontal_diode_size, diodenum);

        %% Calculate size deciptor using bamex code
        %  See dropsize_new for more information
        %  images.diam_bamex(kk) = dropsize_new(c, largest_edge_touching, smallest_edge_touching, diodenum,
corrected_horizontal_diode_size, handles.diodesize, max_vertical_length);

        %% Using OpenCV C program to calculate length, width and radius. This
        %% Get diameter of the smallest-enclosing circle, rectangle and ellipse
        %images.minR(kk)=particlesize_cgal(c);
        images.minR(kk)=CGAL_minR(c);
        images.AreaR(kk)=2*sqrt(images.image_area(kk)/3.1415926);  % Calculate the Darea (area-equivalent diameter)
        images.Perimeter(kk)=ParticlePerimeter(c);

        if 1==iRectEllipse
          [images.RectangleL(kk), images.RectangleW(kk), images.RectangleAngle(kk)] = CGAL_RectSize(c);
          [images.EllipseL(kk), images.EllipseW(kk), images.EllipseAngle(kk)]     = CGAL_EllipseSize(c);
        end
        %% Get the area ratio using the DL=max(DT,DP), only observed area are used
        if images.image_length(kk) > images.image_width(kk)
          images.percent_shadow(kk) = images.image_area(kk) / (pi * images.image_length(kk).^ 2 / 4);
        elseif images.image_width(kk) ~= 0
          images.percent_shadow(kk) = images.image_area(kk) / (pi * images.image_width(kk).^ 2 / 4);
        else
          images.percent_shadow(kk) = 0;
        end

        start = j + 2;
        kk = kk + 1;
        clear c ind_matrix
      %end
    end

    j = j + 1;
  end

  %% Write out the processed information on NETCDF
  if kk > 1


    netcdf.putVar ( f, varid0, wstart, w-wstart+1, rec_time(:) );
    netcdf.putVar ( f, varid1, wstart, w-wstart+1, rec_date(:) );

    netcdf.putVar ( f, varid101, wstart, w-wstart+1, time_in_seconds(:) );
```

```
    netcdf.putVar ( f, varid102, wstart, w-wstart+1, particle_sliceCount );
    netcdf.putVar ( f, varid103, wstart, w-wstart+1, particle_DOF );
    netcdf.putVar ( f, varid104, wstart, w-wstart+1, particle_partNum );


    netcdf.putVar ( f, varid2, wstart, w-wstart+1, rec_millisec(:) );
    %netcdf.putVar ( f, varid3, wstart, w-wstart+1, rec_wkday(:) );
    netcdf.putVar ( f, varid4, [0 wstart], [2 w-wstart+1], images.position' );
    netcdf.putVar ( f, varid5, wstart, w-wstart+1, part_hour(:)*10000+part_min(:)*100+part_sec(:) );
    netcdf.putVar ( f, varid6, wstart, w-wstart+1, part_mil(:) );
    netcdf.putVar ( f, varid7, wstart, w-wstart+1, part_micro(:) );
    netcdf.putVar ( f, varid8, wstart, w-wstart+1, parent_rec_num );
    netcdf.putVar ( f, varid9, wstart, w-wstart+1, particle_num(:) );
    netcdf.putVar ( f, varid10, wstart, w-wstart+1, images.image_length);
    netcdf.putVar ( f, varid11, wstart, w-wstart+1, images.image_width);
    netcdf.putVar ( f, varid12, wstart, w-wstart+1, images.image_area*diode_size*diode_size);
    netcdf.putVar ( f, varid13, wstart, w-wstart+1, images.longest_y_within_a_slice);
    netcdf.putVar ( f, varid14, wstart, w-wstart+1, images.max_top_edge_touching);
    netcdf.putVar ( f, varid15, wstart, w-wstart+1, images.max_bottom_edge_touching);
    netcdf.putVar ( f, varid16, wstart, w-wstart+1, images.image_touching_edge-'0');
    netcdf.putVar ( f, varid17, wstart, w-wstart+1, double(images.auto_reject));
    netcdf.putVar ( f, varid18, wstart, w-wstart+1, images.is_hollow);
    netcdf.putVar ( f, varid19, wstart, w-wstart+1, images.center_in);
    netcdf.putVar ( f, varid20, wstart, w-wstart+1, images.axis_ratio);
    netcdf.putVar ( f, varid21, wstart, w-wstart+1, images.diam_circle_fit);
    netcdf.putVar ( f, varid22, wstart, w-wstart+1, images.diam_horiz_chord);
    netcdf.putVar ( f, varid23, wstart, w-wstart+1, images.diam_horiz_chord ./ images.sf);
    netcdf.putVar ( f, varid24, wstart, w-wstart+1, images.diam_horiz_mean);
    netcdf.putVar ( f, varid25, wstart, w-wstart+1, images.diam_vert_chord);
    netcdf.putVar ( f, varid26, wstart, w-wstart+1, images.minR*diode_size);
    netcdf.putVar ( f, varid27, wstart, w-wstart+1, images.AreaR*diode_size);
    netcdf.putVar ( f, varid45, wstart, w-wstart+1, images.Perimeter*diode_size);
    if 1==iRectEllipse
      netcdf.putVar ( f, varid46, wstart, w-wstart+1, images.RectangleL*diode_size);
      netcdf.putVar ( f, varid47, wstart, w-wstart+1, images.RectangleW*diode_size);
      netcdf.putVar ( f, varid67, wstart, w-wstart+1, images.RectangleAngle);
      netcdf.putVar ( f, varid48, wstart, w-wstart+1, images.EllipseL*diode_size);
      netcdf.putVar ( f, varid49, wstart, w-wstart+1, images.EllipseW*diode_size);
      netcdf.putVar ( f, varid69, wstart, w-wstart+1, images.EllipseAngle);
    end
    netcdf.putVar ( f, varid28, wstart, w-wstart+1, images.percent_shadow);
    netcdf.putVar ( f, varid29, wstart, w-wstart+1, images.max_hole_diameter);
    netcdf.putVar ( f, varid30, wstart, w-wstart+1, images.edge_at_max_hole);
    netcdf.putVar ( f, varid31, wstart, w-wstart+1, images.part_z);
    netcdf.putVar ( f, varid32, wstart, w-wstart+1, images.sf);
    netcdf.putVar ( f, varid33, wstart, w-wstart+1, double(images.holroyd_habit));
    netcdf.putVar ( f, varid34, wstart, w-wstart+1, images.area_hole_ratio);
    netcdf.putVar ( f, varid35, wstart, w-wstart+1, images.int_arrival);
    netcdf.putVar ( f, varid36, diode_stats );

    wstart = w+1;
    kk = 1;
    clear rec_time rec_date rec_millisec part_hour part_min part_sec part_mil part_micro parent_rec_num particle_num
images time_in_seconds particle_sliceCount particle_DOF particle_partNum

  end
  clear images
end
```

```
warning on all

netcdf.close(f);
end
```

SIZEDIST.M

```
%%%%%%%%%%%%%%%%%%%%%%%%%%%%%%%%%%%%%%%%%%%%%%%%%%%%%%%%%%%%%%%%%%%%%%%%%%%
%%%
% Derive the area and size distribution for entire-in particles
% Include the IWC calculation
% Include the effective radius
%       Created by Will Wu, 09/18/2013
%
%       **************************
%       *** Modification Notes ***
%       **************************
%       * Modified to use the new maximum size and derive both maximum size distribution
%   and area-equivalent size distribution.
%                       Will Wu, 10/26/2013
%       * Modified to calculate terminal velocity using Heymsfield and Westbrook (2010) method
%   and precipitation rate.
%                       Will Wu, 01/15/2014
%       * Modified to include mass size distribution with habit info.
%                       Will Wu, 02/09/2014
%       * Modified to include particle area using A-D relations.
%                       Will Wu, 02/14/2014
%       * Special Edition for Boston Cloud workshop.
%                       Wei Wu, 04/01/2014
%       * Gneralized as a new sorting function for all probes.
%                       Wei Wu, 07/25/2014
%       * Modified to allow the option to ingest/use interarrival time dynamic threshold
%                       Dan Stechman, 05/06/2016
%       * Added project and date specific capabilities (including spiral-dependent interarrival
%   thresholding). Also cleaned up code and improved efficiency in places.
%                       Dan Stechman, 06/03/2016
%       * Added shatter removal using array of interarrival time thresholds (either constant or varrying [e.g., different threshold
for
%       each spiral in PECAN project]). Also added experimental shatter reacceptance option to allow for potential diffraction
fringes
%   originally flagged as shattered to be reaccepted.
%                       Dan Stechman, 06/09/2016
%   * Expanded upon time-varying interarrival time thresholds and reacceptance of particles for GPM (GCPEx, OLYMPEX)
campaigns.
%   Also added option to save out information on interarrival times and sample volume.
%   Bug fix for calculation of 'n' and 'count' to un-normalize by binwidth.
%   Bug fix when syncing particle time with flight time.
%     Joe Finlon, 03/03/2017
%  * Added probe default settings for GCPEx campaign
%     Joe Finlon, 06/05/2017
%  * Added metadata for netCDF output & fixed handling of 2DC/2DP data.
%     Joe Finlon, 06/26/17
%
% Usage:
%   infile:   Input filename, string
%   outfile:     Output filename, string
%   tas:       True air speed, double array
```

```
%    timehhmmss:    Time in hhmmss format, double array
%    probename:     Should be one of 'HVPS', 'CIP', 'PIP', '2DC', '2DP', 'F2DC'
%    d_choice:      the definition of Dmax, should use 6 usually. [1-6]
%    SAmethod:      0: Center in; 1: Entire in; 2: With Correction
%    Pres:          1 second pressure data
%    Temp:          1 second temperature data
%    projectname:   Project name, string
%    ddate:         Date to be analyzed, string (YYYYMMDD)
%
%%%%%%%%%%%%%%%%%%%%%%%%%%%%%%%%%%%%%%%%%%%%%%%%%%%%%%%%%%%%%%%%%%%%%%
%%%
function sizeDist(infile, outfile, tas, timehhmmss, probename, d_choice, SAmethod, Pres, Temp, projectname, ddate, varargin)
iCreateBad = 0; % Default not to output bad particles PSDs and other info
iCreateAspectRatio = 0; % Default not to process aspect ratio info
iSaveIntArrSV = 1; % Default not to save inter-arrival and sample volume information
%% Interarrival threshold file specification
% Can be implemented if a time-dependent threshold is required - add 'varargin' to arguments in function header above

if length(varargin) == 1 % Added by Siddhant Gupta - 07/15/2020 to identify file with time-dependent inter-arrival thresholds
  if exist(varargin{1},'file')==2
        iaThreshFile = varargin{1};
        fprintf('Inter-arrival time file being used: %s \n',iaThreshFile)
  else
  iaThreshFile = 'NONE';
        fprintf('Inter-arrival time file being used: %s \n',iaThreshFile)
  end
elseif length(varargin)>1
        display('You have added too many inputs!')
        iaThreshFile = 'NONE';
end

%% Define input and output files and initialize time variable
f = netcdf.open(infile,'nowrite');
mainf = netcdf.create(outfile, 'clobber');

% Fix flight times if they span multiple days - Added by Joe Finlon -
% 03/03/17
timehhmmss(find(diff(timehhmmss)<0)+1:end)=...
  timehhmmss(find(diff(timehhmmss)<0)+1:end) + 240000;


% tas_char = num2str(timehhmmss); %Unused
tas_time = floor(timehhmmss/10000)*3600+floor(mod(timehhmmss,10000)/100)*60+floor(mod(timehhmmss,100));
% averaging_time = 1;

%% Project-, probe-, and date-specific information
switch projectname
  case 'PECAN'
                switch probename
      case 'CIP'
        num_diodes =64;
        diodesize = 0.025; % units of mm
        armdst=100.;
%         num_bins = 64;
%         kk=diodesize/2:diodesize:(num_bins+0.5)*diodesize;
        num_bins=19;
        kk=[50.0  100.0  150.0  200.0  250.0  300.0  350.0  400.0  475.0  550.0  625.0 ...
          700.0  800.0  900.0  1000.0  1200.0  1400.0  1600.0  1800.0  2000.0]/1000; %Array in microns - converted to mm
```

```
        probetype=1;
        tasMax=200; % Max airspeed that can be sampled without under-sampling (images would appear skewed)

                                applyIntArrThresh = 1;
                                    defaultIntArrThresh = 1e-5;
                                reaccptShatrs = 1;
                                    reaccptD = 0.5; % Diammeter (in mm) to reaccept if initially flagged as shattered
                                    reaccptMaxIA = 2.5e-7;      % Max interarrival time in seconds a particle can
have to be reaccepted if
                                                                                    % size criteria are
met. Possible definition of this is the time of one slice, so in
                                                                                    % this case, with an
airspeed of ~100 m/s and a slice of 25 um, this would be 2.5e-7.


                                % Get start and end times (in seconds) of spirals; interarrival time thresholds for each
spiral
                                [startT, endT, ~, ~, intar_threshold_spirals] = getPECANparams(ddate, probename);

                                intar_threshold = ones(size(tas_time))*defaultIntArrThresh;
                                for ix = 1:length(tas_time)
                                    for iz = 1:length(startT)
                                        if (tas_time(ix) >= startT(iz) && tas_time(ix) < endT(iz))
                                            intar_threshold(ix) = intar_threshold_spirals(iz);
                                        end
                                    end
                                end

       case 'PIP'
        num_diodes =64;
        diodesize = 0.1; %units of mm
        armdst=260.;
        num_bins = 64;
%          kk=diodesize/2:diodesize:(num_bins+0.5)*diodesize;
        kk=diodesize/2:diodesize:(num_bins+0.6)*diodesize;
%          num_bins=19;
%          kk=[50.0  100.0  150.0  200.0  250.0  300.0  350.0  400.0  475.0  550.0  625.0 ...
%            700.0  800.0  900.0  1000.0  1200.0  1400.0  1600.0  1800.0  2000.0]*4/1000;
        probetype=1;
        tasMax=200;

                                applyIntArrThresh = 1;
                                    defaultIntArrThresh = 1e-5;
                                reaccptShatrs = 1;
                                    reaccptD = 0.5; % Diammeter (in mm) to reaccept if initially flagged as shattered
                                    reaccptMaxIA = 1e-6; % (Slice size [m])/(avg. airspeed [m/s])

                                % Get start and end times (in seconds) of spirals; interarrival time thresholds for each
spiral
                                [startT, endT, ~, ~, intar_threshold_spirals] = getPECANparams(ddate, probename);

                                intar_threshold = ones(size(tas_time))*defaultIntArrThresh;
                                for ix = 1:length(tas_time)
                                    for iz = 1:length(startT)
                                        if (tas_time(ix) >= startT(iz) && tas_time(ix) < endT(iz))
                                            intar_threshold(ix) = intar_threshold_spirals(iz);
                                        end
                                    end
```

```
                                end
    end

  case 'GPM'
    switch probename
      case '2DS'
        num_diodes =128;
        diodesize = .010;
        armdst=63.;
        num_bins =22;
        kk=[40.0   60.0   80.0   100.0   125.0   150.0   200.0   250.0   300.0   350.0   400.0 ...
          475.0   550.0   625.0   700.0   800.0   900.0   1000.0   1200.0   1400.0   1600.0   1800.0   2000.0]/1000;
        probetype=2;
        tasMax=170;

        % Interarrival threshold and reaccept max interarrival time are often flight-/instrument-specific
                                % **Values here may not be correct**
                                % The interarrival threshold can be modifided to change second-by-second if desired
        applyIntArrThresh = 1;
                                        defaultIntArrThresh = 1e-6;
                                reaccptShatrs = 1;
                                        reaccptD = 0.5;
          %reaccptMaxIA = 1e-7; % (Slice size [m])/(avg. airspeed [m/s])
                                        reaccptMaxIA = 1e-6; % (Slice size [m])/(avg. airspeed [m/s])

      case 'CIP'
        num_diodes =64;
        diodesize = 0.025; % units of mm
        armdst=100.;
        num_bins=19;
        kk=[50.0   100.0   150.0   200.0   250.0   300.0   350.0   400.0   475.0   550.0   625.0 ...
          700.0   800.0   900.0   1000.0   1200.0   1400.0   1600.0   1800.0   2000.0]/1000; %Array in microns - converted to mm
        probetype=1;
        tasMax=200; % Max airspeed that can be sampled without under-sampling (images would appear skewed)

                                applyIntArrThresh = 1;
                                        defaultIntArrThresh = 1e-6;
                                reaccptShatrs = 1;
                                        reaccptD = 0.5; % Diammeter (in mm) to reaccept if initially flagged as shattered
                                        reaccptMaxIA = 2.5e-7;          % Max interarrival time in seconds a particle can
have to be reaccepted if
                                                                                                        % size criteria are
met. Possible definition of this is the time of one slice, so in
                                                                                                        % this case, with an
airspeed of ~100 m/s and a slice of 25 um, this would be 2.5e-7.

      case 'HVPS'
        % For the HVPS
        num_diodes =128;
        diodesize = .150;
        armdst=161.;
        num_bins = 28;
        kk=[200.0   400.0   600.0   800.0   1000.0   1200.0   1400.0   1600.0   1800.0   2200.0   2600.0 ...
           3000.0   3400.0   3800.0   4200.0   4600.0   5000.0   6000.0   7000.0   8000.0   9000.0 10000.0 ...
           12000.0 14000.0 16000.0 18000.0 20000.0 25000.0 30000.0]/1000;
        probetype=2;
        tasMax=170;
```

```
        % Interarrival threshold and reaccept max interarrival time are often flight-/instrument-specific
                                % **Values here may not be correct**
                                % The interarrival threshold can be modified to change second-by-second if desired
        applyIntArrThresh = 0;
                                        defaultIntArrThresh = 1e-6;
                                reaccptShatrs = 0;
                                        reaccptD = 0.5;
                                        reaccptMaxIA = 1e-6; % (Slice size [m])/(avg. airspeed [m/s])

    end

  otherwise
    switch probename
      case 'HVPS'
        % For the HVPS
        num_diodes =128;
        diodesize = .150;
        armdst=161.;
        %num_bins = 28;
        %kk=[200.0   400.0   600.0   800.0  1000.0  1200.0  1400.0  1600.0  1800.0  2200.0  2600.0 ...
        %     3000.0  3400.0  3800.0  4200.0  4600.0  5000.0  6000.0  7000.0  8000.0  9000.0 10000.0 ...
        %     12000.0 14000.0 16000.0 18000.0 20000.0 25000.0 30000.0]/1000;
        num_bins =70;
        kk=diodesize/2:diodesize:(num_bins+0.5)*diodesize;
        probetype=2;
        tasMax=170;

                                % Interarrival threshold and reaccept max interarrival time are often flight-/instrument-
specific
                                % **Values here may not be correct**
                                % The interarrival threshold can be modified to change second-by-second if desired
        applyIntArrThresh = 1;
                                        defaultIntArrThresh = 1e-6; % Changed from 4e-6 to 1e-6 for ORACLES -
Siddhant Gupta - 11/22/17
                                reaccptShatrs = 0;
                                        reaccptD = 0.5;
                                        reaccptMaxIA = 1e-6; % (Slice size [m])/(avg. airspeed [m/s])

                                intar_threshold = ones(size(tas_time))*defaultIntArrThresh;

      case '2DS'
        % For the HVPS
        num_diodes =128;
        diodesize = .010;
        armdst=63.;
        %num_bins = 28;
        %kk=[200.0   400.0   600.0   800.0  1000.0  1200.0  1400.0  1600.0  1800.0  2200.0  2600.0 ...
        %     3000.0  3400.0  3800.0  4200.0  4600.0  5000.0  6000.0  7000.0  8000.0  9000.0 10000.0 ...
        %     12000.0 14000.0 16000.0 18000.0 20000.0 25000.0 30000.0]/1000/15;
        num_bins =128;
        %kk=diodesize/2:diodesize:(num_bins+0.5)*diodesize;
        kk=diodesize/2:diodesize:(num_bins+0.6)*diodesize;
        probetype=2;
        tasMax=170;

                                % Interarrival threshold and reaccept max interarrival time are often flight-/instrument-
specific
                                % **Values here may not be correct**
```

```
                                    % The interarrival threshold can be modified to change second-by-second if desired
    applyIntArrThresh = 1;
                                            defaultIntArrThresh = 6e-6; % Changed from 1e-6 to 6e-6 for ORACLES -
Siddhant Gupta - 11/1/17
                                    reaccptShatrs = 0;
                                            reaccptD = 0.5;
                                            reaccptMaxIA = 1e-6; % (Slice size [m])/(avg. airspeed [m/s])

                                    intar_threshold = ones(size(tas_time))*defaultIntArrThresh;

   case 'CIP'
    % For the CIP
    num_diodes =64;
    diodesize = .025; %units of mm
    armdst=100.;
    num_bins = 64;
    kk=diodesize/2:diodesize:(num_bins+0.5)*diodesize;
%       num_bins=19;
%       kk=[50.0   100.0   150.0   200.0   250.0   300.0   350.0   400.0   475.0   550.0   625.0 ...
%          700.0   800.0   900.0  1000.0  1200.0  1400.0  1600.0  1800.0  2000.0]/1000; %Array in microns - converted to mm
    probetype=1;
    tasMax=200; % Max airspeed that can be sampled without under-sampling (images would appear skewed)

                                    % Interarrival threshold and reaccept max interarrival time are often flight-/instrument-
specific
                                    % **Values here may not be correct**
                                    % The interarrival threshold can be modified to change second-by-second if desired
    applyIntArrThresh = 1;
                                            defaultIntArrThresh = 1e-6;
                                    reaccptShatrs = 0;
                                            reaccptD = 0.5;
                                            reaccptMaxIA = 1e-6; % (Slice size [m])/(avg. airspeed [m/s])

                                    intar_threshold = ones(size(tas_time))*defaultIntArrThresh;

   case 'PIP'
    num_diodes =64;
    diodesize = .1; %units of mm
    armdst=260.;
    num_bins = 64;
%       kk=diodesize/2:diodesize:(num_bins+0.5)*diodesize;
    kk=diodesize/2:diodesize:(num_bins+0.6)*diodesize;
%       num_bins=19;
%       kk=[50.0   100.0   150.0   200.0   250.0   300.0   350.0   400.0   475.0   550.0   625.0 ...
%          700.0   800.0   900.0  1000.0  1200.0  1400.0  1600.0  1800.0  2000.0]*4/1000;
    probetype=1;
    tasMax=200;

                                    % Interarrival threshold and reaccept max interarrival time are often flight-/instrument-
specific
                                    % **Values here may not be correct**
                                    % The interarrival threshold can be modified to change second-by-second if desired
    applyIntArrThresh = 0;
                                            defaultIntArrThresh = 1e-5;
                                    reaccptShatrs = 0;
                                            reaccptD = 0.5;
                                            reaccptMaxIA = 1e-6; % (Slice size [m])/(avg. airspeed [m/s])
```

```
                    intar_threshold = ones(size(tas_time))*defaultIntArrThresh;


    case '2DC'
      % For the 2DC
      num_diodes =32;
      diodesize = .03; %.025;
      armdst=61.;
      %num_bins = 32;
      %kk=diodesize/2:diodesize:(num_bins+0.5)*diodesize;
      num_bins=19;
      kk=[50.0   100.0   150.0   200.0   250.0   300.0   350.0   400.0   475.0   550.0   625.0 ...
         700.0   800.0   900.0  1000.0  1200.0  1400.0  1600.0  1800.0  2000.0]/1000;
      probetype=0;
      tasMax=125;

                    % Interarrival threshold and reaccept max interarrival time are often flight-/instrument-
specific
                    % **Values here may not be correct**
                    % The interarrival threshold can be modifided to change second-by-second if desired
      applyIntArrThresh = 0;
                        defaultIntArrThresh = 4e-6;
                    reaccptShatrs = 0;
                        reaccptD = 0.5;
                        reaccptMaxIA = 1e-6; % (Slice size [m])/(avg. airspeed [m/s])

                    intar_threshold = ones(size(tas_time))*defaultIntArrThresh;

    case '2DP'
      % For the 2DP
      num_diodes =32;
      diodesize = .200; %.025;
      armdst=260.; %75.77; %61.;
      %num_bins = 32;
      %kk=diodesize/2:diodesize:(num_bins+0.5)*diodesize;
      num_bins=19;
      kk=[50.0   100.0   150.0   200.0   250.0   300.0   350.0   400.0   475.0   550.0   625.0 ...
         700.0   800.0   900.0  1000.0  1200.0  1400.0  1600.0  1800.0  2000.0]*8/1000;
      probetype=0;

                    % Interarrival threshold and reaccept max interarrival time are often flight-/instrument-
specific
                    % **Values here may not be correct**
                    % The interarrival threshold can be modifided to change second-by-second if desired
      applyIntArrThresh = 0;
                        defaultIntArrThresh = 4e-6;
                    reaccptShatrs = 0;
                        reaccptD = 0.5;
                        reaccptMaxIA = 1e-6; % (Slice size [m])/(avg. airspeed [m/s])

                    intar_threshold = ones(size(tas_time))*defaultIntArrThresh;

    case 'F2DC'
      % For the 2DC
      num_diodes =64;
      diodesize = .025; %.025;
      armdst=61.; %60; %
      %num_bins = 32;
```

```
        %kk=diodesize/2:diodesize:(num_bins+0.5)*diodesize;
        num_bins=19;
        kk=[50.0   100.0   150.0   200.0   250.0   300.0   350.0   400.0   475.0   550.0   625.0 ...
           700.0   800.0   900.0  1000.0  1200.0  1400.0  1600.0  1800.0  2000.0]/1000;
        probetype=0;

                                        % Interarrival threshold and reaccept max interarrival time are often flight-/instrument-
specific
                                        % **Values here may not be correct**
                                        % The interarrival threshold can be modified to change second-by-second if desired
        applyIntArrThresh = 0;
                                                defaultIntArrThresh = 4e-6;
                                        reaccptShatrs = 0;
                                                reaccptD = 0.5;
                                                reaccptMaxIA = 1e-6; % (Slice size [m])/(avg. airspeed [m/s])

                                        intar_threshold = ones(size(tas_time))*defaultIntArrThresh;
    end
end

if applyIntArrThresh && ~reaccptShatrs
        fprintf('Beginning sizeDist.m for %s %s - %s probe\n\t**Optional parameters active:\n\t- Shatter
removal\n\n',projectname,ddate,probename);
elseif applyIntArrThresh && reaccptShatrs
        fprintf('Beginning sizeDist.m for %s %s - %s probe\n\t**Optional parameters active:\n\t- Shatter removal\n\t- Shatter
reacceptance\n\n',...
                projectname,ddate,probename);
else
        fprintf('Beginning sizeDist.m for %s %s - %s probe\n\n',projectname,ddate,probename);
end

res=diodesize*1000;
binwidth=diff(kk);
% SAmethod = 2;
% for i=1:num_bins+1
%    kk(i)=  (diodesize*i)^2*3.1415926/4;
% end


%% Define Variables

% Good particles (not rejected)
particle_dist_minR  = zeros(length(tas),num_bins)*NaN;
particle_dist_AreaR = zeros(length(tas),num_bins)*NaN;
particle_aspectRatio = zeros(length(tas),num_bins)*NaN;
particle_aspectRatio1 = zeros(length(tas),num_bins)*NaN;
particle_areaRatio1 = zeros(length(tas),num_bins)*NaN;
particle_area = zeros(length(tas),num_bins)*NaN;
cip2_meanp = zeros(length(tas),num_bins)*NaN;
cip2_iwc = zeros(length(tas),num_bins)*NaN;
cip2_iwcbl = zeros(length(tas),num_bins)*NaN;
cip2_vt = zeros(length(tas),num_bins)*NaN;
cip2_pr = zeros(length(tas),num_bins)*NaN;
cip2_partarea = zeros(length(tas),num_bins)*NaN;

cip2_re = zeros(1,length(tas))*NaN;
good_partpercent=zeros(length(tas),1);
goodintpercent=zeros(length(tas),1);
```

```
numGoodparticles=zeros(length(tas),1);
one_sec_ar=zeros(length(tas),1);


cip2_habitsd = zeros(length(tas),num_bins,10)*NaN;
cip2_habitmsd = zeros(length(tas),num_bins,10)*NaN;
area_dist2 = zeros(length(tas),num_bins,10)*NaN;

rejectpercentbycriterion=zeros(length(tas),14);


% Bad particles (rejected)
bad_particle_dist_minR  = zeros(length(tas),num_bins)*NaN;
bad_particle_dist_AreaR = zeros(length(tas),num_bins)*NaN;
bad_particle_aspectRatio = zeros(length(tas),num_bins)*NaN;
bad_particle_aspectRatio1 = zeros(length(tas),num_bins)*NaN;
bad_particle_areaRatio1 = zeros(length(tas),num_bins)*NaN;
bad_particle_area = zeros(length(tas),num_bins)*NaN;
bad_cip2_meanp = zeros(length(tas),num_bins)*NaN;
bad_cip2_iwc = zeros(length(tas),num_bins)*NaN;
bad_cip2_iwcbl = zeros(length(tas),num_bins)*NaN;
bad_cip2_vt = zeros(length(tas),num_bins)*NaN;
bad_cip2_pr = zeros(length(tas),num_bins)*NaN;
bad_cip2_partarea = zeros(length(tas),num_bins)*NaN;

bad_cip2_re = zeros(1,length(tas))*NaN;
badintpercent=zeros(length(tas),1);
numBadparticles=zeros(length(tas),1);
bad_one_sec_ar=zeros(length(tas),1);

bad_cip2_habitsd = zeros(length(tas),num_bins,10)*NaN;
bad_cip2_habitmsd = zeros(length(tas),num_bins,10)*NaN;
bad_area_dist2 = zeros(length(tas),num_bins,10)*NaN;


% particle_dist2 = zeros(length(tas),num_bins)*NaN; %Unused
% time_interval1 = zeros(length(tas), 1); %Unused
% cip2_ar = zeros(1,length(tas))*NaN; %Unused
% throwoutpercent=zeros(length(tas),1); %Used in legacy interarrival time analysis
% totalint=zeros(length(tas),1); %Used in legacy interarrival time analysis
% intsum=zeros(length(tas),1); %Used in legacy interarrival time analysis

area_bins = 0:.1:1.01;
one_sec_times = tas_time;
one_sec_dur = length(one_sec_times);
total_one_sec_locs(1:one_sec_dur) = 0;
start_time = floor(tas_time(1));
end_time = ceil(tas_time(end));
one_sec_tas(1:one_sec_dur) = 0;
one_sec_tas_entire(1:one_sec_dur) = 0;
deadtime(1:one_sec_dur) = 0;

warning off all

one_sec_times=[one_sec_times;one_sec_times(one_sec_dur)+1];
time_interval2 = zeros(one_sec_dur,1);

TotalPC1 = zeros(one_sec_dur,1)';
```

```
TotalPC2 = zeros(one_sec_dur,1)';

% Used for debugging of interarrival time analysis
shatrReject_times = [];
shatrReject_intArr = [];
shatrReject_diam = [];

rccptReject_times = [];
rccptReject_intArr = [];
rccptReject_diam = [];

loopedTimes = [];
loopedIntArr = [];
loopedDiam = [];
loopedAutoRej = [];

%% Load particles for each second, and then process them
% Only for large files cannot be processed at once
[~, NumofPart] = netcdf.inqDim(f,0); % Check the number of particles

if 1==probetype
%    image_time_hhmmssall = netcdf.getVar(f,netcdf.inqVarID(f,'particle_time'));
   image_time_secs = hhmmss2insec(netcdf.getVar(f,netcdf.inqVarID(f,'particle_time')))+tas_time(1);
   image_time_hhmmssall = insec2hhmmss(image_time_secs);

elseif 2==probetype
   image_time_hhmmssallbuffer = netcdf.getVar(f,netcdf.inqVarID(f,'Time'));
%                                                   image_time_hhmmssallbuffer(image_time_hhmmssallbuffer<10000                &
image_time_hhmmssallbuffer>=0)=image_time_hhmmssallbuffer(image_time_hhmmssallbuffer<10000                      &
image_time_hhmmssallbuffer>=0)+240000;
   alltimeinseconds = netcdf.getVar(f,netcdf.inqVarID(f,'Time_in_seconds'));
   time_msec_all = netcdf.getVar(f,netcdf.inqVarID(f,'msec'),0,1);

   indexRollback=find(diff(alltimeinseconds)<-250)+1;
   for i=1:length(indexRollback)
      if mod(i,1000)==0
         disp([num2str(i),' / ',num2str(length(indexRollback)),datestr(now)]) % Joe Finlon
      end
      alltimeinseconds(indexRollback(i):end)=alltimeinseconds(indexRollback(i):end)+(2^32-1)*(res/10^6/tasMax);
   end

%   alltimeinsecondsstart=alltimeinseconds(indexBuffert);
%   increaseAllinseconds= alltimeinseconds-alltimeinseconds(1);
%   increaseAllinseconds(increaseAllinseconds<0)=increaseAllinseconds(increaseAllinseconds<0)+(2^32-1)*(res/10^6/170);
%   image_time_hhmmssall = insec2hhmmss(floor(47069+time_msec_all(1)/1000.0+increaseAllinseconds*170/110));
   image_time_hhmmssall = image_time_hhmmssallbuffer;
else
   image_time_hhmmssall = netcdf.getVar(f,netcdf.inqVarID(f,'Time'));
end
disp('Performing time correction.') % Joe Finlon
% image_time_hhmmssall = netcdf.getVar(f,netcdf.inqVarID(f,'Time'));
%                                        image_time_hhmmssall(image_time_hhmmssall<50000                                &
image_time_hhmmssall>=0)=image_time_hhmmssall(image_time_hhmmssall<50000 & image_time_hhmmssall>=0)+120000;

% Fix particle times if they span multiple days - Added by Joe Finlon -
% 03/03/17
image_time_hhmmssall(find(diff(image_time_hhmmssall)<0)+1:end)=...
   image_time_hhmmssall(find(diff(image_time_hhmmssall)<0)+1:end) + 240000;
```

```
% Find all indices (true/1) with a unique time in hhmmss - in other words, we're getting the particle index where each new
% one-second period starts
startindex=[true;(diff(hhmmss2insec(image_time_hhmmssall))>0)];  %  &  diff(hhmmss2insec(image_time_hhmmssall))<5)];  %
Simplified (tested/changed by DS)

% startindex=int8(image_time_hhmmssall*0);
% for i=1:length(timehhmmss)
%    indexofFirstTime =  find(image_time_hhmmssall==timehhmmss(i),1);
%    if ( ~isempty(indexofFirstTime) )
%       startindex(indexofFirstTime)=1;
%    end
%    disp([i,length(timehhmmss)]);
% end


% Get the start time for each new one-second period
starttime=image_time_hhmmssall(startindex); % Simplified (tested/changed by DS)


% Find all instances where startindex is true (where image_time_hhmmssall changes by more than 0) and shift indices back by
one to
% facilitate proper particle counts for each one-second period
start_all=find(startindex)-1; % Simplified (tested/changed by DS)

% Sort the particle one-second time array in the event it is out of order and redefine the start_all variable as needed
[starttime,newindexofsort]=sort(starttime);
start_all=start_all(newindexofsort);

%% Remove times when there is no tas data available
% nNoTAS=0;
% for i=1:length(starttime)
%     if isempty(timehhmmss(timehhmmss == starttime(i)))
%        starttime(i)=500000;
%        nNoTAS=nNoTAS+1;
%     end
%
%     if i>5 & i<length(starttime)-5 & hhmmss2insec(starttime(i))>mean(hhmmss2insec(starttime(i-5:i+5)))+5
%        starttime(i)=500000;
%     end
% end
% nNoTAS
% start_all = start_all(starttime<500000);
% count_all = count_all(starttime<500000);
% starttime = starttime(starttime<500000);

%% Remove any duplicate times and determine how many particles are present in each one-second period
fprintf('Number of duplicate times = %d\n\n',(length(starttime)-length(unique(starttime))));

[starttime, ia, ~] = unique(starttime,'first');
start_all = start_all(ia);
count_all= [diff(start_all); NumofPart-start_all(end)];
count_all(count_all<0)=1;

%% Remove times when there are less than 10 particles in one second
% starttime = starttime(count_all>10);
% start_all = start_all(count_all>10);
% count_all = count_all(count_all>10);
```

```
%if (int32(timehhmmss(1))>int32(starttime(2)))
%    error('Watch Out for less TAS time from begining!')
%end

%% Main loop over the length of the true air speed variable (1-sec resolution)
jjj=1;
eofFlag=0; % end of the particle data flag - Added by Joe Finlon - 03/03/17

sumIntArrGT1 = 0;
intArrGT1 = [];

% nThrow11=0; % Used in legacy interarrival time analysis
% maxRecNum=1; % Used in legacy interarrival time analysis

fprintf('Beginning size distribution calculations and sorting %s\n\n',datestr(now));

for i=1:length(tas)

%     if (int32(timehhmmss(i))>=int32(starttime(jjj)))
    if (eofFlag==0 && int32(timehhmmss(i))>=int32(starttime(jjj))) % Modified by Joe Finlon - 03/03/17

        % Attempt to sync TAS file time (timehhmmss) with particle time
%         if (int32(timehhmmss(i))>int32(starttime(jjj))) %% Deprecated
%         (Joe Finlon - 03/03/17)
        while (int32(timehhmmss(i))>int32(starttime(jjj))) && jjj<length(start_all) % Added by Joe Finlon - 03/03/17
            jjj=jjj+1;
            if (jjj==length(start_all)) % we've reached the end of the particle data - Added by Joe Finlon - 03/03/17
                eofFlag = 1;
            end

%             switch probename
%                 case 'CIP'
%             if (jjj>length(start_all))
%                 break;
%             end
%             end

        end

        if (jjj==length(start_all)) % we've reached the end of the particle data - Added by Joe Finlon - 03/03/17
            eofFlag = 1;
        end

        start=start_all(jjj);
        count=count_all(jjj);
        jjj=min(jjj+1,length(start_all));

        % Load autoanalysis parameters. Start at beginning (start) of some one-second period and load the values for every
        % particle in that period (count)
        msec = netcdf.getVar(f,netcdf.inqVarID(f,'particle_millisec'),start,count);
        microsec = netcdf.getVar(f,netcdf.inqVarID(f,'particle_microsec'),start,count);
        auto_reject = netcdf.getVar(f,netcdf.inqVarID(f,'image_auto_reject'),start,count);
        im_width = netcdf.getVar(f,netcdf.inqVarID(f,'image_width'),start,count);
        im_length = netcdf.getVar(f,netcdf.inqVarID(f,'image_length'),start,count);
        area = netcdf.getVar(f,netcdf.inqVarID(f,'image_area'),start,count);
        perimeter = netcdf.getVar(f,netcdf.inqVarID(f,'image_perimeter'),start,count);
%         rec_nums = netcdf.getVar(f,netcdf.inqVarID(f,'parent_rec_num'),start,count); %Used in legacy interarrival time analysis
```

```
%       top_edges = netcdf.getVar(f,netcdf.inqVarID(f,'image_max_top_edge_touching'),start,count); %Unused
%       bot_edges = netcdf.getVar(f,netcdf.inqVarID(f,'image_max_bottom_edge_touching'),start,count); %Unused
%       longest_y = netcdf.getVar(f,netcdf.inqVarID(f,'image_longest_y'),start,count); %Unused
    size_factor = netcdf.getVar(f,netcdf.inqVarID(f,'size_factor'),start,count);
    habit1 = netcdf.getVar(f,netcdf.inqVarID(f,'holroyd_habit'),start,count);
    centerin = netcdf.getVar(f,netcdf.inqVarID(f,'image_center_in'),start,count);
    entirein = netcdf.getVar(f,netcdf.inqVarID(f,'image_touching_edge'),start,count);

    particle_diameter_AreaR = netcdf.getVar(f,netcdf.inqVarID(f,'image_diam_AreaR'),start,count);
    particle_diameter_AreaR = particle_diameter_AreaR * diodesize;

    Time_in_seconds = netcdf.getVar(f,netcdf.inqVarID(f,'Time_in_seconds'),start,count);
%       SliceCount = netcdf.getVar(f,netcdf.inqVarID(f,'SliceCount'),start,count); %Unused
    if probetype~=0 % skip reading variables if 2DC/2DP - Joe Finlon - 06/26/17
      DMT_DOF_SPEC_OVERLOAD = netcdf.getVar(f,netcdf.inqVarID(f,'DMT_DOF_SPEC_OVERLOAD'),start,count);
      Particle_count = netcdf.getVar(f,netcdf.inqVarID(f,'Particle_number_all'),start,count);
      TotalPC1(i)=length(Particle_count);
      TotalPC2(i)=Particle_count(end)-Particle_count(1);
    end

    if 1==probetype
      auto_reject(DMT_DOF_SPEC_OVERLOAD~=0)='D';
    end

    if iCreateAspectRatio == 1
      aspectRatio                                                                                                  =
netcdf.getVar(f,netcdf.inqVarID(f,'image_RectangleW'),start,count)./netcdf.getVar(f,netcdf.inqVarID(f,'image_RectangleL'),start
,count);
      aspectRatio1                                                                                                 =
netcdf.getVar(f,netcdf.inqVarID(f,'image_EllipseW'),start,count)./netcdf.getVar(f,netcdf.inqVarID(f,'image_EllipseL'),start,count)
;
    end

    if 0==probetype
      int_arr=Time_in_seconds;
                  else
                          if start-1 <= 0
                                  int_arr = [0;diff(Time_in_seconds)];
                                  int_arr2 = []; %Won't bother reaccepting particles at the beginning or end of dataset

                          else
                                  Time_in_seconds2       =       netcdf.getVar(f,netcdf.inqVarID(f,'Time_in_seconds'),start-
1,count+1);
                                  int_arr = diff(Time_in_seconds2);

                                  if start ~= start_all(end)
                                          Time_in_seconds3                                                         =
netcdf.getVar(f,netcdf.inqVarID(f,'Time_in_seconds'),(start+count)-1,2);
                                          int_arr2 = diff(Time_in_seconds3); %Single value describing interarrival time of
first particle of next 1-sec period
                                  else
                                          int_arr2 = [];
                                  end
                          end

                          int_arr2(int_arr2<0)=0;

                          if reaccptShatrs
```

```
                    if start ~= start_all(end)
                        Time_in_seconds4                                                    =
netcdf.getVar(f,netcdf.inqVarID(f,'Time_in_seconds'),start,count+1);
                        int_arr3 = diff(Time_in_seconds4);
                    else
                        Time_in_seconds4 = Time_in_seconds;
                        int_arr3 = diff(Time_in_seconds4);
                        int_arr3 = [int_arr3;int_arr3(end)];
                    end
                    int_arr3(int_arr3<0)=0;
                end

    end
%       if 2==probetype
%         int_arr=int_arr*(res/10^6/170);
%       end

    if 2==probetype
        int_arr(int_arr<-10)=int_arr(int_arr<-10)+(2^32-1)*(res/10^6/tasMax);
    elseif 0==probetype
        int_arr(int_arr<0)=int_arr(int_arr<0)+(2^24-1)*(res/10^6/tasMax);
    end

    if sum(int_arr<0)>0
                fprintf(2,'\nAt index %d number of int_arr < 0: %d\n',i,sum(int_arr<0));
        disp([int_arr(int_arr<0),int_arr(int_arr<0)+(2^32-1)*(res/10^6/tasMax)]);
    elseif sum(int_arr>1)>0
                sumIntArrGT1 = sumIntArrGT1 + sum(int_arr > 1);
                tempLocs = find(int_arr > 1);
                intArrGT1 = vertcat(intArrGT1,int_arr(tempLocs));

%           fprintf(2,'\nAt index %d number of int_arr > 1: %d\n',i,sum(int_arr>1));
%          disp([int_arr(int_arr>1)-(2^32-1)*(res/10^6/tasMax), int_arr(int_arr>1), Time_in_seconds(int_arr>1)/(0.15/(10^3)/170),
Time_in_seconds((int_arr>1))/(0.15/(10^3)/170)]);
    end

%       auto_reject(int_arr<0 | int_arr>1)='I';
            auto_reject(int_arr<0)='I';
    int_arr(int_arr<0)=0;
%       int_arr(int_arr>1)=0;


%       max_dimension = im_width;
%       max_dimension(im_length>im_width)=im_length(im_length>im_width);


    % Size definition chosen based on the d_choice given in the function call
    if 1==d_choice
        particle_diameter_minR = im_length * diodesize; %(im_length+
    elseif 2==d_choice
        particle_diameter_minR = im_width * diodesize; %(im_length+
    elseif 3==d_choice
        particle_diameter_minR = (im_length + im_width)/2 * diodesize; %(im_length+
    elseif 4==d_choice
        particle_diameter_minR = sqrt(im_width.^2+im_length.^2) * diodesize; %(im_length+
    elseif 5==d_choice
        particle_diameter_minR = max(im_width, im_length) * diodesize; %(im_length+
    elseif 6==d_choice
```

```
        particle_diameter_minR = netcdf.getVar(f,netcdf.inqVarID(f,'image_diam_minR'),start,count); % * diodesize
      end

%       if 1==strcmp('2DC',probename)  % Adjust resolution from 25 to 30
%         particle_diameter_minR=particle_diameter_minR*1.2;
%         area = area*1.44;
%       end



      % Legacy: Added for Paris meeting, 08/25/2014
      % Used in intercomparison with Environment Canada and University of Blaise Pascal
      %{
      diffPartCount=[1;diff(Particle_count)];
      time_interval22(i) = (Time_in_seconds(end)-Time_in_seconds(1));
      time_interval32(i) = sum(int_arr(diffPartCount==1));
      time_interval42(i) = sum(int_arr);
      time_interval52(i) = sum(int_arr(diffPartCount~=1));
      time_interval62(i) = sum(int_arr(DMT_DOF_SPEC_OVERLOAD==0));
      lengthForTemp = im_length * diodesize;
      particle_diameter_minR(entirein~=0)=lengthForTemp(entirein~=0);

      if time_interval22(i)<0
        time_interval22(i)=time_interval22(i)+(2^32-1)*(res/10^6/tasMax); %#ok<*AGROW>
      end

      if RejectCriterier==1
       particle_diameter_minR = particle_diameter_minR .* size_factor;
      end


      if 1==probetype
        image_time_hhmmss    = netcdf.getVar(f,netcdf.inqVarID(f,'particle_time'),start,count);
        image_time_hhmmssnew = netcdf.getVar(f,netcdf.inqVarID(f,'particle_time'),start,count);

      elseif 2==probetype
        alltimeinseconds = netcdf.getVar(f,netcdf.inqVarID(f,'Time_in_seconds'),start,count);
        increaseAllinseconds= alltimeinseconds-alltimeinseconds(1);
        increaseAllinseconds(increaseAllinseconds<0)=increaseAllinseconds(increaseAllinseconds<0)+(2^32-1)*(res/10^6/170);
        image_time_hhmmss                                                                                      =
floor(hhmmss2insec(netcdf.getVar(f,netcdf.inqVarID(f,'Time'),start,count))+netcdf.getVar(f,netcdf.inqVarID(f,'msec'),start,coun
t)/1000+increaseAllinseconds); % 'Time'?
        image_time_hhmmss = insec2hhmmss(image_time_hhmmss);
        image_time_hhmmssnew = image_time_hhmmss;
      end
      %}
      if probetype==0 % skip reading variable if 2DC/2DP - Joe Finlon - 06/26/17
        time_interval72(i) = 0; % 2DC/2DP does not have overload flag
      else
        time_interval72(i) = sum(int_arr(DMT_DOF_SPEC_OVERLOAD~=0));
      end

      % Simplified by DS - Removed image_time_hhmmssnew as it was defined by and never changed from image_time_hhmmss
      image_time_hhmmss = image_time_hhmmssall(start+1:start+count);

      % If image time crosses midnight, add 240000 to all times past midnight
%       image_time_hhmmss(image_time_hhmmss<10000)=image_time_hhmmss(image_time_hhmmss<10000)+240000;
```

```
    % Save an intermediate output file every 8000 steps through the loop
    if i==8000
       save([outfile(1:end-3) 'tempComp.mat']);
    end

    %% Calculate area of particle according to image reconstruction and airspeed (if tasMax exceeded)

    % Correct for airspeeds exceeding the max airspeed for the probe
    if(tas(i) > tasMax) % Set to threshold as necessary - stretch area of particle
                                        fprintf(2,'TAS at tas index %d exceeds tasMax (%.1f) of probe. Reconstructing area...\n\n',...
                                                    i,tasMax);
       area = area*tas(i)/tasMax;
    end

    particle_mass = area*0;
    calcd_area = area*0;
    for iiii=1:length(area)
      particle_mass(iiii)=single_mass(particle_diameter_minR(iiii)/10, habit1(iiii));  % in unit of gram
      calcd_area(iiii)=single_area(particle_diameter_minR(iiii)/10, habit1(iiii));  % in unit of mm^2
    end
    particle_massbl=0.115/1000*area.^(1.218); % in unit of gram


    %% Added by Robert Jackson -- old version did not have area ratio code
    area_ratio = area./(pi/4.*particle_diameter_minR.^2);
    auto_reject(area_ratio < .5) = 'z'; % Changed from .2 to .5 for ORACLES - Siddhant Gupta - 11/1/17

    %% Added by Will to calculate terminal velocity and precipitation rate
    particle_vt = area*0;
    for iiii=1:length(area)
      particle_vt(iiii)=single_vt(particle_diameter_minR(iiii)/1000, area_ratio(iiii), particle_mass(iiii)/1000,Pres(i),Temp(i));  % in
unit of gram
    end
    particle_pr=particle_mass.*particle_vt;


    %% Time-dependent threshold for interarrival time - Added by Dan Stechman - 5/10/16 & Modified by Joe Finlon - 03/03/17
                    % Enable this section to use a time-dependent threshold for interarrival time. Also need to enable section at
top of
                    % script allowing for threshold file to be pulled in

    % Ingest previously calculated interarrival time threshold and flag in auto_reject appropriately to remove particle
                    % flagged with short inter arrv time, and the one immediately before it

    if applyIntArrThresh && length(varargin) == 1 % Edited by Siddhant Gupta to input inter-arrival threshold file or use default
value if not available

       if strcmp(iaThreshFile,'NONE') == 0
       auto_reject_preIAT = auto_reject;
                                        iaThresh_ncid = netcdf.open(iaThreshFile,'nowrite');
                                        iaThresh = netcdf.getVar(iaThresh_ncid,netcdf.inqVarID(iaThresh_ncid,'threshold'),start,count);
                                        netcdf.close(iaThresh_ncid);
       elseif strcmp(iaThreshFile,'NONE') == 1
       iaThresh = ones(count,1)*defaultIntArrThresh;
       end
```

```
if ((length(int_arr) == 1) && (int_arr(1) <= iaThresh(1)))
                auto_reject(1) = 'S';
else
   if int_arr(1) <= iaThresh(1)
                    auto_reject(1) = 'S';
   end

   for ix = 2:length(int_arr)
                    if int_arr(ix) <= iaThresh(ix)
                        auto_reject((ix-1):ix) = 'S';
                    end
   end
end

% Experimental option to reaccept particles flagged as shattered which may in fact be the result of diffraction
            % fringes
            % Added by Dan Stechman - 6/8/2015 & Modified by Joe Finlon - 03/03/17 - with base code by Wei
Wu
            if reaccptShatrs
                % Start by defining the indices for the beginning and end of individual shattering events
                rBegin = ((int_arr > iaThresh & int_arr3 < iaThresh));
                rEnd = ((int_arr < iaThresh & int_arr3 > iaThresh));

                maxParticle = reaccptD;
                eIndex = [];

                % We search through each individual set of shattering events and check to see if any of
the particles are both
                % larger than the reacceptance diameter and have an interarrival time less than the
reacceptance threshold as we'd
                % expect diffraction fringes to be larger than shattered particles and to have a particularly
small interarrival time
   for iEvent = find(rBegin):find(rEnd)
                    if ((particle_diameter_minR(iEvent) > maxParticle) && (int_arr(iEvent) <
reaccptMaxIA))
                        maxParticle = particle_diameter_minR(iEvent);
                        eIndex = iEvent;
                    end
   end

                auto_reject(eIndex) = 'R';
            end


            % Following vars used for verifying shatter removal and reacceptance in external script - can be
commented out if desired

shatterLocs = find(auto_reject == 'S');
            shatterIA = int_arr(shatterLocs);
            shatterTimes = Time_in_seconds(shatterLocs);
shatterDiam = particle_diameter_minR(shatterLocs);

            shatrReject_times = vertcat(shatrReject_times, shatterTimes);
            shatrReject_intArr = vertcat(shatrReject_intArr, shatterIA);
shatrReject_diam = vertcat(shatrReject_diam, shatterDiam);

rccptLocs = find(auto_reject == 'R');
            rccptIA = int_arr(rccptLocs);
```

```
                rccptTimes = Time_in_seconds(rccptLocs);
    rccptDiam = particle_diameter_minR(rccptLocs);

                rccptReject_times = vertcat(rccptReject_times, rccptTimes);
                rccptReject_intArr = vertcat(rccptReject_intArr, rccptIA);
    rccptReject_diam = vertcat(rccptReject_diam, rccptDiam);


                loopedTimes = vertcat(loopedTimes, Time_in_seconds);
                loopedIntArr = vertcat(loopedIntArr, int_arr);
    loopedDiam = vertcat(loopedDiam, particle_diameter_minR);
                loopedAutoRej = vertcat(loopedAutoRej, auto_reject);

  end


  %% Legacy interarrival time integrity analysis
  %{
  % Time and interarrival calculation. Modified by Will Wu 11/12/2013
  % Simplified (tested/changed by DS)
  if strcmp(probename,'2DC')==1 || strcmp(probename,'2DP')==1 || strcmp(probename,'F2DC')==1
    fracseccc= netcdf.getVar(f,netcdf.inqVarID(f,'msec'),start,count);
    image_timeia = hhmmss2insec(image_time_hhmmss)+fracseccc*1e-2; % for 2DC
  elseif strcmp(probename,'CIP')==1 || strcmp(probename,'PIP')==1
    image_timeia = hhmmss2insec(image_time_hhmmss)+msec*1e-3+microsec; % for CIP
  else
    image_timeia = hhmmss2insec(image_time_hhmmss)+msec*1e-3+microsec/10^6; % for HVPS
  end

  disp('Checking Interarrival Times')

  nThrow=0;
  for(itemp=min(rec_nums):max(rec_nums))
    rec_particles = find(rec_nums == itemp);
    rej = auto_reject(rec_particles);
    arr = int_arr(rec_particles);
    sum_arr = sum(arr(2:end));
    if(~isempty(rec_particles) && length(rec_particles) > 1)
      int_arr(rec_particles(1)) = int_arr(rec_particles(2));
    elseif(length(rec_particles) == 1)
      int_arr(rec_particles(1)) = 0;
    end

    if (strcmp(probename,'CIP')==1 || strcmp(probename,'PIP')==1 || strcmp(probename,'HVPS')==1 ) % 2DC use the
interarrival time for every particles, not absolute time

      if(isempty(rec_particles))
        sum_int_arr_good = 0;
      else
        sum_int_arr_good = image_timeia(rec_particles(end))-image_timeia(rec_particles(1));
      end
      if ~(sum_int_arr_good >= .6*sum_arr && sum_int_arr_good <= 1.4*sum_arr)
        auto_reject(rec_particles) = 'I';
        %disp(['Record ' num2str(itemp) ' thrown out: Accepted time = ' num2str(sum_int_arr_good) ' total time = '
num2str(sum_arr)]);
        nThrow=nThrow+1;
        nThrow11=nThrow11+1;
      end
```

```
    end
  end
  disp([num2str(100*nThrow/(max(rec_nums)-min(rec_nums)+1)),'% is thrown out']);
  throwoutpercent(i)=100*nThrow/(max(rec_nums)-min(rec_nums)+1);
  maxRecNum=max(max(rec_nums),maxRecNum);
  totalint(i)=sum_int_arr_good;
  intsum(i)=sum_arr;
  save('intarrhvps.mat','int_arr')
  %}

  %% Shatter identification and removal - Added by Dan Stechman on 5/31/2016
  % Currently this is spiral-dependent and uses a threshold defined in the header of this script
  % Flag particles as shattered if their interarrival time is less than or equal to the threshold. Also flag the particle
  % immediately before the target particle.
  %{
  if applyIntArrThresh
			% If the first particle in the next 1-sec period has a small interarrival time, we flag the last particle
of
			% the current period as shattered as well
			if ~isempty(int_arr2)
				if int_arr2 <= intar_threshold(i)
					auto_reject(end) = 'S';
				end
			end

			if (length(int_arr) == 1 && int_arr(1) <= intar_threshold(i))
				auto_reject(1) = 'S';
			else
				if int_arr(1) <= intar_threshold(i)
					auto_reject(1) = 'S';
				end

				for ix = 2:length(int_arr)
					if int_arr(ix) <= intar_threshold(i)
						auto_reject(ix-1:ix) = 'S';
					end
				end
			end


			% Experimental option to reaccept particles flagged as shattered which may in fact be the result of
diffraction
			% fringes
			% Added by Dan Stechman - 6/8/2015 - with base code by Wei Wu
			if reaccptShatrs
				% Start by defining the indices for the beginning and end of individual shattering events
				rBegin = ((int_arr > intar_threshold(i) & int_arr3 < intar_threshold(i)));
				rEnd = ((int_arr < intar_threshold(i) & int_arr3 > intar_threshold(i)));

				maxParticle = reaccptD;
				eIndex = [];

				% We search through each individual set of shattering events and check to see if any of
the particles are both
				% larger than the reacceptance diameter and have an interarrival time less than the
reacceptance threshold as we'd
```

```
                                        % expect diffraction fringes to be larger than shattered particles and to have a particularly
small interarrival time
                                        for iEvent = find(rBegin):find(rEnd)
                                                if ((particle_diameter_minR(iEvent) > maxParticle) && (int_arr(iEvent) <
reaccptMaxIA))
                                                        maxParticle = particle_diameter_minR(iEvent);
                                                        eIndex = iEvent;
                                                end
                                        end

                                        auto_reject(eIndex) = 'R';
                                end


                                % Following vars used for verifying shatter removal and reacceptance in external script - can be
commented out if desired
                                shatterLocs = find(auto_reject == 'S');
                                shatterIA = int_arr(shatterLocs);
                                shatterTimes = Time_in_seconds(shatterLocs);
        shatterDiam = particle_diameter_minR(shatterLocs);

                                shatrReject_times = vertcat(shatrReject_times, shatterTimes);
                                shatrReject_intArr = vertcat(shatrReject_intArr, shatterIA);
        shatrReject_diam = vertcat(shatrReject_diam, shatterDiam);

        rccptLocs = find(auto_reject == 'R');
                                rccptIA = int_arr(rccptLocs);
                                rccptTimes = Time_in_seconds(rccptLocs);
        rccptDiam = particle_diameter_minR(rccptLocs);

                                rccptReject_times = vertcat(rccptReject_times, rccptTimes);
                                rccptReject_intArr = vertcat(rccptReject_intArr, rccptIA);
        rccptReject_diam = vertcat(rccptReject_diam, rccptDiam);


                                loopedTimes = vertcat(loopedTimes, Time_in_seconds);
                                loopedIntArr = vertcat(loopedIntArr, int_arr);
        loopedDiam = vertcat(loopedDiam, particle_diameter_minR);
                                loopedAutoRej = vertcat(loopedAutoRej, auto_reject);
    end
    %}

    %% Apply rejection criteria and identify good and bad particles
    % Modify the next line to include/exclude any particles you see fit.

    good_particles = (auto_reject == '0' | auto_reject == 'H' | auto_reject == 'h' | auto_reject == 'u' | auto_reject == 'R');
    bad_particles = ~(auto_reject == '0' | auto_reject == 'H' | auto_reject == 'h' | auto_reject == 'u' | auto_reject == 'R');
%                       bad_particles = (auto_reject == 'S');

    % Legacy: Rejection criteria used in the past
    %{
    %if RejectCriterier==0
    %    good_particles = (auto_reject ~= 'c'); %  &  centerin==1; % & int_arr > 1e-5 int_arr > 1e-5 &
    %else
    %      good_particles = (auto_reject == '0' | auto_reject == 'H' | auto_reject == 'h' | auto_reject == 'u' & int_arr >
intar_threshold) % | auto_reject == 'u'); % & centerin==1; % & int_arr > 1e-5;
    %end
    %}
```

```
if SAmethod==0
   good_particles = good_particles & centerin==1;
   bad_particles = bad_particles & centerin==1;
elseif SAmethod==1
   good_particles = good_particles & entirein==0;
   bad_particles = bad_particles & centerin==0;
end

good_partpercent(i)=sum(good_particles)/length(good_particles);

rejectpercentbycriterion(i,1)=sum(centerin==1)/length(good_particles);
rejectpercentbycriterion(i,2)=sum(auto_reject == '0')/length(good_particles);
rejectpercentbycriterion(i,3)=sum(auto_reject == 'H')/length(good_particles);
rejectpercentbycriterion(i,4)=sum(auto_reject == 'h')/length(good_particles);
rejectpercentbycriterion(i,5)=sum(auto_reject == 'u')/length(good_particles);
rejectpercentbycriterion(i,6)=sum(auto_reject == 'a')/length(good_particles);
rejectpercentbycriterion(i,7)=sum(auto_reject == 't')/length(good_particles);
rejectpercentbycriterion(i,8)=sum(auto_reject == 'p')/length(good_particles);
rejectpercentbycriterion(i,9)=sum(auto_reject == 's')/length(good_particles);
rejectpercentbycriterion(i,10)=sum(auto_reject == 'z')/length(good_particles);
rejectpercentbycriterion(i,11)=sum(auto_reject == 'i')/length(good_particles);
rejectpercentbycriterion(i,12)=sum(auto_reject == 'A')/length(good_particles);
rejectpercentbycriterion(i,13)=sum(auto_reject == 'S')/length(good_particles); %Shattered - Added DS
              rejectpercentbycriterion(i,14)=sum(auto_reject == 'R')/length(good_particles); %Reaccepted - Added DS

numGoodparticles(i)=length(good_particles);
numBadparticles(i)=length(bad_particles);
%     disp([int32(timehhmmss(i)), sum(good_particles),length(good_particles),length(good_particles)-sum(good_particles)]);

image_time = hhmmss2insec(image_time_hhmmss);

% Good (accepted) particles
good_image_times = image_time(good_particles);
good_particle_diameter_minR = particle_diameter_minR(good_particles);
good_particle_diameter_AreaR = particle_diameter_AreaR(good_particles);
good_int_arr=int_arr(good_particles);
good_ar = area_ratio(good_particles);
good_area = area(good_particles);
good_perimeter = perimeter(good_particles);
if iCreateAspectRatio == 1
good_AspectRatio = aspectRatio(good_particles & entirein==0);
good_AspectRatio1 = aspectRatio1(good_particles & entirein==0);
end
good_ar1 = area_ratio(good_particles & entirein==0);
good_image_times1 = image_time(good_particles  & entirein==0);
good_iwc=particle_mass(good_particles);
good_partarea=calcd_area(good_particles);
good_iwcbl=particle_massbl(good_particles);
good_vt=particle_vt(good_particles);
good_pr=particle_pr(good_particles);
good_habit=habit1(good_particles);

good_particle_diameter=good_particle_diameter_minR;
good_particle_diameter1 = particle_diameter_minR(good_particles  & entirein==0);

if iCreateBad == 1
```

```
% Bad (rejected) particles
bad_image_times = image_time(bad_particles);
bad_particle_diameter_minR = particle_diameter_minR(bad_particles);
bad_particle_diameter_AreaR = particle_diameter_AreaR(bad_particles);
bad_int_arr=int_arr(bad_particles);
bad_ar = area_ratio(bad_particles);
bad_area = area(bad_particles);
bad_perimeter = perimeter(bad_particles);
if iCreateAspectRatio == 1 % added if statement if not creating aspect ratio - Joe Finlon - 03/03/17
bad_AspectRatio = aspectRatio(bad_particles & entirein==0);
bad_AspectRatio1 = aspectRatio1(bad_particles & entirein==0);
end
bad_ar1 = area_ratio(bad_particles & entirein==0);
bad_image_times1 = image_time(bad_particles  & entirein==0);
bad_iwc=particle_mass(bad_particles);
bad_partarea=calcd_area(bad_particles);
bad_iwcbl=particle_massbl(bad_particles);
bad_vt=particle_vt(bad_particles);
bad_pr=particle_pr(bad_particles);
bad_habit=habit1(bad_particles);

bad_particle_diameter=bad_particle_diameter_minR;
bad_particle_diameter1 = particle_diameter_minR(bad_particles  & entirein==0);
end
%% Perform various status and error checks
if mod(i,1000) == 0
            fprintf('%d/%d | %s\n',i,one_sec_dur,datestr(now));
end

total_one_sec_locs(i) = length(find(image_time >= one_sec_times(i) & image_time < one_sec_times(i+1)));
time_interval2(i) = sum(int_arr(image_time >= one_sec_times(i) & image_time < one_sec_times(i+1)));

if sum(image_time >= one_sec_times(i) & image_time < one_sec_times(i+1)) ~= length(image_time)
            fprintf(2,'%d / %d\tError on sizing at index %d\n',sum(image_time >= one_sec_times(i) &
image_time < one_sec_times(i+1)),length(image_time),i);
end

if(total_one_sec_locs(i) == 0)
 time_interval2(i) = 1;
end

%% Sort good (accepted) particles into size distributions
good_one_sec_locs = find(good_image_times >= one_sec_times(i) & good_image_times < one_sec_times(i+1));
good_one_sec_locs1 = find(good_image_times1 >= one_sec_times(i) & good_image_times1 < one_sec_times(i+1));

goodintpercent(i) = sum(good_int_arr(good_image_times >= one_sec_times(i) & good_image_times <
one_sec_times(i+1)))/time_interval2(i);

one_sec_ar(i) = mean(good_ar1(good_one_sec_locs1));

if ~isempty(good_one_sec_locs)

   for j = 1:num_bins
     particle_dist_minR(i,j)  = length(find(good_particle_diameter_minR(good_one_sec_locs) >= kk(j) &...
        good_particle_diameter_minR(good_one_sec_locs) < kk(j+1)));
     particle_dist_AreaR(i,j) = length(find(good_particle_diameter_AreaR(good_one_sec_locs) >= kk(j) &...
        good_particle_diameter_AreaR(good_one_sec_locs) < kk(j+1)));
```

```
        % Create Habit Number Size Distribution
        cip2_habitsd(i,j,1) = length(find(good_habit(good_one_sec_locs)=='s' & good_particle_diameter(good_one_sec_locs) >=
kk(j) &...
          good_particle_diameter(good_one_sec_locs) < kk(j+1)));
        cip2_habitsd(i,j,2) = length(find(good_habit(good_one_sec_locs)=='l' & good_particle_diameter(good_one_sec_locs) >=
kk(j) &...
          good_particle_diameter(good_one_sec_locs) < kk(j+1)));
        cip2_habitsd(i,j,3) = length(find(good_habit(good_one_sec_locs)=='o' & good_particle_diameter(good_one_sec_locs)
>= kk(j) &...
          good_particle_diameter(good_one_sec_locs) < kk(j+1)));
        cip2_habitsd(i,j,4) = length(find(good_habit(good_one_sec_locs)=='t' & good_particle_diameter(good_one_sec_locs) >=
kk(j) &...
          good_particle_diameter(good_one_sec_locs) < kk(j+1)));
        cip2_habitsd(i,j,5) = length(find(good_habit(good_one_sec_locs)=='h' & good_particle_diameter(good_one_sec_locs)
>= kk(j) &...
          good_particle_diameter(good_one_sec_locs) < kk(j+1)));
        cip2_habitsd(i,j,6) = length(find(good_habit(good_one_sec_locs)=='i' & good_particle_diameter(good_one_sec_locs) >=
kk(j) &...
          good_particle_diameter(good_one_sec_locs) < kk(j+1)));
        cip2_habitsd(i,j,7) = length(find(good_habit(good_one_sec_locs)=='g' & good_particle_diameter(good_one_sec_locs)
>= kk(j) &...
          good_particle_diameter(good_one_sec_locs) < kk(j+1)));
        cip2_habitsd(i,j,8) = length(find(good_habit(good_one_sec_locs)=='d' & good_particle_diameter(good_one_sec_locs)
>= kk(j) &...
          good_particle_diameter(good_one_sec_locs) < kk(j+1)));
        cip2_habitsd(i,j,9) = length(find(good_habit(good_one_sec_locs)=='a' & good_particle_diameter(good_one_sec_locs)
>= kk(j) &...
          good_particle_diameter(good_one_sec_locs) < kk(j+1)));
        cip2_habitsd(i,j,10) = length(find(good_habit(good_one_sec_locs)=='I' & good_particle_diameter(good_one_sec_locs)
>= kk(j) &...
          good_particle_diameter(good_one_sec_locs) < kk(j+1)));

        % Create Habit Mass Size Distribution
        cip2_habitmsd(i,j,1) = sum(good_iwc(good_habit(good_one_sec_locs)=='s' &
good_particle_diameter(good_one_sec_locs) >= kk(j) &...
          good_particle_diameter(good_one_sec_locs) < kk(j+1)));
        cip2_habitmsd(i,j,2) = sum(good_iwc(good_habit(good_one_sec_locs)=='l' &
good_particle_diameter(good_one_sec_locs) >= kk(j) &...
          good_particle_diameter(good_one_sec_locs) < kk(j+1)));
        cip2_habitmsd(i,j,3) = sum(good_iwc(good_habit(good_one_sec_locs)=='o' &
good_particle_diameter(good_one_sec_locs) >= kk(j) &...
          good_particle_diameter(good_one_sec_locs) < kk(j+1)));
        cip2_habitmsd(i,j,4) = sum(good_iwc(good_habit(good_one_sec_locs)=='t' &
good_particle_diameter(good_one_sec_locs) >= kk(j) &...
          good_particle_diameter(good_one_sec_locs) < kk(j+1)));
        cip2_habitmsd(i,j,5) = sum(good_iwc(good_habit(good_one_sec_locs)=='h' &
good_particle_diameter(good_one_sec_locs) >= kk(j) &...
          good_particle_diameter(good_one_sec_locs) < kk(j+1)));
        cip2_habitmsd(i,j,6) = sum(good_iwc(good_habit(good_one_sec_locs)=='i' &
good_particle_diameter(good_one_sec_locs) >= kk(j) &...
          good_particle_diameter(good_one_sec_locs) < kk(j+1)));
        cip2_habitmsd(i,j,7) = sum(good_iwc(good_habit(good_one_sec_locs)=='g' &
good_particle_diameter(good_one_sec_locs) >= kk(j) &...
          good_particle_diameter(good_one_sec_locs) < kk(j+1)));
        cip2_habitmsd(i,j,8) = sum(good_iwc(good_habit(good_one_sec_locs)=='d' &
good_particle_diameter(good_one_sec_locs) >= kk(j) &...
          good_particle_diameter(good_one_sec_locs) < kk(j+1)));
```

```
    cip2_habitmsd(i,j,9) = sum(good_iwc(good_habit(good_one_sec_locs)=='a' &
good_particle_diameter(good_one_sec_locs) >= kk(j) &...
      good_particle_diameter(good_one_sec_locs) < kk(j+1)));
    cip2_habitmsd(i,j,10) = sum(good_iwc(good_habit(good_one_sec_locs)=='I' &
good_particle_diameter(good_one_sec_locs) >= kk(j) &...
      good_particle_diameter(good_one_sec_locs) < kk(j+1)));


    particle_area(i,j) = nansum(good_area(good_one_sec_locs(good_particle_diameter(good_one_sec_locs) >= kk(j) &...
      good_particle_diameter(good_one_sec_locs) < kk(j+1))));

    cip2_meanp(i,j) = nanmean(good_perimeter(good_one_sec_locs(good_particle_diameter(good_one_sec_locs) >= kk(j)
&...
      good_particle_diameter(good_one_sec_locs) < kk(j+1))));

    if iCreateAspectRatio == 1

    particle_aspectRatio(i,j) =
nanmean(good_AspectRatio(good_one_sec_locs1(good_particle_diameter1(good_one_sec_locs1) >= kk(j) &...
      good_particle_diameter1(good_one_sec_locs1) < kk(j+1))));

    particle_aspectRatio1(i,j) =
nanmean(good_AspectRatio1(good_one_sec_locs1(good_particle_diameter1(good_one_sec_locs1) >= kk(j) &...
      good_particle_diameter1(good_one_sec_locs1) < kk(j+1))));
    end
    particle_areaRatio1(i,j) = nanmean(good_ar1(good_one_sec_locs1(good_particle_diameter1(good_one_sec_locs1) >=
kk(j) &...
      good_particle_diameter1(good_one_sec_locs1) < kk(j+1))));


    cip2_iwc(i,j) = nansum(good_iwc(good_one_sec_locs(good_particle_diameter(good_one_sec_locs) >= kk(j) &...
      good_particle_diameter(good_one_sec_locs) < kk(j+1))));

    cip2_partarea(i,j) = nansum(good_partarea(good_one_sec_locs(good_particle_diameter(good_one_sec_locs) >= kk(j)
&...
      good_particle_diameter(good_one_sec_locs) < kk(j+1))));

    cip2_iwcbl(i,j) = nansum(good_iwcbl(good_one_sec_locs(good_particle_diameter(good_one_sec_locs) >= kk(j) &...
      good_particle_diameter(good_one_sec_locs) < kk(j+1))));

    cip2_vt(i,j) = nansum(good_vt(good_one_sec_locs(good_particle_diameter(good_one_sec_locs) >= kk(j) &...
      good_particle_diameter(good_one_sec_locs) < kk(j+1))));

    cip2_pr(i,j) = nansum(good_pr(good_one_sec_locs(good_particle_diameter(good_one_sec_locs) >= kk(j) &...
      good_particle_diameter(good_one_sec_locs) < kk(j+1))));


    for k = 1:length(area_bins)-1
      area_dist2(i,j,k) = length(find(good_ar(good_one_sec_locs) >= area_bins(k) & ...
        good_ar(good_one_sec_locs) < area_bins(k+1) & good_particle_diameter(good_one_sec_locs) >= kk(j) &...
        good_particle_diameter(good_one_sec_locs) < kk(j+1)));
    end
   end

  % Normalize by binwidth and convert from mm to cm
  particle_dist_minR(i,:)=particle_dist_minR(i,:)./binwidth*10;
  particle_dist_AreaR(i,:)=particle_dist_AreaR(i,:)./binwidth*10;
  cip2_iwc(i,:)=cip2_iwc(i,:)./binwidth*10; %g/cm
```

```
        cip2_iwcbl(i,:)=cip2_iwcbl(i,:)./binwidth*10;
        cip2_vt(i,:)=cip2_vt(i,:)./binwidth*10;
        cip2_pr(i,:)=cip2_pr(i,:)./binwidth*10;
        cip2_partarea(i,:)=cip2_partarea(i,:)./binwidth*10;
        particle_area(i,:)=particle_area(i,:)./binwidth*10;

        for mmmmmm=1:10
           cip2_habitsd(i,:,mmmmmm)=cip2_habitsd(i,:,mmmmmm)./binwidth*10;
           cip2_habitmsd(i,:,mmmmmm)=cip2_habitmsd(i,:,mmmmmm)./binwidth*10;
        end

        for mmmmmm = 1:length(area_bins)-1
           area_dist2(i,:,mmmmmm) =area_dist2(i,:,mmmmmm)./binwidth*10 ;
        end

        % Generalized effective radius calculation from Fu (1996)
        cip2_re(i) = (sqrt(3)/(3*0.91))*1000*(sum(cip2_iwc(i,:)./binwidth,2)/sum(particle_area(i,:)./binwidth,2))*1000; % in unit of
um

                    else

        particle_dist_minR(i,1:num_bins) = 0;
        particle_dist_AreaR(i,1:num_bins) = 0;
        area_dist2(i,1:num_bins,1:length(area_bins)-1) = 0;
        cip2_partarea(i,:) = 0;
        cip2_iwc(i,:) = 0;
        cip2_iwcbl(i,:) = 0;
        cip2_vt(i,:) = 0;
        cip2_pr(i,:) = 0;
        cip2_re(i) = 0;
        cip2_habitsd(i,:,:) = 0;
        cip2_habitmsd(i,:,:) = 0;
        time_interval2(i) = 1;

        % Legacy: used in Paris intercomparison
        %{
        time_interval22(i) = 1;
        time_interval32(i) = 1;
        time_interval42(i) = 1;
        time_interval52(i) = 0;
        time_interval62(i) = 1;
        %}
        time_interval72(i) = 0;

        TotalPC1(i)=1;
        TotalPC2(i)=1;

      end

      if iCreateBad == 1
      %% Sort bad (rejected) particles into size distributions
      bad_one_sec_locs = find(bad_image_times >= one_sec_times(i) & bad_image_times < one_sec_times(i+1));
      bad_one_sec_locs1 = find(bad_image_times1 >= one_sec_times(i) & bad_image_times1 < one_sec_times(i+1));

      badintpercent(i) = sum(bad_int_arr(bad_image_times >= one_sec_times(i) & bad_image_times <
one_sec_times(i+1)))/time_interval2(i);

      bad_one_sec_ar(i) = mean(bad_ar1(bad_one_sec_locs1));
```

```
if ~isempty(bad_one_sec_locs)

  for j = 1:num_bins
    bad_particle_dist_minR(i,j)  = length(find(bad_particle_diameter_minR(bad_one_sec_locs) >= kk(j) &...
      bad_particle_diameter_minR(bad_one_sec_locs) < kk(j+1)));
    bad_particle_dist_AreaR(i,j) = length(find(bad_particle_diameter_AreaR(bad_one_sec_locs) >= kk(j) &...
      bad_particle_diameter_AreaR(bad_one_sec_locs) < kk(j+1)));

    % Create Habit Number Size Distribution
    bad_cip2_habitsd(i,j,1) = length(find(bad_habit(bad_one_sec_locs)=='s' & bad_particle_diameter(bad_one_sec_locs) >=
kk(j) &...
      bad_particle_diameter(bad_one_sec_locs) < kk(j+1)));
    bad_cip2_habitsd(i,j,2) = length(find(bad_habit(bad_one_sec_locs)=='l' & bad_particle_diameter(bad_one_sec_locs) >=
kk(j) &...
      bad_particle_diameter(bad_one_sec_locs) < kk(j+1)));
    bad_cip2_habitsd(i,j,3) = length(find(bad_habit(bad_one_sec_locs)=='o' & bad_particle_diameter(bad_one_sec_locs)
>= kk(j) &...
      bad_particle_diameter(bad_one_sec_locs) < kk(j+1)));
    bad_cip2_habitsd(i,j,4) = length(find(bad_habit(bad_one_sec_locs)=='t' & bad_particle_diameter(bad_one_sec_locs) >=
kk(j) &...
      bad_particle_diameter(bad_one_sec_locs) < kk(j+1)));
    bad_cip2_habitsd(i,j,5) = length(find(bad_habit(bad_one_sec_locs)=='h' & bad_particle_diameter(bad_one_sec_locs)
>= kk(j) &...
      bad_particle_diameter(bad_one_sec_locs) < kk(j+1)));
    bad_cip2_habitsd(i,j,6) = length(find(bad_habit(bad_one_sec_locs)=='i' & bad_particle_diameter(bad_one_sec_locs) >=
kk(j) &...
      bad_particle_diameter(bad_one_sec_locs) < kk(j+1)));
    bad_cip2_habitsd(i,j,7) = length(find(bad_habit(bad_one_sec_locs)=='g' & bad_particle_diameter(bad_one_sec_locs) >=
kk(j) &...
      bad_particle_diameter(bad_one_sec_locs) < kk(j+1)));
    bad_cip2_habitsd(i,j,8) = length(find(bad_habit(bad_one_sec_locs)=='d' & bad_particle_diameter(bad_one_sec_locs)
>= kk(j) &...
      bad_particle_diameter(bad_one_sec_locs) < kk(j+1)));
    bad_cip2_habitsd(i,j,9) = length(find(bad_habit(bad_one_sec_locs)=='a' & bad_particle_diameter(bad_one_sec_locs) >=
kk(j) &...
      bad_particle_diameter(bad_one_sec_locs) < kk(j+1)));
    bad_cip2_habitsd(i,j,10) = length(find(bad_habit(bad_one_sec_locs)=='I' & bad_particle_diameter(bad_one_sec_locs)
>= kk(j) &...
      bad_particle_diameter(bad_one_sec_locs) < kk(j+1)));

    % Create Habit Mass Size Distribution
    bad_cip2_habitmsd(i,j,1) = sum(bad_iwc(bad_habit(bad_one_sec_locs)=='s' &
bad_particle_diameter(bad_one_sec_locs) >= kk(j) &...
      bad_particle_diameter(bad_one_sec_locs) < kk(j+1)));
    bad_cip2_habitmsd(i,j,2) = sum(bad_iwc(bad_habit(bad_one_sec_locs)=='l' &
bad_particle_diameter(bad_one_sec_locs) >= kk(j) &...
      bad_particle_diameter(bad_one_sec_locs) < kk(j+1)));
    bad_cip2_habitmsd(i,j,3) = sum(bad_iwc(bad_habit(bad_one_sec_locs)=='o' &
bad_particle_diameter(bad_one_sec_locs) >= kk(j) &...
      bad_particle_diameter(bad_one_sec_locs) < kk(j+1)));
    bad_cip2_habitmsd(i,j,4) = sum(bad_iwc(bad_habit(bad_one_sec_locs)=='t' &
bad_particle_diameter(bad_one_sec_locs) >= kk(j) &...
      bad_particle_diameter(bad_one_sec_locs) < kk(j+1)));
    bad_cip2_habitmsd(i,j,5) = sum(bad_iwc(bad_habit(bad_one_sec_locs)=='h' &
bad_particle_diameter(bad_one_sec_locs) >= kk(j) &...
      bad_particle_diameter(bad_one_sec_locs) < kk(j+1)));
```

```
        bad_cip2_habitmsd(i,j,6)            =            sum(bad_iwc(bad_habit(bad_one_sec_locs)=='i'            &
bad_particle_diameter(bad_one_sec_locs) >= kk(j) &...
          bad_particle_diameter(bad_one_sec_locs) < kk(j+1)));
        bad_cip2_habitmsd(i,j,7)            =            sum(bad_iwc(bad_habit(bad_one_sec_locs)=='g'            &
bad_particle_diameter(bad_one_sec_locs) >= kk(j) &...
          bad_particle_diameter(bad_one_sec_locs) < kk(j+1)));
        bad_cip2_habitmsd(i,j,8)            =            sum(bad_iwc(bad_habit(bad_one_sec_locs)=='d'            &
bad_particle_diameter(bad_one_sec_locs) >= kk(j) &...
          bad_particle_diameter(bad_one_sec_locs) < kk(j+1)));
        bad_cip2_habitmsd(i,j,9)            =            sum(bad_iwc(bad_habit(bad_one_sec_locs)=='a'            &
bad_particle_diameter(bad_one_sec_locs) >= kk(j) &...
          bad_particle_diameter(bad_one_sec_locs) < kk(j+1)));
        bad_cip2_habitmsd(i,j,10)            =            sum(bad_iwc(bad_habit(bad_one_sec_locs)=='l'            &
bad_particle_diameter(bad_one_sec_locs) >= kk(j) &...
          bad_particle_diameter(bad_one_sec_locs) < kk(j+1)));


        bad_particle_area(i,j) = nansum(bad_area(bad_one_sec_locs(bad_particle_diameter(bad_one_sec_locs) >= kk(j) &...
          bad_particle_diameter(bad_one_sec_locs) < kk(j+1))));

        bad_cip2_meanp(i,j) = nanmean(bad_perimeter(bad_one_sec_locs(bad_particle_diameter(bad_one_sec_locs) >= kk(j)
&...
          bad_particle_diameter(bad_one_sec_locs) < kk(j+1))));

        if iCreateAspectRatio == 1 % added if statement if not creating aspect ratio - Joe Finlon - 03/03/17
        bad_particle_aspectRatio(i,j)                                                                  =
nanmean(bad_AspectRatio(bad_one_sec_locs1(bad_particle_diameter1(bad_one_sec_locs1) >= kk(j) &...
          bad_particle_diameter1(bad_one_sec_locs1) < kk(j+1))));

        bad_particle_aspectRatio1(i,j)                                                                 =
nanmean(bad_AspectRatio1(bad_one_sec_locs1(bad_particle_diameter1(bad_one_sec_locs1) >= kk(j) &...
          bad_particle_diameter1(bad_one_sec_locs1) < kk(j+1))));
        end

        bad_particle_areaRatio1(i,j) = nanmean(bad_ar1(bad_one_sec_locs1(bad_particle_diameter1(bad_one_sec_locs1) >=
kk(j) &...
          bad_particle_diameter1(bad_one_sec_locs1) < kk(j+1))));


        bad_cip2_iwc(i,j) = nansum(bad_iwc(bad_one_sec_locs(bad_particle_diameter(bad_one_sec_locs) >= kk(j) &...
          bad_particle_diameter(bad_one_sec_locs) < kk(j+1))));

        bad_cip2_partarea(i,j) = nansum(bad_partarea(bad_one_sec_locs(bad_particle_diameter(bad_one_sec_locs) >= kk(j)
&...
          bad_particle_diameter(bad_one_sec_locs) < kk(j+1))));

        bad_cip2_iwcbl(i,j) = nansum(bad_iwcbl(bad_one_sec_locs(bad_particle_diameter(bad_one_sec_locs) >= kk(j) &...
          bad_particle_diameter(bad_one_sec_locs) < kk(j+1))));

        bad_cip2_vt(i,j) = nansum(bad_vt(bad_one_sec_locs(bad_particle_diameter(bad_one_sec_locs) >= kk(j) &...
          bad_particle_diameter(bad_one_sec_locs) < kk(j+1))));

        bad_cip2_pr(i,j) = nansum(bad_pr(bad_one_sec_locs(bad_particle_diameter(bad_one_sec_locs) >= kk(j) &...
          bad_particle_diameter(bad_one_sec_locs) < kk(j+1))));


        for k = 1:length(area_bins)-1
          bad_area_dist2(i,j,k) = length(find(bad_ar(bad_one_sec_locs) >= area_bins(k) & ...
```

```
            bad_ar(bad_one_sec_locs) < area_bins(k+1) & bad_particle_diameter(bad_one_sec_locs) >= kk(j) &...
            bad_particle_diameter(bad_one_sec_locs) < kk(j+1)));
        end
      end

      % Normalize by binwidth and convert from mm to cm
      bad_particle_dist_minR(i,:)=bad_particle_dist_minR(i,:)./binwidth*10;
      bad_particle_dist_AreaR(i,:)=bad_particle_dist_AreaR(i,:)./binwidth*10;
      bad_cip2_iwc(i,:)=bad_cip2_iwc(i,:)./binwidth*10; %g/cm
      bad_cip2_iwcbl(i,:)=bad_cip2_iwcbl(i,:)./binwidth*10;
      bad_cip2_vt(i,:)=bad_cip2_vt(i,:)./binwidth*10;
      bad_cip2_pr(i,:)=bad_cip2_pr(i,:)./binwidth*10;
      bad_cip2_partarea(i,:)=bad_cip2_partarea(i,:)./binwidth*10;
      bad_particle_area(i,:)=bad_particle_area(i,:)./binwidth*10;

      for mmmmmm=1:10
        bad_cip2_habitsd(i,:,mmmmmm)=bad_cip2_habitsd(i,:,mmmmmm)./binwidth*10;
        bad_cip2_habitmsd(i,:,mmmmmm)=bad_cip2_habitmsd(i,:,mmmmmm)./binwidth*10;
      end

      for mmmmmm = 1:length(area_bins)-1
        bad_area_dist2(i,:,mmmmmm)=bad_area_dist2(i,:,mmmmmm)./binwidth*10 ;
      end

      % Generalized effective radius calculation from Fu (1996)
      bad_cip2_re(i)                                                                              =
(sqrt(3)/(3*0.91))*1000*(sum(bad_cip2_iwc(i,:)./binwidth,2)/sum(bad_particle_area(i,:)./binwidth,2))*1000; % in unit of um

    else
      bad_particle_dist_minR(i,1:num_bins) = 0;
      bad_particle_dist_AreaR(i,1:num_bins) = 0;
      bad_area_dist2(i,1:num_bins,1:length(area_bins)-1) = 0;
      bad_cip2_partarea(i,:) = 0;
      bad_cip2_iwc(i,:) = 0;
      bad_cip2_iwcbl(i,:) = 0;
      bad_cip2_vt(i,:) = 0;
      bad_cip2_pr(i,:) = 0;
      bad_cip2_re(i) = 0;
      bad_cip2_habitsd(i,:,:) = 0;
      bad_cip2_habitmsd(i,:,:) = 0;

    end
    end
    warning on all
%    elseif (int32(timehhmmss(i))<int32(starttime(jjj)))
   elseif (eofFlag==1 || int32(timehhmmss(i))<int32(starttime(jjj))) % Modified by Joe Finlon - 03/03/17

    particle_dist_minR(i,1:num_bins) = NaN;
    particle_dist_AreaR(i,1:num_bins) = NaN;
    area_dist2(i,1:num_bins,1:length(area_bins)-1) = NaN;
    cip2_partarea(i,:) = NaN;
    cip2_iwc(i,:) = NaN;
    cip2_iwcbl(i,:) = NaN;
    cip2_vt(i,:) = NaN;
    cip2_pr(i,:) = NaN;
    cip2_re(i) = NaN;
    cip2_habitsd(i,:,:) = NaN;
    cip2_habitmsd(i,:,:) = NaN;
```

```
        one_sec_ar(i) = NaN;
        good_partpercent(i)=1;
        rejectpercentbycriterion(i,:)=NaN;
        numGoodparticles(i)=NaN;
        time_interval2(i) = 1;

        % Legacy: used in Paris intercomparison
        %{
        time_interval22(i) = 1;
        time_interval32(i) = 1;
        time_interval42(i) = 1;
        time_interval52(i) = 0;
        time_interval62(i) = 1;
        %}
        time_interval72(i) = 0;

        TotalPC1(i)=1;
        TotalPC2(i)=1;

    end

end

% Finished Sorting and close input file.
netcdf.close(f);

fprintf('int_arr > 1 mean: %.4f, max: %.4f\nNumber of particles with int_arr > 1: %d\n\n',...
            mean(intArrGT1),max(intArrGT1),sumIntArrGT1);

fprintf('Size distribution calculations and sorting completed %s\n\n', datestr(now));


%% Check TAS length, should be the same
% if (jjj~=length(start_all))
%     disp([jjj, length(start_all)])
%     %error('Watch Out for less TAS time at the end!')
% end

%disp([num2str(100*nThrow11/maxRecNum),'% is thrown out IN TOTAL']);

%% Combine - calculate sample volumes, and divide by sample volumes
% Modified by Will, Nov 27th, 2013. For flexible bins
cip2_binmin = kk(1:end-1);
cip2_binmax = kk(2:end);
cip2_binmid = (cip2_binmin+cip2_binmax)/2;
cip2_bindD = diff(kk);

% Legacy bin and surface area calculations
%{
% cip2_binmin = diodesize/2:diodesize:(num_bins-0.5)*diodesize; %(12.5:25:(num_bins-0.5)*25);
% cip2_binmax = 3*diodesize/2:diodesize:(num_bins+0.5)*diodesize; %(37.5:25:(num_bins+0.5)*25);
% cip2_binmid = diodesize:diodesize:num_bins*diodesize; %(25:25:num_bins*25);
% cip2_bindD = diodesize*ones(1,num_bins);

% sa2 = calc_sa(num_bins,res,armdst,num_bins);  %mm2
% switch probename
%     case 'PIP'
%         sa2 = calc_sa_randombins_PIP(cip2_binmid,res,armdst,num_diodes, SAmethod); %(bins_mid,res,armdst,num_diodes)
```

```
%     case '2DS'
%         sa2 = calc_sa_randombins(cip2_binmid,res,armdst,num_diodes, SAmethod); %(bins_mid,res,armdst,num_diodes)
% end
%}

sa2 = calc_sa_randombins(cip2_binmid,res,armdst,num_diodes,SAmethod, probetype); %(bins_mid,res,armdst,num_diodes)

% Clocking problem correction
vol_scale_factor = tas/tasMax;
vol_scale_factor(vol_scale_factor < 1) = 1;

TotalPC2_pre = TotalPC2;

if probetype==2
   time_interval200=1-time_interval72';

elseif probetype==1
            % Correct offset in probe particle count (TotalPC2) when we have negative values
   TotalPC2(TotalPC2<0)=TotalPC2(TotalPC2<0)+2^16;

            % Derive a linear scale factor based on the difference between number of images (TotalPC1)
            % and number of particles counted by the probe (TotalPC2).
   time_interval199=(TotalPC1./TotalPC2)';

elseif 0==probetype
   time_interval200=1-time_interval72';
end

% Experimental - Use with care!
% It was discovered that for data collected during the PECAN project, there were quite
% a few periods of time when the number of images we had for a 1-sec period of time was
% up to twice that of the number of particles the probe counted.
% This next if-statement contains code to find and change these instances to 1, resolving
% the far exaggerated concentrations that resulted otherwise.

if probetype==1
%           TotalPCerrIx = find(time_interval199 > 1);
            time_interval200 = time_interval199;
%           time_interval200(TotalPCerrIx) = 1;
%   fprintf(['Total image count exceeded probe particle count %d times\ntime_interval200',...
%       ' was set to 1 in these cases. See TotalPCerrIx variable for indices of occurence.\n\n'],...
%       length(TotalPCerrIx)); % moved inside if statement - Joe Finlon - 03/03/17
end
% disp(time_interval200)

for j=1:num_bins
   % Sample volume is in m-3
%     svol_old(j,:)=dof/100.*sa/100.*tas;
   svol2(j,:) = sa2(j)*(1e-3)^2*time_interval200.*tas; %m3 .*vol_scale_factor
end

svol2 = svol2*100^3; %cm3

for j = 1:10
   svol2a(:,:,j) = svol2';
end

% Good (accepted) particles
```

```
cip2_conc_minR  = particle_dist_minR./svol2';
cip2_conc_AreaR = particle_dist_AreaR./svol2';
cip2_area = particle_area./svol2';
cip2_partarea = cip2_partarea./svol2';
cip2_iwc = cip2_iwc./svol2';
cip2_iwcbl = cip2_iwcbl./svol2';
cip2_vt = cip2_vt./svol2';
cip2_pr = cip2_pr./svol2';

cip2_countP_no  = particle_dist_minR.*repmat(binwidth,[length(tas) 1])/10; % un-normalized by binwitdh - Joe Finlon - 03/03/17
cip2_conc_areaDist = permute(double(area_dist2)./svol2a, [3 2 1]);
cip2_n = nansum(cip2_conc_minR.*repmat(binwidth,[length(tas) 1]),2)/10; % un-normalized by binwitdh & converted to cm^-3
- Joe Finlon - 03/03/17
cip2_lwc = lwc_calc(cip2_conc_minR,cip2_binmid);

% Bad (rejected) particles
bad_cip2_conc_minR  = bad_particle_dist_minR./svol2';
bad_cip2_conc_AreaR = bad_particle_dist_AreaR./svol2';
bad_cip2_area = bad_particle_area./svol2';
bad_cip2_partarea = bad_cip2_partarea./svol2';
bad_cip2_iwc = bad_cip2_iwc./svol2';
bad_cip2_iwcbl = bad_cip2_iwcbl./svol2';
bad_cip2_vt = bad_cip2_vt./svol2';
bad_cip2_pr = bad_cip2_pr./svol2';

bad_cip2_countP_no  = bad_particle_dist_minR.*repmat(binwidth,[length(tas) 1])/10; % un-normalized by binwitdh - Joe Finlon
- 03/03/17
bad_cip2_conc_areaDist = permute(double(bad_area_dist2)./svol2a, [3 2 1]);
bad_cip2_n = nansum(bad_cip2_conc_minR.*repmat(binwidth,[length(tas) 1]),2)/10; % un-normalized by binwitdh & converted
to cm^-3 - Joe Finlon - 03/03/17
bad_cip2_lwc = lwc_calc(bad_cip2_conc_minR,cip2_binmid);



%% Output results into NETCDF files (mainf)

fprintf('Now writing output files %s\n\n',datestr(now));

if applyIntArrThresh
		save([outfile(1:end-3) 'noShatters.mat']);
else
		save([outfile(1:end-3) 'withShatters.mat']);
end


% Define Dimensions
dimid0 = netcdf.defDim(mainf,'CIPcorrlen',num_bins);
dimid1 = netcdf.defDim(mainf,'CIParealen',10);
dimid2 = netcdf.defDim(mainf,'Time',length(timehhmmss));
dimid3 = netcdf.defDim(mainf,'Habit',10);

% Define Global Attributes
NC_GLOBAL = netcdf.getConstant('NC_GLOBAL');
netcdf.putAtt(mainf, NC_GLOBAL, 'Software', 'UIOPS/sizeDist');
netcdf.putAtt(mainf, NC_GLOBAL, 'Institution', 'Univ. Illinois, Dept. Atmos. Sciences');
netcdf.putAtt(mainf, NC_GLOBAL, 'Creation Time', datestr(now, 'yyyy/mm/dd HH:MM:SS'));
netcdf.putAtt(mainf, NC_GLOBAL, 'Description', ['Contains size distributions of ',...
   'particle count, mass, etc. & various bulk properties.']);
```

```
netcdf.putAtt(mainf, NC_GLOBAL, 'Project', projectname);
netcdf.putAtt(mainf, NC_GLOBAL, 'Data Source', infile);
netcdf.putAtt(mainf, NC_GLOBAL, 'Probe Type', probename);
if SAmethod==0
   netcdf.putAtt(mainf, NC_GLOBAL, 'SA Method', 'Center-in');
elseif SAmethod==1
   netcdf.putAtt(mainf, NC_GLOBAL, 'SA Method', 'Entire-in');
elseif SAmethod==2
   netcdf.putAtt(mainf, NC_GLOBAL, 'SA Method', 'Using Heymsfield & Parrish (1978) correction');
end
if d_choice==1
   netcdf.putAtt(mainf, NC_GLOBAL, 'Dmax Definition', 'L_x');
elseif d_choice==2
   netcdf.putAtt(mainf, NC_GLOBAL, 'Dmax Definition', 'L_y');
elseif d_choice==3
   netcdf.putAtt(mainf, NC_GLOBAL, 'Dmax Definition', 'mean(L_x,L_y)');
elseif d_choice==4
   netcdf.putAtt(mainf, NC_GLOBAL, 'Dmax Definition', 'hypotenuse(L_x,L_y)');
elseif d_choice==5
   netcdf.putAtt(mainf, NC_GLOBAL, 'Dmax Definition', 'max(L_x,L_y)');
elseif d_choice==6
   netcdf.putAtt(mainf, NC_GLOBAL, 'Dmax Definition', 'D of minimum enclosing circle');
end
if applyIntArrThresh && reaccptShatrs
   netcdf.putAtt(mainf, NC_GLOBAL, 'Shattering Algorithm',...
      'Applied w/ reacceptance of particles');
   netcdf.putAtt(mainf, NC_GLOBAL, 'Reacceptance Criteria',...
      ['D > ', num2str(reaccptD*1000), ' um; inter-arrival < ',...
      num2str(reaccptMaxIA), ' sec'])
elseif applyIntArrThresh && ~reaccptShatrs
   netcdf.putAtt(mainf, NC_GLOBAL, 'Shattering Algorithm',...
      'Applied without reacceptance of particles');
else
   netcdf.putAtt(mainf, NC_GLOBAL, 'Shattering Algorithm', 'Not applied');
end
if iCreateBad && iCreateAspectRatio && iSaveIntArrSV
   netcdf.putAtt(mainf, NC_GLOBAL, 'Optional Parameters Saved',...
      'SDs from rejected particles, SDs w/ aspect ratio, Sample volume info');
elseif iCreateBad && ~iCreateAspectRatio && iSaveIntArrSV
   netcdf.putAtt(mainf, NC_GLOBAL, 'Optional Parameters Saved',...
      'SDs from rejected particles, Sample volume info');
elseif iCreateBad && iCreateAspectRatio && ~iSaveIntArrSV
   netcdf.putAtt(mainf, NC_GLOBAL, 'Optional Parameters Saved',...
      'SDs from rejected particles, SDs w/ aspect ratio');
elseif iCreateBad && ~iCreateAspectRatio && ~iSaveIntArrSV
   netcdf.putAtt(mainf, NC_GLOBAL, 'Optional Parameters Saved',...
      'SDs from rejected particles');
elseif ~iCreateBad && iCreateAspectRatio && iSaveIntArrSV
   netcdf.putAtt(mainf, NC_GLOBAL, 'Optional Parameters Saved',...
      'SDs w/ aspect ratio, Sample volume info');
elseif ~iCreateBad && ~iCreateAspectRatio && iSaveIntArrSV
   netcdf.putAtt(mainf, NC_GLOBAL, 'Optional Parameters Saved',...
      'Sample volume info');
elseif ~iCreateBad && iCreateAspectRatio && ~iSaveIntArrSV
   netcdf.putAtt(mainf, NC_GLOBAL, 'Optional Parameters Saved',...
      'SDs w/ aspect ratio');
else
   netcdf.putAtt(mainf, NC_GLOBAL, 'Optional Parameters Saved', 'None');
```

```
end

% Define Variables
varid0 = netcdf.defVar(mainf,'time','double',dimid2);
netcdf.putAtt(mainf, varid0,'units','HHMMSS');
netcdf.putAtt(mainf, varid0,'name','Time');

varid1 = netcdf.defVar(mainf,'bin_min','double',dimid0);
netcdf.putAtt(mainf, varid1,'units','millimeter');
netcdf.putAtt(mainf, varid1,'long_name','bin minimum size');
netcdf.putAtt(mainf, varid1,'short_name','bin min');

varid2 = netcdf.defVar(mainf,'bin_max','double',dimid0);
netcdf.putAtt(mainf, varid2,'units','millimeter');
netcdf.putAtt(mainf, varid2,'long_name','bin maximum size');
netcdf.putAtt(mainf, varid2,'short_name','bin max');

varid3 = netcdf.defVar(mainf,'bin_mid','double',dimid0);
netcdf.putAtt(mainf, varid3,'units','millimeter');
netcdf.putAtt(mainf, varid3,'long_name','bin midpoint size');
netcdf.putAtt(mainf, varid3,'short_name','bin mid');

varid4 = netcdf.defVar(mainf,'bin_dD','double',dimid0);
netcdf.putAtt(mainf, varid4,'units','millimeter');
netcdf.putAtt(mainf, varid4,'long_name','bin size');
netcdf.putAtt(mainf, varid4,'short_name','bin size');

% Good (accepted) particles
varid5 = netcdf.defVar(mainf,'conc_minR','double',[dimid0 dimid2]);
netcdf.putAtt(mainf, varid5,'units','cm-4');
netcdf.putAtt(mainf, varid5,'long_name','Size distribution using Dmax');
netcdf.putAtt(mainf, varid5,'short_name','N(Dmax)');

varid6 = netcdf.defVar(mainf,'area','double',[dimid1 dimid0 dimid2]);
netcdf.putAtt(mainf, varid6,'units','cm-4');
netcdf.putAtt(mainf, varid6,'long_name','binned area ratio');
netcdf.putAtt(mainf, varid6,'short_name','binned area ratio');

varid7 = netcdf.defVar(mainf,'conc_AreaR','double',[dimid0 dimid2]);
netcdf.putAtt(mainf, varid7,'units','cm-4');
netcdf.putAtt(mainf, varid7,'long_name','Size distribution using area-equivalent Diameter');
netcdf.putAtt(mainf, varid7,'short_name','N(Darea)');

varid8 = netcdf.defVar(mainf,'n','double',dimid2);
netcdf.putAtt(mainf, varid8,'units','cm-3');
netcdf.putAtt(mainf, varid8,'long_name','number concentration');
netcdf.putAtt(mainf, varid8,'short_name','N');

varid9 = netcdf.defVar(mainf,'total_area','double',[dimid0 dimid2]);
netcdf.putAtt(mainf, varid9,'units','mm2/cm4');
netcdf.putAtt(mainf, varid9,'long_name','projected area (extinction)');
netcdf.putAtt(mainf, varid9,'short_name','Ac');

varid10 = netcdf.defVar(mainf,'mass','double',[dimid0 dimid2]);
netcdf.putAtt(mainf, varid10,'units','g/cm4');
netcdf.putAtt(mainf, varid10,'long_name','mass using m-D relations');
netcdf.putAtt(mainf, varid10,'short_name','mass');
```

```
varid11 = netcdf.defVar(mainf,'habitsd','double',[dimid3 dimid0 dimid2]);
netcdf.putAtt(mainf, varid11,'units','cm-4');
netcdf.putAtt(mainf, varid11,'long_name','Size Distribution with Habit');
netcdf.putAtt(mainf, varid11,'short_name','habit SD');

varid12 = netcdf.defVar(mainf,'re','double',dimid2);
netcdf.putAtt(mainf, varid12,'units','mm');
netcdf.putAtt(mainf, varid12,'long_name','effective radius');
netcdf.putAtt(mainf, varid12,'short_name','Re');

varid13 = netcdf.defVar(mainf,'ar','double',dimid2);
netcdf.putAtt(mainf, varid13,'units','100/100');
netcdf.putAtt(mainf, varid13,'long_name','Area Ratio');
netcdf.putAtt(mainf, varid13,'short_name','AR');

varid14 = netcdf.defVar(mainf,'massBL','double',[dimid0 dimid2]);
netcdf.putAtt(mainf, varid14,'units','g/cm4');
netcdf.putAtt(mainf, varid14,'long_name','mass using Baker and Lawson method');
netcdf.putAtt(mainf, varid14,'short_name','mass_BL');

varid15 = netcdf.defVar(mainf,'Reject_ratio','double',dimid2);
netcdf.putAtt(mainf, varid15,'units','100/100');
netcdf.putAtt(mainf, varid15,'long_name','Reject Ratio');

varid16 = netcdf.defVar(mainf,'vt','double',[dimid0 dimid2]);
netcdf.putAtt(mainf, varid16,'units','g/cm4');
netcdf.putAtt(mainf, varid16,'long_name','Mass-weighted terminal velocity');

varid17 = netcdf.defVar(mainf,'Prec_rate','double',[dimid0 dimid2]);
netcdf.putAtt(mainf, varid17,'units','mm/hr');
netcdf.putAtt(mainf, varid17,'long_name','Precipitation Rate');

varid18 = netcdf.defVar(mainf,'habitmsd','double',[dimid3 dimid0 dimid2]);
netcdf.putAtt(mainf, varid18,'units','g/cm-4');
netcdf.putAtt(mainf, varid18,'long_name','Mass Size Distribution with Habit');
netcdf.putAtt(mainf, varid18,'short_name','Habit Mass SD');

varid19 = netcdf.defVar(mainf,'Calcd_area','double',[dimid0 dimid2]);
netcdf.putAtt(mainf, varid19,'units','mm^2/cm4');
netcdf.putAtt(mainf, varid19,'long_name','Particle Area Calculated using A-D realtions');
netcdf.putAtt(mainf, varid19,'short_name','Ac_calc');

varid20 = netcdf.defVar(mainf,'count','double',[dimid0 dimid2]);
netcdf.putAtt(mainf, varid20,'units','1');
netcdf.putAtt(mainf, varid20,'long_name','number count for partial images without any correction');

if iCreateAspectRatio == 1
varid21 = netcdf.defVar(mainf,'mean_aspect_ratio_rectangle','double',[dimid0 dimid2]);
netcdf.putAtt(mainf, varid21,'units','1');
netcdf.putAtt(mainf, varid21,'long_name','Aspect Ratio by Rectangle fit');

varid22 = netcdf.defVar(mainf,'mean_aspect_ratio_ellipse','double',[dimid0 dimid2]);
netcdf.putAtt(mainf, varid22,'units','1');
netcdf.putAtt(mainf, varid22,'long_name','Aspect Ratio by Ellipse fit');
end
varid23 = netcdf.defVar(mainf,'mean_area_ratio','double',[dimid0 dimid2]);
netcdf.putAtt(mainf, varid23,'units','1');
netcdf.putAtt(mainf, varid23,'long_name','Area Ratio');
```

```
varid24 = netcdf.defVar(mainf,'mean_perimeter','double',[dimid0 dimid2]);
netcdf.putAtt(mainf, varid24,'units','um');
netcdf.putAtt(mainf, varid24,'long_name','mean perimeter');

if iCreateBad == 1

% Bad (rejected) particles
varid25 = netcdf.defVar(mainf,'REJ_conc_minR','double',[dimid0 dimid2]);
netcdf.putAtt(mainf, varid25,'units','cm-4');
netcdf.putAtt(mainf, varid25,'long_name','Size distribution of rejected particles using Dmax');
netcdf.putAtt(mainf, varid25,'short_name','N(Dmax) rejected');

varid26 = netcdf.defVar(mainf,'REJ_area','double',[dimid1 dimid0 dimid2]);
netcdf.putAtt(mainf, varid26,'units','cm-4');
netcdf.putAtt(mainf, varid26,'long_name','binned area ratio of rejected particles');
netcdf.putAtt(mainf, varid26,'short_name','binned area ratio of rejected particles');

varid27 = netcdf.defVar(mainf,'REJ_conc_AreaR','double',[dimid0 dimid2]);
netcdf.putAtt(mainf, varid27,'units','cm-4');
netcdf.putAtt(mainf, varid27,'long_name','Size distribution of rejected particles using area-equivalent Diameter');
netcdf.putAtt(mainf, varid27,'short_name','N(Darea) rejected');

varid28 = netcdf.defVar(mainf,'REJ_n','double',dimid2);
netcdf.putAtt(mainf, varid28,'units','cm-3');
netcdf.putAtt(mainf, varid28,'long_name','number concentration of rejected particles');
netcdf.putAtt(mainf, varid28,'short_name','N_rejected');

varid29 = netcdf.defVar(mainf,'REJ_total_area','double',[dimid0 dimid2]);
netcdf.putAtt(mainf, varid29,'units','mm2/cm4');
netcdf.putAtt(mainf, varid29,'long_name','projected area (extinction) of rejected particles');
netcdf.putAtt(mainf, varid29,'short_name','Ac_rejected');

varid30 = netcdf.defVar(mainf,'REJ_mass','double',[dimid0 dimid2]);
netcdf.putAtt(mainf, varid30,'units','g/cm4');
netcdf.putAtt(mainf, varid30,'long_name','mass of rejected particles using m-D relations');
netcdf.putAtt(mainf, varid30,'short_name','mass_rejected');

varid31 = netcdf.defVar(mainf,'REJ_habitsd','double',[dimid3 dimid0 dimid2]);
netcdf.putAtt(mainf, varid31,'units','cm-4');
netcdf.putAtt(mainf, varid31,'long_name','Size Distribution with Habit of rejected particles');
netcdf.putAtt(mainf, varid31,'short_name','habit SD rejected');

varid32 = netcdf.defVar(mainf,'REJ_re','double',dimid2);
netcdf.putAtt(mainf, varid32,'units','mm');
netcdf.putAtt(mainf, varid32,'long_name','effective radius of rejected particles');
netcdf.putAtt(mainf, varid32,'short_name','Re_rejected');

varid33 = netcdf.defVar(mainf,'REJ_ar','double',dimid2);
netcdf.putAtt(mainf, varid33,'units','100/100');
netcdf.putAtt(mainf, varid33,'long_name','Area Ratio of rejected particles');
netcdf.putAtt(mainf, varid33,'short_name','AR_rejected');

varid34 = netcdf.defVar(mainf,'REJ_massBL','double',[dimid0 dimid2]);
netcdf.putAtt(mainf, varid34,'units','g/cm4');
netcdf.putAtt(mainf, varid34,'long_name','mass of rejected particles using Baker and Lawson method');
netcdf.putAtt(mainf, varid34,'short_name','mass_BL_rejected');
```

```
varid35 = netcdf.defVar(mainf,'REJ_vt','double',[dimid0 dimid2]);
netcdf.putAtt(mainf, varid35,'units','g/cm4');
netcdf.putAtt(mainf, varid35,'long_name','Mass-weighted terminal velocity of rejected particles');

varid36 = netcdf.defVar(mainf,'REJ_Prec_rate','double',[dimid0 dimid2]);
netcdf.putAtt(mainf, varid36,'units','mm/hr');
netcdf.putAtt(mainf, varid36,'long_name','Precipitation Rate of rejected particles');

varid37 = netcdf.defVar(mainf,'REJ_habitmsd','double',[dimid3 dimid0 dimid2]);
netcdf.putAtt(mainf, varid37,'units','g/cm-4');
netcdf.putAtt(mainf, varid37,'long_name','Mass Size Distribution with Habit of rejected particles');
netcdf.putAtt(mainf, varid37,'short_name','Habit Mass SD rejected');

varid38 = netcdf.defVar(mainf,'REJ_Calcd_area','double',[dimid0 dimid2]);
netcdf.putAtt(mainf, varid38,'units','mm^2/cm4');
netcdf.putAtt(mainf, varid38,'long_name','Particle Area of rejected particles Calculated using A-D realtions');
netcdf.putAtt(mainf, varid38,'short_name','Ac_calc_rejected');

varid39 = netcdf.defVar(mainf,'REJ_count','double',[dimid0 dimid2]);
netcdf.putAtt(mainf, varid39,'units','1');
netcdf.putAtt(mainf, varid39,'long_name','number count of rejected particles for partial images without any correction');

varid40 = netcdf.defVar(mainf,'REJ_mean_aspect_ratio_rectangle','double',[dimid0 dimid2]);
netcdf.putAtt(mainf, varid40,'units','1');
netcdf.putAtt(mainf, varid40,'long_name','Aspect Ratio of rejected particles by Rectangle fit');

varid41 = netcdf.defVar(mainf,'REJ_mean_aspect_ratio_ellipse','double',[dimid0 dimid2]);
netcdf.putAtt(mainf, varid41,'units','1');
netcdf.putAtt(mainf, varid41,'long_name','Aspect Ratio of rejected particles by Ellipse fit');

varid42 = netcdf.defVar(mainf,'REJ_mean_area_ratio','double',[dimid0 dimid2]);
netcdf.putAtt(mainf, varid42,'units','1');
netcdf.putAtt(mainf, varid42,'long_name','Area Ratio of rejected particles');

varid43 = netcdf.defVar(mainf,'REJ_mean_perimeter','double',[dimid0 dimid2]);
netcdf.putAtt(mainf, varid43,'units','um');
netcdf.putAtt(mainf, varid43,'long_name','mean perimeter of rejected particles');
end

if iSaveIntArrSV == 1
varid44 = netcdf.defVar(mainf,'sum_IntArr','double',dimid2);
netcdf.putAtt(mainf, varid44,'units','s');
netcdf.putAtt(mainf, varid44,'long_name','sum of inter-arrival times, excluding the overload time for particles affected by saving
of image data');

varid45 = netcdf.defVar(mainf,'sample_vol','double',[dimid0 dimid2]);
netcdf.putAtt(mainf, varid45,'units','cm^3');
netcdf.putAtt(mainf, varid45,'long_name','sample volume for each bin');
end

netcdf.endDef(mainf)

% Output Variables
netcdf.putVar ( mainf, varid0, timehhmmss );
netcdf.putVar ( mainf, varid1, cip2_binmin );
netcdf.putVar ( mainf, varid2, cip2_binmax );
netcdf.putVar ( mainf, varid3, cip2_binmid );
netcdf.putVar ( mainf, varid4, cip2_bindD );
```

```
% Good (accepted) particles
netcdf.putVar ( mainf, varid5, cip2_conc_minR' );
netcdf.putVar ( mainf, varid6, cip2_conc_areaDist);
netcdf.putVar ( mainf, varid7, cip2_conc_AreaR' );
netcdf.putVar ( mainf, varid8, cip2_n);
netcdf.putVar ( mainf, varid9, cip2_area');
netcdf.putVar ( mainf, varid10, cip2_iwc');
netcdf.putVar ( mainf, varid11, permute(double(cip2_habitsd)./svol2a, [3 2 1]) );
netcdf.putVar ( mainf, varid12, cip2_re );
netcdf.putVar ( mainf, varid13, one_sec_ar );
netcdf.putVar ( mainf, varid14, cip2_iwcbl' );
netcdf.putVar ( mainf, varid15, 1-good_partpercent );
netcdf.putVar ( mainf, varid16, cip2_vt' );
netcdf.putVar ( mainf, varid17, cip2_pr' );
netcdf.putVar ( mainf, varid18, permute(double(cip2_habitmsd)./svol2a, [3 2 1]) );
netcdf.putVar ( mainf, varid19, cip2_partarea');
netcdf.putVar ( mainf, varid20, cip2_countP_no');
if iCreateAspectRatio == 1
netcdf.putVar ( mainf, varid21, particle_aspectRatio);
netcdf.putVar ( mainf, varid22, particle_aspectRatio1);
end
netcdf.putVar ( mainf, varid23, particle_areaRatio1);
netcdf.putVar ( mainf, varid24, cip2_meanp');

if iCreateBad == 1

% Bad (rejected) particles
netcdf.putVar ( mainf, varid25, bad_cip2_conc_minR' );
netcdf.putVar ( mainf, varid26, bad_cip2_conc_areaDist);
netcdf.putVar ( mainf, varid27, bad_cip2_conc_AreaR' );
netcdf.putVar ( mainf, varid28, bad_cip2_n);
netcdf.putVar ( mainf, varid29, bad_cip2_area');
netcdf.putVar ( mainf, varid30, bad_cip2_iwc');
netcdf.putVar ( mainf, varid31, permute(double(bad_cip2_habitsd)./svol2a, [3 2 1]) );
netcdf.putVar ( mainf, varid32, bad_cip2_re );
netcdf.putVar ( mainf, varid33, bad_one_sec_ar );
netcdf.putVar ( mainf, varid34, bad_cip2_iwcbl' );
netcdf.putVar ( mainf, varid35, bad_cip2_vt' );
netcdf.putVar ( mainf, varid36, bad_cip2_pr' );
netcdf.putVar ( mainf, varid37, permute(double(bad_cip2_habitmsd)./svol2a, [3 2 1]) );
netcdf.putVar ( mainf, varid38, bad_cip2_partarea');
netcdf.putVar ( mainf, varid39, bad_cip2_countP_no');
netcdf.putVar ( mainf, varid40, bad_particle_aspectRatio);
netcdf.putVar ( mainf, varid41, bad_particle_aspectRatio1);
netcdf.putVar ( mainf, varid42, bad_particle_areaRatio1);
netcdf.putVar ( mainf, varid43, bad_cip2_meanp');
end

if iSaveIntArrSV == 1
   % Inter-arrival time and sample volume information
netcdf.putVar ( mainf, varid44, time_interval200');
netcdf.putVar ( mainf, varid45, svol2);
end

netcdf.close(mainf) % Close output NETCDF file
fprintf('sizeDist.m script completed %s\n',datestr(now));
end
```

6 REFERENCES

Abel, S. J. and Boutle, I. A.: An improved representation of the raindrop size distribution for single-moment microphysics schemes, Q. J. Roy. Meteorol. Soc., 138, 2151–2162, https://doi.org/10.1002/qj.1949, 2012.

Abel, S. J., Barrett, P. A., Zuidema, P., Zhang, J., Christensen, M., Peers, F., Taylor, J. W., Crawford, I., Bower, K. N., and Flynn, M.: Open cells exhibit weaker entrainment of free-tropospheric biomass burning aerosol into the south-east Atlantic boundary layer, Atmos. Chem. Phys., 20, 4059–4084, https://doi.org/10.5194/acp-20-4059-2020, 2020.

Ackerman, A. S., Kirkpatrick, M. P., Stevens, D. E., and Toon, O. B.: The impact of humidity above stratiform clouds on indirect aerosol climate forcing, Nature, 432, 1014–1017, 2004.

Ackerman, A. S., Toon, O. B., Stevens, D. E., Heymsfield, A. J., Ramanathan, V., and Welton, E. J.: Reduction of tropical cloudiness by soot, Science, 288, 1042–1047, 2000.

Adebiyi, A. A. and Zuidema, P.: The role of the southern African easterly jet in modifying the southeast Atlantic aerosol and cloud environments, Q. J. Roy. Meteor. Soc., 142, 1574–1589, https://doi.org/10.1002/qj.2765, 2016.

Afchine, A., Rolf, C., Costa, A., Spelten, N., Riese, M., Buchholz, B., Ebert, V., Heller, R., Kaufmann, S., Minikin, A., Voigt, C., Zöger, M., Smith, J., Lawson, P., Lykov, A., Khaykin, S., and Krämer, M.: Ice particle sampling from aircraft – influence of the probing position on the ice water content, Atmos. Meas. Tech., 11, 4015–4031, https://doi.org/10.5194/amt-11-4015-2018, 2018.

Ahlgrimm M, Randall DA, Kohler M.. Evaluating cloud frequency of ¨ occurrence and cloud-top height using spaceborne lidar observations. Mon. Weather Rev. 137: 4225–4237, 2009.

Ahlgrimm, M. and Forbes, R.: Improving the Representation of Low Clouds and Drizzle in the ECMWF Model Based on ARM Observations from the Azores, Mon. Weather Rev., 142, 668– 685, doi:10.1175/mwr-d-13-00153.1, 2014.

Ahn, E., Huang, Y., Siems, S. T., and Manton, M. J.: A comparison of cloud microphysical properties derived from MODIS and CALIPSO with in situ measurements over the wintertime Southern Ocean, J. Geophys. Res.-Atmos., 123, 11120–11140, https://doi.org/10.1029/2018JD028535, 2018.

Albrecht, B.: Aerosols, Cloud Microphysics, and Fractional Cloudiness, Science, 245, 1227–1230, 1989.

Alexandrov, M. D., Cairns, B., Emde, C., Ackerman, A. S., and van Diedenhoven, B.: Accuracy assessments of cloud droplet size retrievals from polarized reflectance measurements by the research scanning polarimeter, Remote Sens. Environ., 125, 92–111, https://doi.org/10.1016/j.rse.2012.07.012, 2012.

Bai, H., Gong, C., Wang, M., Zhang, Z., and L'Ecuyer, T.: Estimating precipitation susceptibility in warm marine clouds using multi-sensor aerosol and cloud products from A-Train satellites, Atmos. Chem. Phys., 18, 1763–1783, https://doi.org/10.5194/acp-18-1763-2018, 2018.

Baumgardner, D., Abel, S. J., Axisa, D., Cotton, R., Crosier, J., Field, P., Gurganus, C., Heymsfield, A., Korolev, A., Kraemer, M., Lawson, P., McFarquhar, G., Ulanowski, Z., and Um, J.: Cloud ice properties: in situ measurement challenges, Meteor. Monographs, 58, 9.1–9.23, https://doi.org/10.1175/AMSMONOGRAPHS-D-16-0011.1, 2017.

Baumgardner, D., Jonsson, H., Dawson, W., Connor, D. O., and Newton, R.: The cloud, aerosol and precipitation spectrometer (CAPS): A new instrument for cloud investigations, Atmos. Res., 59, 59–60, 2001.

Behrangi, A., Stephens, G., Adler, R. F., Huffman, G. J., Lambrigtsen, B., and Lebsock, M.: An update on the oceanic precipitation rate and its zonal distribution in light of advanced observations from space, J. Climate, 27, 3957–3965, https://doi.org/10.1175/JCLI-D-13-00679.1, 2014.

Bennartz, R.: Global assessment of marine boundary layer cloud droplet number concentration from satellite, J. Geophys. Res., 112, D02201, doi:10.1029/2006JD007547, 2007.

Boers, R., Acarreta, J. R., and Gras, J. L.: Satellite monitoring of the first indirect aerosol effect: Retrieval of the droplet concentration of water clouds, J. Geophys. Res.-Atmos., 111, D22208, https://doi.org/10.1029/2005JD006838, 2006.

Bony, S. and Dufrense, J.-L.: Marine boundary layer clouds at the heart of tropical feedback uncertainties in climate models, Geophys. Res. Lett., 32, L20806, doi:10.1029/2005GL023851, 2005.

Boucher, O., Randall, D., Artaxo, P., Bretherton, C., Feingold, G., Forster, P., Kerminen, V.-M., Kondo, Y., Liao, H., Lohmann, U., Rasch, P., Satheesh, S. K., Sherwood, S., Stevens, B., and Zhang, X. Y.: Clouds and Aerosols. In: Climate Change 2013: The Physical Science Basis, Contribution of Working Group I to the Fifth Assessment Report of the Intergovernmental Panel on Climate Change, edited by: Stocker, T. F., Qin, D., Plattner, G.-K., Tignor, M., Allen, S. K., Boschung, J., Nauels, A., Xia, Y., Bex, V., and Midgley, P. M., Cambridge University Press, Cambridge, United Kingdom and New York, NY, USA, 571–657, 2013.

Boutle, I. A., Abel, S. J., Hill, P. G., and Morcrette, C. J.: Spatial variability of liquid cloud and rain: observations and microphysical effects, Q. J. Roy. Meteorol. Soc., 140, 583–594, https://doi.org/10.1002/qj.2140, 2014.

Braun, R. A., Dadashazar, H., MacDonald, A. B., Crosbie, E., Jonsson, H. H., Woods, R. K., Flagan, R. C., Seinfeld, J. H., and Sorooshian, A.: Cloud Adiabaticity and Its Relationship to Marine Stratocumulus Characteristics Over the Northeast Pacific Ocean, J. Geophys. Res.-Atmos., 123, 13790–13806, https://doi.org/10.1029/2018JD029287, 2018.

Brenguier, J.-L., Burnet, F., and Geoffroy, O.: Cloud optical thickness and liquid water path – does the *k* coefficient vary with droplet concentration?, Atmos. Chem. Phys., 11, 9771–9786, https://doi.org/10.5194/acp-11-9771-2011, 2011.

Brenguier, J.-L., Pawlowska, H., Schüller, L., Preusker, R., Fischer, J., and Fouquart, Y.: Radiative properties of boundary layer clouds: Droplet effective radius versus number concentration, J. Atmos. Sci., 57, 803–821, 2000.

Bretherton, C. S., Wood, R., George, R. C., Leon, D., Allen, G., and Zheng, X.: Southeast Pacific stratocumulus clouds, precipitation and boundary layer structure sampled along 20° S during VOCALS-REx, Atmos. Chem. Phys., 10, 10639–10654, https://doi.org/10.5194/acp-10-10639-2010, 2010.

Brioude, J., Cooper, O. R., Feingold, G., Trainer, M., Freitas, S. R., Kowal, D., Ayers, J. K., Prins, E., Minnis, P., McKeen, S. A., Frost, G. J., and Hsie, E.-Y.: Effect of biomass burning on marine stratocumulus clouds off the California coast, Atmos. Chem. Phys., 9, 8841–8856, https://doi.org/10.5194/acp-9-8841-2009, 2009.

Cai, Y., Snider, J. R., and Wechsler, P.: Calibration of the passive cavity aerosol spectrometer probe for airborne determination of the size distribution, Atmos. Meas. Tech., 6, 2349–2358, https://doi.org/10.5194/amt-6-2349-2013, 2013.

CDS, ERA5: Fifth generation of ECMWF atmospheric reanalyses of the global climate, https://cds.climate.copernicus. eu/cdsapp#!/home, accessed 2019-11-26, 2017.

Chand, D., Wood, R., Anderson, T. L., Satheesh, S. K., and Charlson, R. J.: Satellite-derived direct radiative effect of aerosols dependent on cloud cover, Nat. Geosci., 2, 181–184, 2009.

Chang, F.-L. and Li, Z.: Estimating the vertical variation of cloud droplet effective radius using multispectral near-infrared satellite measurements, J. Geophys. Res., 107, AAC 7-1–AAC 7-12, https://doi.org/10.1029/2001JD0007666, 2002.

Chang, I., Gao, L., Burton, S. P., Chen, H., Diamond, M., Ferrare, R. A., Flynn, C. J., Kacenelenbogen, M., LeBlanc, S. E., Meyer, K. G., Pistone, K., Schmidt, S., Segal-Rozenhaimer, M., Shinozuka, Y., Wood, R., Zuidema, P., Redemann, J., and Christopher, S. A.: Spatiotemporal heterogeneity of aerosol and cloud properties over the southeast Atlantic: An observational analysis, Geophys. Res. Lett., 48, e2020GL091469, https://doi.org/10.1029/2020GL091469, 2021.

Chen, Y.-C., Christensen, M. W., Stephens, G. L., and Seinfeld, J. H.: Satellite-based estimate of global aerosol–cloud radiative forcing by marine warm clouds, Nat. Geosci., 7, 643–646, doi:10.1038/ngeo2214, 2014.

Christensen, M. W. and Stephens, G. L.: Microphysical and macrophysical responses of marine stratocumulus polluted by underlying ships. Part 2: Impacts of haze on precipitating clouds, J. Geophys. Res., 117, D11203, doi:10.1029/2011JD017125, 2012.

Christensen, M. W., Chen, Y.-C., and Stephens, G. L.: Aerosol indirect effect dictated by liquid clouds, J. Geophys. Res.-Atmos., 121, 14636–14650, https://doi.org/10.1002/2016JD025245, 2016.

Chuang, P. Y., Saw, E. W., Small, J. D., Shaw, R. A., Sipperley, C. M., Payne, G. A., and Bachalo, W.: Airborne Phase 495 Doppler Interferometry for Cloud Microphysical Measurements, Aerosol Sci. Technol., 42, 685–703, 2008.

Coakley Jr., J. A. and Walsh, C. D.: Limits to the aerosol indirect radiative forcing derived from observations of ship tracks, J. Atmos. Sci., 59, 668–680, 2002.

Cochrane, S. P., Schmidt, K. S., Chen, H., Pilewskie, P., Kittelman, S., Redemann, J., LeBlanc, S., Pistone, K., Kacenelenbogen, M., Segal Rozenhaimer, M., Shinozuka, Y., Flynn, C., Platnick, S., Meyer, K., Ferrare, R., Burton, S., Hostetler, C., Howell, S., Freitag, S., Dobracki, A., and Doherty, S.: Above-cloud aerosol radiative effects based on ORACLES 2016 and ORACLES 2017 aircraft experiments, Atmos. Meas. Tech., 12, 6505–6528, https://doi.org/10.5194/amt-12-6505-2019, 2019.

Coddington, O., Pilewskie, P., Redemann, J., Platnick, S., Russell, P., Schmidt, K., Gore, W., Livingston, J., Wind, G., and Vukicevic, T.: Examining the impact of overlying aerosols on the retrieval of cloud optical properties from passive remote sensing, J. Geophys. Res., 115, D10211, doi:10.1029/2009JD012829, 2010.

Costantino, L. and Breon, F.-M.: Analysis of aerosol-cloud interaction from multi-sensor satellite observations, Geophys. Res. Lett., 37, L11801, https://doi.org/10.1029/2009GL041828, 2010.

Das, S., Harshvardhan, H., & Colarco, P. R.: The influence of elevated smoke layers on stratocumulus clouds over the SE Atlantic in the NASA Goddard Earth Observing System (GEOS) model. Journal of Geophysical Research: Atmospheres, 125, e2019JD031209. https://doi.org/10.1029/2019JD031209, 2020.

Deaconu, L. T., Ferlay, N., Waquet, F., Peers, F., Thieuleux, F., and Goloub, P.: Satellite inference of water vapour and above-cloud aerosol combined effect on radiative budget and cloud-top processes in the southeastern Atlantic Ocean, Atmos. Chem. Phys., 19, 11613–11634, https://doi.org/10.5194/acp-19-11613-2019, 2019.

Delene, D. J.: Airborne Data Processing and Analysis Software Package, Earth Sci. Inform., 4, 29–44, 2011.

Delene, D. J., Skow, A., O'Brien, J., Gapp, N., Wagner, S., Hibert, K., Sand, K., and Sova, G.: Airborne Data Processing and Analysis Software Package (Version 3981), Zenodo, https://doi.org/10.5281/zenodo.3733448, 2020.

Devasthale, A. and Thomas, M. A.: A global survey of aerosol-liquid water cloud overlap based on four years of CALIPSO-CALIOP data, Atmos. Chem. Phys., 11, 1143–1154, https://doi.org/10.5194/acp-11-1143-2011, 2011.

Diamond, M. S., Dobracki, A., Freitag, S., Small Griswold, J. D., Heikkila, A., Howell, S. G., Kacarab, M. E., Podolske, J. R., Saide, P. E., and Wood, R.: Time-dependent entrainment of smoke presents an observational challenge for assessing aerosol–cloud interactions over the southeast Atlantic Ocean, Atmos. Chem. Phys., 18, 14623–14636, https://doi.org/10.5194/acp-18- 14623-2018, 2018.

Doherty, S. J., Saide, P. E., Zuidema, P., Shinozuka, Y., Ferrada, G. A., Gordon, H., Mallet, M., Meyer, K., Painemal, D., Howell, S. G., Freitag, S., Dobracki, A., Podolske, J. R., Burton, S. P., Ferrare, R. A., Howes, C., Nabat, P., Carmichael, G. R., da Silva, A., Pistone, K., Chang, I., Gao, L., Wood, R., and Redemann, J.: Modeled and observed properties related to the direct aerosol radiative effect of biomass burning aerosol over the Southeast Atlantic, Atmos. Chem. Phys. Discuss. [preprint], https://doi.org/10.5194/acp-2021-333, in review, 2021.

Douglas, A. and L'Ecuyer, T.: Quantifying variations in shortwave aerosol–cloud–radiation interactions using local meteorology and cloud state constraints, Atmos. Chem. Phys., 19, 6251–6268, https://doi.org/10.5194/acp-19-6251-2019, 2019.

Douglas, A. and L'Ecuyer, T.: Quantifying cloud adjustments and the radiative forcing due to aerosol–cloud interactions in satellite observations of warm marine clouds, Atmos. Chem. Phys., 20, 6225–6241, https://doi.org/10.5194/acp-20-6225-2020, 2020.

Douglas, A. and L'Ecuyer, T.: Global evidence of aerosol-induced invigoration in marine cumulus clouds, Atmos. Chem. Phys., 21, 15103–15114, https://doi.org/10.5194/acp-21-15103-2021, 2021.

Drewnick, F., Hings, S., De Carlo, P., Jayne, J., Gonin, M., Fuhrer, K., Weimer, S., Jimenez, J., Demerjian, K., Borrmann, S., and Worsnop, D.: A new time-of-flight aerosol mass spectrometer (TOF-AMS) – Instrument description and first field deployment, Aerosol Sci. Tech., 39, 637–658, https://doi.org/10.1080/02786820500182040, 2005.

Dunagan, S. E., Johnson, R., Zavaleta, J., Russell, P. B., Schmid, B., Flynn, C., Redemann, J., Shinozuka, Y., Livingston, J., and Segal-Rosenhaimer, M.: Spectrometer for Sky-Scanning

Sun-Tracking Atmospheric Research (4STAR): Instrument technology, Remote Sens., 5, 3872–3895, https://doi.org/10.3390/rs5083872, 2013.

Duong, H. T., Sorooshian, A., and Feingold, G.: Investigating potential biases in observed and modeled metrics of aerosol-cloud-precipitation interactions, Atmos. Chem. Phys., 11, 4027–4037, https://doi.org/10.5194/acp-11-4027-2011, 2011.

Dzambo, A. M., L'Ecuyer, T. S., Sy, O. O., and Tanelli, S.: The Observed Structure and Precipitation Characteristics of Southeast Atlantic Stratocumulus from Airborne Radar during ORACLES 2016–17, J. Appl. Meteor. Climatol., 58, 2197–2215, https://doi.org/10.1175/JAMC-D-19-0032.1, 2019.

Dzambo, A. M., L'Ecuyer, T., Sinclair, K., van Diedenhoven, B., Gupta, S., McFarquhar, G., O'Brien, J. R., Cairns, B., Wasilewski, A. P., and Alexandrov, M.: Joint cloud water path and rainwater path retrievals from airborne ORACLES observations, Atmos. Chem. Phys., 21, 5513–5532, https://doi.org/10.5194/acp-21-5513-2021, 2021.

Eastman, R., Warren, S. G., and Hahn, C. J.: Variations in Cloud Cover and Cloud Types over the Ocean from Surface Observations, 1954–2008, J. Clim., 24, 5914–5934, doi:10.1175/2011JCLI3972.1, 2011.

Feingold, G. and Siebert, H.: Cloud – Aerosol Interactions from the Micro to the Cloud Scale, from the Strungmann Forum Report, Clouds in the Perturbed Climate System: Their Relationship to Energy Balance, Atmospheric Dynamics, and Precipitation, edited by: Heintzenberg, J. and Charlson, R. J., MIT Press, ISBN 978-0-262-01287-4, 2009.

Feingold, G., Koren, I., Yamaguchi, T., and Kazil, J.: On the reversibility of transitions between closed and open cellular convection, Atmos. Chem. Phys., 15, 7351–7367, https://doi.org/10.5194/acp-15-7351-2015, 2015.

Field, P., Heymsfield, A., and Bansemer, A.: Shattering and particle interarrival times measured by optical array probes in ice clouds, J. Atmos. Ocean. Tech., 23, 1357–1371, 2006.

Formenti, P., D'Anna, B., Flamant, C., Mallet, M., Piketh, S. J., Schepanski, K., Waquet, F., Auriol, F., Brogniez, G., Burnet, F., Chaboureau, J.-P., Chauvigné, A., Chazette, P., Denjean, C., Desboeufs, K., Doussin, J.-F., Elguindi, N., Feuerstein, S., Gaetani, M., Giorio, C., Klopper, D., Mallet, M. D., Nabat, P., Monod, A., Solmon, F., Namwoonde, A., Chikwililwa, C., Mushi, R., Welton, E. J., and Holben, B.: The Aerosols, Radiation and Clouds in southern Africa (AEROCLO-sA) field campaign in Namibia: overview, illustrative observations and way forward, B. Am. Meteorol. Soc., 100, 1277–1298, https://doi.org/10.1175/BAMS-D-17-0278.1, 2019.

Fu, D., Di Girolamo, L., Liang, L., & Zhao, G.: Regional biases in MODIS marine liquid water cloud drop effective radius deduced through fusion with MISR. Journal of Geophysical Research: Atmospheres, 124, 2019JD031063, 2019.

Fuchs, J., Cermak, J., and Andersen, H.: Building a cloud in the southeast Atlantic: understanding low-cloud controls based on satellite observations with machine learning, Atmos. Chem. Phys., 18, 16537–16552, https://doi.org/10.5194/acp-18-16537-2018, 2018.

Gettelman, A., Morrison, H., Terai, C. R., and Wood, R.: Microphysical process rates and global aerosol–cloud interactions, Atmos. Chem. Phys., 13, 9855–9867, doi:10.5194/acp-13-9855-2013, 2013.

Geoffroy, O., Brenguier, J.-L., and Burnet, F.: Parametric representation of the cloud droplet spectra for LES warm bulk microphysical schemes, Atmos. Chem. Phys., 10, 4835–4848, doi:10.5194/acp-10-4835-2010, 2010.

Geoffroy, O., Brenguier, J.-L., and Sandu, I.: Relationship between drizzle rate, liquid water path and droplet concentration at the scale of a stratocumulus cloud system, Atmos. Chem. Phys., 8, 4641–4654, doi:10.5194/acp-8-4641-2008, 2008.

Gordon, H., Field, P. R., Abel, S. J., Dalvi, M., Grosvenor, D. P., Hill, A. A., Johnson, B. T., Miltenberger, A. K., Yoshioka, M., and Carslaw, K. S.: Large simulated radiative effects of smoke in the south-east Atlantic, Atmos. Chem. Phys., 18, 15261–15289, https://doi.org/10.5194/acp-18-15261-2018, 2018.

Grosvenor, D. P. and Wood, R.: The effect of solar zenith angle on MODIS cloud optical and microphysical retrievals within marine liquid water clouds, Atmos. Chem. Phys., 14, 7291–7321, https://doi.org/10.5194/acp-14-7291-2014, 2014.

Grosvenor, D. P., Sourdeval, O., Zuidema, P., Ackerman, A., Alexandrov, M. D., Bennartz, R., Boers, R., Cairns, B., Chiu, J. C., Christensen, M., Deneke, H., Diamond, M., Feingold, G., Fridlind, A., Hünerbein, A., Knist, C., Kollias, P., Marshak, A., McCoy, D., Merk, D., Painemal, D., Rausch, J., Rosenfeld, D., Russchenberg, H., Seifert, P., Sinclair, K., Stier, P., van Diedenhoven, B., Wendisch, M., Werner, F., Wood, R., Zhang, Z., and Quaas, J.: Remote Sensing of Droplet Number Concentration in Warm Clouds: A Review of the Current State of Knowledge and Perspectives, Rev. Geophys., 56, 409–453, https://doi.org/10.1029/2017RG000593, 2018.

Gryspeerdt, E., Goren, T., Sourdeval, O., Quaas, J., Mülmenstädt, J., Dipu, S., Unglaub, C., Gettelman, A., and Christensen, M.: Constraining the aerosol influence on cloud liquid water path, Atmos. Chem. Phys., 19, 5331–5347, https://doi.org/10.5194/acp-19-5331-2019, 2019.

Gryspeerdt, E., Mülmenstädt, J., Gettelman, A., Malavelle, F. F., Morrison, H., Neubauer, D., Partridge, D. G., Stier, P., Takemura, T., Wang, H., Wang, M., and Zhang, K.: Surprising similarities in model and observational aerosol radiative forcing estimates, Atmos. Chem. Phys., 20, 613–623, https://doi.org/10.5194/acp-20-613-2020, 2020.

Gupta, S., McFarquhar, G. M., O'Brien, J. R., Delene, D. J., Poellot, M. R., Dobracki, A., Podolske, J. R., Redemann, J., LeBlanc, S. E., Segal-Rozenhaimer, M., and Pistone, K.: Impact of the variability in vertical separation between biomass burning aerosols and marine stratocumulus on cloud microphysical properties over the Southeast Atlantic, Atmos. Chem. Phys., 21, 4615–4635, https://doi.org/10.5194/acp-21-4615-2021, 2021a.

Gupta, S., McFarquhar, G. M., O'Brien, J. R., Poellot, M. R., Delene, D. J., Miller, R. M., and Small Griswold, J. D.: Precipitation Susceptibility of Marine Stratocumulus with Variable Above and Below-Cloud Aerosol Concentrations over the Southeast Atlantic, Atmos. Chem. Phys. Discuss. [preprint], https://doi.org/10.5194/acp-2021-677, in review, 2021b.

Hannay, C., Williamson, D., Hack, J., Kiehl, J., Olson, J., Klein, S., Bretherton, C., and Kohler, M.: Evaluation of forecasted south- ¨ east pacific stratocumulus in the NCAR, GFDL, and ECMWF Models, J. Climate, 22, 2871–2889, 2009.

Hansen, J. and Travis, L. D.: Light scattering in planetary atmospheres, Space Sci. Rev., 16, 527–610, 1974.

Hansen, J., Sato, M., and Ruedy, R.: Radiative forcing and climate response, J. Geophys. Res., 102, 6831–6864, 1997.

Hartmann, D. L., Ockert-Bell, M. E., and Michelsen, M. L.: The effect of cloud type on Earth's energy balance: Global analysis, J. Climate, 5, 1281–1304, 1992.

Haywood, J. M., Abel, S. J., Barrett, P. A., Bellouin, N., Blyth, A., Bower, K. N., Brooks, M., Carslaw, K., Che, H., Coe, H., Cotterell, M. I., Crawford, I., Cui, Z., Davies, N., Dingley, B., Field, P., Formenti, P., Gordon, H., de Graaf, M., Herbert, R., Johnson, B., Jones, A. C., Langridge, J. M., Malavelle, F., Partridge, D. G., Peers, F., Redemann, J., Stier, P., Szpek, K., Taylor, J. W., Watson-Parris, D., Wood, R., Wu, H., and Zuidema, P.: The CLoud–Aerosol–Radiation Interaction and Forcing: Year 2017 (CLARIFY-2017) measurement campaign, Atmos. Chem. Phys., 21, 1049–1084, https://doi.org/10.5194/acp-21-1049-2021, 2021.

Haywood, J. M. and Shine, K. P.: Multi-spectral calculations of the radiative forcing of tropospheric sulfate and soot aerosols using a column model, Q. J. Roy. Meteor. Soc., 123, 1907–1930, 1997.

Haywood, J. M., Osborne, S. R., and Abel, S. J.: The effect of overlying absorbing aerosol layers on remote sensing retrievals of cloud effective radius and cloud optical depth, Q. J. R. Meteorol. Soc., 130, 779–800, 2004.

Herbert, R. J., Bellouin, N., Highwood, E. J., and Hill, A. A.: Diurnal cycle of the semi-direct effect from a persistent absorbing aerosol layer over marine stratocumulus in large-eddy simulations, Atmos. Chem. Phys., 20, 1317–1340, https://doi.org/10.5194/acp-20-1317-2020, 2020.

Hersbach, H., Bell, B., Berrisford, P., Hirahara, S., Horányi, A., Muñoz-Sabater, J., Nicolas, J., Peubey, C., Radu, R., Schepers, D., Simmons, A., Soci, C., Abdalla, S., Abellan, X., Balsamo, G., Bechtold, P., Biavati, G., Bidlot, J., Bonavita, M., De Chiara, G., Dahlgren, P., Dee, D., Diamantakis, M., Dragani, R., Flemming, J., Forbes, R., Fuentes, M., Geer, A., Haimberger, L., Healy, S., Hogan, R. J., Hólm, E., Janisková, M., Keeley, S., Laloyaux, P., Lopez, P., Lupu, C., Radnoti, G., de Rosnay, P., Rozum, I., Vamborg, F., Villaume, S., and Thépaut, J.-N.: The ERA5 Global Reanalysis, Q. J. Roy. Meteor. Soc., 146, 730, 1999– 2049, https://doi.org/10.1002/qj.3803, 2020.

Heymsfield, A. J. and McFarquhar, G. M.: Microphysics of INDOEX clean and polluted trade wind cumulus clouds, J. Geophys. Res., 106, 28653–28673, 2001.

Hill, A. A., Dobbie, S., and Yin, Y.: The impact of aerosols on non-precipitating marine stratocumulus. Model description and prediction of the indirect effect, Q. J. Roy. Meteorol. Soc., 134, 1143–1154, doi:10.1002/qj.278, 2008.

Hintze, J. L. and Nelson, R. D.: Violin Plots: A Box Plot-Density Trace Synergism, Am. Stat., 52, 181–184, 1998.

IFS Documentation CY47R1: IFS Documentation CY47R1 – Part IV: Physical Processes, ECMWF, doi:10.21957/cpmkqvhja

Janssen, R. H. H., Ganzeveld, L. N., Kabat, P., Kulmala, M., Nieminen, T., and Roebeling, R. A.: Estimating seasonal variations in cloud droplet number concentration over the boreal forest from satellite observations, Atmos. Chem. Phys., 11, 7701–7713, https://doi.org/10.5194/acp-11-7701-2011, 2011.

Jiang, H., Feingold, G., and Sorooshian, A.: Effect of aerosol on the susceptibility and efficiency of precipitation in trade cumulus clouds, J. Atmos. Sci., 67, 3525–3540, 2010.

Johnson, B. T., Shine, K. P., and Forster, P. M.: The semi-direct aerosol effect: Impact of absorbing aerosols on marine stratocumulus, Q. J. Roy. Meteor. Soc., 130, 1407–1422, 2004.

Johnson, B., Turnbull, K., Brown, P., Burgess, R., Dorsey, J., Baran, A. J., Webster, H., Haywood, J., Cotton, R., Ulanowski, Z., Hesse, E., Woolley, A., and Rosenberg, P.: In situ observations of volcanic ash clouds from the FAAM aircraft during the eruption of Eyjafjallajökull in 2010, J. Geophys. Res.-Atmos., 117, D00U24, https://doi.org/10.1029/2011JD016760, 2012.

Jung, E., Albrecht, B. A., Sorooshian, A., Zuidema, P., and Jonsson, H. H.: Precipitation susceptibility in marine stratocumulus and shallow cumulus from airborne measurements, Atmos. Chem. Phys., 16, 11395–11413, https://doi.org/10.5194/acp-16-11395-2016, 2016.

Kacarab, M., Thornhill, K. L., Dobracki, A., Howell, S. G., O'Brien, J. R., Freitag, S., Poellot, M. R., Wood, R., Zuidema, P., Redemann, J., and Nenes, A.: Biomass burning aerosol as a modulator of the droplet number in the southeast Atlantic region, Atmos. Chem. Phys., 20, 3029–3040, https://doi.org/10.5194/acp-20-3029-2020, 2020.

Keil, A. and Haywood, J. M.: Solar radiative forcing by biomass burning aerosol particles during SAFARI 2000: A case study based on measured aerosol and cloud properties, J. Geophys. Res., 108, 8467, https://doi.org/10.1029/2002JD002315, 2003.

Khairoutdinov, M. and Kogan, Y.: A new cloud physics parameterization in a large-eddy simulation model of marine stratocumulus, Mon. Weather Rev., 128, 229–243, 2000.

King, M. D., Tsay, S. C., Platnick, S., Wang, M., & Liou, K. N. (1998). Cloud retrieval algorithms for MODIS: Optical thickness, effective particle radius, and thermodynamic phase. In Algorithm Theor. Basis Doc. ATBD-MOD-05. Greenbelt, Md: Goddard Space Flight Center.

King, N. J., Bower, K. N., Crosier, J., and Crawford, I.: Evaluating MODIS cloud retrievals with in situ observations from VOCALS-REx, Atmos. Chem. Phys., 13, 191–209, https://doi.org/10.5194/acp-13-191-2013, 2013.

King, W. D., Parkin, D. A., and Handsworth, R. J.: A hot-wire liquid water device having fully calculable response characteristics, J. Appl. Meteorol., 17, 1809–1813, https://doi.org/10.1175/1520-0450(1978)017<1809:AHWLWD>2.0.CO;2, 1978.

Klein, S. A. and Hartmann, D. L.: The seasonal cycle of low stratiform clouds, J. Climate, 6, 1587–1606, 1993.

Köhler, M., Ahlgrimm, M., and Beljaars, A.: Unified treatment of dry convective and stratocumulus-topped boundary layers in the ECMWF model, Q. J. Roy. Meteor. Soc., 137, 43–57, 2011.

Korolev, A.: Reconstruction of the sizes of spherical particles from their shadow images. Part I: Theoretical considerations, J. Atmos. Ocean. Tech., 24, 376–389, 2007.

Kubar, T. L., Hartmann, D. L., and Wood, R.: Understanding the importance of microphysics and macrophysics for warm rain in marine low clouds. Part I: Satellite observations, J. Atmos. Sci. 66, 2953–2972, 2009.

Kuo, H. and Schubert, W.: Stability of cloud-topped boundary layers, Q. J. Roy. Meteor. Soc., 114, 887–916, 1988.

Lance, S., Brock, C. A., Rogers, D., and Gordon, J. A.: Water droplet calibration of the Cloud Droplet Probe (CDP) and in-flight performance in liquid, ice and mixed-phase clouds during ARCPAC, Atmos. Meas. Tech., 3, 1683–1706, https://doi.org/10.5194/amt-3-1683-2010, 2010.

Lance, S.: Coincidence Errors in a Cloud Droplet Probe (CDP) and a Cloud and Aerosol Spectrometer (CAS), and the Improved Performance of a Modified CDP, J. Atmos. Ocean. Tech., 29, 1532– 1541, doi:10.1175/JTECH-D-11-00208.1, 2012.

Lawrence, M. G.: The relationship between relative humidity and the dewpoint temperature in moist air: A simple conversion and applications, Bull. Am. Met. Soc., 86, 225–233, 2005.

Lawson, R. P., Stewart, R. E., and Angus, L. J.: Observations and numerical simulations of the origin and development of very large snowflakes, J. Atmos. Sci., 55, 3209–3229, 1998.

Lawson, R. P., O'Connor, D., Zmarzly, P.,Weaver, K., Baker, B. A., Mo, Q., and Jonsson, H.: The 2D-S (Stereo) probe: Design and preliminary tests of a new airborne, high-speed, high-resolution imaging probe, J. Atmos. Ocean. Tech., 23, 1462–1477, 2006.

LeBlanc, S. E., Redemann, J., Flynn, C., Pistone, K., Kacenelenbogen, M., Segal-Rosenheimer, M., Shinozuka, Y., Dunagan, S., Dahlgren, R. P., Meyer, K., Podolske, J., Howell, S. G., Freitag, S., Small-Griswold, J., Holben, B., Diamond, M., Wood, R., Formenti, P., Piketh, S., Maggs-Kölling, G., Gerber, M., and Namwoonde, A.: Above-cloud aerosol optical depth from airborne observations in the southeast Atlantic, Atmos. Chem. Phys., 20, 1565–1590, https://doi.org/10.5194/acp-20-1565-2020, 2020.

Lock, A. P.: Factors influencing cloud area at the capping inversion for shallow cumulus clouds, Q. J. Roy. Meteor. Soc., 135, 941–952, 2009.

Loeb, N. G., Wielicki, B. A., Doelling, D. R., Smith, G. L., Keyes, D. F., Kato, S., Manalo-Smith, N., and Wong, T.: Toward optimal closure of the Earth's Top-of-Atmosphere radiation budget, J. Climate, 22, 3, 748–766, https://doi.org/10.1175/2008JCLI2637.1, 2009.

Mallet, M., Nabat, P., Johnson, B., Michou, M., Haywood, J. M., Chen, C., Dubovik, O.: Climate models generally underrepresent the warming by Central Africa biomass-burning aerosols over the Southeast Atlantic. Sci. Adv., 7, eabg9998, 2021.

Mardi, A. H., Dadashazar, H., MacDonald, A. B., Braun, R. A., Crosbie, E., Xian, P., Thorsen, T. J., Coggon, M. M., Fenn, M. A., Ferrare, R. A., Hair, J. W., Woods, R. K., Jonsson, H. H., Flagan, R. C., Seinfeld, J. H., and Sorooshian, A.: Biomass Burning Plumes in the Vicinity of the California Coast: Airborne Characterization of Physicochemical Properties, Heating Rates, and Spatiotemporal Features, J. Geophys. Res.-Atmos., 123, 13560–13582, https://doi.org/10.1029/2018JD029134, 2018.

Mardi, A. H., Dadashazar, H., MacDonald, A. B., Crosbie, E., Coggon, M. M., Aghdam, M. A., Woods, R. K., Jonsson, H. H., Flagan, R. C., Seinfeld, J. H., and Sorooshian, A.: Effects of Biomass Burning on Stratocumulus Droplet Characteristics, Drizzle Rate, and Composition, J. Geophys. Res.-Atmos., 124, 12301–12318, https://doi.org/10.1029/2019jd031159, 2019.

Martin, G. M., Johnson, D. W., and Spice, A.: The measurement and parameterization of effective radius of droplets in warm stratocumulus clouds, J. Atmos. Sci., 51, 1823–1842, 1994.

Mauger, G. S. and Norris, J. R.: Meteorological bias in satellite estimates of aerosol-cloud relationships, Geophys. Res. Lett., 34, L16824, doi:10.1029/2007GL029952, 2007.

McComiskey, A. and Feingold, G.: The scale problem in quantifying aerosol indirect effects, Atmos. Chem. Phys., 12, 1031–1049, https://doi.org/10.5194/acp-12-1031-2012, 2012.

McFarquhar, G. M. and Heymsfield, A. J. : The definition and significance of an effective radius for ice clouds, J. Atmos. Sci., 55, 2039–2052, 1998.

McFarquhar, G. M. and Heymsfield, A. J.: Parameterizations of INDOEX microphysical measurements and calculations of cloud susceptibility: Applications for climate studies, J. Geophys. Res., 106, 28675–28698, 2001.

McFarquhar, G. M. and Wang, H.: Effects of Aerosols on Trade Wind Cumuli over the Indian Ocean: Model Simulations, Q. J. R. Meteor. Soc., 132, 821–843, 2006.

McFarquhar, G. M., Baumgardner, D., Bansemer, A., Abel, S. J., Crosier, J., French, J., Rosenberg, P., Korolev, A., Schwarzoenboeck, A., Leroy, D., Um, J., Wu, W., Heymsfield, A. J., Twohy, C., Detwiler, A., Field, P., Neumann, A., Cotton, R., Axisa, D., Dong, J., McFarquhar, G. M., Baumgardner, D., Bansemer, A., Abel, S. J., Crosier, J., French, J., Rosenberg, P., Korolev, A., Schwarzoenboeck, A., Leroy, D., Um, J., Wu, W., Heymsfield, A. J., Twohy, C., Detwiler, A., Field, P., Neumann, A., Cotton, R., Axisa, D., and Dong, J.: Processing of Ice Cloud In Situ Data Collected by Bulk Water, Scattering, and Imaging Probes: Fundamentals, Uncertainties, and Efforts toward Consistency, Meteor. Mon., 58, 11.1–11.33, https://doi.org/10.1175/AMSMONOGRAPHS-D-16-0007.1, 2017.

McFarquhar, G. M., Finlon, J. A., Stechman, D. M., Wu, W., Jackson, R. C., and Freer, M.: University of Illinois/Oklahoma Optical Array Probe (OAP) Processing Software, https://doi.org/10.5281/zenodo.1285969, 2018.

McFarquhar, G. M., Zhang, G., Poellot, M. R., Kok, G. L., McCoy, R., Tooman, T., Fridlind, A., and Heymsfield, A. J.: Ice properties of single-layer stratocumulus during the Mixed-Phase Arctic Cloud Experiment: 1. Observations, J. Geophys. Res., 112, D24201, doi:10.1029/2007jd008633, 2007.

Mellado, J. P.: Cloud-top entrainment in stratocumulus clouds, Annu. Rev. Fluid Mech., 49, 145–169, 2017.

Merk, D., Deneke, H., Pospichal, B., and Seifert, P.: Investigation of the adiabatic assumption for estimating cloud micro- and macrophysical properties from satellite and ground observations, Atmos. Chem. Phys., 16, 933–952, https://doi.org/10.5194/acp-16-933-2016, 2016.

Meyer, K., Platnick, S., and Zhang, Z.: Simultaneously inferring above-cloud absorbing aerosol optical thickness and underlying liquid phase cloud optical and microphysical properties using MODIS, J. Geophys. Res.-Atmos., 120, 5524–5547, doi:10.1002/2015JD023128, 2015.

Michibata, T., Suzuki, K., Sato, Y., and Takemura, T.: The source of discrepancies in aerosol–cloud–precipitation interactions between GCM and A-Train retrievals, Atmos. Chem. Phys., 16, 15413–15424, https://doi.org/10.5194/acp-16-15413-2016, 2016.

Middlebrook, A. M., Bahreini, R., Jimenez, J. L., and Canagaratna, M. R.: Evaluation of composition-dependent collection efficiencies for the aerodyne aerosol mass spectrometer using field data, Aerosol Sci. Tech., 46, 258–271, https://doi.org/10.1080/02786826.2011.620041s, 2012.

Min, Q., Joseph, E., Lin, Y., Min, L., Yin, B., Daum, P. H., Kleinman, L. I., Wang, J., and Lee, Y.-N.: Comparison of MODIS cloud microphysical properties with in-situ measurements over the Southeast Pacific, Atmos. Chem. Phys., 12, 11261–11273, https://doi.org/10.5194/acp-12-11261-2012, 2012.

Morrison, H. and Gettelman, A.: A new two-moment bulk stratiform cloud microphysics scheme in the community atmosphere model, version 3 (CAM3). Part I: Description and numerical tests, J. Climate, 21, 3642–3659, doi:10.1175/2008JCLI2105.1, 2008.

Myhre, G., Shindell, D., Bréon, F.-M., Collins, W., Fuglestvedt, J., Huang, J., Koch, D., Lamarque, J.-F., Lee, D., Mendoza, B., Nakajima, T., Robock, A., Stephens, G., Takemura, T. and Zhang, H.: Anthropogenic and Natural Radiative Forc-ing. In: Climate Change 2013: The Physical Science Basis. Contribution of Working Group I to the Fifth Assessment Report of the Intergovernmental Panel on Climate Change, edited by: Stocker, T. F., Qin, D., Plattner, G.-K., Tignor, M., Allen, S. K., Boschung, J., Nauels, A., Xia, Y., Bex, V., and Midgley, P. M., Cambridge University Press, 571–657, 2013.

Nakajima, T. and King, M. D.: Determination of the optical thickness and effective particle radius of clouds from reflected solar radiation measurements. Part I: Theory, J. Atmos. Sci., 47, 1878– 1893, 1990.

Nakajima, T.Y., Suzuki, K., and Stephens, G.L.: Droplet growth in warm water clouds observed by the A-Train. Part I: Sensitivity analysis of the MODIS-derived cloud droplet sizes. *Journal of the Atmospheric Sciences*, *67*(6), pp.1884-1896, 2010.

Noble, S. R., and Hudson, J. G.: MODIS comparisons with northeastern Pacific in situ stratocumulus microphysics, J. Geophys. Res. Atmos., 120, 8332–8344, doi:10.1002/2014JD022785, 2015.

ORACLES Science Team: Suite of Aerosol, Cloud, and Related Data Acquired Aboard P3 During ORACLES 2018, Version 2, NASA Ames Earth Science Project Office, https://doi.org/10.5067/Suborbital/ORACLES/P3/2018_V2, 2020a.

ORACLES Science Team: Suite of Aerosol, Cloud, and Related Data Acquired Aboard P3 During ORACLES 2017, Version 2, NASA Ames Earth Science Project Office, https://doi.org/10.5067/Suborbital/ORACLES/P3/2017_V2, 2020b.

ORACLES Science Team: Suite of Aerosol, Cloud, and Related Data Acquired Aboard P3 During ORACLES 2016, Version 2, NASA Ames Earth Science Project Office, https://doi.org/10.5067/Suborbital/ORACLES/P3/2016_V2, 2020c.

Oreopoulos, L. and Rossow, W. B.: The cloud radiative effects of International Satellite Cloud Climatology Project weather states, J. Geophys. Res.-Atmos., 116, D12202, doi:10.1029/2010JD015472, 2011.

Painemal, D. and Zuidema, P.: Assessment of MODIS cloud effective radius and optical thickness retrievals over the Southeast Pacific with VOCALS-REx in situ measurements, J. Geophys. Res.-Atmos., 116, D24206, doi:10.1029/2011JD016155, 2011.

Painemal, D., Chang, F.-L., Ferrare, R., Burton, S., Li, Z., Smith Jr., W. L., Minnis, P., Feng, Y., and Clayton, M.: Reducing uncertainties in satellite estimates of aerosol–cloud interactions over the subtropical ocean by integrating vertically resolved aerosol observations, Atmos. Chem. Phys., 20, 7167–7177, https://doi.org/10.5194/acp-20-7167-2020, 2020.

Painemal, D., Spangenberg, D., Smith Jr., W. L., Minnis, P., Cairns, B., Moore, R. H., Crosbie, E., Robinson, C., Thornhill, K. L., Winstead, E. L., and Ziemba, L.: Evaluation of satellite retrievals of liquid clouds from the GOES-13 imager and MODIS over the midlatitude North Atlantic during the NAAMES campaign, Atmos. Meas. Tech., 14, 6633–6646, https://doi.org/10.5194/amt-14-6633-2021, 2021.

Pawlowska, H. and Brenguier, J. L.: An observational study of drizzle formation in stratocumulus clouds for general circulation model (GCM) parameterizations, J. Geophys. Res.-Atmos., 108, 8630, doi:10.1029/2002JD002679, 2003.

Peers, F., Francis, P., Abel, S. J., Barrett, P. A., Bower, K. N., Cotterell, M. I., Crawford, I., Davies, N. W., Fox, C., Fox, S., Langridge, J. M., Meyer, K. G., Platnick, S. E., Szpek, K., and Haywood, J. M.: Observation of absorbing aerosols above clouds over the south-east Atlantic Ocean from the geostationary satellite SEVIRI – Part 2: Comparison with MODIS and aircraft measurements from the CLARIFY-2017 field campaign, Atmos. Chem. Phys., 21, 3235–3254, https://doi.org/10.5194/acp-21-3235-2021, 2021.

Penner, J. E., Quaas, J., Storelvmo, T., Takemura, T., Boucher, O., Guo, H., Kirkevåg, A., Kristjánsson, J. E., and Seland, Ø.: Model intercomparison of indirect aerosol effects, Atmos. Chem. Phys., 6, 3391–3405, https://doi.org/10.5194/acp-6-3391-2006, 2006.

Pennypacker, S., Diamond, M., and Wood, R.: Ultra-clean and smoky marine boundary layers frequently occur in the same season over the southeast Atlantic, Atmos. Chem. Phys., 20, 2341–2351, https://doi.org/10.5194/acp-20-2341-2020, 2020.

Pistone, K., Redemann, J., Doherty, S., Zuidema, P., Burton, S., Cairns, B., Cochrane, S., Ferrare, R., Flynn, C., Freitag, S., Howell, S. G., Kacenelenbogen, M., LeBlanc, S., Liu, X., Schmidt, K.

S., Sedlacek III, A. J., Segal-Rozenhaimer, M., Shinozuka, Y., Stamnes, S., van Diedenhoven, B., Van Harten, G., and Xu, F.: Intercomparison of biomass burning aerosol optical properties from in situ and remote-sensing instruments in ORACLES-2016, Atmos. Chem. Phys., 19, 9181–9208, https://doi.org/10.5194/acp-19-9181-2019, 2019.

Pistone, K., Zuidema, P., Wood, R., Diamond, M., da Silva, A. M., Ferrada, G., Saide, P., Ueyama, R., Ryoo, J.-M., Pfister, L., Podolske, J., Noone, D., Bennett, R., Stith, E., Carmichael, G., Redemann, J., Flynn, C., LeBlanc, S., Segal-Rozenhaimer, M., and Shinozuka, Y.: Exploring the elevated water vapor signal associated with the free-tropospheric biomass burning plume over the southeast Atlantic Ocean, Atmos. Chem. Phys. Discuss. [preprint], https://doi.org/10.5194/acp-2020-1322, in review, 2021.

Platnick, S. (2000). Vertical photon transport in cloud remote sensing problems. Journal of Geophysical Research, 105(D18), 22,919–22,935. https://doi.org/10.1029/2000JD900333

Platnick, S., King, M. D., Ackerman, S. A., Menzel, W. P., Baum, B. A., Riedi, J. C., & Frey, R. A., 2003: The MODIS cloud products: Algorithms and examples from Terra. IEEE Transactions on Geoscience and Remote Sensing, 41(2), 459–473. https://doi.org/10.1109/tgrs.2002.808301.

Platnick, S. and Twomey, S.: Determining the susceptibility of cloud albedo to changes in droplet concentration with the advanced very high resolution radiometer, J. Appl. Meteor., 33, 334–346, 1994.

Platnick, S., K. G. Meyer, M. D. King, G. Wind, N. Amarasinghe, B. Marchant, G. T. Arnold, Z. Zhang, P. A. Hubanks, R. E. Holz, P. Yang, W. L. Ridgway, and J. Riedi, 2017: The MODIS cloud optical and microphysical products: Collection 6 updates and examples from Terra and Aqua. *IEEE Trans. Geosci. Remote Sens.*, 55, 502-525.

Possner, A., Eastman, R., Bender, F., and Glassmeier, F.: Deconvolution of boundary layer depth and aerosol constraints on cloud water path in subtropical stratocumulus decks, Atmos. Chem. Phys., 20, 3609–3621, https://doi.org/10.5194/acp-20-3609-2020, 2020.

Quaas, J., Arola, A., Cairns, B., Christensen, M., Deneke, H., Ekman, A. M. L., Feingold, G., Fridlind, A., Gryspeerdt, E., Hasekamp, O., Li, Z., Lipponen, A., Ma, P.-L., Mülmenstädt, J., Nenes, A., Penner, J. E., Rosenfeld, D., Schrödner, R., Sinclair, K., Sourdeval, O., Stier, P., Tesche, M., van Diedenhoven, B., and Wendisch, M.: Constraining the Twomey effect from satellite observations: issues and perspectives, Atmos. Chem. Phys., 20, 15079–15099, https://doi.org/10.5194/acp-20-15079-2020, 2020.

Rajapakshe, C., Zhang, Z., Yorks, J. E., Yu, H., Tan, Q., Meyer, K., Platnick, S., and Winker, D. M.: Seasonally transported aerosol layers over southeast Atlantic are closer to underlying clouds than previously reported, Geophys. Res. Lett., 44, 5818–5825, https://doi.org/10.1002/2017GL073559, 2017.

Rao S., Dey S.: Consistent signal of aerosol indirect and semi-direct effect on water clouds in the oceanic regions adjacent to the Indian subcontinent. Atmos Res, 232:104677. https://doi.org/10.1016/j.atmosres.2019.104677, 2020.

Rausch, J., Meyer, K., Bennartz, R., and Platnick, S.: Differences in liquid cloud droplet effective radius and number concentration estimates between MODIS collections 5.1 and 6 over global oceans, Atmos. Meas. Tech., 10, 2105–2116, https://doi.org/10.5194/amt-10-2105-2017, 2017.

Redemann, J., Wood, R., Zuidema, P., Doherty, S. J., Luna, B., LeBlanc, S. E., Diamond, M. S., Shinozuka, Y., Chang, I. Y., Ueyama, R., Pfister, L., Ryoo, J.-M., Dobracki, A. N., da Silva, A. M., Longo, K. M., Kacenelenbogen, M. S., Flynn, C. J., Pistone, K., Knox, N. M., Piketh, S. J., Haywood, J. M., Formenti, P., Mallet, M., Stier, P., Ackerman, A. S., Bauer, S. E., Fridlind, A. M., Carmichael, G. R., Saide, P. E., Ferrada, G. A., Howell, S. G., Freitag, S., Cairns, B., Holben, B. N., Knobelspiesse, K. D., Tanelli, S., L'Ecuyer, T. S., Dzambo, A. M., Sy, O. O., McFarquhar, G. M., Poellot, M. R., Gupta, S., O'Brien, J. R., Nenes, A., Kacarab, M., Wong, J. P. S., Small-Griswold, J. D., Thornhill, K. L., Noone, D., Podolske, J. R., Schmidt, K. S., Pilewskie, P., Chen, H., Cochrane, S. P., Sedlacek, A. J., Lang, T. J., Stith, E., Segal-Rozenhaimer, M., Ferrare, R. A., Burton, S. P., Hostetler, C. A., Diner, D. J., Seidel, F. C., Platnick, S. E., Myers, J. S., Meyer, K. G., Spangenberg, D. A., Maring, H., and Gao, L.: An overview of the ORACLES (ObseRvations of Aerosols above CLouds and their intEractionS) project: aerosol–cloud–radiation interactions in the southeast Atlantic basin, Atmos. Chem. Phys., 21, 1507–1563, https://doi.org/10.5194/acp-21-1507-2021, 2021.

Rogers, R. R. and Yau, M. K.: A Short Course in Cloud Physics, 3rd Edn., International Series in Natural Philosophy, 290 pp., 1989.

Rosenfeld, D., Andreae, M. O., Asmi, A., Chin, M., de Leeuw, G., Donovan, D., Kahn, R., Kinne, S., Kivekäs, N., Kulmala, M., Lau, W., Schmidt, S., Suni, T., Wagner, T., Wild, M., and Quaas, J.: Global observations of aerosol-cloud precipitation-climate interactions, Rev. Geophys., 52, 750–808, https://doi.org/10.1002/2013RG000441, 2014.

Sakaeda, N., Wood, R., and Rasch, P. J.: Direct and semidirect aerosol effects of southern African biomass burning aerosol, J. Geophys. Res., 116, D12205, doi:10.1029/2010JD015540, 2011.

Sinclair, K., van Diedenhoven, B., Cairns, B., Alexandrov, M., Dzambo, A. M., & L'Ecuyer, T.: Inference of precipitation in warm stratiform clouds using remotely sensed observations of the cloud top droplet size distribution, Geophysical Research Letters, *48*, e2021GL092547. https://doi.org/10.1029/2021GL092547, 2021.

Slingo, A.: Sensitivity of the Earth's radiation budget to changes in low clouds, Nature, 343, 49–51, https://doi.org/10.1038/343049a0, 1990.

Small, J. D., Chuang, P. Y., Feingold, G., and Jiang, H.: Can aerosol decrease cloud lifetime?, Geophys. Res. Lett., 36, 16806, doi:10.1029/2009GL038888, 2009.

Sorooshian, A., Anderson, B., Bauer, S. E., Braun, R. A., Cairns, B., Crosbie, E., Dadashazar, H., Diskin, G., Ferrare, R., Flagan, R. C., Hair, J., Hostetler, C., Jonsson, H. H., Kleb, M. M., Liu, H. Y., MacDonald, A. B., McComiskey, A., Moore, R., Painemal, D., Russell, L. M., Seinfeld, J. H., Shook, M., Smith, W. L., Thornhill, K., Tselioudis, G., Wang, H. L., Zeng, X. B., Zhang, B., Ziemba, L., and Zuidema, P.: Aerosol-Cloud-Meteorology Interaction Airborne Field Investigations: Using Lessons Learned from the US West Coast in the Design of ACTIVATE off the US East Coast, B. Am. Meteorol. Soc., 100, 1511–1528, https://doi.org/10.1175/Bams-D-18-0100.1, 2019.

Sorooshian, A., Feingold, G., Lebsock, M. D., Jiang, H., and Stephens, G. L.: On the precipitation susceptibility of clouds to aerosol perturbations, Geophys. Res. Lett., 36, L13803, doi:10.1029/2009GL038993, 2009.

Sorooshian, A., Feingold, G., Lebsock, M. D., Jiang, H., and Stephens, G.: Deconstructing the precipitation susceptibility construct: improving methodology for aerosol cloud precipitation studies, J. Geophys. Res., 115, D17201, doi:10.1029/2009JD013426, 2010.

Stein, A. F., Draxler, R. R., Rolph, G. D., Stunder, B. J. B., Cohen, M. D., and Ngan, F.: NOAA's HYSPLIT Atmospheric Transport and Dispersion Modeling System, B. Am. Meteorol. Soc., 96, 2059–2077, https://doi.org/10.1175/BAMS-D-14-00110.1, 2015.

Stephens, G. L., L'Ecuyer, T., Forbes, R., Gettlemen, A., Golaz, J. C., Bodas-Salcedo, A., Suzuki, K., Gabriel, P., and Haynes, J.: Dreary state of precipitation in global models, J. Geophys. Res.-Atmos., 115, D24211, doi:10.1029/2010jd014532, 2010.

Stephens, M., Turner, N., and Sandberg, J.: Particle identification by laser-induced incandescence in a solid-state laser cavity, Appl. Optics, 42, 3726–3736, 2003.

Stevens, B. and Feingold, G.: Untangling aerosol effects on clouds and precipitation in a buffered system, Nature, 461, 607–613, doi:10.1038/nature08281, 2009.

Strapp, J. W., Leaitch, W. R., and Liu, P. S. K.: Hydrated and Dried Aerosol-Size-Distribution Measurements from the Particle Measuring Systems FSSP-300 Probe and the Deiced PCASP-100x Probe, J. Atmos. Ocean. Tech., 9, 548–555, 1992.

Stubenrauch, C. J., Rossow, W. B., Kinne, S., Ackerman, S., Cesana, G., Chepfer, H., Di Girolamo, L., Getzewich, B., Guignard, A., Heidinger, A., Maddux, B. C., Menzel, W. P., Minnis, P., Pearl, C., Platnick, S., Poulsen, C., Riedi, J., Sun-Mack, S., Walther, A., Winker, D., Zeng, S., and Zhao, G.: Assessments of Global Cloud Datasets from Satellites: Project and Database initiated by the GEWEX Radiation Panel, B. Am. Meteorol. Soc., 94, 1031–1049, 2013.

Szczodrak, M., Austin, P. H., and Krummel, P. B.: Variability of Optical Depth and Effective Radius in Marine Stratocumulus Clouds, J. Atmos. Sci., 58, 2912–2926, https://doi.org/10.1175/1520-0469(2001)058<2912:VOODAE>2.0.CO;2, 2001.

Terai, C. R., Wood, R., Leon, D. C., and Zuidema, P.: Does precipitation susceptibility vary with increasing cloud thickness in marine stratocumulus?, Atmos. Chem. Phys., 12, 4567–4583, doi:10.5194/acp-12-4567-2012, 2012.

Thornhill, K. L., Anderson, B. E., Barrick, J. D. W., Bagwell, D. R., Friesen, R., and Lenschow, D.: Air motion inter-comparison flights during Transport and Chemical Evolution in the Pacific (TRACE-P)/ACE-ASIA, J. Geophys. Res., 108, https://doi.org/10.1029/2002JD003108, 2003.

Toll, V., Christensen, M., Quaas, J., and Bellouin, N.: Weak average liquid-cloud-water response to anthropogenic aerosols, Nature, 572, 51–55, https://doi.org/10.1038/s41586-019-1423-9, 2019.

Trenberth, K. and Fasullo, J.: Global warming due to increasing absorbed solar radiation, Geophys. Res. Lett., 36, L07706, doi:10.1029/2009GL037527, 2009.

Twomey, S.: Pollution and the Planetary Albedo, Atmos. Environ., 8, 1251–1256, 1974.

Twomey, S.: The influence of pollution on the shortwave albedo of clouds. J. Atmos. Sci., 34, 1149-1152, 1977.

Twomey, S.: Aerosols, clouds and radiation, Atmos. Environ., 25A, 2435–2442, 1991.

van der Werf, G. R., Randerson, J. T., Giglio, L., Collatz, G. J., Mu, M., Kasibhatla, P. S., Morton, D. C., DeFries, R. S., Jin, Y., and van Leeuwen, T. T.: Global fire emissions and the contribution of deforestation, savanna, forest, agricultural, and peat fires (1997–2009), Atmos. Chem. Phys., 10, 11707–11735, https://doi.org/10.5194/acp-10-11707-2010, 2010.

Wang, H. and Su, W.: Evaluating and understanding top of the atmosphere cloud radiative effects in Intergovernmental Panel on Climate Change (IPCC) Fifth Assessment Report (AR5) Coupled Model Intercomparison Project Phase 5 (CMIP5) models using satellite observations, J. Geophys. Res., 118, 683–699, https://doi.org/10.1029/2012JD018619, 2013.

Wang, Y., McFarquhar, G. M., Rauber, R. M., Zhao, C., Wu, W., Finlon, J. A., Stechman, D. M., Stith, J., Jensen, J. B., Schnaiter, M., J?rvinen, E., Waitz, F., Vivekanandan, J., Dixon, M., Rainwater, B., and Toohey, D. W.: Microphysical properties of generating cells over the Southern Ocean: Results from SOCRATES, J. Geophys. Res., 125, e2019JD032237, https://doi.org/10.1029/2019JD032237, 2020.

Weigel, R., Spichtinger, P., Mahnke, C., Klingebiel, M., Afchine, A., Petzold, A., Krämer, M., Costa, A., Molleker, S., Reutter, P., Szakáll, M., Port, M., Grulich, L., Jurkat, T., Minikin, A., and Borrmann, S.: Thermodynamic correction of particle concentrations measured by underwing probes on fast-flying aircraft, Atmos. Meas. Tech., 9, 5135–5162, https://doi.org/10.5194/amt-9-5135-2016, 2016.

Wilcox, E. M.: Stratocumulus cloud thickening beneath layers of absorbing smoke aerosol, Atmos. Chem. Phys., 10, 11769–11777, https://doi.org/10.5194/acp-10-11769-2010, 2010.

Witte, M. K., Yuan, T., Chuang, P. Y., Platnick, S., Meyer, K. G., Wind, G., & Jonsson, H. H.: MODIS retrievals of cloud effective radius in marine stratocumulus exhibit no significant bias.

Geophysical Research Letters, 45, 10,656–10,664. https://doi.org/10.1029/2018GL079325, 2018.

Wood, R.: Stratocumulus Clouds, Mon. Weather Rev., 140, 2373–2423, doi:10.1175/MWR-D-11-00121.1, 2012.

Wood, R. and Bretherton, C. S.: On the relationship between stratiform low cloud cover and lower-tropospheric stability, J. Climate, 19, 6425–6432, 2006.

Wood, R. and Hartmann, D. L.: Spatial variability of liquid water path in marine low cloud: the importance of mesoscale cellular convection, J. Climate, 19, 1748–1764, 2006.

Wood, R., Kubar, T. L., and Hartmann, D. L.: Understanding the Importance of Microphysics and Macrophysics for Warm Rain in Marine Low Clouds. Part II: Heuristic Models of Rain Formation, J. Atmos. Sci., 66, 2973–2990, doi:10.1175/2009JAS3072.1, 2009.

Xue, H. and Feingold, G.: Large eddy simulations of trade wind cumuli: investigation of aerosol indirect effects, J. Atmos. Sci., 63, 1605–1622, 2006.

Yamaguchi, T., Feingold, G., Kazil, J., and McComiskey, A.: Stratocumulus to cumulus transition in the presence of elevated smoke layers, Geophys. Res. Lett., 42, 10478–10485, https://doi.org/10.1002/2015GL066544, 2015.

Zeng, S., Riedi, J., Trepte, C. R., Winker, D. M., and Hu, Y.-X.: Study of global cloud droplet number concentration with A-Train satellites, Atmos. Chem. Phys., 14, 7125–7134, https://doi.org/10.5194/acp-14-7125-2014, 2014.

Zhang, Z. and Platnick, S.: An assessment of differences between cloud effective particle radius retrievals for marine water clouds from three MODIS spectral bands, J. Geophys. Res.-Atmos., 116, D20215, doi:10.1029/2011JD016216, 2011.

Zhou, X., Ackerman, A. S., Fridlind, A. M., Wood, R., and Kollias, P.: Impacts of solar-absorbing aerosol layers on the transition of stratocumulus to trade cumulus clouds, Atmos. Chem. Phys., 17, 12725–12742, https://doi.org/10.5194/acp-17-12725-2017, 2017.

Zinner, T., Wind, G., Platnick, S., and Ackerman, A. S.: Testing remote sensing on artificial observations: impact of drizzle and 3-D cloud structure on effective radius retrievals, Atmos. Chem. Phys., 10, 9535–9549, https://doi.org/10.5194/acp-10-9535-2010, 2010.

Zuidema, P., Redemann, J., Haywood, J., Wood, R., Piketh, S., Hipondoka, M. and Formenti, P.: Smoke and Clouds above the Southeast Atlantic: Upcoming Field Campaigns Probe Absorbing Aerosol's Impact on Climate, Bull. Am. Meteorol. Soc., 160129100143006, doi:10.1175/BAMS-D-15-00082.1, 2016.